GaAs Nano-Ridge Lasers Epitaxially Grown on Silicon

GaAs-nanorichellasers epitaxiaal gegroeid op silicium

Yuting Shi

Promotor: prof. dr. ir. D. Van Thourhout
Proefschrift ingediend tot het behalen van de graad van
Doctor in de ingenieurswetenschappen: fotonica

Vakgroep Informatietechnologie
Voorzitter: prof. dr. ir. B. Dhoedt
Faculteit Ingenieurswetenschappen en Architectuur
Academiejaar 2019 - 2020

ISBN 978-94-6355-330-8
NUR 965, 971
Wettelijk depot: D/2020/10.500/7

Universiteit Gent
Faculteit Ingenieurswetenschappen en Architectuur
Vakgroep Informatietechnologie

Promotor:

Prof. Dr. Ir. Dries Van Thourhout

Examencommissie:

Prof. Dr. Ir. Daniël De Zutter (voorzitter)	Universiteit Gent
Prof. Dr. Ir. Geert Morthier	Universiteit Gent
Prof. Dr. Benoit Bakeroot	Universiteit Gent
Prof. Dr. Ir. Andrea Fiore	TU/e
Dr. rer. nat. Bernardette Kunert	imec

Universiteit Gent
Faculteit Ingenieurswetenschappen en Architectuur

Vakgroep Informatietechnologie
Technologiepark-Zwijnaarde 126, 9052 Gent, België

Tel.: +32-9-264.33.30
Fax.: +32-9-331.35.93

Proefschrift tot het bekomen van de graad van
Doctor in de ingenieurswetenschappen: fotonica
Academiejaar 2019-2020

Acknowledgements

It was a coincidence that I switched my study field from electronics to photonics after graduation from college in 2013. I've always been curious about all aspects of the world, physics, biology, geography, the universe, etc. But at that time, I didn't find a way to fulfill my black-hole-like curiosity. A turning point appeared until another coincidence happened —I came to Ghent and followed the course of micro-photonics given by Prof. Roel Beats. I was suddenly lightened up by the vivid passion and deep understanding that Roel has towards photonics science and engineering. This drove me to dig the photonics world further by starting doing a Ph.D. research from 2015. This also allows me a new way to detect the world.

I knew people need some luck to have a friendly, patient, knowledgeable and graceful promoter to lead the way along their research, which could be lonely, tough, full of uncertainty and misunderstanding. I did not knew how luck brought me to meet such promoter—Prof. Dries Van Thourhout. In the past 4.5 years, I enjoyed every single discussion with him and felt excited for long afterward. To be honest, I failed to find out if it is because of the charm of scientific puzzles or his charisma. It was like I'm a stimulated photon excited by his rigorous logic reasoning and fancy ideas, promoted to work more efficiently and coherently like a laser.

I want to thank the rest of the members of my examination board: Prof. Dr. Ir. Daniël De Zutter, Prof. Dr. Ir. Geert Morthiers, Prof. Dr. Benoit Bakeroot, Prof. Dr. Ir. Andrea Fiore and Dr. rer. nat. Bernardette Kunert for their efforts in reviewing my thesis. Their incisive remarks and questions are highly valuable in achieving the final shape of the thesis.

I always complained that I was the only student in Ghent working on the nano-ridge topic. Of course, I was querulous because I'm aware that there is a big research family working on the same project in imec. Bernardette, if you have not grown such fancy nano-ridges, I believe many of us would have been unemployed. Joris, Marianna, Marina, Yannick, Nadezda and Cenk, although we only met once a month at the progress meeting, there were always sparkling discussions and brainstorms happening. You let me know how cheerful it is to work with you as a united front.

I want to express my thanks to the whole photonics research group. Steven, Liesbet and Muhammad, without you, I can not imagine how I have made my

lasers. Also a tip for new Ph.Ds: never test a new process when any of them are on holiday; otherwise, you will doubt the meaning of life. Micheal and Jasper, you've got magic hands to fix any bugs in measurement labs. All colleagues, because of your delightful talks and conversations, my work has been colorful in the rural area of Ghent.

My Chinese colleagues have been doing more than just being colleagues. Yanlu, Zhechao, Bin, Weiqiang, Yunpeng, Chen and Weiqiang willingly shared their senior experience, which smoothed the beginning of my Ph.D. Jing, Yufei, Xiaomin, Xiaoning, Chonghuai, Xiangfeng, Yang, Zuyang, Chupao, Mi and Hong, thank you for your company, no matter the hotpot parties or skiing trips. These moments made living in a place 8,000 km from China a warm experience.

Finally, I would like to sincerely thank my parents. I deeply understand who I am is strongly influenced and shaped by you from all aspects. These positive impacts came in a way full of love, supports and understandings. Freedom is a luxury for most Chinese children, who have to live a life that their parents expect. How lucky I am that I was always given the freedom and respect to explore whatever things that interested me. You let me foreseen the numerous possibilities in my life.

January 2020, Gent
Yuting Shi

Table of Contents

Acknowledgements **i**

Nederlandse samenvatting **xxv**

English summary **xxix**

1 Introduction **1-1**
1.1 Research background . . . 1-2
1.1.1 Si photonics integrated circuits . . . 1-2
1.1.2 III-V on Si . . . 1-6
1.1.3 III-V heteroepitaxy on Si - state-of-the-art . . . 1-11
1.2 Research objectives . . . 1-19
1.3 Outline of this thesis . . . 1-20
1.4 Publications . . . 1-21
1.4.1 Patent . . . 1-21
1.4.2 Publications in international journals . . . 1-21
1.4.3 Publications in international conferences . . . 1-22
References . . . 1-23

2 InGaAs/GaAs nano-ridge growth **2-1**
2.1 Introduction to heteroepitaxy . . . 2-2
2.1.1 Lattice mismatch . . . 2-2
2.1.2 Defect formation . . . 2-4
2.1.3 Approaches for heteroepitaxy . . . 2-7
2.2 Growth by aspect ratio trapping . . . 2-8
2.2.1 Introduction to ART and NRE . . . 2-8
2.2.2 Nano-ridge growth process . . . 2-11
2.2.3 Inspection of nano-ridge growth quality through electron microscopy . . . 2-12
2.3 Conclusion . . . 2-19
References . . . 2-20

3 Optical characterization of InGaAs/GaAs nano-ridges **3-1**
3.1 Electron-photon interaction . . . 3-2
3.1.1 Energy band diagram for the InGaAs/GaAs nano-ridge . . . 3-2
3.1.2 Effect of strain on optical gain . . . 3-4

3.2 Photoluminescence characterization 3-6
3.2.1 Setup 3-6
3.2.2 Results 3-8
3.3 Time-resolved photoluminescence characterization 3-10
3.3.1 Setup 3-10
3.3.2 Results 3-11
3.4 Characterisation of optical gain 3-21
3.4.1 Setup 3-22
3.4.2 Results 3-24
3.5 Conclusion 3-28
References 3-30

4 1 µm-wavelength nano-ridge lasers **4-1**
4.1 Transversal optical mode 4-2
4.2 Fabry-Perot laser 4-5
4.2.1 Cavity design 4-5
4.2.2 Results 4-7
4.3 Index-coupled DFB laser 4-9
4.3.1 Introduction 4-9
4.3.2 $\lambda/4$ shifted DFB simulation 4-12
4.3.3 Fabrication and Characterization 4-14
4.4 Loss-coupled DFB laser 4-21
4.4.1 Cavity simulation 4-22
4.4.2 Fabrication and Characterization 4-26
4.4.3 Alternative metallic grating 4-31
4.5 Conclusion 4-32
References 4-34

5 1.3 µm-wavelength InGaAs nano-ridge light emitter **5-1**
5.1 Extension of wavelength to 1.3 µm 5-2
5.2 InGaAs nano-ridge epitaxial growth 5-3
5.3 Optical characterization 5-6
5.3.1 Energy band diagram 5-6
5.3.2 Photoluminescence characterization 5-7
5.3.3 Time-resolved PL 5-8
5.3.4 Optical gain characterization 5-9
5.4 ASE in DFB cavity 5-11
5.4.1 Bragg grating simulation 5-12
5.4.2 Fabrication and Characterization 5-13
5.5 Conclusion 5-15
References 5-17

6 Proposals for coupling between nano-ridge and waveguide 6-1
6.1 Introduction: interface with Si devices 6-2
6.2 Integration Process and Design Methodology 6-3
6.2.1 Integration Process 6-3
6.2.2 Design Methodology and Simulation Tools 6-4
6.3 Directional coupler 6-5
6.4 Linearly Tapered Adiabatic coupler 6-7
6.4.1 Proposed Configuration 6-7
6.4.2 Optimisation of Coupler Width 6-8
6.4.3 Optimisation of Coupler Length 6-11
6.4.4 Tolerance to Fabrication Variations 6-16
6.5 Optimized Adiabatic Coupler 6-17
6.5.1 Proposed Configuration 6-17
6.5.2 Tolerance to Fabrication Variations 6-20
6.6 Conclusion 6-21
References 6-23

7 Conclusions and perspectives 7-1
7.1 Conclusion of the presented work 7-1
7.2 Perspectives for future work 7-4
References 7-6

A Fabrication of GaAs nano-ridge lasers A-1
A.1 Optimization of GaAs nano-ridge dry etching A-1
A.2 planarization with BCB A-3
A.3 Metalization for loss-coupled DFB laser A-4
References A-6

B Heating of nano-ridge laser device B-1
References B-4

List of Figures

1.1 Integrated transceiver from Intel. (a) transmitter integrated with hybrid laser with modulator for data encoding and a multiplexer to put 4 optical channel onto one fiber. (b) Receiver integrated with a coupler to receive incoming light with a demultiplexer to split optical signals and Ge-on-Si photodiodes to convert photons to electrons. Reproduced from [16] 1-4

1.2 8×28 Gbps PSM8 Chipset & 200 Gbps Module from Luxtera, wire bonding is used for electrical connections. Reproduced from [17]. 1-5

1.3 Schematic process flow for O_2 plasma-assisted SiO_2 covalent direct wafer bonding. Reproduced from [36]. 1-8

1.4 Release process for transfer printing. (a) III-V starting layer stack (source), (b) III-V device patterning on source substrate, (c) Tether definition and release etching, (d) Top view of tether on source substrate, (e) Pick-up of the coupon from the source substrate, (f) Printing of the III-V coupon to the SOI target substrate. Reproduced from [44]. 1-10

1.5 Epitaxial InAs QDs micro-disks on GoVS substrate. (a) Procedure of growing antiphase-domain-free GaAs thin films out of a highly ordered array of planar GaAs nanowires on Si substrates with diamond-shaped pockets. (b) AFM image of approximately 1 μm coalesced GaAs thin film grown on the nanowire arrays. The vertical bar is 25 nm. (c) Schematic of the as-grown structure. (d)(f) Cross- sectional TEM images of the V-grooved structure, showing stacking faults (indicated by the blue arrows) trapped by the Si pockets. Reproduced from [50]. 1-12

1.6 (a)-(c) SEM images of a fabricated micro-disk device. (d) 90° tilted zoomed in SEM image of the mesa. Reproduced from [50]. . 1-12

1.7 (a) High-angle annular dark-field scanning TEM image of the interface between the AlAs nucleation layer and a Si substrate. (b) Bright-field scanning TEM image of DFLs. (c) Dislocation density measured at different positions, as indicated in (b). (d) PL spectrum for a QD active region grown on Si. Inset: representative AFM image of an uncapped QD sample grown on Si. (e) High-resolution bright-field scanning TEM images of a single dot (top left), corrected high-angle annular dark-field scanning TEM images (false colour) of a single QD (bottom left) and bright-field scanning TEM image of the QD active layers (right). (f) Schematic of the layer structure of an InAs/GaAs QD laser on a Si substrate. (g) A cross-sectional SEM image of the fabricated laser with as-cleaved facets, showing very good facet quality. (h) SEM overview of the complete IIIV laser on Si. Reproduced from [57]. 1-13

1.8 Two-types of directional epitaxy after microchannel growth: horizontal microchannel epitaxy (left) and vertical microchannel epitaxy (right). Reproduced from [63]. 1-15

1.9 CELOG for threading dislocation filtration. Reproduced from [64]. 1-16

1.10 (a) A SEM image showing the well-faceted geometry of the nanopillar optical cavity. Reproduced from [65]. (b) Left: thirty degree-tilted SEM images of a nanowire array cavity integrated with a waveguide and an output coupler (upper), and a close-up image of the nanowire array in the dashed box (lower). Right: PL spectra measured on top of a nanowire array and on top of an output coupler above the lasing threshold. Reproduced from [67]. 1-17

1.11 (a) Cross-sectional TEM image of the InP/InGaAs nanowire perpendicular to the wire direction, showing five $\{111\}$ InGaAs QWs embedded inside a InP nanowire; the dark area at the InP/Si interface contains a high density of stacking faults generated for strain relaxation. (b) Schematic of the designed InP/InGaAs nanolaser array grown on a SOI substrate. (c) Fabrication process of the InP/InGaAs nanolaser on SOI. Reproduced from [72]. 1-18

1.12 (a) Schematic plot of the monolithically integrated InGaAs/InP DFB lasers on silicon. The silicon pedestal (and the silicon oxide hard mask) under the near end has been removed for a better view of the IIIV waveguide. (b) STEM image of a typical cross-section of the grown InGaAs/InP/Si waveguide. (c) A zoom-in STEM image of the InGaAs/InP interface. Reproduced from [75]. 1-18

2.1 Plot of bandgap energy vs. lattice constant of common semiconductors. The right axis indicates the corresponding wavelength. Reproduced from [4]. 2-2

2.2 Epitaxial growth of III-V material on substrate with the lattice constant $a_{III\text{-}V} < a_{sub}$, the epitaxial III-V material undergoes tensile strain. 2-3

2.3 Epitaxial growth of III-V material on substrate with the lattice constant $a_{III\text{-}V} > a_{sub}$, the epitaxial III-V material undergoes compressive strain. 2-3
2.4 Misfits formation after critical thickness h_{crt} to allow elastic strain relaxiation. 2-4
2.5 The formation of misfit dislocations (red line) at the interface of hetero-layer and substrate and threading dislocation (yellow line) along slip plane marked with dashed black lines. 2-6
2.6 planar defects (a)stacking faults (b) anti phase domain. Reproduced from [10]. 2-7
2.7 Sketch of aspect ratio trapping (ART) in narrow trenches. TDs gliding along a $\{111\}$ plane are trapped in both directions (a) and (b) whereas a PD is only trapped in a plane parallel to the trench orientation (c). A PD in a plane perpendicular to the trench sidewalls will penetrate the full III-V layer. Reproduced from [10]. . . 2-9
2.8 (a)-(d) are cross-section SEM images of GaAs nano-ridges deposited under very different MOVPE growth conditions. The simplified sketch next to each SEM image compares the growth rates on the different facets indicated by the size of the red arrow. Reproduced from [21]. 2-10
2.9 The GaAs nano-ridge epitaxy process. (a) the process starts with a Si wafer patterned with a SiO_2 mask using an STI step. (b) the Si trenches with V-shape are obtained by TMAH wet etching. (c) the growth of GaAs, first inside and then outside the trench. (d) the growth of three $In_{0.2}Ga_{0.8}As$ QWs. (e) top GaAs barrier is grown and (f) a passivation layer of InGaP is deposited. 2-11
2.10 The SEM images of the cleaved nano-ridges with trench width (a) 60 nm, (b) 100 nm, (c)300 nm and (d)500 nm on the same scale. . . 2-13
2.11 HAADF-STEM images of the GaAs nano-ridge waveguide of sample S_{Ref}. The right upper one shows zoomed-in QWs, and barriers while the lower STEM shows the InGaP passivation layer. 2-14
2.12 BF-STEM images of the nano-ridges of sample S_{Ref}. (a) lateral cut along nano-ridge for 100nm wide trench. (b) lateral cut along nano-ridge for 200nm wide trench (same scale with (a)), (c) a zoom-in image showing defects-free QW region, (d) a zoom-in image showing dislocations at GaAs/Si interface. 2-15
2.13 Images of sample S_{Ref}. (a)The pop view SEM image of nano-ridge array with trench width from 60 to 100 nm. (b) Tilted view of cleaved nano-ridge array with trench width of 80nm. 2-16
2.14 The (224) Resonance Shear Measurement(XRD-RSM) of the nano-ridge. QWs are fully strained to the fully relaxed GaAs nano-ridge and InGaP cap is lattice-matched 2-17
2.15 HAADF-STEM images of the GaAs nano-ridge waveguide of sample S'_{Ref}. The right image shows the GaAs root grown in SiO_2 trench. 2-17

3.1 Calculated energy band diagram of the nano-ridge at temperature 300 K(left) and 80 K(right) respectively. Only one QW is plotted in the image instead of 3QWs in the real samples. 3-4

3.2 Qualitative shifts of the conduction band and heavy-hole (HH) and light-hole (LH) levels in the valence band for unstrained, biaxial compressive and tensile strain. Reproduced from [10]. 3-5

3.3 Polarization-dependent gain spectra for 0.25% compressive strain (dotted) and tensile strain (solid) under $2 \times 10^{18} cm^{-3}$ carrier density injection. Reproduced from [11]. 3-6

3.4 Schematic diagram of the experimental PL setup. 3-7

3.5 The photoluminescence spectra of sample S_{Ref}. Nano-ridges with trench width from 20 nm to 500 nm under CW 532 nm excitation.(a) on linear scale (b) on logarithmic scale. 3-8

3.6 The PL spectra of an optimized nano-ridges sample S'_{Ref}. This selected sample is taken for laser device process in the following chapter. 3-9

3.7 Schematic diagram of the experimental TRPL setup. The cryo chamber is only used for the low T measurements. 3-11

3.8 (a)TRPL result of sample S_{Ref}, as function of wavelength and time. Dashed lines in wavelength span indicate integration interval over wavelength range for nano-ridge QWs and GaAs respectively. Dashed lines in time span show the time range for PL lifetime fitting range. (b) Nano-ridges QW PL integrated over wavelength 872 nm to 1100 nm as a function of time. The region in between the dashed lines again indicates the fitting range. 3-12

3.9 (a) Extracted PL lifetime for sample S_{Ref} with trench width from 20 nm to 500 nm at room temperature under 800 nm and 900 nm excitation wavelength respectively. (b) PL lifetime as a function of excitation power. The excitation power is chosen to be 500 μW for the other room-temperature measurement. 3-14

3.10 Room-temperature PL lifetime from the reference sample (S_{ref}) with 50 nm InGaP passivation layer, the sample without passivation layer $S_{0\times Cap}$ and the sample with 100 nm $S_{2\times Cap}$ passivation layer. (a) Lifetime τ_{QW} for QWs PL emission and (b) τ_{GaAs} for GaAs. 3-16

3.11 (a) XSEM image of nano-ridge with 2 QWs and an extra InGaP blocking layer. (b) PL lifetime of sample S_{Ref}, $S_{2\times QW}$, S_{blk1} and S_{blk2}. 3-17

3.12 Extracted PL lifetime for sample S_{Ref} and S_{dope} as a function of trench width from 20 nm to 500 nm at room temperature. 3-18

3.13 (a) Normalized spectra of sample S_{Ref} with 100 nm trench under 0.5 mW without cryo at 300 K, under 20 mW with cryo at 300 K and under 20 mW with cryo at 80 K respectively.(b) PL lifetime of sample S_{Ref} and $S_{0\times Cap}$ as a function of trench width at low temperature 80 K. The excitation is 750 nm in wavelength and 20 mW in power. 3-20
3.14 Schematic diagram of the VSL setup for characterizing optical gain. 3-22
3.15 CMOS camera images of edge coupling between nano-ridges(left) and lensed fiber(right) (a) under a magnification of 6×. (b) under a magnification of 50×. 3-23
3.16 The output power versus pump length, for sample S'_{Ref} at different pump intensities. Dots are experimental results and dashed lines are the fitting. The modal gain can be derived from the slope of the linear region. 3-24
3.17 The extracted model gain vs. pump power for nano-ridges with 80 nm, 100 nm, 150 nm and 200 nm trench respectively of sample S'_{Ref}. The HR-STEM images of three samples with 40 nm-, 100 nm- and 300 nm- trench are shown at the top. 3-25
3.18 The extracted model gain vs. pump power for nano-ridges with 100 nm, 150 nm and 200 nm trench respectively of sample S_{Ref}. . 3-26
3.19 The extracted modal gain vs pump power for nano-ridges with 2×QWs and 3×QWs respectively. The two samples are not listed in Table 2.2, but they are suppposed to have the same configuration as the reference sample except for the number of QWs. 3-27
3.20 The emission spectra of nano-ridges under different pump lengths of sample $S_{Ref'}$, at CW pump intensity $990W/cm^2$. PL peak redshifts with increasing pump length. 3-28

4.1 The first four optical modes of the nano-ridge with trench width 100 nm. The polarization of the modes is labelled at the bottom of the images. 4-3
4.2 The TE-like ground modes of the nano-ridges with trench width 60 nm, 80 nm, 100 nm and 120 nm (left to right). As the III-V volume increases with trench width, the optical field is better confined inside the larger nano-ridges. 4-5
4.3 (a) Simulation setup of etched nano-ridge facet with an angle $-30°$ (left) or $30°$ (right). (b) The reflectivity of etched Fabry-Perot cavity as a function of etched sidewall angle. 4-7
4.4 The SEM images of fabricated FP device. (a)A tilted view of the FP array. (b) A tilted view of one FP cavity facet. 4-8
4.5 The 80 μm long FP laser array under optical excitation seen by a Si CMOS camera. The luminescent array includes ten nano-ridges of each trench width from $20-150$ nm. Wider trenches are not visible as they are less luminescent under the same excitation. . . 4-9

4.6 (a) The spectrum of pumped nano-ridges with 100 nm trench width. (b) The output light in wavelength range $1000-1020$ nm as a function of pump intensity. 4-10
4.7 The calculated optical field reflection spectrum of the Bragg grating for four different values of coupling strength κL, versus the detuning parameter $\delta = \beta - \beta_0$. 4-12
4.8 The transfer function S_{21} spectra of three different kinds of index coupled DFB lasers (a)standard DFB laser (b) $\frac{\lambda}{4}$ shifted DFB laser (c) DFB with AR/HR coatings at the end facets. Source of figures [19]. 4-13
4.9 The side-view of the DFB laser with etched gratings at the top of the nano-ridge. The etch depth is set to be 110 nm which gives good index modulation and meanwhile leaves the QWs untouched. Duty cycle and the sidewall angle are set as 25% and 65°, as obtained from the fabrication results. 4-14
4.10 Bragg grating simulation result of 100 nm wide nano-ridge. (a) The stopband of the gratings versus grating period. (b) The field reflection spectra of the Bragg gratings with increasing number of grating periods N=50, 100, 200, 300. 4-15
4.11 The ebeam lithographic mask of the DFB gratings at the top of nano-ridges from 60 nm (right) to 500 nm (left). The trenches of nano-ridges are in purple lines and the gratings are depicted in green, which can be more clearly seen from the magnifications. . 4-16
4.12 Tilted SEMs of (a) a DFB laser array, (b) the zoomed-in $\lambda/4$ phase shift section, and (c) the second-order grating coupler section. . . 4-16
4.13 The same device region as shown in Figure 4.11 on a optically pumped sample seen by a Si CMOS camera. 4-17
4.14 (a) Room-temperature spectra of a DFB laser under different pump powers (100 nm trench width, 170 nm grating period, and 340 nm second-order grating coupler period). (b) L-L curve on logarithmic and linear (inset) scale of the measured DFB nano-ridge laser. Black circles and solid line represent the experimental data and the rate equations fit, respectively. 4-18
4.15 (a) Measured lasing spectra of DFB laser array with grating period 170 nm. (b) Lasing wavelength versus grating period for trench size varying from 60 nm to 120 nm. 4-20
4.16 Schematic diagram of the nano-ridge DFB device with metallic gratings on top. 4-22
4.17 (a) The refractive index profile along the PLC-DFB and the field distribution of the two first-order Bloch modes along the PLC-DFB. One is high-loss E_{BH} while the other is low-loss E_{BL}. (b) The calculated coupling strength and loss of a metallic grating with length of 300 μm as a function of grating duty cycle. 4-24

4.18 Modal gain of the InGaAs/GaAs nano-ridges at different pump intensity levels. The black squared dots are the experimental result already shown in Chapter 3, Figure 3.17 TW= 100 nm, the red dashed line is a fit to this experimental data. 4-26

4.19 (a)-(d) The top-view SEM images of PLC DFB lasers with grating duty cycle 0.17, 0.26, 0.37, 0.46 respectively. 4-27

4.20 (a) Spectra of a PLC DFB laser with grating duty cycle 0.37 under different pump intensities. (b) The Light-in Light-out curve of the same laser at its lasing peak 1024 nm in logarithm scale. Insert is the same data plotted in linear scale. 4-28

4.21 The spectra of PLC DFB lasers with grating duty cycle of 0.17, 0.26, 0.37, 0.46, 0.57 respectively, all under 417 kW/cm^2 excitation. 4-29

4.22 (a) The light-in light-out curves for PLC DFB lasers with grating duty cycle of 0.17, 0.26, 0.37, 0.46, 0.57 respectively. The dots are experimental data while the dashed lines are the fitting for their linear part with the intersections on horizontal axis the thresholds of lasers. (b) Experimental threshold with error bar, calculated threshold and the measured peak power of the lasers as a function of grating duty cycle. 4-30

4.23 The top-view SEM image of the fabricated device starting from a nano-ridge with a trench width of 100 nm. 4-32

4.24 Characterization of the device. (a) Emission spectra at different pump intensities and (b) the light-in light-out (L-L) curve of the 1019 nm peak 4-32

5.1 Bandgap vs. lattice constant of semiconductor compounds relevant for the nano-ridges. The materials of the $1\,\mu$m GaAs nano-ridges and the $1.3\,\mu$m InGaAs nano-ridges are highlight in blue and red, respectively. 5-4

5.2 The bright-field (BF) STEM image of 100 nm-trench GaAs nano-ridge with $In_{0.45}Ga_{0.55}As$ QWs. The sample is cut along nano-ridge where both the trench (bottom) and the QWs can be observed. Besides than the defects formed from the GaAs/Si interface, new defects formation in QWs appears. 5-4

5.3 The schematic of the cross-section of the $In_{0.25}GaAs$ nano-ridge array with $In_{0.45}GaAs$ QWs on Si substrate. The nano-ridges are planarized with $\sim 1\,\mu$m SiO_2 after the epitaxial growth. 5-5

5.4 The SEM image of cleaved 100 nm-trench $In_{0.25}GaAs$ nano-ridge array with $In_{0.45}GaAs$ QWs. The nano-ridges are planarized with $\sim 1\,\mu$m SiO_2. 5-6

5.5 The calculated energy band diagram of the $In_{0.25}GaAs$ nano-ridge at temperature 300 K. Only one QW is plotted in the image instead of three QWs in the real situation. 5-7

5.6 PL spectra of $In_{0.25}Ga_{0.75}As$ nano-ridges with trench width 60 nm, 80 nm, 100 nm and 120 nm, respectively under 411 W/cm^2 532 nm optical pumping. The peaks of the PL red-shift to $\sim 1.3\,\mu$m. . . . 5-8

5.7 The PL spectra of InGaAs nano-ridges with trench width 100 nm, excited by a 532 nm pulsed laser at different pump intensity from 6 kW/cm^2 to 127 kW/cm^2. 5-8

5.8 (a) The experimental TRPL result of 100 nm-trench $In_{0.25}GaAs$ nano-ridges as a function of wavelength and time. (b) Nano-ridges QW PL integrated over wavelength 1050 nm to 1150 nm as a function of time. The red crosses indicate the fitted data. 5-10

5.9 The extracted optical modal gain versus pump intensity. The data are from $In_{0.25}GaAs$ nano-ridges with 80 nm, 100 nm and 120 nm trench width. 5-11

5.10 The first three optical modes of the InGaAs nano-ridge with trench width 100 nm. The polarization and effective refractive index of the modes are labelled in the images. 5-12

5.11 The simulated Bragg stopband of etched gratings at the top of 100 nm-trench InGaAs nano-ridge with depth 100 nm as a function of grating period. 5-13

5.12 Tilted SEMs of a DFB laser array with $\lambda/4$ phase shift. Zoomed-in: the $\lambda/4$ phase shift section of a DFB device with trench width 100 nm. 5-14

5.13 The characterization of the DFB device. (a) The ASE spectra of the DFB device with period 232 nm at different optical pump intensities. (b) The light-in light-out curve of the device measured at the peak 1330 nm. 5-15

6.1 Tilted scanning electron microscopy (SEM) images of the nano-ridge array show the irregular shape of the end facets both at a front view and a end view. 6-2

6.2 Schematic cross-section of the proposed coupler, consisting of the active GaAs nano-ridge and the passive Si waveguide on Si layer. . 6-4

6.3 Proposed process flow of the III-V/Si coupler. (a) The process starts from a SOI wafer. (b) STI process to define high aspect ratio trench and Si WG by lithographic patterning, Si dry etch and SiO_2 deposition and CMP (chemical-mechanical polishing). (c) Prepare SiO_2 trench for III-V epitaxy by Si wet etch. (d) III-V nano-ridge epitaxy. Small structures(QWs and passivation layer) are not sketched. After this the sample is planarized with SiO_2, see Figure 6.2. 6-4

6.4 (a) The 3D schematic view of the directional coupler. (b) The calculated effective refractive indices of the TE-like and TM-like ground modes of the Si WG as a function of the width W_{Si} of the Si waveguide. The insert shows the lowest order TE-like mode of the III-V nano-ridge WG. 6-6

6.5 The 2-D top view of the optical field propagating in the coupler with $W_{Si} = W_{match} = 295$ nm at wavelength 1310 nm. 6-7

6.6 Coupling length and coupling efficiency as a function of wavelength. 6-8

6.7 (a) 3-D schematic view of the linearly tapered coupler. (b) Top view of the tapered coupler and the field profile of the TE-like modes at different cross sections of the coupler. 6-9

6.8 The overlap between TE-like supermode Ψ_{+}^{TE} and TE-like modes Φ_{III-V}^{TE} (solid lines) and Φ_{Si}^{TE}(dashed lines) of the standalone WGs as a function of W_{Si} for $W_{Gap} = 150$ nm, 240 nm and 320 nm respectively. 6-10

6.9 The effective refractive indices n_{neff} of the TE/TM-like ground modes of the separated III-V/Si WGs and of the first four supermodes as function of W_{Si}, for $W_{Gap} = 150$ nm (a) and 240 nm (b). 6-11

6.10 Simulation results for the configurations $W_{Gap} = 150$ nm, $W_1 = 235$ nm, $W_2 = 370$ nm. (a) shows the coupling to several modes as function of taper length L_2. (b) depicts the field exchange between the III-V nano-ridge and Si waveguide along the propagation axis for the optimised taper lengths $L_2 = 150\,\mu$m. 6-13

6.11 2-D image of the field exchange between the III-V nano-ridge and the Si waveguide for the optimised couplers with parameters in Figure 6.10. 6-14

6.12 Simulation results for the configurations $W_{Gap} = 240$ nm, $W_1 = 275$ nm, $W_2 = 315$ nm. (a) shows the coupling to several modes as function of taper length L_2. (b) depicts the field exchange between the III-V nano-ridge and Si waveguide along the propagation axis for the optimised taper lengths $L_2 = 310\,\mu$m. 6-15

6.13 2-D image of the field exchange between the III-V nano-ridge and the Si waveguide for the optimised couplers with parameters in Figure 6.12. 6-15

6.14 Coupling efficiency (left axis) and effective refractive index n_{III-V}^{TE} (right axis) as a function of (a) nano-ridge height variation, (b) width variation and (c) wavelength. 6-16

6.15 (a)The 3D schematic view of the advanced adiabatic coupler. (b) Top view of the optimized adiabatic coupler. The gap W_{Gap} and Si WG width W_{Gap} are functions of the propagation direction z. Note that W_{Gap} is measured from the side of the III-V trench, at the bottom of the nano-ridge, see Figure 6.2 6-18

6.16 (a) The calculated effective refractive index of the Si WG n_{neff} (left axis) and normalized coupling coefficient $\frac{\kappa(z)}{\kappa_{max}}$ as functions of propagation direction z. (b) Calculated Si WG width $W_{Si}(z)$ and gap $W_{Gap}(z)$ along taper. 6-18

6.17 Simulation results for the optimized adiabatic coupler configuration shown in Figure 6.16. (a) The coupling efficiency as a function of coupler length L. A coupling efficiency $\eta_C > 99\%$ can be reached for $L = 200\,\mu$m. (b) Field exchange between III-V nano-ridge and Si waveguide along propagation direction when $W_{Si}(\frac{L}{2}) = W_{match} = 295$ nm, $W_{Si}(0) = 280$ nm, $W_{Si}(L) = 310$ nm, $W_{Gap}(\frac{L}{2}) = 150$ nm, $W_{Gap}(0) = W_{Gap}(L) = 820$ nm, $L = 200\,\mu$m. 6-19
6.18 2-D image of field exchange between III-V nano-ridge and Si waveguide for $L = 200\,\mu$m for the optimized adiabatic coupler configuration shown in Figure 6.16. 6-20
6.19 Coupling efficiency of the optimized adiabatic coupler with length $200\,\mu$m as a function of (a) nano-ridge height variation, (b) width variation and (c) wavelength. 6-21

A.1 The SEM image of a GaAs sample after three-minute etching. The insert is a zoom-in image of the sidewall. A-2
A.2 (a)The SEM image of etched facets of a FP device array using an unoptimized etching recipe with a layer of photoresist (AZ5214) as mask. (b) The SEM image of an improved FP facet with Si_3N_4 hard mask. A-3
A.3 a)The SEM image of a planarized nano-ridge. (b)The SEM image of the same sample after dry etching grating at the top of the nano-ridge. A-4
A.4 (a) The top view of an incompletely lifted-off sample with 80 nm thick Au (b) The tilted view of a complete lifted-off sample. . . . A-4

B.1 The steady-state thermal simulation results under 37 mW optical excitation (threshold) for nano-ridge with (a) 40 nm-wide trench, (b) 100 nm-wide trench and (c) 150 nm-wide trench respectively. . B-2
B.2 Thermal simulation of 100 nm-wide-trench nano-ridge at an optical pump of 37 mW of (a) nano-ridge grown on SOI substrate, (b) nano-ridge grown on SOI substrate planarized with $2\,\mu$m SiO_2, (c) nano-ridge with SiO_2 planarization and Au metallization. B-3

List of Tables

2.1 GaAs nano-ridges parameters noted in Figure 2.11. d: trench width; a: ridge width; b: ridge height; c: position of the lowest QW. 2-14
2.2 The nano-ridge samples studied in this work. All of them are grown on a similar SiO_2-patterned substrate but with slightly different layer stacks or material compositions from the reference sample S_{Ref}. 2-18

4.1 The transverse electrical polarization fraction $TE\ fraction$, effective refractive index n_{neff}, QWs confinement factor Γ_{QW} and leakage loss α_{leak} of the first 4 modes of the nano-ridge with 100 nm wide trench. 4-4
4.2 The effective refractive index n_{neff}, QWs confinement factor Γ_{QW} and absorption of the TE-like ground modes of nano-ridge with trench widths 60 nm, 80 nm, 100 nm and 120 nm respectively. * The absorption coefficient of 532nm optical pump vertically illuminating sample surface. 4-5
4.3 The properties of 5 PLC DFB lasers. $\Lambda_{Au}/\Lambda(design)$ is the designed duty cycle while $\Lambda_{Au}/\Lambda(fab)$ is the measurement from SEMs of fabricated devices. $Loss_{Au}$ is the calculated metallic loss for mode E_{BL}. κL, g_{th}, I_{th} are calculated coupling strength, optical modal gain at threshold and laser threshold respectively. . . 4-31

5.1 InGaAs nano-ridges parameters noted in Figure 5.4. d: trench width; a: ridge width; b: ridge height. 5-6

6.1 Conditions imposed on W_1, W_2 by our requirements for high coupling efficiency and avoiding coupling to TM-like modes (Unit: nm). The gray-colored cells indicate inconsistent conditions, excluding these values W_{Gap} for practical implementation. 6-12

List of Acronyms

A

APB	Anti-Phase Boundary
APD	Anti-Phase Domain
AR	Anti-Reflection
ART	Aspect Ratio Trapping
ASE	Amplified Spontaneous Emission
AWG	Arrayed Waveguide Grating

C

CELOG	Corrugated Epitaxial Lateral Overgrowth
CMOS	Complementary Metal-Oxide-Semiconductor
CMP	Chemical Mechanical Polishing
CW	Continous Wave
CWDM	Coarse Wavelength Division Multiplexing

D

DFB	Distributed Feedback
DFL	Dislocation Filter Layer
DM	Dielectric Mirror
DPSS	Diode-Pumped Solid-State Laser
DWELL	Dot in a WELL
DWDM	Dense Wavelength Division Multiplexing

E

EBL Electron Beam Lithography
ECCI Electron Channeling Contrast Imaging

F

FDE Finite Difference Eigenmode
FDTD Finite-Difference Time-Domain
FP Fabry Perot
FSR Free Spectral Range
FWHM Full Width at Half Maximum

H

HBT Hetero-junction Bipolar Transistors
HEMT High Electron Mobility Transmissions
HH Heavy Hole
HR High Reflection

I

IC Integrated Circuit
ICP Inductively Coupled Plasma

L

LH Light Hole
LPE Liquid-Phase Epitaxy

M

MEMS Microelectronic Mechanic System
MBE Molecular-Beam Epitaxy
MCE Microchannel Epitaxy

MD	Misfit Dislocation
MMI	Multi-Mode Interferometer
MOSFET	Metal Oxide Semiconductor Field-Effect Transistors
MOVPE	Metalorganic Vapour-Phase Epitaxy
MZI	Mach-Zehnder Interferometer

N

NRE	Nano-Ridge Engineering

P

PCB	Printed Circuit Board
PCG	Planar Concave Grating
PD	Photodiode / Planar Defect
PECVD	Plasma-Enhanced Chemical Vapor Deposition
PIC	Photonic Integrated Circuit
PL	Photoluminescence
PLC DFB	Partly Loss-Coupled Distributed Feedback
PSM	Parallel Single Mode

Q

QD	Quantum Dot
QSFP	Quad Small Form-factor Pluggable
QW	Quantum Well

R

RIE	Reactive-Ion Etching
RSM	Reciprocal Space Mapping
RT	Room Temperature
R&D	Research and Development

S

SAG	Selective Area Growth
SEM	Scanning Electron Microscope
SLS	Strained-Layer superlattice
SMF	Single Mode Fiber
SMSR	Side Mode Suppression Ratio
SNR	Signal-to-Noise Ratio
SO	Split-off (bands)
SOI	Silicon On Insulator
STI	Shallow Trench Isolation
S/V	Surface-to-Volume Ratio

T

TD	Threading Dislocation
TDD	Threading Dislocation Density
TE	Transverse-Electric
TM	Transverse-Magnetic
TEM	Transverse-Electromagnetic / Transmission Electron Microscopy
TRPL	Time Resolved Photoluminescence

V

VCSEL	Vertical-Cavity Surface-Emitting Laser
VSL	Variable Strip Length

W

WDM	Wavelength-Division Multiplexing

X

XRD	X-ray Diffraction

Nederlandse samenvatting –Summary in Dutch–

Het aantal toepassingen van silicum gebaseerde fotonische geïntegreerde schakelingen (PICs) is in het afgelopen decennium explosief gegroeid, voornamelijk omdat voor hun fabricage gebruik kan gemaakt worden van mature technologieën uit de elektronica wereld. Verschillende passieve optische Si-componenten, zoals compacte golfgeleiders (waveguides, WGs), roosterkoppelaars, directionele koppelaars en golflengte demultiplexers, evenals actieve componenten zoals modulatoren en fotodetectoren, zijn al gedemonstreerd. Gezien Si een indirecte bandgap heeft, die efficiënte lichtemissie belemmert, is er echter een gebrek aan hoogwaardige optische bronnen monolithisch geïntegreerd op Si. Integratie van III-V halfgeleiders met een directe bandgap, die bekend staan als efficiënte lichtemitters, wordt beschouwd als de meest veelbelovende aanpak om dit probleem te overkomen. Maar gezien de aanzienlijke mismatch tussen de roosterconstante van Si ($\alpha_{Si} = 5.431$ Å) en die van de meeste III-V-halfgeleiders, die een roosterconstante vertonen tussen 5.6 Å and 6.5 Å, blijft directe integratie een aanzienlijke uitdaging. Om dit probleem te omzeilen, zijn hybride en heterogene integratieprocessen ontwikkeld. Deze technieken zijn bruikbaar voor een breed scala van materialen en apparaten, maar introduceren extra processtappen, wat leidt tot een reductie van de yield en throughput.

Naast de twee bovengenoemde benaderingen wordt algemeen aangenomen dat III-V heteroepitaxiale groei op Si de ultieme oplossing is in termen van schaalbaarheid en kosten. Daarbij moeten altijd specifieke groeitechnieken worden gebruikt om de defecten die door rooster-mismatch worden geïntroduceerd te reduceren. Het gebruik van tussenliggende bufferlagen (bv. Ge/GeSi/Si-substraten) die een geleidelijke aanpassing van de roosterconstante mogelijk maken, kan het aantal defecten gevoelig doen afnemen. Een alteratief is selectieve groei (selective area growth, SAG) van III-V, waarbij groei alleen is toegestaan in vooraf gedefinieerde gebieden. Verticale nanodraden, gegroeid in nanoschaalopeningen, ontlasten bijvoorbeeld efficiënt de rek aan de interfaces en kunnen daarom vrij zijn van dislocaties.

Gedreven door de snelgroeiende markt van PICs, begon imec enkele jaren geleden met het ontwikkelen van GaAs/InGaAs nanorichels, heteroepitaxiaal gegroeid op standaard 300 mm Si-wafels voor fotonica-toepassingen. De heteroepitaxie van de nanorichels combineert twee technieken: aspect ratio trapping (ART), die toelaat om efficiënt defecten te blokkeren in nauwe SiO_2 openingen en nanorichel

engineering (NRE), waarbij de groeiomstandigheden worden geoptimaliseerd om nanorichels met gewenste afmetingen te vormen boven de nauwe maskeropeningen. De SiO_2 openingen werden nat geëtst om $\{111\}_{\rm Si}$ oppervlakken te creëren die anti-fase domeinen voorkomen. De defectdichtheid van de nanorichels kan tot een extreem laag niveau worden onderdrukt, met een bovengrens voor de dislocatiedichtheid van 3×10^6 cm^{-2} (gemeten door elektronenkanaalcontrastbeeldvorming, ECCI). Verdere inspectie toonde aan dat het GaAs volledig gerelaxeerd is, dat de roosterconstante van de InGaP passivatielaag gematched is aan die van GaAs en dat de QWs onder compressieve spanning staan. M.b.v. elektronenmicroscopie vonden we sterke correlaties van de defectdichtheid met de breedte van de openingen in het SiO_2 masker: nanorichels gegroeid in bredere openingen (vaste hoogte) bevatten meer defecten.

- **Resultaten**

Het werk beschreven in dit proefschrift maakt deel uit van het imec nanorichelprogramma, gewijd aan het demonstreren van op nanorichel gebaseerde lichtbronnen op het Si-fotonica platform. Voordat met de demonstratie van effectieve componenten werd begonnen, werden de gegroeide materialen eerst optisch gekarakteriseerd. Meten van het foto-luminescentie spectrum, ladingsdragerlevensduur en optische versterking, lieten toe om een beter inzicht in de materiaalkwaliteit van de nanorichels te verkrijgen. De berekening van het energiebanddiagram van de GaAs nanorichel laat zien dat de E_{1-1HH} overgang in het $In_{0.2}Ga_{0.8}As$ kwantumput fotonen kan genereren met een golflengte van $1\,\mu$m. Deze theoretische berekening werd geverifieerd tijdens de PL-karakterisering, die een duidelijke emissiepiek vertoonde bij $1.02\,\mu$m. De PL-levensduur van de nanorichels werd bepaald m.b.v. een tijdsgeresolveerde PL (TRPL) setup, bij zowel 300 K als 80 K (in samenwerking met de groep van N. Gherhardt, Universiteit Bochum). Deze metingen bevestigden de correlatie tussen de breedte van de maskeropeningen en de defectdichtheid. Bovendien toonden deze metingen aan dat oppervlakte-recombinatie en recombinatie ter hoogte van de defecten in de nauwe maskeropeningen de belangrijkste overblijvende verliesmechanismes zijn voor de ladingsdragers. Het passiveren van de nanorichel met een InGaP-laag en het toevoegen van een InGaP blokkeringslaag onderdrukken deze verliezen sterk en verlengt de PL-levensduur tot 2 ns. Ook de karakterisering van de optische versterking door middel van een "variable stripe length"methodiek vertoont de correlatie tussen defectreductie en breedte van de maskeropening. De optische winst van het optimale materiaal werd geschat op meer dan 5000 cm^{-1}, wat vergelijkbaar is met conventioneel GaAs-materiaal. De optische karakterisering bevestigen dat het combineren van ART en NRE de integratie van hoogwaardige III-V nanorichel materialen op Si-substraten voor lasertoepassingen mogelijk maakt.

Eens de optische eigenschappen van de nanorichels goed begrepen waren, werden Fabry-Perot (FP) lasers, index-gekoppelde DFB-lasers en gedeeltelijk verliesgekoppelde (partly loss-coupled, PLC) DFB-lasers gedemonstreerd. De FP-lasers met twee geëtste facetten vertoonden emissie bij meerdere golflengtes. Vervolgens

werden meer geavanceerde indexgekoppelde DFB-lasers ontwikkeld, die single-mode lasing onder optisch pompen, bij kamertemperatuur, vertonen. De meting van deze lasers toonde een sidemode-onderdrukking van meer dan $28\,$dB, een drempel van $33\,$kW/cm^2 (37 mW) voor een $102\,\mu$m lang DFB-laser en de optie om de laseremissiegolflengte nauwkeurig te selecteren, zowel door aanpassing van de roosterperiode als door aanpassing van de richelbreedte. Vervolgens presenteerden we PLC DFB-lasers met een metaalrooster gedefinieerd op de bovenkant van de nanorichel. De optimalisatie van de vulfactor van het rooster maakt het mogelijk het verlies in het metaal en de koppelingssterkte te balanceren. De PLC DFB nanorichel lasers vertonen single-mode laserwerking en een drempelwaarde van $\sim 10\,$kW/cm^2 bij een geoptimaliseerde roostervulfactor van 0.4. De succesvolle demonstratie van verschillende soorten lasers bewijst de hoge kwaliteit van de nanorichels en wijst op de haalbaarheid van elektrische injectie in de toekomst.

Gezien de huidige telecommunicatiesystemen bij golflengtes in het gebied $1.3 - 1.6\mu$m opereren, ontwikkelde het epi-team van imec een nieuwe generatie nanorichels, waarbij $In_{0.45}Ga_{0.55}As$ kwantumputlagen gegroeid werden in een $In_{0.25}Ga_{0.75}As$ nanorichel. De PL-spectra van deze InGaAs-nanorichels vertoont brede spectra met een piek rond $1350\,$nm. Niettemin blijkt de emissie die wordt waargenomen bij TRPL-metingen onder een hoge pompintensiteit alleen uit de $In_{0.25}Ga_{0.75}As$ nanorichel te komen. Dit toont aan dat het PL-signaal van de $In_{0.45}$-$Ga_{0.55}As$ QWs extreem snel vervalt. De gemeten PL-levensduur voor de InGaAs-nanorichel is $191\,$ps, veel korter dan die voor de GaAs nanorichel. De gemeten modale winst is $200\,$/cm bij $300\,$kW/cm^2, ook lager dan die voor de GaAs nanorichel ($350\,$/cm). Om lasing van dit materiaal aan te tonen, werd een indexgekoppelde DFB-caviteit ontworpen en gefabriceerd voor O-bandemissie. De karakterisering van een dergelijke component vertoonde een enkele piek bij $1330\,$nm bij een lage pompintensiteit, maar helaas begon een ongewenste piek bij $1220\,$nm te verschijnen wanneer het pompvermogen toenam. De onverwachte piek wordt verondersteld de emissie van de nanorichel zelf te zijn. Hoewel verdere verbetering van de kristalkwaliteit vereist is, geven deze experimenten aan dat O-bandemissie van QWs met een verhoogde Indium-fractie in principe mogelijk is.

Om de koppeling tussen III-V-nanorichels en standaard Si-fotonica componenten te adresseren, werden nieuwe adiabatische koppelaars voorgesteld die in de O-band werken. De koppelingen zijn compatibel met het hierboven beschreven epitaxyproces en vereisen geen extra processen om ze te fabriceren. We hebben eerst aangetoond dat een directionele koppelaar een efficiëntie van 100% kan bereiken, maar zeer gevoelig is voor proces- en golflengtevariaties. Om dit te verbeteren, wordt een robuust lineair taps toelopende adiabatische koppeling voorgesteld, die toleranter is voor procesvariaties en nog steeds een koppelingsefficiëntie van 98% kan bereiken. Dit gaat echter ten koste van grotere afmetingen en enige resterende koppeling met ongewenste modi. Om te voorkomen dat deze ongewenste koppeling de laserwerking beïnvloedt, werd vervolgens een geavanceerdere adiabatische koppelaar voorgesteld, die de modi aan het begin en het einde van de koppeling beter ontkoppelt. De afmetingen van de geoptimaliseerde adiabatische koppelaar zijn zodanig gekozen dat een koppelingsefficiñtie $> 99\%$ wordt bereikt voor een kop-

pelingslengte van 200 μm, zonder koppeling naar ongewenste modi. De tolerantie met betrekking tot procesvariaties van de geoptimaliseerde adiabatische koppeling is niet zo goed als die van de lineaire koppelaar maar kan worden verbeterd door de lengte te vergroten. Op deze manier biedt het ontwerp, afhankelijk van de toepassing, de vrijheid om te optimaliseren naar compacte afmetingen of naar hoge toleranties voor procesvariaties. Van de gepresenteerde adiabatische koppelingen wordt verwacht dat ze III-V lasers verbinden met het on-chip Si-fotonica circuit en helpen bij het verder ontwikkelen van het potentieel van de heteroepitaxiale III-V lasers om complexere circuits te realizeren.

- **Conclusie en perspectieven**

Dit doctoraatswerk presenteert de ontwikkeling van een nieuw materiaalplatform - InGaAs/GaAs nanorichels monolithisch gegroeid op 300 mm Si-substraten - voor de realisatie van geïntegreerde lasers. De optische eigenschappen van dit materiaal werden experimenteel onderzocht en voor het eerst werden optisch gepompte single-mode lasers gedemonstreerd in dit platform. Ook verdere verkennende studies, inclusief de ontwikkeling van alternatieve laserconcepten compatibel met elektrische injectie, de uitbreiding van de emissiegolflengte naar de O-band en de koppeling met externe Si-componenten, werden uitgevoerd. Desalniettemin staat dit onderzoek nog maar in zijn kinderschoenen. Er moeten nog grote inspanningen worden gedaan om mature en betrouwbare lasers compatibel met commerciële toepassingen te realiseren. Zo zijn bv. het verder verbeteren van de materiaalkwaliteit om CW-gepompte laserwerking mogelijk te maken, de realisatie van elektrische injectie, de verschuiving van de golflengte naar de O-band en de C-band, en uiteindelijk de integratie met standaard Si-componenten nog nodig.

English summary

- **Introduction**

The market size of Si photonic integrated circuits (PICs) has gained explosive growth in the past decade by leveraging the well-established Si complementary metal-oxide-semiconductor (CMOS) platform. Various passive Si optical components, including highly-confining waveguides (WGs), grating couplers, directional/tapered couplers and arrayed waveguide gratings (AWGs), as well as some active devices such as modulators and photodetectors, have been demonstrated. However, given the fact that Si has an indirect bandgap, which inhibits efficient light emission, there is a lack of high-performance optical sources monolithically integrated on Si. Integration of direct-bandgap III-V semiconductors, which are known as efficient light emitters, is believed to be the most promising approach. Nevertheless, given the significant lattice mismatch between Si ($\alpha_{Si} = 5.431\,\text{Å}$) and most direct-bandgap III-V compounds, which exhibit a lattice constant between $5.6\,\text{Å}$ and $6.5\,\text{Å}$, direct integration remains a considerable challenge. To circumvent this issue, hybrid integration and heterogeneous integration have been developed. These techniques are applicable for a wide range of materials and devices, but introduce extra processing steps, making the integration complicated and not compatible with mass production.

Besides the two approaches mentioned above, III-V heteroepitaxial growth on Si is broadly believed to be the ultimate solution in terms of scalability and cost. Specific growth techniques are always employed to reduce the defects introduced by lattice mismatch. Exploiting intermediate buffer layers or graded Ge/GeSi/Si substrates to enable a gentle gradient of lattice mismatch improves the defect density several folds. Also, inserting strained-layer superlattices is found helpful to reduce threading dislocations (TDs). However, instead of growing on a blanket substrate, selective area growth (SAG) of III-V, whereby growth is only allowed at defined areas, has specific advantages. For example, vertical nanowires grown on nanoscale openings are efficiently relaxed at the interfaces and, therefore, can be free of TDs.

Driven by the rapidly growing market of PICs, imec started to develop novel GaAs/InGaAs nano-ridges heteroepitaxially grown on standard 300 mm Si wafer for photonics applications several years ago. The heteroepitaxy of the nano-ridges combines two techniques: aspect ratio trapping (ART) to efficiently trap defects inside narrow SiO_2 trenches and nano-ridge engineering (NRE), by which the growth conditions are optimized to form box-shaped nano-ridges above the de-

fective trenches. The SiO_2 trenches were wet-etched to have $\{111\}_{Si}$ surfaces to eliminate anti-phase boundaries. The defect density of the nano-ridges can be suppressed to an extremely low level, with an upper limit of TD density of 3×10^6 cm^{-2}, measured by electron channeling contrast imaging (ECCI). Furthermore, the (224) reciprocal space map (RSM) measurement using X-ray diffraction (XRD) shows fully relaxed GaAs, lattice-matched InGaP cap and fully strained-to-GaAs QWs of the nano-ridge. Through electron microscopy inspections, we found strong correlations of the defect density with the aspect ratio of the trenches: nano-ridges with broader trenches (fixed height) contain more defects.

- **Results**

Starting from 2015, this thesis work is a part of the GaAs nano-ridge program, devoted to demonstrating nano-ridge based light sources on the Si photonics platform.

Before commencing on the device aspect of the work, optical characterization of the as-grown materials, i.e., the measurements of photoluminescence, PL lifetime and optical gain, were first experimentally conducted to obtain a fundamental understanding of the material quality of the nano-ridges. The calculation of the energy band diagram of the GaAs nano-ridge shows that the E_{1-1HH} transition in the $In_{0.2}Ga_{0.8}As$ QWs emit photons at a wavelength of $1\,\mu$m. This theoretical calculation was verified by the PL characterization, which showed a distinct emission peak at $1.02\,\mu$m. The PL lifetime of the nano-ridge was characterized on a time-resolved PL (TRPL) set-up at both 300 K and 80 K. The close dependence of the reduction of defect density on narrow trenches with a high aspect ratio was confirmed. Besides, surface recombination and recombination in defective trenches were found to be two loss mechanisms of carriers. Passivating the nano-ridge with an InGaP cap and inserting a carrier-blocking layer of InGaP strongly suppress the loss and prolong the PL lifetime up to 2 ns. The characterization of the optical gain by variable stripe length (VSL) approach shows excellent agreement with defects reduction by ART too. The optical gain of the optimal material was estimated to be above 5000 cm^{-1}, which is comparable with conventional GaAs material. The optical characterizations confirm that combining ART and NRE enables the integration of high-quality III-V nano-ridge materials on Si substrates for laser application.

With the optical properties of the nano-ridges well understood, Fabry-Perot (FP) lasers, $\lambda/4$-shifted index-coupled DFB lasers and partly loss-coupled (PLC) DFB lasers were demonstrated. The FP lasers with two etched facets showed multiple-peak emission. Then more advanced $\lambda/4$-shifted index-coupled DFB lasers were developed, demonstrating optically pumped room-temperature single-mode lasing. The measurement of these devices showed a sidemode-suppression ratio better than 28 dB, a threshold of 33 kW/cm^2 (37 mW) for a $102\,\mu$m long DFB device and the ability to precisely control the laser emission wavelength by both grating design and trench width. Next, we presented PLC DFB cavity formed by a metallic grating deposited at the top of the nano-ridge. The optimization of the grating duty cycle allows to balance the cavity mode loss and the coupling strength.

The PLC DFB nano-ridge lasers established single-mode lasing and a threshold of $\sim 10\,\text{kW/cm}^2$ at an optimized grating duty cycle of 0.4. The successful demonstration of different types of lasers proves the high quality of the nano-ridges and provides a first feasibility test towards future electrical injection.

To align with nowadays optical communication systems working with $1.3 - 1.6\mu\text{m}$ wavelengths, $In_{0.25}Ga_{0.75}As$ nano-ridges with $In_{0.45}Ga_{0.55}As$ QWs were grown by on Si by imec to extend the emission wavelength beyond $1.3\mu\text{m}$. The static PL characterization of the InGaAs nano-ridges exhibits broad spectra from the QWs emission centered around $1350\,\text{nm}$. Nevertheless, the emission observed in TRPL measurement under a high pump intensity is found to originate from the barriers only, revealing that the PL signal from the $In_{0.45}Ga_{0.55}As$ QWs decays extremely fast. The extracted PL lifetime for the InGaAs barrier is $191\,\text{ps}$, much shorter than that for GaAs nano-ridge. The extracted modal gain is $200\,\text{/cm}$ at $300\,\text{kW/cm}^2$, also lower than that for GaAs nano-ridge ($350\,\text{/cm}$). In order to demonstrate lasing from this material, a $\lambda/4$-shifted index-coupled DFB cavity was designed and fabricated for O-band emission. The characterization of such a device showed a single peak at $1330\,\text{nm}$ at a low pump intensity, but unfortunately, an undesired peak at $1220\,\text{nm}$ started to appear when the pump power increased. The unexpected peak is thought to be the emission from the barrier. Although further improvement of the crystal quality is demanded, we have shown O-band emission from QWs with an increased Indium fraction as a first trial to extend the emission wavelength.

To address the interfacing between III-V nano-ridges and standard Si photonics devices, novel adiabatic couplers working in the O-band were proposed. The couplers are compatible with the process for the monolithic epitaxy of GaAs on Si using ART and NRE and require no extra effort to fabricate. We first showed that a directional coupler design can reach a coupling efficiency of 100% but is very sensitive to process and wavelength variations. To improve this, a more robust linearly tapered adiabatic coupler is presented, which is more tolerant to process variations and can still achieve a 98% coupling efficiency. However, this comes at the cost of an increased footprint and some residual coupling to unwanted modes. To prevent this undesired coupling from influencing the laser operation, a more advanced adiabatic coupler, which better decouples the modes at the beginning and end of the coupler, was then proposed. The dimensions of the optimized adiabatic coupler are varied in a way such that a coupling efficiency $> 99\%$ is achieved for a coupler length of $200\,\mu\text{m}$, without coupling to undesired modes. The tolerance with respect to process variations of the optimized adiabatic coupler is not as good as that of the linearly tapered coupler but can be improved by increasing the taper length. In this way, the design provides, depending on the application, the freedom to optimize either towards compact size or towards high processing tolerance. The presented adiabatic couplers are expected to connect III-V devices with the whole on-chip Si photonics circuit and helps explore the potential of the heteroepitaxial III-V to make more complex and fundamental devices.

- **Conclusion and perspectives**

To conclude, this Ph.D. work presented the development of a leading-edge material - the novel InGaAs/GaAs nano-ridge monolithically grown on 300 mm Si substrate for light source applications. The optical properties of this material were experimentally investigated, and single-mode lasing under optical pumping was demonstrated for the first time. Further explorations on the nano-ridges, including alternatives for electrical injection, the extension of the emission wavelength to the O-band and the interfacing with external Si devices, were also conducted.

Due to the limited time, this four-year work was only able to do some initial research in the infancy of the nano-ridge development. Great efforts still have to be invested in producing mature devices for the commercial market. Full exploitation of the epitaxial nano-ridges includes but not limits to improving the material quality to enable CW-pumped lasing, realizing electrical injection, extending the operating wavelength to the O-band and even the C-band, and finally developing the III-V nano-ridges on Si into a more versatile platform with diverse active III-V devices and passive Si components.

1 Introduction

For over a half-century, electronic followed Moore's law stating that the number of transistors in integrated circuits (IC) doubles every two years [1]. By the early 2020s, the feature size of the smallest complementary metal-oxide-semiconductor (CMOS) transistors will probably get to the limit of $2-3$ nm, where the size is just ~ 10 atoms across [2]. This exponential growth of the device density has fuelled faster logical and memory devices and lower cost per device in digital processing systems. Nevertheless, the electrical interconnections did not keep scaling up with the devices due to the huge loss at high frequencies in electrical wires. To overcome this limit, a better interconnection medium can be the solution. Optical interconnections, without the limitations brought by electrical resistance and capacitance, are superior in low-power-cost and high-speed applications. They use photons to generate, transmit, detect and process information more efficiently. Leveraging the well-established CMOS manufacturing processes developed initially by the electronics industry, optics on Si substrates—Si photonic integrated circuits (PICs)—has been intensively studied for over a decade. The applications of Si PICs have been extended from interconnections in the data center to long-distance fiber-optic communication, computing, sensing, etc.

In this Chapter, we will first introduce the current state-of-the-art for Si PICs through some examples of commercial products in subsection 1.1.1. This will be followed by a discussion on the challenges that Si PICs face, especially the lack of efficient light sources. In subsection 1.1.2, the most popular approaches to integrate III-V materials, including bonding, transfer printing and heteroepitaxy, as a solution for on-chip light sources, will be introduced. Among the different

approaches, III-V epitaxially grown on Si, which is the topic of this thesis, is widely considered as the ultimate technique. We will review the state of art of III-V materials grown on Si conducted worldwide in subsection 1.1.3. In Section 1.2 and 1.3, the objectives and outline of this thesis are given. The publications are listed in Section 1.4.

1.1 Research background

1.1.1 Si photonics integrated circuits

Analogous to the concept of electronic IC, integrated optics was first introduced in 1969 to minimize the size of optical circuits [3]. Compared to free space optics, integration on one substrate saves space and, more importantly, strengthens the tolerance to ambient temperature/humidity gradients and mechanical vibrations. Research of Si PICs, motivated by the success of the well-established Si CMOS platform, started initially in the 1980s and accelerated in the early 2000s. A broad range of applications were investigated thus far, but in particular telecommunication and interconnection in data centers where breakneck speed and low power consumption (down to 10 fJ/bit) are typically required [4] came into focus. In line with the establishment and commercialization of fiber-optic communication system, whereby $1.3\,\mu$m- (the so-called optical O-band) and $1.5\,\mu$m-wavelength (the so-called optical C-band) light suffers the least dispersion and the lowest propagation loss respectively, Si PICs were first and most developed for the O-band and C-band wavelength ranges.

Si passive devices

Throughout all the passive photonic devices, low-loss integrated transmission lines for photons - waveguides - are the most fundamental component. In Si PICs, the waveguides always consist of high-index Si (refractive index $n \approx 3.5$ at $1.31\,\mu$m) or Si_3N_4 ($n \approx 2$ at $1.31\,\mu$m) as core and low-index SiO_2 ($n \approx 1.44$ at $1.31\,\mu$m) and/or air ($n \approx 1.0$) as cladding. Si is transparent at O-band and C-band wavelengths if multiple-photon absorption is not considered, but the scattering loss caused by the roughness of waveguide side surfaces can be problematic. The loss of rectangular single-mode Si waveguide on Silicon-on-insulator (SOI) wafer with a size of $450\,nm \times 220\,nm$ is now routinely below 1.8 dB/cm, due to improved fabrication processes based on 193 nm lithography [5]. Further reduction in the loss could be achieved by using rib waveguides, with a reported propagation loss of ~ 0.5 dB/cm for single-mode Si rib waveguide [6].

Fuelled by the achievement of low-loss Si waveguides on SOI substrate, almost all key passive components needed in optical data communication have been demonstrated [7]. The insertion loss of connecting an optical fiber directly to a

Si PIC chip is far from acceptable, as the huge mode mismatch between a single-mode fiber (SMF) with a core diameter of $9\,\mu$m and a Si waveguide with a width of 450 nm at $1.3\,\mu$m wavelength induces $15-20$ dB loss. Si couplers such as inverse tapers and grating couplers could reduce the coupling loss to ~ 0.5 dB [8] and < 3 dB respectively. Also several type of splitters, including Y-junction, directional coupler and multimode interference (MMI) coupler, have been investigated. Among them, MMI couplers are popular due to their compact size [9], large bandwidth, low excess loss down to 0.2 dB [10] and fabrication-tolerant operation. Wavelength selective devices, including ring resonators, Mach-Zehnder interferometers (MZIs), arrayed waveguide gratings (AWGs) and planar concave gratings (PCGs) [11], are essential devices for wavelength division multiplexing (WDM) communications and sensing. Ring resonators in SOI can be scaled down to $10 \times 10\,\mu m^2$ and yield very sharp channel selection with a free spectral range (FSR) larger than 10 nm. A MZI consists of two optical arms, whereby the interference generates a sinusoidal filter characteristic.

Si active devices

Besides these passive devices, also active devices that generate, modulate and detect light are essential. Unfortunately, Si with an indirect bandgap of 1.14 eV (1090 nm) at room temperature, is an inefficient light emitter. Although Si Raman lasers have been demonstrated [12], they showed a very low radiant efficiency and required critical working conditions, like high optical pump power, low temperature and mitigation of two-photon absorption induced optical losses. Optical modulators typically exploit either the electro-optic Pockels effect, which modifies the refractive index by applying a field, or the electro-absorption effect, which changes the intensity of the light. Because of the lack of a strong electro-optic effect in silicon, the thermo-optic effect micro-electro-mechanical systems (MEMS) or carrier manipulation (refractive index changed by manipulating carriers in a PN junction) can be utilized for realizing Si modulators. However, both the thermal effect and MEMS are slow, making that Si modulators based on carrier manipulation are dominant for high-speed applications, with now device speeds beyond 50 Gb/s routinely demonstrated. Finally, Si is a rather poor absorber at wavelengths longer than 1100 nm. Even though two-photon absorption happens in this wavelength range, the low efficiency has driven the search for new materials to be integrated on Si. Instead of Si, Ge monolithically grown on Si has been developed as the dominant approach for photodetector (PD) application owing to its excellent optoelectronic properties [13]. The state-of-the-art Ge-on-Si PD is reported a bandwidth higher than 50 GHz [14].

Noteworthy commercial products

After decades of study, numerous high-performance Si photonic devices have now been demonstrated and Si photonics has made the transition from pure re-

search to practical applications. Many of the semiconductor giants have claimed activities in the Si photonics area. Numerous start-ups, e.g., Luxtera (now acquired by Cisco), Sicoya, Kotura (now acquired by Mellanox), are also actively developing Si PICs. Several commercial products that integrate electronics and photonics on a CMOS platform have hit the market for some time now [15]. To scale up the bandwidth, two configurations are adopted: parallel single mode (PSM) channels, which uses parallel single-mode fiber (SMF) for each channel and wavelength division multiplexing (WDM), which combines multiple signals at various wavelengths in one fiber.

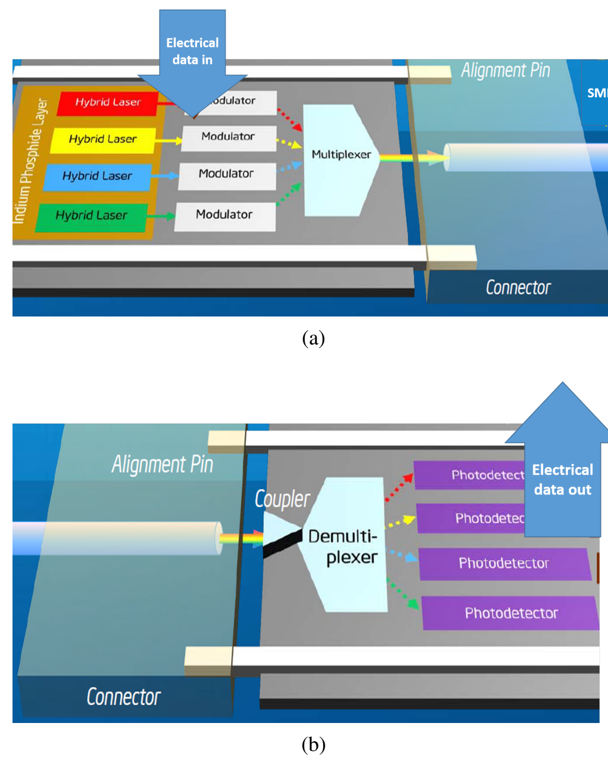

Figure 1.1: Integrated transceiver from Intel. (a) transmitter integrated with hybrid laser with modulator for data encoding and a multiplexer to put 4 optical channel onto one fiber. (b) Receiver integrated with a coupler to receive incoming light with a demultiplexer to split optical signals and Ge-on-Si photodiodes to convert photons to electrons. Reproduced from [16]

Intel claims that it has been the top one provider of 100G CWDM4 (coarse WDM) QSFP (quad small-factor pluggable) optics for the last six quarters [16]. The integrated transmitter/receiver chip and driver ICs on printable circuit board (PCB) enables high volume assembly. Launched in the third quarter of 2017, the

100G CWDM4 QSFP28 optical transceiver features up to 10 km reach on duplex SMF with high speed, low-power consumption and extended operating temperature ($-40\,°C$ to $85\,°C$). An 100G PSM4 QSFP28 optical transceiver with up to 2 km reach on parallel SMF is also available. Intel is expecting a 400G Si photonics optical transceiver with $4 \times 100G$ or $8 \times 50G$ in the near future (the year 2020). Taking the coarse WDM (CWDM) product as an example, the transmitter and receiver chip with fiber connector are sketched in Figure 1.1 (a) and (b), respectively. Four Si modulators for data encoding and a multiplexer to combine four channels onto one SMF are integrated on the transmitter chip. As Si is not efficient in light emission, hybrid InP lasers are integrated on the chip using bonding technology. The receiver side integrates a demultiplexer to split optical signals and four Ge-on-Si photodetectors to convert photons to electrons.

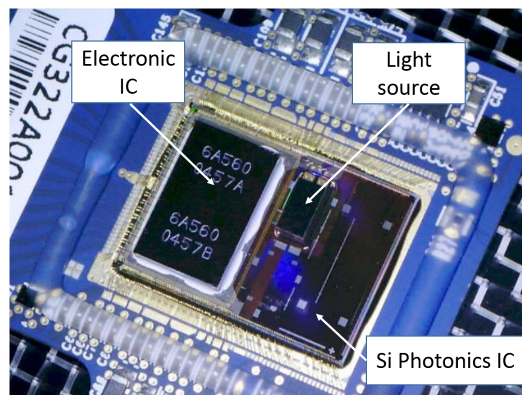

Figure 1.2: 8×28 *Gbps PSM8 Chipset* & 200 *Gbps Module from Luxtera, wire bonding is used for electrical connections. Reproduced from [17].*

The first commercial Si transceiver was launched in 2006 by Luxtera, which is a young company founded in 2001. The product monolithically integrates photonics and electronics, reaching 40Gbps (WDM, 4×10 Gbps). In 2014, the first 200 Gbps (WDM, 8×25 Gbps) Si photonics transceiver was realized by the same company utilizing hybrid integration of a photonics chip and an electronics chip. Instead of monolithic integration, multiple chips (single laser source, Si photonics and electronic IC) are combined on a PCB, where the electrical connections between chips are realized by wire bonding (Figure 1.2). Luxtera claimed that hybrid integration reduces the cost compared to fully monolithic integration. However, the high parasitics between separate photonics and electronics become the bottleneck.

Challenges for Si photonics

Despite the fact that Si photonics has become a relative mature platform following 15-year intensive R&D and the launch of the first Si photonics transceivers in the market, further commercialization of the technology is still facing several issues. One factor comes from the fabrication fluctuations, which limits device yield. The variations in Si layer thickness and linewidth changes the effective refractive index of waveguides. Thus results in uncertainty in the coupling efficiency of couplers, splitting ratio of splitters and phase accuracy of wavelength-selective components. Another challenge is associated with the packaging of Si PICs with fibers and electronic ICs, which is said to dominate the overall cost of a Si PIC product [18]. In addition to providing protection from physical damage and addressing heat dissipation, the package also should support optical connections with fibers and internal/external electrical contacts. Different packaging strategies are under development. It still remains to be proved, which is the most advantaged approach.

The other challenge, the lack of efficient Si active devices, and in particular lasers, is considered as the bottleneck for Si PIC. The integration of novel materials on Si, as an alternative, has drawn a wealth of attention. For efficient light sources, a material with adequate electrical-optical (E-O) conversion is needed. Ge-on-Si has the most potential in terms of material and processing compatibility with Si technology. Ge lasers, exploiting strong doping and tensile strain to engineer the band diagram [19] have been demonstrated, but the required threshold current densities are prohibitively high [20]. Colloidal quantum dots with engineerable optical and electric properties present competences as a light-emitting material as well [21]. Again, a practical methodology to bring the colloidal QDs in a top-down PICs manufacturing process is needed. Also achieving the desired emission wavelengths have not been demonstrated. Therefore, III-V semiconductors, e.g., GaAs, GaN, InAs, InP and their ternaries and quaternaries with a direct bandgap, remain the most promising candidates, yet a cost-efficient and compatible integration scheme is required. For high-speed, power-efficient optical modulators, materials with strong electro-optic effect, including SiGe [22], graphene [23], organics [24] and III-compounds [25], have been demonstrated on Si substrate. Most of the active devices made from the new materials exhibit superior performance and present significant potentials for Si PICs. However, a versatile material system, which is cost-effective and compatible with the current CMOS technology, is still under exploration.

1.1.2 III-V on Si

As aforementioned, the integration of a series of new materials with efficient electro-optic effect and/or sufficient electron-photon conversion, such as III-V semiconductors, germanium, graphene, organics, polymers, is promising to achieve

a fully functional PIC. Many III-V semiconductors have been proven practical to produce light emitters [26], optical modulators [27] and PDs [28] due to their direct bandgap and lack of inversion symmetry that results in efficient electron-photon conversion and a strong electro-optic effect. Considering that the majority of III-V-on-Si R&D activities target on-chip light sources for optical interconnects and fiber-optic communication systems, most of the investigations have been focusing on the following requirements: electrical injection to cooperate with electronic ICs; emission at communication wavelengths ($1310\,\text{nm}$ or $1550\,\text{nm}$); ability to couple with Si photonics devices; and CMOS-compatible mass-production capability.

Nevertheless, given the significant mismatch between the lattice constant of Si (a_{Si} = 5.431 Å) and most direct bandgap III-V compounds (lattice constant between 5.6 Å and 6.5 Å), the integration of III-V on Si remains a huge challenge for high-volume and low-cost industrialization. To circumvent this, external light sources have been used [29]. The separate light emitter allows maintaining its performance in terms of efficiency, lifetime and reliability but this approach suffers from extra coupling loss with Si photonics chip. Therefore the off-chip approach is not within the scope of the discussion in the following section, which focuses on four III-V-on-Si integration methods: hybrid integration by flip-chip [30], heterogeneous integration by bonding [31], transfer printing [32] and monolithic integration by heteroepitaxy [33].

Flip-chip integration

As the first widely-used approach to integrating III-V laser dies on Si substrate, flip-chip was initially developed for multi-chip arrangements. To apply flip-chip to laser integration, individual III-V laser diode dies are mounted face down, or flipped on an SOI substrate. Before flip-chip mounting, the III-V device has already been fabricated on its native substrate and alignment markers have to be defined on the SOI chip. Efficient coupling between the III-V lasers and waveguides is required such that the individual dies have to be accurately aligned and placed on the surface. While flip-chip integration is versatile and compatible with various device types and materials, it is a slow and costly process. Also, the integration density is limited and the usage of the III-V material is insufficient.

Heterogeneous integration by bonding

Widely explored in the past decade, hybrid integration of III-V compounds on Si using bonding is now widely used. The technology is compatible with a wide range of materials, showing great versatility for integration of Si PICs with varied interesting materials. III-V dies as well as full wafers can be integrated, employing direct bonding or adhesive bonding approaches. Direct bonding utilizes relatively weak Van der Waals forces or hydrogen bonds to attach III-V on Si without additional adhesive material. Afterwards these bonds are strengthened

through annealing. A key challenge for direct bonding of dissimilar materials (e.g., compound semiconductor to Si) is the mismatch in thermal expansion coefficient making a conventional high-temperature ($> 600\,°$) anneal process impossible. Therefore some low-temperature processes, e.g., O_2 plasma-assisted bonding have been developed [34, 35]. Besides direct bonding , adhesive bonding is also used to integrate III-V semiconductors on Si. DVS-BCB (divinylsiloxane-bis-benzocyclobutene) is a thermosetting polymer that is highly adhesive, void-free, light-transparent and easy-to-apply, and is a broadly exploited as bonding agent. Accurate control of the thickness of the bonding layers, needed for efficient optical coupling between the III-V and the Si waveguide, and the thermal dissipation of active devices via the adiabatic DVS-BCB are the two challenges remaining in the field.

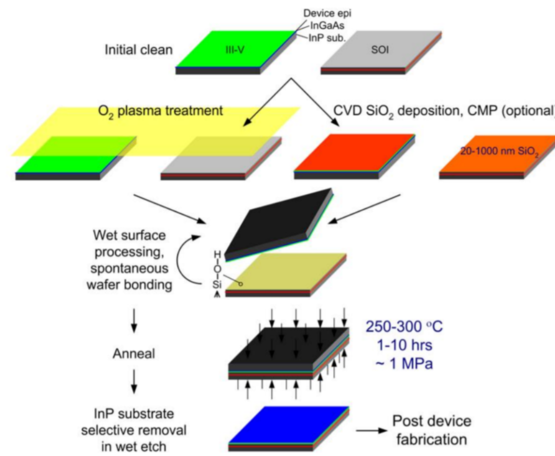

Figure 1.3: Schematic process flow for O_2 plasma-assisted SiO_2 covalent direct wafer bonding. Reproduced from [36].

Figure 1.3 shows the typical flow of a O_2-plasma-assisted direct wafer bonding process for fabricating III-V-on-Si photonics devices. In order to achieve a good bond, the III-V and SOI wafer surfaces need to be perfectly clean, since the inclusion of any particle at the bonding interfaces can result in voids. After a cleaning procedure, the native oxides on both material surfaces are removed in HF and NH_4OH solutions respectively. The hydrophobic sample surfaces are then rendered hydrophilic by an O_2 plasma treatment to grow a thin layer of highly reactive native oxide. After physical mating in air at room temperature, the bonded sample is annealed at $300\,°C$ under external pressure to form strong covalent bonds. Then the III-V substrate is removed and the bonded III-V membrane then undergoes a series of processes, e.g., etching, metallization and passivation, to produce

photonic devices.

Using the bonding technology, demonstrations of various laser sources, including Fabry-Perot lasers [31], distributed feedback (DFB) lasers [37], microdisk/ring lasers [38], vertical-cavity surface-emitting laser (VCSEL) [39], etc. have been realized on Si. Impressive results have been demonstrated: ultra-high speed III-V lasers with a large signal modulation beyond even 67Gbit/s [25, 40], ultra-dense optical comb lasers with 1 GHz repetition rate [41], III-V lasers with emission wavelength longer than 2 μm [42]. And commercial products based on bonding technology are now also available, e.g. the 100G transceiver released by Intel [16] discussed in the previous section.

Heterogeneous integration by transfer printing

Integration by bonding is doubtlessly a successful technology. Nevertheless, the inefficient usage of III-V material in the bonding process, where the majority of the bonded material has to be removed, stimulated the development of transfer printing. As first proposed by Menard et al. in 2004 [43], this technology allows for the transfer of micron-scale components from a III-V source substrate to a target substrate. Instead of the one-by-one device integration allowed by classical flip-chip, devices can be picked up in dense arrays from their source substrate and printed simultaneously onto a target substrate in a massive parallel manner through transfer printing. It leads to a sufficient use of III-V material and a fast integration speed. This technology gains attention from both academia and industry, holding the potential for cost-effective and scalable integration of III-V semiconductors devices on Si PICs.

Figure 1.4 illustrates the transfer printing process, where (a) is a III-V source wafer incorporating the epitaxial active stack and a sacrificial release layer in between. The III-V devices (hereafter referred to as a coupon) are fabricated on the original substrate, as shown in Figure 1.4 (b). The coupons are then encapsulated in a layer of photoresist with local openings for etchant to access the release layer (the front view in Figure 1.4 (c) and top view in (d)). The release etchant needs to exhibit a high selectivity (1000), such that several micrometers of the release layer is removed while only nanometers of the active stacks is sacrificed. By using a polydimethylsiloxane (PDMS) stamp, these III-V devices can then be rapidly picked from the substrate with breaking the tether structures (Figure 1.4 (e)), and slowly printed on a Si photonic target wafer (Figure 1.4 (f)). As both the III-V and Si devices are premade before the transfer printing process, accurate alignment is critical for efficient coupling between the devices. A misalignment less than 1.5 μm (3σ) is typically desired for tolerant coupling.

A number of active devices have been demonstrated using this technique. In 2012, wafer-scale integration of high-performance GaAs FP lasers on Si substrates achieved low-threshold continuous-wave lasing at a wavelength of 824 nm [32]. At

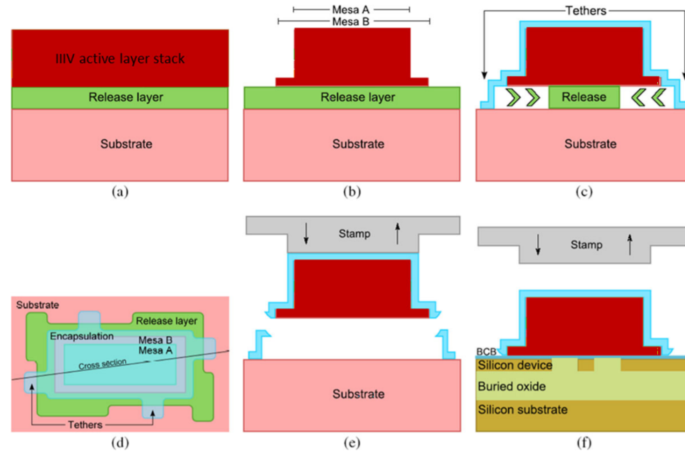

Figure 1.4: Release process for transfer printing. (a) III-V starting layer stack (source), (b) III-V device patterning on source substrate, (c) Tether definition and release etching, (d) Top view of tether on source substrate, (e) Pick-up of the coupon from the source substrate, (f) Printing of the III-V coupon to the SOI target substrate. Reproduced from [44].

almost the same time, a surface-emitting laser with membrane reflectors, consisting of a transferred IIIV InGaAsP QW heterostructure as the gain medium and two thin, single-layer Si photonic crystal reflectors was demonstrated [45]. More recent results have focused on the coupling between transferred III-V devices with on-chip Si devices. Evanescent coupling between a transferred electrically pumped DFB laser with Si WGs has been demonstrated [46]. Fabry-Perot lasers transfer printed onto a SOI chip is successfully butt-coupled to the photonic circuit using a Si inverse taper [47].

The main challenges of transfer printing stems from two aspects. First, the high aspect ratio (length vs. width) of in-plane lasers (e.g., FP laser, DFB laser) means they can easily undergo some degrees of bending and/or twisting during the pick-and-place process, which would, in turn, degrade the bonding quality. Second, the alignment of the premade devices becomes of major importance for device performance. An alignment deviation of 1 μm could result in a 3 dB loss in coupling.

Monolithic integration by heteroepitaxy

Integration of III-V on Si by flip-chip and bonding is already relatively mature. However, the inefficient use of the material and low throughput prohibit it from high-volume and low-cost production. Transfer printing as an upstart extends the scale of integration to some degree. Yet the limitations in terms of e.g. alignment as discussed above remain troublesome and might prevent super-high-volume fab-

rication. Besides the three approaches described above, monolithic integration of III-V on Si by heteroepitaxy remains the most challenging but promising method. This technique, the basis of the thesis work, will be discussed in detail in the following section.

1.1.3 III-V heteroepitaxy on Si - state-of-the-art

Widely believed to be the ultimate approach to fabricate III-V devices on Si substrates, III-V heteroepitaxy on Si for photonics applications has drawn worldwide attention recently. The start of the research can be traced back several decades ago, initially for electronics applications such as metal-oxide-semiconductor field-effect transistors (MOSFETs), high electron mobility transistors (HEMTs) and heterojunction bipolar transistors (HBTs). Due to the large lattice mismatch and the difference in polarity, the defect density of III-V material grown on Si easily exceeds 1×10^8 cm^{-2}, which is detrimental to the device's performance. Driven by the explosive growth of Silicon Photonics, the heteroepitaxy of III-V on Si has gained new interest. Here we review, non-exhaustively, the state-of-the-art of the novel techniques being developed to overcome the large differences in material properties, including planar growth combined with specific techniques, growth along specific directions, heteroepitaxy of III-V nanowires and nano-ridges.

Planar heteroepitaxy

By exploiting particular techniques, e.g., inserting intermediate layers [48] or using graded Ge/GeSi/Si substrate [49], the quality of the materials grown during planar growth can be improved. Defect reduction of several orders in bulk III-V material has been reported.

One example is the work from J. Bowers' group at the University of California Santa Barbara [50]. Instead of growing from a blanket Si substrate, they utilized GaAs-on-V-grooved-Si (GoVS) templates to grow InAs QDs for O-band lasing. The template (shown in Figure 1.5 (a)) started with selectively growing closely pitched GaAs nanowires on SiO_2 patterned Si (001) substrates with V-grooved Si (111) surfaces to prevent APDs. These GaAs nanowire arrays were used as seed templates for the subsequent epitaxial planar overgrowth to achieve coalesced GaAs thin film with a flat surface [51]. The GoVS template with 1 μm GaAs, which was estimated to have a defect density on the order of $\sim 10^8$ cm^{-2}, forms the initial platform for the following growth. A 600 nm $Al_{0.7}Ga_{0.3}As$ layer and a five-layer InAs/InGaAs dot-in-a-well (DWELL) structure were grown in a molecular beam epitaxy (MBE) system (Figure 1.5 (c)). Defects were suppressed by the epitaxial necking effect from the design of the diamond-shaped Si pockets, shown in the TEMs in Figure 1.5 (d)-(f).

Electrically pumped micro-disk laser made from the as-grown material were demonstrated in 2017 [50]. The SEM-images of the fabricated micro-disk laser is

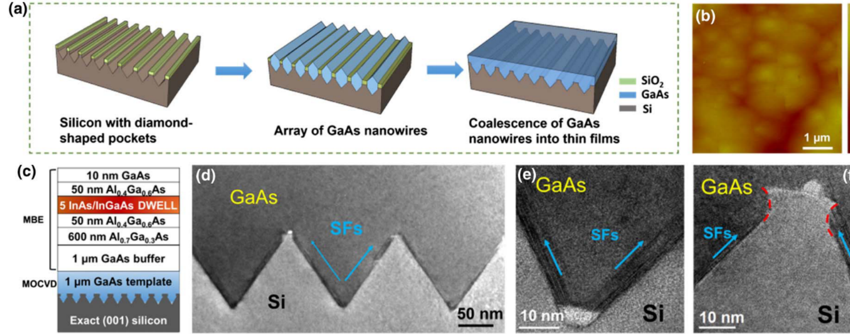

Figure 1.5: Epitaxial InAs QDs micro-disks on GoVS substrate. (a) Procedure of growing antiphase-domain-free GaAs thin films out of a highly ordered array of planar GaAs nanowires on Si substrates with diamond-shaped pockets. (b) AFM image of approximately 1 μm coalesced GaAs thin film grown on the nanowire arrays. The vertical bar is 25 nm. (c) Schematic of the as-grown structure. (d)(f) Cross- sectional TEM images of the V-grooved structure, showing stacking faults (indicated by the blue arrows) trapped by the Si pockets. Reproduced from [50].

shown in Figure 1.6. Furthermore, the group also utilized Si substrate with a 45 nm thick pseudomorphic GaP buffer layer. APDs that form at the GaP/Si interface could terminate within the GaP layer due to some special Si surface preparations. A series of breakthroughs for FP-laser devices made from the heteroepitaxial material have been reported by the group, including single-facet output powers as high as 175 mW [52], up to 119 °C temperature continuous-wave operation [53], ultra-low linewidth enhancement factor [54], isolator-free stability with optical feedback level of up to 90% [55] and more than 100, 000 h lifetime at 35 °C [56].

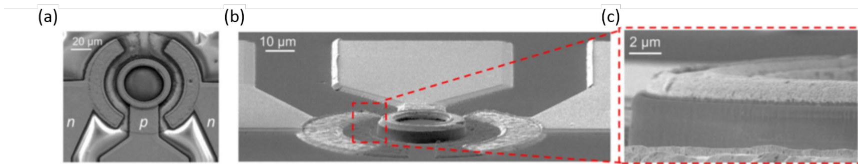

Figure 1.6: (a)-(c) SEM images of a fabricated micro-disk device. (d) 90° tilted zoomed in SEM image of the mesa. Reproduced from [50].

Another successful demonstration of a laser planarily grown on Si is from H. Liu's group at the University of College London [57]. They started with a blanket Si wafer but with 4° offcut to the [001] plane to prevent the formation of APDs. Then a thin AlAs nucleation layer shown in Figure 1.7 (a) was deposited, followed by a three-step 1, μm-thick GaAs epitaxial growth, where a TDs density of 1×10^9 cm^{-2} was still observed. Further improvement of the material quality

was achieved by adopting strained-layer superlattices (SLSs) as dislocation filter layers (DFLs). The strain relaxation of the SLS applies in-plane forces to the TDs, and hence enhances the lateral mobility and coalescence probability of TDs during thermal annealing. After six layers of such DFL (Figure 1.7 (b)), with each DFL reducing the amount of TDs further, the number of TDs is claimed to be suppressed to the order of 10^5 cm^{-2} (Figure 1.7 (c)). A standard five-layer QD laser structure was then grown on the developed template showing a defect density of $\sim 3.0 \times 10^{10}$ cm^{-2} and PL emission around $1.3\,\mu$m as illustrated in Figure 1.7 (d). The research group claimed that a nearly defect-free dot-in-well (DWELL) active region was achieved (Figure 1.7 (e)). FP lasers with as-cleaved facets were fabricated as shown in Figure 1.7 (f,g,h). Room-temperature CW lasing with a threshold of 62.5 A cm^{-2} was reported for the laser. The measured output power from both facets exceeds 105 mW and the operation temperature is as high as $120°C$. Over $3,100$ h of CW operating data have been collected, revealing an extrapolated time to failure of over $100,000$ h.

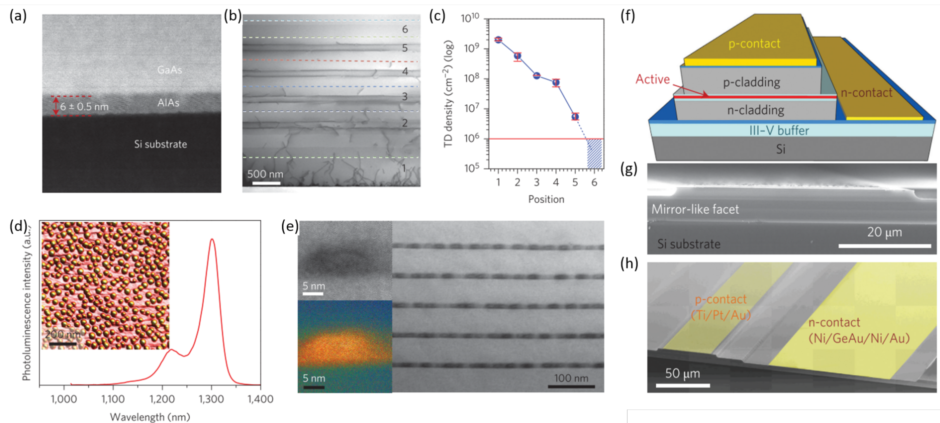

Figure 1.7: (a) High-angle annular dark-field scanning TEM image of the interface between the AlAs nucleation layer and a Si substrate. (b) Bright-field scanning TEM image of DFLs. (c) Dislocation density measured at different positions, as indicated in (b). (d) PL spectrum for a QD active region grown on Si. Inset: representative AFM image of an uncapped QD sample grown on Si. (e) High-resolution bright-field scanning TEM images of a single dot (top left), corrected high-angle annular dark-field scanning TEM images (false colour) of a single QD (bottom left) and bright-field scanning TEM image of the QD active layers (right). (f) Schematic of the layer structure of an InAs/GaAs QD laser on a Si substrate. (g) A cross-sectional SEM image of the fabricated laser with as-cleaved facets, showing very good facet quality. (h) SEM overview of the complete IIIV laser on Si. Reproduced from [57].

Also Kwoen et al. demonstrated InAs/GaAs QD lasers grown on GaAs/Si (001) substrates [58] using a dislocation filter layer. The heteroepitaxial stacks

include, in the order of growth, a seed layer on the Si substrate, a buffer layer, a dislocation filter layer to reduce the dislocation density, a lower cladding layer, the QD laser layers and an upper cladding layer. The seed layer is important to avoid anti-phase boundaries at the interface [59]. After the dislocation filter layer, the threading dislocation density is reported to drop to 4.7×10^7/cm^2, corresponding to only one threading location per 1000 QDs. The threshold current of the laser fabricated from such material is 27.6 mA at room temperature, corresponding to a current density of 370 A/cm^2. Continuous-wave operation is observed at up to $101\,^{\circ}C$ on the fabricated devices.

As we noticed from the above three examples, planar growth combined with some particular techniques, like utilizing a GoVS or GaP template, starting with an offcut Si substrate, applying strained dislocation filters, allows defect reduction to a density at the order of 10^5 /cm^2. QDs were then grown on the low-defect-density epitaxial material as an active region. The demonstrated lasers made from the epitaxial material with QDs as the active region, reveal excellent performance, e.g., low threshold, high-temperature operation and long lifetime. Benefiting from the broad and tunable emission spectrum of QDs, lasing within the widely-used O-band is achievable. These advantages are attributed to the small dimension and three-dimensional carrier confinement of the QDs. Due to the quantum effect, the electronic states of QDs are discrete such that a low density of carriers is needed for population inversion and laser operation. The three-dimensional carrier confinement, which provides few-hundred-meV separation between the dot ground state and the barrier state, decreases carrier diffusion. Therefore, the thermalization of the QDs is highly suppressed and non-radiative recombination at defective sites (e.g., exposed surfaces or defects) is strongly avoided. Moreover, electrical injection into these lasers is not an impossible task given that planar growth leaves spacious room for electrical design. However, a problem does exist when the epitaxial lasers have to ”communicate” with Si photonic devices. The few-micrometer intermediate layers between the active layers and Si prevent efficient coupling between the laser and a Si waveguide.

Selective Area Growth

While light coupling to a Si waveguide remains a difficulty for planar growth, selective area growth (SAG), which requires no thick buffer layer, is investigated by some other groups. SAG is conducted on patterned Si substrates, with a SiO_2 mask, where the growth rate is dramatically faster on Si than that on SiO_2. The growth from the uncovered Si region on a patterned substrate allows the freedom to define growth position/area, form 3D structures and combine with other techniques to reduce defect density. Examples of SAG together with directional heteroepitaxy, vertical/planar nanowires growth, aspect ratio trapping are described here-under.

Directional heteroepitaxy

Nishinaga et al. from Meijo University discovered dislocations can be eliminated when the material grows along one of two specific directions: horizontal and vertical after microchannel epitaxy (MCE) [60, 61]. MCE consists of SAG in a narrow opening on a mask, referred to as a microchannel, as a seed for subsequent growth. As growth continues, the dislocations in the initial layer were eliminated from the top or the side surfaces through directional growth using liquid-phase epitaxy (LPE). As a result of horizontal MCE, as shown in Figure 1.8 left, the laterally-grown areas are dislocation-free and can be used for photonic devices. In contrast, dislocations are stopped on the side surfaces when applying vertical-MCE such that the top region of the grown layer can be used for devices (Figure 1.8 right). Besides the horizontal and vertical directional epitaxy achieved by LPE, growth along an inclined direction has been realized by the superior molecular-beam epitaxy (MBE) technique [62]. An AlGaAs FP laser array on Si was demonstrated by such a process. The lasers were fabricated on a GaAs dislocation-free area grown by horizontal MCE and showed laser operation at a wavelength of 844 nm [63].

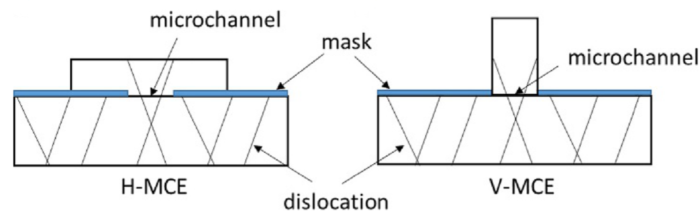

Figure 1.8: Two-types of directional epitaxy after microchannel growth: horizontal microchannel epitaxy (left) and vertical microchannel epitaxy (right). Reproduced from [63].

Another directional-epitaxy technology developed by Sun et al. from KTH-Royal Institute of Technology, focuses on corrugated epitaxial lateral overgrowth (CELOG) [64], which grows III-V material both horizontally and vertically after MCE (shown in Figure 1.9) instead of the unidirectional growth in Nishinaga's work. The crystal grows first vertically from the microchannel opening and then laterally after exceeding the brim of the spacer. The dislocation-rich region only remains in the area right above the opening but not outside. The spacers block the propagation of dislocations into the lateral overgrowth part, which is dislocation-free and suitable for subsequent active device fabrication.

The trapping of TDs in directional epitaxy mostly relies on material physical boundaries (Figure 1.8). Reduction of other types of defects, e.g., anti-phase boundaries due to the different polarity of III-V and Si, point defects originating from impurities and planar defects, is absent. Very limited devices fabricated

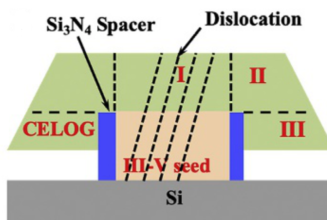

Figure 1.9: CELOG for threading dislocation filtration. Reproduced from [64].

through directional epitaxy are reported in the literature, which may be regarded as collateral evidence of its insufficient material quality.

Heteroepitaxy of vertical nanowires

Enabled by SAG, also vertical III-V nanowires on a Si template with nanometer-scale openings have been demonstrated. Due to the small nanowire cross-section, the strain from the lattice-mismatched Si can be easily relaxed without metamorphic buffer layers. In 2011, R. Chen et al. demonstrated nanowires with InGaAs as the active core for light emission and GaAs as the shell for surface passivation on a Si substrate [65]. The structures (shown in Figure 1.10 (a)) are grown at a temperature of $400\,^{\circ}$C, which is drastically lower than typical III-V growth temperatures and thus compatible with CMOS platform. Due to the single-crystal wurtzite structure, the nanowire has a hexagonal cross-section. The dimensions (height and diameter) of the nanowires with a typical footprint of $\sim 0.34\,\mu m^2$ can be scaled by controlling the growth time. With a certain height, the 2D nanowires forms a natural optical cavity, which supports helical cavity modes. Lasing from these nanowires was first realized at wavelengths ranging between $900 - 950$ nm, dependent on the Indium fraction of the InGaAs core. The achievable lasing wavelength was then extended to $1.15 - 1.3\,\mu$m by growing InP nanowires with InGaAs QWs [66].

Another remarkable work combining SAG and vertical nanowire growth is from a research group at the University of California Los Angeles, where nanowires were grown not only on a planar SOI layer but also on a 3D-structured Si layer, by MOCVD [67, 68]. The structured SOI wafer was covered with a layer of SiO_2 mask, which was patterned with openings to reach Si for highly selective growth. By growing on patterned SOI where the heteroepitaxy of InGaAs nanowires only started from Si, the position of the nanowires can be precisely controlled, reaching a high degree of freedom in designing nanowire-based devices. The emission of the nanowires could cover all telecommunication wavelengths from 1.2 to $1.8\,\mu$m by adjusting Indium fraction. An optically pumped array of III-V nanowire lasers monolithically integrated on Si was demonstrated on this platform [67] as shown in Figure 1.10 (b). Not only room-temperature lasing is achieved, but also the

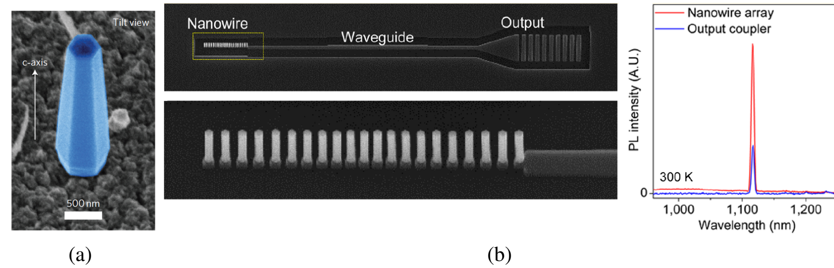

(a) (b)

Figure 1.10: (a) A SEM image showing the well-faceted geometry of the nanopillar optical cavity. Reproduced from [65]. (b) Left: thirty degree-tilted SEM images of a nanowire array cavity integrated with a waveguide and an output coupler (upper), and a close-up image of the nanowire array in the dashed box (lower). Right: PL spectra measured on top of a nanowire array and on top of an output coupler above the lasing threshold. Reproduced from [67].

coupling from the nanowire array laser to SOI waveguides is obtained. Also other works unitize nanowire heteroepitaxy including but not limited to [69–71].

Although the nanowires grown on Si are typically free of threading dislocations due to the efficient relaxation of strain at the nanoscale interface, a high density of stacking defects was observed. Further improvements are needed to eliminate the undesirable stacking faults, which degrade electrical and optical properties. While the technique allows a high density of devices on the Si platform due to its small footprint, the limited volume is likely to hinder high-power operation. Another difficulty is the realization of electrical injection on such a tiny structure.

Planar nanowire heteroepitaxy

Strain relaxation in vertical nanowires relies on the nanometer-scale cross-section, which restricts the achievable volume of the gain material and leaves difficulties in realizing electrical injection. Planar nanowire heteroepitaxy seems a better technique with respect to scaling the length.

Y. Han et al. demonstrated room-temperature telecom-band InP/InGaAs nanowire lasers grown on Si [72–74]. The nanowires were grown from a Si substrate, which was initially patterned with $\sim 500\,\text{nm}$ thick SiO_2 stripes along the [110] direction with a line pitch of $1\,\mu$m and an opening of $450\,\text{nm}$. V-grooved pockets enclosed by Si (111) planes were formed by immersing the sample in a KOH solution to eliminate the formation of APDs. Using MOCVD, five layers of InGaAs quantum wells were embedded inside the grown InP nanowires as gain material. The as-grown nanowires finally formed a diamond profile with a width of $450\,\text{nm}$, a height of $1.0\,\mu m$ and emit around $1.5\,\mu m$ (Figure 1.11 (a)) [73]. It was observed that most of the defects generated at the InP/Si interface were confined in the lower diamond-shaped pocket while the upper InP nanowire was less defective. Room-

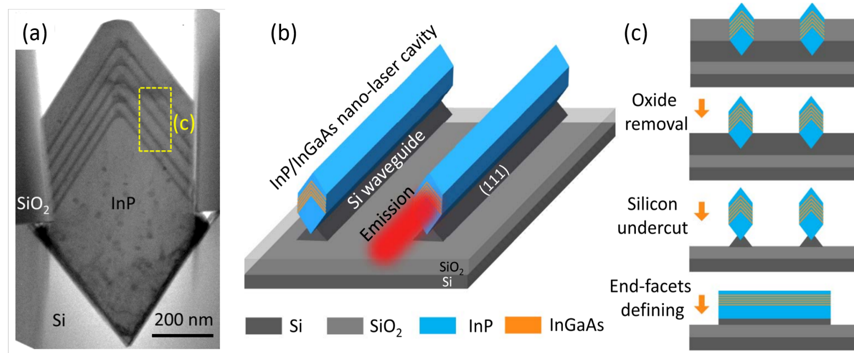

Figure 1.11: (a) Cross-sectional TEM image of the InP/InGaAs nanowire perpendicular to the wire direction, showing five $\{111\}$ InGaAs QWs embedded inside a InP nanowire; the dark area at the InP/Si interface contains a high density of stacking faults generated for strain relaxation. (b) Schematic of the designed InP/InGaAs nanolaser array grown on a SOI substrate. (c) Fabrication process of the InP/InGaAs nanolaser on SOI. Reproduced from [72].

temperature lasing was first realized by etching two mirror-like facets to produce a FP cavity on the nanowire and moving it from the original Si wafer to a SOI wafer to eliminate leakage loss [74]. The latest result demonstrated optically pumped lasing from the InP/InGaAs nanowires by undercutting the Si substrate partially ((Figure 1.11 (b) and (c))) and a cavity-length-dependent emission wavelength covering the $1.4 - 1.6\,\mu m$ range [72].

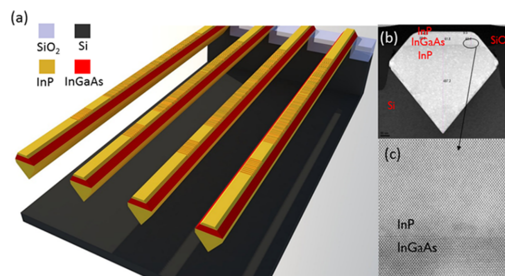

Figure 1.12: (a) Schematic plot of the monolithically integrated InGaAs/InP DFB lasers on silicon. The silicon pedestal (and the silicon oxide hard mask) under the near end has been removed for a better view of the IIIV waveguide. (b) STEM image of a typical cross-section of the grown InGaAs/InP/Si waveguide. (c) A zoom-in STEM image of the InGaAs/InP interface. Reproduced from [75].

Z. Wang et al. from our research group reported single-mode InP nanolaser array epitaxially grown on Si [75, 76]. The InP waveguides were grown from

a 300 mm (001)-Si wafer, on which 500 nm-wide Si ridges planarized with SiO_2 were defined in a standard shallow-trench-isolation (STI) process. The ridges were selectively etched, forming a V-groove with two flat $\{111\}$ planes at the bottom of the resulting trench. The subsequent InP growth inside this trench was carried out by MOVPE. The InP protruding above the SiO_2 mask was planarized by a chemical mechanical polishing (CMP) process. Except for some stacking faults near the InP-Si interface, TEM imaging found no dislocations in the material. For laser demonstration, $\lambda/4$ phase-shifted DFB devices were fabricated and show single-mode lasing around 930 nm [76]. A second generation of the InP waveguide was fabricated with a layer of high-quality InGaAs (Figure 1.12 (b) and (c)) targeting O-band emission. Laser operation at a single wavelength of $\sim$ 1340 nm was demonstrated starting from the 2nd generation of the InP waveguide. Nevertheless, the InP nanolasers have to be suspended from the Si substrate because of the huge leakage loss and absorption loss (only for 930 nm emission) of Si. The removal of the Si substrate makes it more challenging to achieve electrical injection and coupling with a Si waveguide.

Nano-ridge heteroepitaxy

Due to the outstanding electron transport properties of III-V compound semiconductors, III-V materials grown on Si where long considered a promising next step in CMOS scaling. Motivated by this aspiration, imec commenced the research on the heteroepitaxy of InP [77] and GaAs [78] on standard 300-mm wafer for electronics applications. In the mean time this work, for standard logic devices, was mostly stopped. However, the results are directly applicable for photonics applications. The InP nanolasers [76] discussed in the last paragraph were one of the first results of this research. These were followed by the development of a new process, i.e. GaAs nano-ridges epitaxially grown on Si, which will be the topic of this work and will be discussed in full detail in the coming chapters.

1.2 Research objectives

The objective of the Ph.D. work is to investigate the possibility of using the GaAs nano-ridges for on-chip light sources. It can be listed in four aspects:

- The characterization of the optical properties of the nano-ridges
- The demonstration of nano-ridge lasers
- The extension of lasing wavelength to O-band
- Considering the challenges of realizing electrical injection and interfacing with Si WGs.

Considering that the technology is in its infancy, the first goal of the work was to inspect the crystal quality of the nano-ridges through the characterization of their optical properties. This would provide valuable information for the following laser design and direct feedback to the heteroepitaxy growth process. Once the material quality is proved, the second objective was to demonstrate lasers. The design of different types of lasers should be carried out before developing the fabrication process. The fabricated devices would be characterized afterwards. As we target the telecommunication application, the extension of lasing wavelength to O-band was also one of the objectives. Besides, we also considered the challenges of realizing electrical injection and interfacing with Si WGs in this work.

The research was carried out in the Photonics Research Group (PRG) at Ghent University as a part of the optical interconnect program at imec, which also provided the nano-ridge material. Additionally, a collaboration with Bochum Univerisity in Germany was set up for the characterization of the PL lifetime of the nano-ridges.

1.3 Outline of this thesis

In the introduction chapter, we reviewed the background of Si photonic integrated circuits, III-V material on Si and the state-of-art III-V heteroepitaxy on Si substrate. Requirements, opportunities and challenges for accomplishing III-V integration on Si were discussed. Based on this, we introduced the objectives of this research work, which is the development of nano-ridge lasers heteroepitaxially grown on Si. Then appropriate goals of the thesis were defined.

In Chapter 2, we will focus on the heteroepitaxy process itself: the challenges of growing lattice-mismatched material, the specific technologies (aspect ratio trapping and nano-ridge engineering) used to eliminate the defects and the inspection of the crystal quality by electron microscopy.

Chapter 3 deals with the optical characterization of the material. The energy diagram of the nano-ridge is first presented for a basic understanding of the characterization. After that, we will show the results from the PL measurements. Discussions on the impact of growth conditions on nano-ridge quality are given afterwards through the PL lifetime extracted from TRPL characterization. Then we present the optical gain of the nano-ridges characterized by the variable strip length (VSL) method.

In Chapter 4, we will describe the nano-ridge lasers that we demonstrated. The starting point is Fabry-Perot lasers for their uncomplicated design and fabrication. After that, $\lambda/4$ shifted DFB lasers are presented, showing single-mode lasing and wavelength tunability. As a first step towards electrical injection, single-mode partly-loss-coupled DFB lasers, whose cavities are defined by metal gratings, are then demonstrated.

Chapter 5 shows the first trial to extend the wavelength from 1 μm to 1.3 μm for optic communication applications. The InGaAs nano-ridges are grown with more Indium both in QWs and barriers and the quality is inspected first through SEM and TEM. Investigations of the optical properties are also carried out, revealing a red-shifted PL spectrum, a reduced PL lifetime < 200 ps and an optical gain lower than for the GaAs nano-ridges. InGaAs nano-ridges with DFB cavities are fabricated and found out to have an emission of around $\sim 1.3\,\mu$m-wavelength.

In Chapter 6, three types of III-V-to-Si couplers are proposed to address the interfacing problem. The initial design is a directional coupler, which shows full power exchange between the nano-ridge and Si WG can be realized theoretically. Next, we will design a linear-tapered adiabatic coupler to improve the robustness and manufacturability of the coupler and a more advanced adiabatic coupler, which has a relatively compact footprint.

Chapter 7 finally concludes the work of the whole thesis and introduces proposals for future work.

1.4 Publications

1.4.1 Patent

- B. Kunert, M. Pantouvaki, **Y. Shi**, J. Van Campenhout, D. Van Thourhout, A. Srinivasan, ”Active-Passive waveguide photonic system”,US-2019/0101711 A1 (Published, 10/2018)

1.4.2 Publications in international journals

1. **Y. Shi**, M. Baryshnikova, M. Pantouvaki, B. Kunert, J. Van Campenhout and D. Van Thourhout, ”Loss-Coupled DFB Nano-ridge Laser Monolithically Grown on a Standard 300-mm Si Wafer”, (under preparation).

2. **Y. Shi**, L. C. Kreuzer, N. C. Gerhardt, M. Pantouvaki, J. Van Campenhout, M. Baryshnikova, R. Langer, D. Van Thourhout and B. Kunert, ”Time-Resolved Photoluminescence Characterization of InGaAs/GaAs Nano-Ridges monolithically Grown on 300mm Si Substrates”, (submitted).

3. **Y. Shi**, B. Kunert, Y. De Koninck, M. Pantouvaki, J. Van Campenhout and D. Van Thourhout, ”Novel adiabatic coupler for III-V nano-ridge laser grown on a Si photonics platform”, Optics Express, 27(26), 37781-37794, (2019).

4. **Y. Shi**, Z. Wang, J. Van Campenhout, M. Pantouvaki, W. Guo, B. Kunert, D. Van Thourhout, Optical pumped InGaAs/GaAs nano-ridge laser epitaxially grown on a standard 300-mm Si wafer, Optica, 4(12), p.1468-1473 (2017).

5. Z. Wang, A. Abbasi, U.D. Dave, A. De Groote, S. Kumari, B. Kunert, C. Merckling , M. Pantouvaki, **Y. Shi**, B. Tian, K. Van Gasse, J. Verbist, R. Wang, W. Xie, J. Zhang, Y. Zhu, J. Bauwelinck, X. Yin, Z. Hens, J. Van Campenhout, B. Kuyken, R. Baets, G. Morthier, D. Van Thourhout, G. Roelkens, Novel light source integration approaches for Si photonics, Laser & Photonics Reviews, 11(4), p.1700063 (21 pages) (2017).

6. B. Kunert, W. Guo, Y. Mols, B. Tian, Z. Wang, **Y. Shi**, D. Van Thourhout, M. Pantouvaki, J. Van Campenhout, R. Langer, K. Barla, III/V nano ridge structures for optical applications on patterned 300mm Si substrate, Applied Physics Letters, 109(9), (2016).

1.4.3 Publications in international conferences

1. **Y. Shi**, M. Baryshnikova, Y. Mols, M. Pantouvaki, J. Van Campenhout, B. Kunert, D. Van Thourhout, Loss-Coupled DFB Nano-ridge Laser Monolithically Grown on a Standard 300-mm Si Wafer,Conference on Lasers and Electro-Optics Europe (CLEO Europe 2019), Germany, CB-1.4 SUN.

2. **Y. Shi**, B. Kunert, M. Pantouvaki, J. Van Campenhout, D. Van Thourhout, Novel adiabatic tapered coupler for small III-V lasers grown on SOI wafer, European Conference on Integrated Optics (ECIO 2019), Belgium, p.W.P01.23 (2019).

3. B. Kunert, M. Baryshnikova, Y. Mols, **Y. Shi**, D. Van Thourhout, N. Kuznetsova, S. Kim, C. Ozdemir, M. Pantouvaki, J. Van Campenhout, R. Langer, III-V photonic devices on Si, Joint ISTDM/ICSI 2018 Conference, Germany.

4. **Y. Shi**, B. Kunert, M. Baryshnikova, M. Pantouvaki, J. Van Campenhout, D. Van Thourhout, Optical gain characterization of nano-ridge epitaxially grown on a standard Si wafer, Conference on Lasers and Electro-Optics, United States, p.paper JTu2A.21, (2018).

5. **Y. Shi**, Z. Wang, J. Van Campenhout, M. Pantouvaki, B. Kunert, D. Van Thourhout, Monolithic InGaAs/GaAs multi-QWs DFB nanoridge laser directly grown on 300 mm Si Wafer, Advanced Photonics Congress, OSA, United States, p.paper ITu2A.2, (2017).

6. D. Van Thourhout, **Y. Shi**, B. Tian, Z. Wang, M. Pantouvaki, C. Merckling, B. Kunert, W. Guo, J. Van Campenhout, III-V on Si DFB Laser Arrays, Group IV conference (invited), China, p.FA6 (2016).

7. D. Van Thourhout, **Y. Shi**, B. Tian, Z. Wang, M. Pantouvaki, C. Merckling, B. Kunert, W. Guo, J. Van Campenhout, III-V on Si DFB Laser Arrays, Summer Topicals 2016 (invited), United States.

References

[1] GE Moore. *Cramming more components onto integrated circuits , Electronics, 38 (8), S. 114-117,(1965) oder: GE Moore*. IEEE Solid-State Circuits Newsletter, 11(5):33–35.

[2] M Mitchell Waldrop. *More than moore*. Nature, 530(7589):144–148, 2016.

[3] Stewart E Miller. *Integrated optics: An introduction*. The Bell System Technical Journal, 48(7):2059–2069, 1969.

[4] Martijn JR Heck and John E Bowers. *Energy efficient and energy proportional optical interconnects for multi-core processors: Driving the need for on-chip sources*. IEEE Journal of Selected Topics in Quantum Electronics, 20(4):332–343, 2013.

[5] Wim Bogaerts, Peter De Heyn, Thomas Van Vaerenbergh, Katrien De Vos, Shankar Kumar Selvaraja, Tom Claes, Pieter Dumon, Peter Bienstman, Dries Van Thourhout, and Roel Baets. *Silicon microring resonators*. Laser & Photonics Reviews, 6(1):47–73, 2012.

[6] S Lardenois, D Pascal, L Vivien, E Cassan, S Laval, R Orobtchouk, M Heitzmann, N Bouzaida, and L Mollard. *Low-loss submicrometer silicon-on-insulator rib waveguides and corner mirrors*. Optics letters, 28(13):1150–1152, 2003.

[7] Harish Subbaraman, Xiaochuan Xu, Amir Hosseini, Xingyu Zhang, Yang Zhang, David Kwong, and Ray T Chen. *Recent advances in silicon-based passive and active optical interconnects*. Optics express, 23(3):2487–2511, 2015.

[8] Vilson R Almeida, Roberto R Panepucci, and Michal Lipson. *Nanotaper for compact mode conversion*. Optics letters, 28(15):1302–1304, 2003.

[9] Amir Hosseini, David N Kwong, Yang Zhang, Harish Subbaraman, Xiaochuan Xu, and Ray T Chen. *1$\times$ N Multimode interference beam splitter design techniques for on-chip optical interconnections*. IEEE Journal of Selected Topics in Quantum Electronics, 17(3):510–515, 2011.

[10] Wim Bogaerts, Shankar Kumar Selvaraja, Pieter Dumon, Joost Brouckaert, Katrien De Vos, Dries Van Thourhout, and Roel Baets. *Silicon-on-insulator spectral filters fabricated with CMOS technology*. IEEE journal of selected topics in quantum electronics, 16(1):33–44, 2010.

[11] Joost Brouckaert, Wim Bogaerts, Pieter Dumon, Dries Van Thourhout, and Roel Baets. *Planar concave grating demultiplexer fabricated on a nanophotonic silicon-on-insulator platform*. Journal of Lightwave Technology, 25(5):1269–1275, 2007.

[12] Richard Jones, Haisheng Rong, Ansheng Liu, Alexander W Fang, Mario J Paniccia, Dani Hak, and Oded Cohen. *Net continuous wave optical gain in a low loss silicon-on-insulator waveguide by stimulated Raman scattering*. Optics Express, 13(2):519–525, 2005.

[13] Jurgen Michel, Jifeng Liu, and Lionel C Kimerling. *High-performance Ge-on-Si photodetectors*. Nature photonics, 4(8):527, 2010.

[14] S Klinger, M Berroth, M Kaschel, M Oehme, and E Kasper. *Ge-on-Si pin photodiodes with a 3-dB bandwidth of 49 GHz*. IEEE Photonics Technology Letters, 21(13):920–922, 2009.

[15] Andrew Rickman. *The commercialization of silicon photonics*. Nature Photonics, 8(8):579, 2014.

[16] *Moving data with light*. www.intel.com/content/www/us/en/architecture-and-technology/silicon-photonics/silicon-photonics-overview.html. Online; Accessed: 2019-10-30.

[17] *Complete Transceiver in a Single Chipset*. http://www.luxtera.com/silicon-photonics-technology/. Online; Accessed: 2019-11-10.

[18] Tom Baehr-Jones, Thierry Pinguet, Patrick Lo Guo-Qiang, Steven Danziger, Dennis Prather, and Michael Hochberg. *Myths and rumours of silicon photonics*. Nature Photonics, 6(4):206, 2012.

[19] Jifeng Liu, Xiaochen Sun, Rodolfo Camacho-Aguilera, Lionel C Kimerling, and Jurgen Michel. *Ge-on-Si laser operating at room temperature*. Optics letters, 35(5):679–681, 2010.

[20] Michael R. Barget, Michele Virgilio, Giovanni Capellini, Yuji Yamamoto, and Thomas Schroeder. *The impact of donors on recombination mechanisms in heavily doped Ge/Si layers*. Journal of Applied Physics, 121(24):245701, 2017.

[21] Yasuhiro Shirasaki, Geoffrey J Supran, Moungi G Bawendi, and Vladimir Bulović. *Emergence of colloidal quantum-dot light-emitting technologies*. Nature photonics, 7(1):13, 2013.

[22] Dazeng Feng, Shirong Liao, Hong Liang, Joan Fong, Bhavin Bijlani, Roshanak Shafiiha, B Jonathan Luff, Ying Luo, Jack Cunningham, Ashok V Krishnamoorthy, et al. *High speed GeSi electro-absorption modulator at 1550 nm wavelength on SOI waveguide*. Optics express, 20(20):22224–22232, 2012.

[23] Ming Liu, Xiaobo Yin, Erick Ulin-Avila, Baisong Geng, Thomas Zentgraf, Long Ju, Feng Wang, and Xiang Zhang. *A graphene-based broadband optical modulator*. Nature, 474(7349):64, 2011.

[24] Christian Koos, Wolfgang Freude, Tobias J Kippenberg, Juerg Leuthold, Larry R Dalton, Jörg Pfeifle, Claudius Weimann, Matthias Lauermann, Robert Palmer, Sebastian Koeber, et al. *Terabit/s optical transmission using chip-scale frequency comb sources*. In 2014 The European Conference on Optical Communication (ECOC), pages 1–3. IEEE, 2014.

[25] Yongbo Tang, Jonathan D Peters, and John E Bowers. *Over 67 GHz bandwidth hybrid silicon electroabsorption modulator with asymmetric segmented electrode for 1.3 μm transmission*. Optics Express, 20(10):11529–11535, 2012.

[26] Robert N Hall, Gunther E Fenner, JD Kingsley, TJ Soltys, and RO Carlson. *Coherent light emission from GaAs junctions*. Physical Review Letters, 9(9):366, 1962.

[27] Robert G Walker. *High-speed III-V semiconductor intensity modulators*. IEEE Journal of Quantum Electronics, 27(3):654–667, 1991.

[28] Dong Pan, Elias Towe, and Steve Kennerly. *Normal-incidence intersubband (In, Ga) As/GaAs quantum dot infrared photodetectors*. Applied Physics Letters, 73(14):1937–1939, 1998.

[29] Xuezhe Zheng, Eric Chang, Ivan Shubin, Guoliang Li, Ying Luo, Jin Yao, Hiren Thacker, Jin-Hyoung Lee, Jon Lexau, Frankie Liu, et al. *A 33mW 100Gbps CMOS silicon photonic WDM transmitter using off-chip laser sources*. In 2013 Optical Fiber Communication Conference and Exposition and the National Fiber Optic Engineers Conference (OFC/NFOEC), pages 1–3. IEEE, 2013.

[30] T Mitze, M Schnarrenberger, L Zimmermann, J Bruns, F Fidorra, J Kreissl, K Janiak, S Fidorra, H Heidrich, and K Petermann. *Hybrid integration of III/V lasers on a silicon-on-insulator (SOI) optical board*. In IEEE International Conference on Group IV Photonics, 2005. 2nd, pages 210–212. IEEE, 2005.

[31] Alexander W Fang, Hyundai Park, Oded Cohen, Richard Jones, Mario J Paniccia, and John E Bowers. *Electrically pumped hybrid AlGaInAs-silicon evanescent laser*. Optics express, 14(20):9203–9210, 2006.

[32] John Justice, Chris Bower, Matthew Meitl, Marcus B Mooney, Mark A Gubbins, and Brian Corbett. *Wafer-scale integration of group III–V lasers on silicon using transfer printing of epitaxial layers*. Nature Photonics, 6(9):610, 2012.

[33] Sebastian Lourdudoss, John Bowers, and Chennupati Jagadish. *Future Directions in Silicon Photonics*, volume 101. Academic Press, 2019.

[34] Edward M Liston. *Plasma treatment for improved bonding: a review*. The Journal of Adhesion, 30(1-4):199–218, 1989.

[35] Donato Pasquariello and Klas Hjort. *Plasma-assisted InP-to-Si low temperature wafer bonding*. IEEE Journal of Selected Topics in Quantum Electronics, 8(1):118–131, 2002.

[36] Günther Roelkens, Liu Liu, Di Liang, Richard Jones, Alexander Fang, Brian Koch, and John Bowers. *III-V/silicon photonics for on-chip and intra-chip optical interconnects*. Laser & Photonics Reviews, 4(6):751–779, 2010.

[37] Stevan Stankovic, Richard Jones, Matthew N Sysak, John M Heck, Günther Roelkens, and Dries Van Thourhout. *Hybrid III–V/Si distributed-feedback laser based on adhesive bonding*. IEEE Photonics Technology Letters, 24(23):2155–2158, 2012.

[38] Di Liang, Marco Fiorentino, Tadashi Okumura, Hsu-Hao Chang, Daryl T Spencer, Ying-Hao Kuo, Alexander W Fang, Daoxin Dai, Raymond G Beausoleil, and John E Bowers. *Electrically-pumped compact hybrid silicon microring lasers for optical interconnects*. Optics Express, 17(22):20355–20364, 2009.

[39] Daniel M Kuchta, Tam N Huynh, Fuad E Doany, Laurent Schares, Christian W Baks, Christian Neumeyr, Aidan Daly, Benjamin Kögel, Jürgen Rosskopf, and Markus Ortsiefer. *Error-free 56 Gb/s NRZ modulation of a 1530-nm VCSEL link*. Journal of Lightwave Technology, 34(14):3275–3282, 2016.

[40] Amin Abbasi, Leili Abdollahi Shiramin, Bart Moeneclaey, Jochem Verbist, Xin Yin, Johan Bauwelinck, Dries Van Thourhout, Gunther Roelkens, and Geert Morthier. *III–V-on-silicon C-band high-speed electro-absorption-modulated DFB Laser*. Journal of Lightwave Technology, 36(2):252–257, 2018.

[41] Zhechao Wang, Kasper Van Gasse, Valentina Moskalenko, Sylwester Latkowski, Erwin Bente, Bart Kuyken, and Gunther Roelkens. *A III-V-on-Si ultra-dense comb laser*. Light: Science & Applications, 6(5):e16260, 2017.

[42] Ruijun Wang, Stephan Sprengel, Gerhard Boehm, Roel Baets, Markus-Christian Amann, and Gunther Roelkens. *Broad wavelength coverage 2.3 μm III-V-on-silicon DFB laser array*. Optica, 4(8):972–975, 2017.

[43] E Menard, KJ Lee, D-Y Khang, Ralph G Nuzzo, and John A Rogers. *A printable form of silicon for high performance thin film transistors on plastic substrates*. Applied Physics Letters, 84(26):5398–5400, 2004.

[44] Zhechao Wang, Amin Abbasi, Utsav Dave, Andreas De Groote, Sulakshna Kumari, Bernadette Kunert, Clement Merckling, Marianna Pantouvaki, Yuting Shi, Bin Tian, et al. *Novel light source integration approaches for silicon photonics*. Laser & Photonics Reviews, 11(4):1700063, 2017.

[45] Hongjun Yang, Deyin Zhao, Santhad Chuwongin, Jung-Hun Seo, Weiquan Yang, Yichen Shuai, Jesper Berggren, Mattias Hammar, Zhenqiang Ma, and Weidong Zhou. *Transfer-printed stacked nanomembrane lasers on silicon*. Nature Photonics, 6(9):615, 2012.

[46] Jing Zhang, Bahawal Haq, James OCallaghan, Angieska Gocalinska, Emanuele Pelucchi, António José Trindade, Brian Corbett, Geert Morthier, and Gunther Roelkens. *Transfer-printing-based integration of a III-V-on-silicon distributed feedback laser*. Optics express, 26(7):8821–8830, 2018.

[47] Joan Juvert, Tommaso Cassese, Sarah Uvin, Andreas De Groote, Brad Snyder, Lieve Bogaerts, Geraldine Jamieson, Joris Van Campenhout, Günther Roelkens, and Dries Van Thourhout. *Integration of etched facet, electrically pumped, C-band Fabry-Pérot lasers on a silicon photonic integrated circuit by transfer printing*. Optics express, 26(17):21443–21454, 2018.

[48] Tetsuo Soga, Shuzo Hattori, Shiro Sakai, Masanari Takeyasu, and Masayoshi Umeno. *Characterization of epitaxially grown GaAs on Si substrates with III-V compounds intermediate layers by metalorganic chemical vapor deposition*. Journal of applied physics, 57(10):4578–4582, 1985.

[49] JA Carlin, SA Ringel, EA Fitzgerald, M Bulsara, and BM Keyes. *Impact of GaAs buffer thickness on electronic quality of GaAs grown on graded Ge/GeSi/Si substrates*. Applied Physics Letters, 76(14):1884–1886, 2000.

[50] Yating Wan, Justin Norman, Qiang Li, MJ Kennedy, Di Liang, Chong Zhang, Duanni Huang, Zeyu Zhang, Alan Y Liu, Alfredo Torres, et al. *1.3 μm submilliamp threshold quantum dot micro-lasers on Si*. Optica, 4(8):940–944, 2017.

[51] Qiang Li, Kar Wei Ng, and Kei May Lau. *Growing antiphase-domain-free GaAs thin films out of highly ordered planar nanowire arrays on exact (001) silicon*. Applied Physics Letters, 106(7):072105, 2015.

[52] Daehwan Jung, Justin Norman, MJ Kennedy, Chen Shang, Bongki Shin, Yating Wan, Arthur C Gossard, and John E Bowers. *High efficiency low threshold current 1.3 μ m InAs quantum dot lasers on on-axis (001) GaP/Si*. Applied Physics Letters, 111(12):122107, 2017.

[53] Alan Y Liu, Chong Zhang, Justin Norman, Andrew Snyder, Dmitri Lubyshev, Joel M Fastenau, Amy WK Liu, Arthur C Gossard, and John E Bowers. *High performance continuous wave 1.3 μ m quantum dot lasers on silicon*. Applied Physics Letters, 104(4):041104, 2014.

[54] Zeyu Zhang, Daehwan Jung, Justin C Norman, Pari Patel, Weng W Chow, and John E Bowers. *Effects of modulation p doping in InAs quantum dot lasers on silicon*. Applied Physics Letters, 113(6):061105, 2018.

[55] Jianan Duan, Heming Huang, Bozhang Dong, Daehwan Jung, Justin C Norman, John E Bowers, and Frédéric Grillot. *1.3-\mu m Reflection Insensitive InAs/GaAs Quantum Dot Lasers Directly Grown on Silicon*. IEEE Photonics Technology Letters, 31(5):345–348, 2019.

[56] Daehwan Jung, Zeyu Zhang, Justin Norman, Robert Herrick, MJ Kennedy, Pari Patel, Katherine Turnlund, Catherine Jan, Yating Wan, Arthur C Gossard, et al. *Highly reliable low-threshold InAs quantum dot lasers on on-axis (001) Si with 87% injection efficiency*. ACS photonics, 5(3):1094–1100, 2017.

[57] Siming Chen, Wei Li, Jiang Wu, Qi Jiang, Mingchu Tang, Samuel Shutts, Stella N Elliott, Angela Sobiesierski, Alwyn J Seeds, Ian Ross, et al. *Electrically pumped continuous-wave III–V quantum dot lasers on silicon*. Nature Photonics, 10(5):307, 2016.

[58] Jinkwan Kwoen, Bongyong Jang, Joohang Lee, Takeo Kageyama, Katsuyuki Watanabe, and Yasuhiko Arakawa. *All MBE grown InAs/GaAs quantum dot lasers on on-axis Si (001)*. Optics express, 26(9):11568–11576, 2018.

[59] Jinkwan Kwoen, Joohang Lee, Katsuyuki Watanabe, and Yasuhiko Arakawa. *Elimination of anti-phase boundaries in a GaAs layer directly-grown on an on-axis Si (001) substrate by optimizing an AlGaAs nucleation layer*. Japanese Journal of Applied Physics, 58(SB):SBBE07, 2019.

[60] Tatau Nishinaga, Tsuyoshi Nakano, and Suian Zhang. *Epitaxial lateral overgrowth of GaAs by LPE*. Japanese journal of applied physics, 27(6A):L964, 1988.

[61] Tatau Nishinaga. *Microchannel epitaxy: an overview*. Journal of crystal growth, 237:1410–1417, 2002.

[62] G Bacchin and T Nishinaga. *A new way to achieve both selective and lateral growth by molecular beam epitaxy: low angle incidence microchannel epitaxy*. Journal of crystal growth, 208(1-4):1–10, 2000.

[63] Shigeya Naritsuka. *Microchannel epitaxy*. Progress in Crystal Growth and Characterization of Materials, 62(2):302–316, 2016.

[64] Yan-Ting Sun, Himanshu Kataria, Wondwosen Metaferia, and Sebastian Lourdudoss. *Realization of an atomically abrupt InP/Si heterojunction via corrugated epitaxial lateral overgrowth*. CrystEngComm, 16(34):7889–7893, 2014.

[65] Roger Chen, Thai-Truong D Tran, Kar Wei Ng, Wai Son Ko, Linus C Chuang, Forrest G Sedgwick, and Connie Chang-Hasnain. *Nanolasers grown on silicon*. Nature Photonics, 5(3):170, 2011.

[66] Fanglu Lu, Indrasen Bhattacharya, Hao Sun, Thai-Truong D Tran, Kar Wei Ng, Gilliard N Malheiros-Silveira, and Connie Chang-Hasnain. *Nanopillar quantum well lasers directly grown on silicon and emitting at silicon-transparent wavelengths*. Optica, 4(7):717–723, 2017.

[67] Hyunseok Kim, Wook-Jae Lee, Alan C Farrell, Juan SD Morales, Pradeep Senanayake, Sergey V Prikhodko, Tomasz J Ochalski, and Diana L Huffaker. *Monolithic InGaAs nanowire array lasers on silicon-on-insulator operating at room temperature*. Nano letters, 17(6):3465–3470, 2017.

[68] Hyunseok Kim, Alan C Farrell, Pradeep Senanayake, Wook-Jae Lee, and Diana L Huffaker. *Monolithically integrated InGaAs nanowires on 3D structured silicon-on-insulator as a new platform for full optical links*. Nano letters, 16(3):1833–1839, 2016.

[69] Myungil Kang, Jong-Soo Lee, Sung-Kyu Sim, Hyunsuk Kim, Byungdon Min, Kyoungah Cho, Gyu-Tae Kim, Man-Young Sung, Sangsig Kim, and Hyon Soo Han. *Photocurrent and photoluminescence characteristics of networked GaN nanowires*. Japanese journal of applied physics, 43(10R):6868, 2004.

[70] Thomas Mårtensson, C Patrik T Svensson, Brent A Wacaser, Magnus W Larsson, Werner Seifert, Knut Deppert, Anders Gustafsson, L Reine Wallenberg, and Lars Samuelson. *Epitaxial III- V nanowires on silicon*. Nano Letters, 4(10):1987–1990, 2004.

[71] Seokhyoung Kim, David J Hill, Christopher W Pinion, Joseph D Christesen, James R McBride, and James F Cahoon. *Designing morphology in epitaxial silicon nanowires: the role of gold, surface chemistry, and phosphorus doping*. ACS nano, 11(5):4453–4462, 2017.

[72] Yu Han, Wai Kit Ng, Ying Xue, Qiang Li, Kam Sing Wong, and Kei May Lau. *Telecom InP/InGaAs nanolaser array directly grown on (001) silicon-on-insulator*. Optics letters, 44(4):767–770, 2019.

[73] Yu Han, Qiang Li, Shih-Pang Chang, Wen-Da Hsu, and Kei May Lau. *Growing InGaAs quasi-quantum wires inside semi-rhombic shaped planar InP nanowires on exact (001) silicon*. Applied Physics Letters, 108(24):242105, 2016.

[74] Yu Han, Wai Kit Ng, Chao Ma, Qiang Li, Si Zhu, Christopher CS Chan, Kar Wei Ng, Stephen Lennon, Robert A Taylor, Kam Sing Wong, et al. *Room-temperature InP/InGaAs nano-ridge lasers grown on Si and emitting at telecom bands*. Optica, 5(8):918–923, 2018.

[75] Bin Tian, Zhechao Wang, Marianna Pantouvaki, Philippe Absil, Joris Van Campenhout, Clement Merckling, and Dries Van Thourhout. *Room temperature O-band DFB laser array directly grown on (001) silicon*. Nano letters, 17(1):559–564, 2016.

[76] Zhechao Wang, Bin Tian, Marianna Pantouvaki, Weiming Guo, Philippe Absil, Joris Van Campenhout, Clement Merckling, and Dries Van Thourhout. *Room-temperature InP distributed feedback laser array directly grown on silicon*. Nature Photonics, 9(12):837–842, 2015.

[77] Niamh Waldron, Clement Merckling, Weiming Guo, Patrick Ong, Lieve Teugels, Sheikh Ansar, Diana Tsvetanova, Farid Sebaai, DH Van Dorp, Alexey Milenin, et al. *An InGaAs/InP quantum well finfet using the replacement fin process integrated in an RMG flow on 300mm Si substrates*. In 2014 Symposium on VLSI Technology (VLSI-Technology): Digest of Technical Papers, pages 1–2. IEEE, 2014.

[78] Weiming Guo, L Date, V Pena, X Bao, C Merckling, N Waldron, N Collaert, M Caymax, E Sanchez, E Vancoille, et al. *Selective metal-organic chemical vapor deposition growth of high quality GaAs on Si (001)*. Applied Physics Letters, 105(6):062101, 2014.

2

InGaAs/GaAs nano-ridge growth

In Chapter 1, we have emphasized the importance of co-integration of III-V materials with Silicon and discussed the advantages of heteroepitaxy compared with other approaches. The quality of the epitaxial material is essential though as it has been proved that high defect density has a definite impact on device performance and reliability [1–3]. Although the epitaxial growth of the III-V material used in this work was carried out by the imec epi-team led by dr. B. Kunert, a discussion on defects formation and crystal quality of the novel nano-ridges is essential for the furhter understanding of this thesis.

Therefore, in this Chapter, we will first explain what the technical difficulties are in order to grow single-crystal lattice-mismatched III-V materials on a Si substrate. The significant lattice mismatch between III-V materials and Si generates a high defect density, which is detrimental for laser devices. This section is followed by the introduction of the specific growth technology adopted in this work, InGaAs/GaAs nano-ridge growth by aspect-ratio trapping (ART) and nano-ridge engineering (NRE). The detailed growth process is described and the quality inspection of the as-grown nano-ridges by means of scanning electron microscope (SEM), transmission electron microscope (TEM) and reciprocal space map (XRD-RSM) is discussed.

2.1 Introduction to heteroepitaxy

2.1.1 Lattice mismatch

Stacking a III-V layer on a Si substrate by epitaxy has to take the lattice constant contrast of the materials into account. If the lattice constant of the III-V material $a_{III\text{-}V}$ happens to be equal to the lattice constant of the substrate a_{sub}, it is said the two materials are lattice-matched and good crystal quality can be relatively easily obtained by heteroepitaxy. Unfortunately, nearly no III-V material has exactly the same lattice constant as Si does. Furthermore, in order to develop laser devices for a specific application, emitting at the right wavelength is one of the fundamental requirements when selecting the material. For telecommunication applications, the O-band or the-C band are demanded.

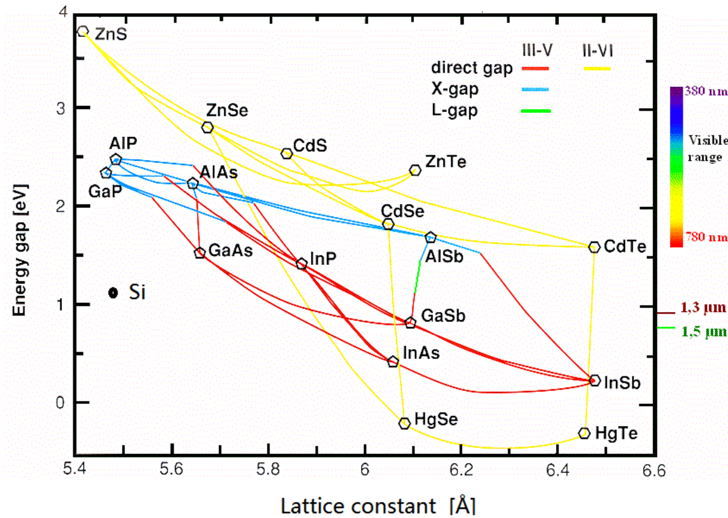

Figure 2.1: Plot of bandgap energy vs. lattice constant of common semiconductors. The right axis indicates the corresponding wavelength. Reproduced from [4].

In more realistic cases, most semiconductors of interest have a lattice constant $a_{III\text{-}V}$ larger than a_{sub}, as illustrated in Figure 2.1. The III-V layer with $a_{III\text{-}V}$ grown on a substrate has to follow the lattice of the substrate a_{sub} at the growth interface. Thereby local strain is generated and material defects are formed driven by the lattice mismatch. If $a_{III\text{-}V} < a_{sub}$ as shown in Figure 2.2, the III-V material grown on the substrate undergoes tensile strain which distorts the epitaxial material laterally to fit the substrate lattice in plane. Likewise, if $a_{III\text{-}V} > a_{sub}$ as shown in Figure 2.3, the III-V material grown on the substrate undergoes compressive strain, again distorting the epitaxial material laterally. The strength of the

local strain is proportional to the lattice mismatch, which is defined as

$$\Delta_{III\text{-}V\text{-}sub} = \frac{a_{III\text{-}V} - a_{sub}}{a_{III\text{-}V}} \quad (2.1)$$

When III-V material is tensile strained, $\Delta_{III\text{-}V\text{-}sub} < 0$ and when III-V material is compressively strained, $\Delta_{III\text{-}V\text{-}sub} > 0$. For instance, the lattice mismatch between GaAs and Si is $\Delta_{GaAs\text{-}Si} \approx 4.09\%$ with the lattice constant of Si $a_{Si} = 5.431$Å, and of GaAs $a_{GaAs} = 5.653$Å.

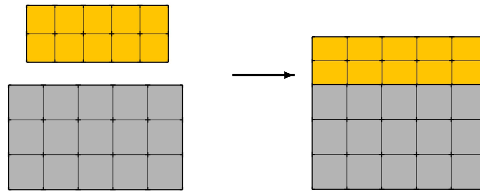

Figure 2.2: Epitaxial growth of III-V material on substrate with the lattice constant $a_{III\text{-}V} < a_{sub}$, the epitaxial III-V material undergoes tensile strain.

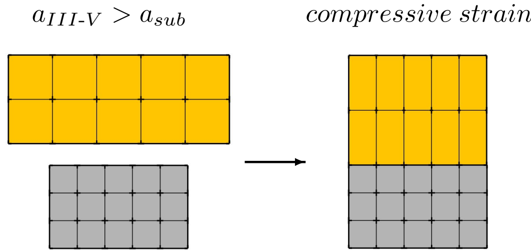

Figure 2.3: Epitaxial growth of III-V material on substrate with the lattice constant $a_{III\text{-}V} > a_{sub}$, the epitaxial III-V material undergoes compressive strain.

The lines connecting two binaries in Figure 2.1 present III-V ternary compounds, which are alloys of the binaries. These ternaries provide a high degree of freedom to adjust their bandgap (emitting wavelength) and lattice constant. The lattice constant of the ternary $A_xB_{1-x}C$ can be calculated from Vegard's law, expressed as

$$a_{A_xB_{1-x}C} = x \times a_{AC} + (1-x) \times a_{BC} \quad (2.2)$$

with x the fraction of AC in $A_xB_{1-x}C$ and $1-x$ the fraction of BC. For example for $In_{0.2}Ga_{0.8}As$, the lattice constant $a_{In_{0.2}Ga_{0.8}As} = 5.734$Å. The bandgap of

the ternary $A_xB_{1-x}C$ can also be interpolated in a similar fashion, but a second-order bowing parameter has to be added to fit the curved lines between two binaries

$$E_{gA_xB_{1-x}C} = x \times E_{gAC} + (1-x) \times E_{gBC} - x(1-x)C_{ABC} \tag{2.3}$$

where C_{ABC} is an empirical bowing parameter.

2.1.2 Defect formation

Given that most direct-bandgap III-V compounds exhibit a lattice constant between $5.6\,\text{Å}$ and $6.5\,\text{Å}$, the mismatch between Si and III-V compounds is quite large. Therefore, the grown material is highly distorted in its first few lattice units to match the Si substrate lattice and experiences strong local strain. However, beyond a certain thickness, the crystal lattice tends to release the accumulated strain by forming defects. This thickness is the so-called critical thickness h_{crt}. Within h_{crt} the epitaxial material is defect-free, yet the defect density dramatically raises when the growth thickness exceeds h_{crt}. The value of h_{crt} is closely related to $\Delta_{III\text{-}V\text{-}sub}$, typically thought to be $\approx 20nm$ when the lattice mismatch is small ($\Delta_{III\text{-}V\text{-}sub} = 1\%$) [5]. However, to grow the widely used laser-materials GaAs or InP on Si with $\Delta_{III\text{-}V\text{-}sub} \approx 4\%$ or 7%, defect formation starts almost immediately from the interface between the two materials. The release of strain by forming defects is illustrated in Figure 2.4, where a misfit appears to allow the heteroepitaxial material to return to its natural lattice configuration.

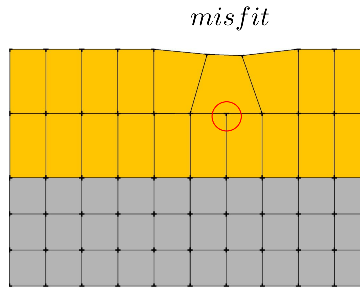

Figure 2.4: Misfits formation after critical thickness h_{crt} to allow elastic strain relaxiation.

A defect, generally speaking, can be any kind of deviation from a perfect crystal layout of the semiconductor atoms. Considering the dimensionality as a criterion, defects can be categorized as zero-, one, two- and three- dimensional. Point defects, like interstitials, vacancies, anti-sites and impurity atoms in semiconductors, are zero-dimensional. Misfit defects (MD) and threading dislocations (TD) are one-dimensional line defects, which always spread following specific crystal

directions. Two-dimensional defects are planar defects like free surfaces, internal interfaces, stacking faults and anti-phase boundaries (APBs) between crystal regions of different polarities. Defects expanding in three dimensions like twinned regions, grains and precipitates are considered as volume defects.

Point defects, as the name indicates, interrupt the crystal at an isolated site. They can be classified into intrinsic defects and extrinsic defects, depending on the source of the defects. Vacancies and interstitials are intrinsic point defects where an intrinsic atom is missing or appears at an unnatural location. An anti-site defect is another type of point defect and fairly common in semiconductors as GaAs [6]. Extrinsic point defects are formed by foreign atoms. They are impurities if added unintentionally but can be manipulated on purpose to control the semiconductor electrical properties. Generally, through optimizing the growth conditions and using advanced tools with low contamination level, impurities can be well controlled during epitaxy.

As we mentioned, when a hetero-layer exceeds the critical thickness h_{crt}, dislocations start to appear in the crystal structure to reduce the strong elastic strain energy. Figure 2.5 illustrates the formation of misfit dislocations (MDs) in red line and TDs in yellow line in a 3D perspective, where the so-called slip plane is marked by dashed lines. MDs shift the atom positions in the vicinity of the defect lines. Dislocations are mobile so that the pre-existing TDs originating from the substrate bend over and glide along the slip planes to drive MD segments to the interface and coalesce with other MD segments forming a half loop. Energy states introduced by dislocations inside the bandgap of the III-V material usually form deep level traps for carriers. They can act as electrical defects and non-radiative recombination centers, limiting the photon emission efficiency and the minority carrier lifetime. It has been shown in many works [7–9] that MDs and TDs in the active region have a detrimental effect on the device performance and lifetime. Consequently, engineering dislocation density is one of the key requirements to develop new heteroepitaxial materials for device applications. The approach taken in our case is discussed in Section 2.2.

Planar defects in a crystal can be divided into two types: interfaces, which are either the interface between the outer crystal surface and the surrounding vapor or liquid or the interface between two different solid crystals, and internal defects that disrupt the crystalline pattern within a crystal. The free outer surfaces not only determine the shape of the crystal profile but also bring many dangling bonds. These bonds providing favorable sites for external atoms and creating defect states in the semiconductor energy bandgap lead to carrier loss by non-radiative recombination. The surface issue becomes more prominent for the nano-ridges case, whereby the surface-to-volume ratio (S/V) is high with the one $\{001\}$, two $\{111\}$ and two $\{110\}$ planes exposed to the air or silicon dioxide. Approaches to passivate the surfaces were investigated therefore and already showed some positive effects, as

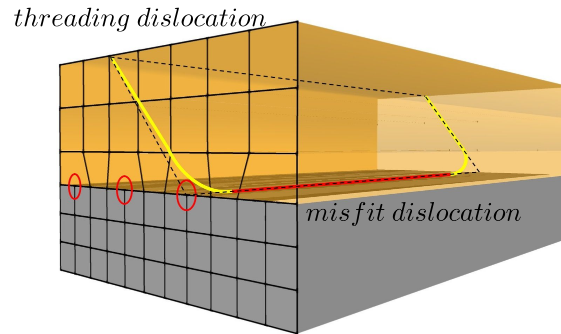

Figure 2.5: The formation of misfit dislocations (red line) at the interface of hetero-layer and substrate and threading dislocation (yellow line) along slip plane marked with dashed black lines.

will be discussed in the following sections.

Stacking faults and anti-phase boundaries (only for polar compounds) are frequently observed at the interface of hetero-layers. Stacking fault is a defect in the sequence of atom distribution over the crystal planes. Assuming a natural stacking sequence of a III-V ternary ...ABCABC..., the local stacking sequence ...ABCBABC...constitutes a stacking fault with an extra B plane in the middle. It is formed by inserting or removing one double atom $\{111\}$ plane and easily caused by any kinds of surface damages or impurities. Therefore, the cleaning and pretreatment of the Si surface before III-V growth is an essential step to avoid the nucleation of stacking faults. Figure 2.6 (a) shows the stacking fault plane marked by red dashed lines.

APBs only occur in ordered polar compounds, where at least two types of atoms can be chosen to bond with another atom. For example, the normal bonds in binary III-V compounds are polar III-V, but anti-phase domains (APDs) of homopolar III-III or V-V bonds can exist. Because Si is a nonpolar semiconductor, heteroepitaxy of III-V on Si risks the formation of APDs at each monoatomic $\{001\}_{Si}$ plane, which induces an anti-phase boundary as shown in Figure 2.6 (b) marked by red dashed lines. A monoatomic surface step on a $\{111\}_{si}$ excludes APBs, which simplifies the heteroepitaxial III-V growth on Si. Applying this trick to reduce the defect density in the nano-ridge will be discussed in the following section.

Volume defects (three-dimensional defects) in crystals are usually precipitates, dispersants, inclusions and voids. Normally for a well-controlled epitaxy process with highly purified precursors, the volume defect density should be negligible and is not further considered here. Readers who are interested in this part can find

more information in [6].

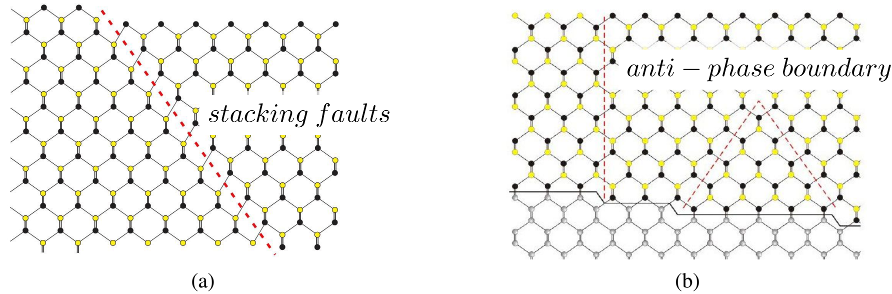

Figure 2.6: planar defects (a)stacking faults (b) anti phase domain. Reproduced from [10].

2.1.3 Approaches for heteroepitaxy

Given that III-V semiconductors exhibit a significant lattice mismatch with the Si substrate, as discussed above, specific strategies are always applied to obtain sufficient crystal quality. As discussed in the state-of-art Section 1.1.3, several different approaches were utilized individually or in combination to reduce defect density. Here we shortly summarize the approaches presented in literature, including but not limited to the use of off-cut Si substrates with a small angle, Si substrates patterned with V-grooves, using thick buffer layers, utilization of intermediate layers, insertion of dislocation filter layers (DFLs), selective-area growth (SAG), aspect ratio trapping (ART) and growth along specific directions.

The standard Si wafers used in the electronics industry are on-axis of $\langle 001 \rangle$. Also the $\langle 011 \rangle$ or $\langle 111 \rangle$ crystal orientations are sometimes used. However, the wafer can be sliced also with an off-angle, so-called off-axis substrate. The off-cut angle is found to have an impact on the heteroepitaxy growth rate, doping, crystal quality and so on [11, 12]. A relative large off-angle (e.g., $8\,^{\circ}$) is discovered to help decline APBs. An alternative to obtaining a growth surface with specific crystal orientation is to expose the desired crystal planes by anisotropic etching. For instance, a V-grooved Si substrate etched by KOH from a standard $\langle 001 \rangle$ wafer has the $\{111\}_{Si}$ planes exposed to avoid APDs.

The insertion of additional layers between the heteroepitaxial stack and the substrate, e.g., thick buffer layers, intermediate layers and DFLs, is another approach often used. It was observed that the TD density at the epitaxial material surface is decreased by around two orders of magnitude when the buffer layer thickness increases by one order of magnitude [13]. The decline is due to the mobility of TDs, which leads to interaction, coalescence and annihilation when TDs meet during growth. With a thickness of the buffer layer of several tens of mi-

crometers, the TD density could typically drop from 10^{10} cm^{-2} to 10^{5} cm^{-2}. Nevertheless, a thicker buffer layer shows more limited efficiency on defect reduction. Germanium with a lattice constant between that of Si and most III-V semiconductors (even identical to that of GaAs) is also a popular buffer material. It can be inserted between the Si substrate and III-V as an intermediate layer to decrease the lattice mismatch for heteroepitaxial growth [14]. As for DFLs, they are actually so-called strained-layer superlattices. By adding DFLs, which apply in-plane forces to the TDs and enhance their lateral motions, the probability of annihilation of TDs is increased.

Instead of growing on a blanket substrate, SAG was also adopted as a technique to reduce defects [15]. For SAG of III-V materials, typically, a SiO_2 mask is fabricated on Si wafer. Due to a high growth selectivity for epitaxy on Si vs. SiO_2 when using an MOCVD process, accurate positioning of the III-V material can be achieved. Moreover, defects are unable to protrude through SiO_2, and therefore III-V/SiO_2interfaces can be used as defects blockades. This is always combined with structures with a high aspect ratio (AR). High-AR SiO_2 openings on Si enable III-V growth and sufficient trapping of TDs inside these openings once the aspect ratio is high enough. This technique is called aspect ratio trapping (ART) [16].

Growth with high AR is always accompanied with the restriction on achievable III-V volume, hence controlling the growth out of high-AR structures is also a crucial technique. The overgrowth can be very anisotropic, dependent upon the growth rate of different crystal planes, which is controlled by the epitaxy conditions. We have mentioned lateral epitaxy and vertical epitaxy in Section 1.1.3, where the growth is faster in one direction compared to the other, to avoid defect-rich regions [17, 18]. Additionally, manipulation of the growth rate of multiple crystal planes through adjusting the growth parameters is possible to form defined 2D or even 3D shapes of III-V material. For example, control of the growth rate of the {001}, {110} and {111} crystal planes of GaAs and InP has demonstrated elongated rectangles, different diamond-like, pyramidal or triangular shapes [19, 20]. Furthermore, the cross-sectional design facilitated by engineering the growth rate of different surfaces can produce optical elements by itself, e.g. optical waveguides, without any post-processing.

2.2 Growth by aspect ratio trapping

2.2.1 Introduction to ART and NRE

Adopting practical defect-reducing approaches is of utmost importance to grow III-V materials for devices with superior lifetime and reliability. However, this could be especially challenging for the heteroepitaxy of nanometer-scale structures, which leaves little room for applying buffer layers or extra DFLs. There-

fore, the imec epi-team endeavored to find a way out by utilizing a combination of ART and so-called nano-ridge engineering (NRE) for developing GaAs/InGaAs nano-ridges heteroepitaxially grown on 300 mm-wafers for photonic applications.

- **ART**

The simplified schematic of Figure 2.7 illustrates the trapping mechanism for III-V TDs and PDs along with the two different crystal orientations inside oxide trenches on a Si substrate. As aforementioned, the growth of lattice-mismatched III-V material will initiate the nucleation of TDs and MDs to release strain. If the lattice is highly mismatched, most defects are nucleated close to the III/V-Si interface. The remaining strain fields typically lead to the formation of TD half-loops terminated at the epitaxial material surface, as shown in Figure 2.5. During the growth, the TD half-loops start to glide down towards the hetero-interface along the $\{111\}$ plane. As the TDs extend, the two dislocation ends will finally hit the oxide sidewalls. For a $\{111\}$ slip plane parallel to the trench orientation, the dislocation ends will finally collide with the oxide walls as the trench gets filled due to the inclined angle of 54.7° between the slip plane and the vertical mask sidewall (Figure 2.7 (a)). The 54.7° inclined angle determines the minimal AR of $tan(54.7°) = 1.43$, which is required, in theory, to trap all TDs initiated at the interface. In practice a larger AR is required. This trapping mechanism is more obvious in the case where the $\{111\}$ plane is perpendicular to the oxide sidewalls, as shown for the case (b) in Figure 2.7. PDs such as stacking faults and twins expand in a $\{111\}$ plane in a two-dimensional way such that only PDs in a $\{111\}$ plane parallel to the trench orientation are blocked (Figure 2.7 (c)). A PD perpendicular to the oxide sidewalls will extend out of the trench as no trapping along the trench occurs (Figure 2.7 (d)). Hence nucleation of this type of PDs should be avoided as much as possible.

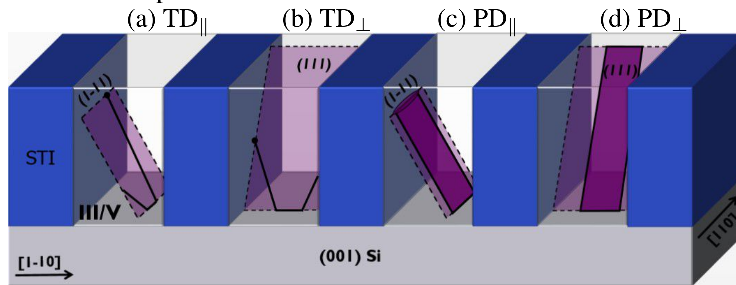

Figure 2.7: Sketch of aspect ratio trapping (ART) in narrow trenches. TDs gliding along a $\{111\}$ plane are trapped in both directions (a) and (b) whereas a PD is only trapped in a plane parallel to the trench orientation (c). A PD in a plane perpendicular to the trench sidewalls will penetrate the full III-V layer. Reproduced from [10].

Another concern comes from the different polarities, whereby III-V compound

semiconductors are polar while Si is nonpolar. As mentioned, the monolithic growth of polar III/V on nonpolar Si bears the risk of forming APDs if no specific surface treatment is carried out before growth. The trick is to create a monoatomic surface step on a $\{111\}$ Si substrate to reduce defects. On $\{001\}$ oriented wafers, $\{111\}$ facets can be exposed by wet etching into the Si substrate during the STI process to produce V-shaped grooves. This technique is used for the III-V nano-ridges growth to exclude the formation of APDs efficiently.

- **NRE**

After growth inside SiO_2 trenches, NRE, exploiting differences in growth rate on different crystal planes is key to obtain well-defined nano-ridges' profiles. Taking a GaAs nano-ridge as an example, when GaAs is grown in a trench with V-grooved $\{111\}$ Si surfaces, it typically has Ga-terminated top $\{111\}_{Ga}$ and As-terminated lower $\{111\}_{As}$, $\{110\}$ and (001) nano-ridge planes, as illustrated by the sketches in Figure 2.8 (from [21]). By adjusting the MOVPE growth conditions, it is possible to manipulate the growth rate hierarchy of these different crystal planes (facets of nano-ridge) due to their unique surface properties. The facets with higher growth rates will finally disappear, whereas the facets with lower growth rates construct the nano-ridge profile. This leads to the formation of distinct nano-ridge shapes, such as elongated rectangles, diamond profiles with different sizes and triangles, as shown in the SEMs in Figure 2.8.

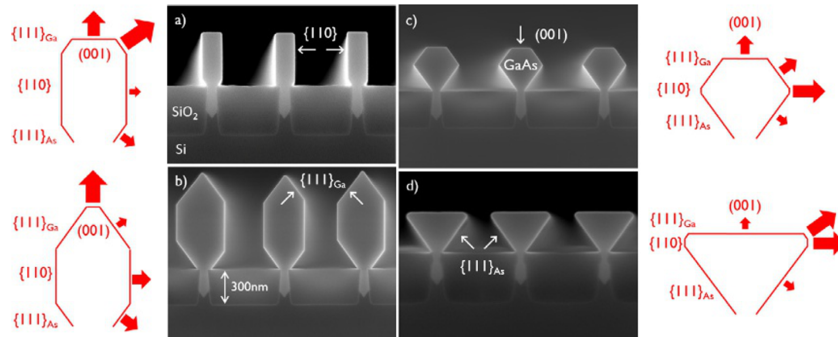

Figure 2.8: (a)-(d) are cross-section SEM images of GaAs nano-ridges deposited under very different MOVPE growth conditions. The simplified sketch next to each SEM image compares the growth rates on the different facets indicated by the size of the red arrow. Reproduced from [21].

For photonic applications, a good confinement of light in waveguides is always preferred, and therefore the nano-ridges are designed to have a rectangular-shape. In addition the defective trenches could induce high carrier loss while the Si substrate with a high refractive index might cause light leakage. Therefore, elongated

rectangles, which facilitate small overlap between the optical mode and the trenches/Si substrate, are recommendeded to avoid high losses. Having the $\{111\}_{Ga}$ planes grow faster and the $\{110\}$ planes grow slower will produce such a structure as is clear now from the above discussion.

2.2.2 Nano-ridge growth process

In order to meet the requirements of the envisaged applications, the nano-ridges must provide efficient radiative combination, have a low defect density and emit at the desired wavelengths. Particularly for fiber-optic communication systems, the frequently used wavelength ranges are the O-band (1260-1360nm) and the C-band (1530-1570nm) with the smallest dispersion and the lowest loss, respectively, in fiber optics. According to the III-V energy bandgap diagram shown in Figure 2.1, only GaAs, InP, InAs, GaSb and their compounds have a direct bandgap and meanwhile cover the O-band and/or the C-band. InP-based structures were investigated in previous work [22]. In this dissertation, we primarily focus on GaAs-based nano-ridges with InGaAs as the active QW region.

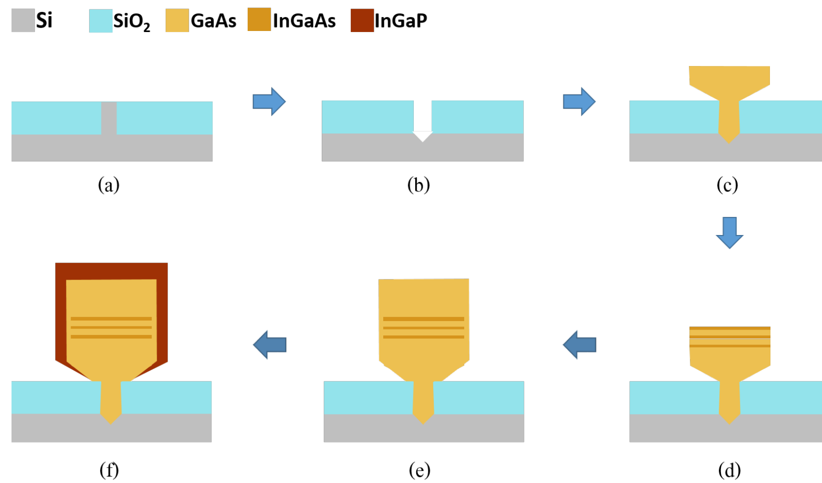

Figure 2.9: The GaAs nano-ridge epitaxy process. (a) the process starts with a Si wafer patterned with a SiO_2 mask using an STI step. (b) the Si trenches with V-shape are obtained by TMAH wet etching. (c) the growth of GaAs, first inside and then outside the trench. (d) the growth of three $In_{0.2}Ga_{0.8}As$ QWs. (e) top GaAs barrier is grown and (f) a passivation layer of InGaP is deposited.

As aforementioned, we combined the ART and NRE techniques to grow GaAs nano-ridges on a Si substrate with a SiO_2 mask. The high-quality nano-ridges can further serve as a fully relaxed buffer for the pseudomorphic growth of compres-

sively strained InGaAs QWs. The epitaxy process of the reference sample S_{Ref} is illustrated in Figure 2.9. The growth starts from a 300nm-thick oxide mask on Si, which is obtained by a standard shallow trench isolation (STI) process flow whereby trenches of 5 mm in length and widths varying from 60 nm to 500 nm are patterned on exact $\{001\}$ 300-mm Si substrate. There are ten trenches of each configuration, and the ratio of the Si trench surface versus the total area is kept constant to 9%, decided by previously defined mask. V-shaped Si grooves with exposed $\{111\}$ facets are achieved by a tetramethylammonium hydroxide (TMAH) wet-etch step to avoid APD formation. As mentioned, the high-aspect-ratio trench in turn efficiently traps TDs and inclined PDs by its two vertical SiO_2 sidewalls, stopping defects from going out of the trench into the upper ridge. The growth is carried out using metal-organic vapor phase epitaxy (MOVPE) with tertiarybutyl arsine (TBAs), tertiarybutyl phosphine (TBP), trimethylindium (TMIn), triethylgallium (TEGa), and trimethylgallium (TMGa) as the precursors. The GaAs epitaxy starts with a thin nucleation layer, followed by the growth of the main GaAs structure, first inside and then outside of the trenches. The embedded active region consists of three compressively strained InGaAs QWs with about 20% indium. The growth process is completed by depositing a passivation layer of InGaP covering the full ridge to suppress non-radiative surface recombination and provide better carrier confinement in the lateral direction. The profile of the ridges and the position of the QWs is carefully engineered by carefully selecting the growth conditions to control the growth rates of different crystal planes such that the nano-ridges support a low-loss and high-gain optical mode for photonics applications.

2.2.3 Inspection of nano-ridge growth quality through electron microscopy

Dependent on the growth rate and time, the elongated-rectangular nano-ridge are typically several hundred nanometers wide. The size can be well determined by scanning electron microscope (SEM) (accuracy $\sim$ 10 nm). QWs, as well as defects, on the scale of several nanometers or even smaller, can only be observed by transmission electron microscopy (TEM), whereby atom-scale structures can be seen. Through the direct imaging of the as-grown materials by SEM and TEM, a first insight into the nano-ridge quality is obtained. This inspection (except table 2.1) was carried out by the imec-epi team but is included here because it is needed to understand the results reported further in this thesis. Figure 2.10 (a)-(d) shows SEM images of the cleaved nano-ridges with trench width (marked as d in Figure 2.11) 60 nm, 100 nm, 300 nm and 500 nm respectively. All figures are on the same scale. These figures show the nano-ridge volume increases as the trench opening and spacing between the nano-ridges are getting broader, which allows more precursors reaching the nano-ridges.

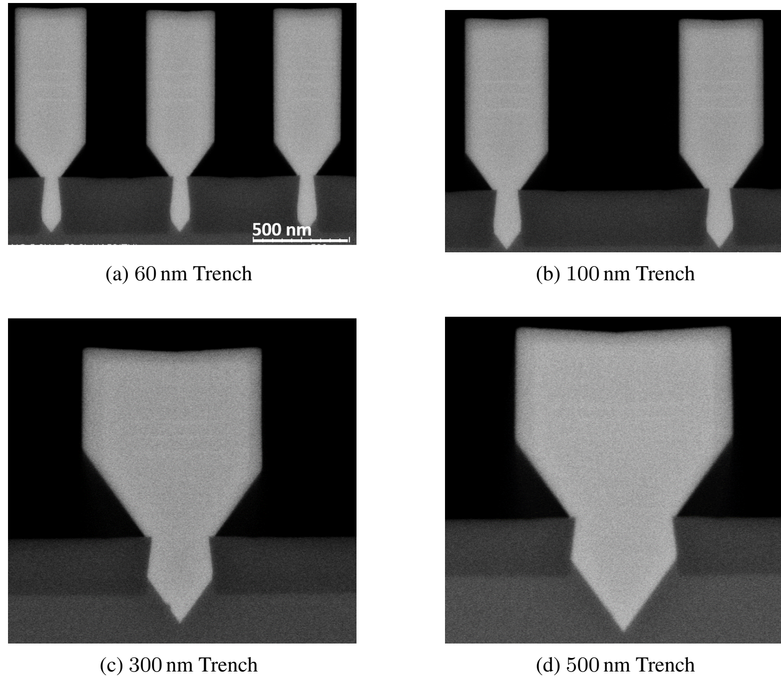

(a) 60 nm Trench

(b) 100 nm Trench

(c) 300 nm Trench

(d) 500 nm Trench

Figure 2.10: The SEM images of the cleaved nano-ridges with trench width (a) 60 *nm, (b)* 100 *nm, (c)*300 *nm and (d)*500 *nm on the same scale.*

Figure 2.11 shows high-angle annular dark-field (HAADF) scanning transmission electron microscope (STEM) images of the GaAs nano-ridge with a trench width of 100 nm of the reference sample S_{Ref}. In the left image, each layer in the stack, including the $\sim 10nm$ thick QWs, is resolved. The right upper one is a zoomed-in image of the QW region where not only the horizontal QWs and barriers are shown, but also the < 5 nm InGaAs layers on $\{110\}$ crystal planes can be observed. The right lower image is a magnification of the passivation layer, where the InGaP-layer is ~ 50 nm thick at the $\{110\}$ facet and very thin at the lower $\{111\}$ facet. The relevant geometrical parameters of sample S_{Ref} shown in Figure 2.11 are listed in Table 2.1. e is the thickness of the SiO_2 mask layer, which is always set to 300 nm in the simulations and measured to be around 291 nm in real cases. Given that the $\{111\}$ planes are inclined at an angle of 54.7°, all the geometrical parameters of the nano-ridges can be derived by knowing the trench width d, ridge width a, and ridge height b.

The fact that ART leads to a very efficient defect trapping in 100 nm wide trenches has been further confirmed by HR bight field (BF)-STEM images of a lateral cut along a nano-ridge (length of 5.0μ m) as shown in Figure 2.12 (a). The

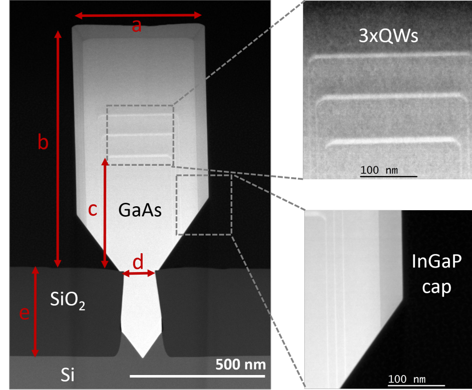

Figure 2.11: HAADF-STEM images of the GaAs nano-ridge waveguide of sample S_{Ref}. The right upper one shows zoomed-in QWs, and barriers while the lower STEM shows the InGaP passivation layer.

d(nm)	**60**	**80**	**100**	**300**	**500**
a(nm)	348	389	432	882	1068
b(nm)	869	880	872	903	955
c(nm)	389	393	398	407	408

Table 2.1: GaAs nano-ridges parameters noted in Figure 2.11. d: trench width; a: ridge width; b: ridge height; c: position of the lowest QW.

position of the QWs and the thickness of the SiO_2 layer are labeled. All TDs are observed to be confined inside the SiO_2 trench. No indication of any misfits or TDs was found in the upper ridge structure. Planar defects such as twins are typically visible in a $5.0\,\mu$m long transverse section however. The formation of planar defects can have various sources. In this case, it is suspected that twins or stacking faults are caused by either a non-optimal GaAs seed layer or by residuals and contamination on the Si surface due to an insufficient cleaning procedure. In comparison, the image of a 200 nm-wide-trench nano-ridge is shown in Figure 2.12 (b). The significant difference is that TDs start to exceed the SiO_2 neck and appear in the upper GaAs region. Following the rule of ART that trenches with an aspect ratio higher than $\tan 54.7° = 1.41$ are theoretically capable of blocking all TDs within the trench region, trenches wider than 206 nm under the fixed height of 230 nm (the least measured value) bear the risk of escaping TDs. The complete blocking of TDs within the sufficiently narrow trench region is a notable achievement towards laser integration with sufficient lifetime. Figure 2.12

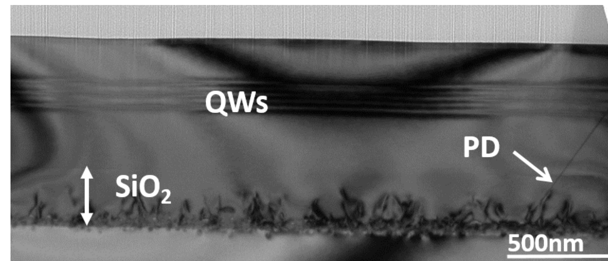

(a) 100nm Trench

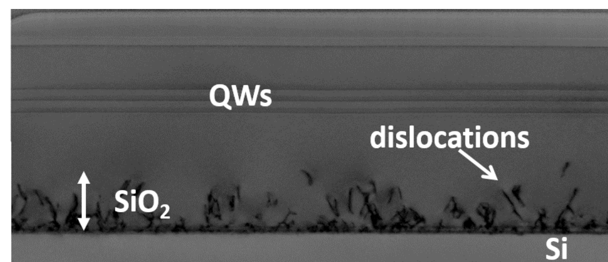

(b) 200nm Trench

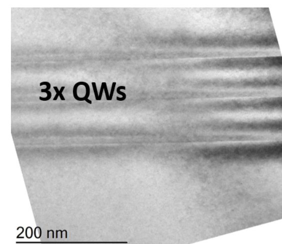

(c) Quantum well

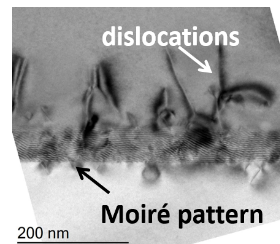

(d) Dislocations at GaAs/Si interface

Figure 2.12: BF-STEM images of the nano-ridges of sample S_{Ref}. (a) lateral cut along nano-ridge for 100nm wide trench. (b) lateral cut along nano-ridge for 200nm wide trench (same scale with (a)), (c) a zoom-in image showing defects-free QW region, (d) a zoom-in image showing dislocations at GaAs/Si interface.

(c) and (d) are the magnifications of the QWs and the GaAs/Si interface region respectively, where good quality of the active region and defect nucleation starting at the interface can be seen.

Besides the investigation on the crystal quality focusing only on one single nano-ridge, Figure 2.13(a) shows a SEM image from a larger scale sample: the top-view SEM image of the nano-ridge array with trench width from 60 nm to 100 nm with a length of 5 mm. Figure 2.13 (b) shows the tilted cross-section SEM

image of three 80-nm trench nano-ridges, where the flat top $\{001\}$ surfaces are observed. The straight nano-ridges and smooth surfaces illustrate the excellent uniformity and high yield of the epitaxial growth.

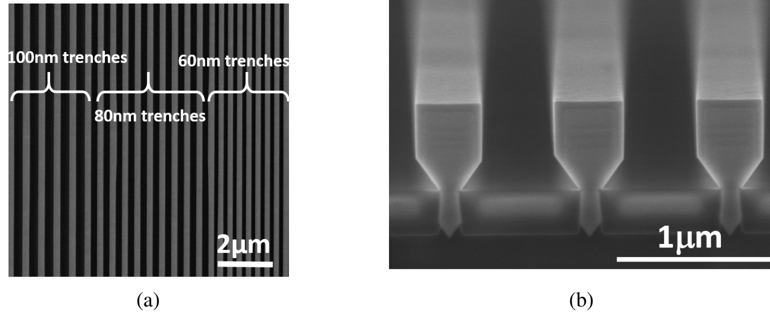

(a) (b)

Figure 2.13: Images of sample S_{Ref}. (a)The pop view SEM image of nano-ridge array with trench width from 60 to 100 nm. (b) Tilted view of cleaved nano-ridge array with trench width of 80nm.

The (224) reciprocal space map by X-ray diffraction (XRD-RSM) in Figure 2.14 shows the lattice parameter of the nano-ridge in the reciprocal space (unit $\AA^{-1}$). The x-axis value $Q(x) = 0.5003\AA^{-1}$ corresponds to the $5.653\AA$ GaAs lattice constant [23]. From this figure we can derive the GaAs nano-ridge is fully relaxed, the InGaP cap is lattice matched to the GaAs nano-ridge and the QWs are fully-strained.

Besides a high crystal quality also the detailed layer stack build up is essential. The optical modal gain is highly dependent on (approximately proportional to) the number of QWs. A proper capping layer to passivate the nano-ridges' surfaces could efficiently reduce carrier loss through non-radiative surface recombination. A carrier blocking layer underneath the QWs, which prevents carriers in the active region from traveling to the defective trenches, is expected to suppress carrier loss. In order to study the impact of different configurations, a series of samples grown on a similar SiO_2-patterned substrate with slightly different layer stacks or material compositions were fabricated. The overall dimensions of the nano-ridge with the same trench width can slightly vary from sample to sample, dependent on the detailed process. The samples discussed in this Ph.D. work are listed in Table 2.2. For sample S'_{Ref}, a thin GaPAs layer with about 11% phosphor is inserted to induce a slightly tensile strain before depositing the compressively strained QWs. Figure 2.15 shows the high-angle annular dark-field (HAADF) scanning transmission electron microscope (STEM) images of sample S'_{Ref}. In the left image, the GaAsP layer is shown below the QWs. The right image is a high-resolution (HR) STEM of the GaAs root showing defects nucleated from the V-shaped GaAs/Si in-

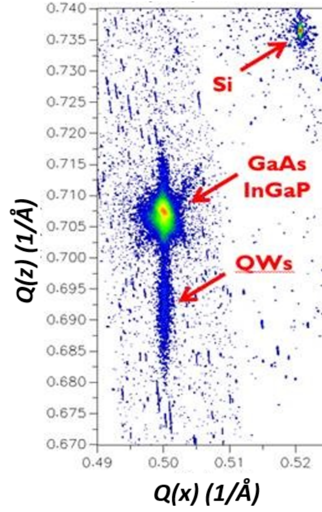

Figure 2.14: The (224) Resonance Shear Measurement(XRD-RSM) of the nano-ridge. QWs are fully strained to the fully relaxed GaAs nano-ridge and InGaP cap is lattice-matched .

terface. This is the sample we selected for laser development. $S_{2\times cap}$ and $S_{0\times cap}$ have ~ 100 nm thick passivation layer and no passivation layer respectively. While S_{Ref} has three QWs, $S_{2\times QWs}$ has two. S_{blk1} and S_{blk2} have a blocking layer of InGaP and GaAsP respectively below the QWs to prevent carriers from travelling to the defective trench region. Sample S_{dope} includes a p-i-n junction. To extend the emission wavelength, $S_{InGaAs1}$ and $S_{InGaAs2}$ have a different material compositions of bulk and QWs. The results obtained with these samples will be given in the coming Chapters. For convenience, their figure indexes are also given in the table if their images are included in the book.

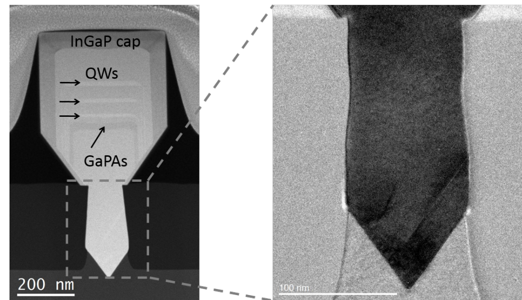

Figure 2.15: HAADF-STEM images of the GaAs nano-ridge waveguide of sample S'_{Ref}. The right image shows the GaAs root grown in SiO_2 trench.

Sample	Barrier	QWs	QWs No.	Cap	Blocking layer	Image	Remarks
S_{Ref}	$GaAs$	$Ga_{0.2}As_{0.8}$	3	$In_{0.5}Ga_{0.5}P$	-	Figure 2.11	standard configuration
S'_{Ref}	$GaAs$	$Ga_{0.2}As_{0.8}$	3	$In_{0.5}Ga_{0.5}P$	$GaAs_{0.89}P_{0.11}$	Figure 2.15	for 1 μm-lasers in Chapter 4
$S_{2\times cap}$	$GaAs$	$Ga_{0.2}As_{0.8}$	3	$In_{0.5}Ga_{0.5}P$	-	-	double thick cap
$S_{0\times cap}$	$GaAs$	$Ga_{0.2}As_{0.8}$	3	$In_{0.5}Ga_{0.5}P$	-	-	no cap
$S_{2\times QWs}$	$GaAs$	$Ga_{0.2}As_{0.8}$	2	$In_{0.5}Ga_{0.5}P$	-	-	-
S_{blk1}	$GaAs$	$Ga_{0.2}As_{0.8}$	2	$In_{0.5}Ga_{0.5}P$	$In_{0.5}Ga_{0.5}P$	Figure 3.11	shows the longest PL lifetime of 2.5 ns
S_{blk2}	$GaAs$	$Ga_{0.2}As_{0.8}$	2	$In_{0.5}Ga_{0.5}P$	$GaAs_{0.76}P_{0.24}$	-	-
S_{dope}	$GaAs$	$Ga_{0.2}As_{0.8}$	3	$In_{0.5}Ga_{0.5}P$	-	-	p-doped GaAs, intrinsic QWs, n-doped trench,
$S_{InGaAs1}$	$GaAs$	$Ga_{0.45}As_{0.55}$	3	$In_{0.72}Ga_{0.28}P$	-	Figure 5.2	-
$S_{InGaAs2}$	$Ga_{0.25}As_{0.75}$	$Ga_{0.45}As_{0.55}$	3	$In_{0.72}Ga_{0.28}P$	-	Figure 5.4	1.3 μm-light emitter in Chapter 5

Table 2.2: The nano-ridge samples studied in this work. All of them are grown on a similar SiO_2-patterned substrate but with slightly different layer stacks or material compositions from the reference sample S_{Ref}.

2.3 Conclusion

In this Chapter, we presented that lattice mismatch between two different materials is the crucial challenge for high-quality heteroepitaxy. The mechanics of the formation of all kinds of defects: point, line and planar defects are discussed. The defects definitely matter because the performance and lifetime of photonic devices are highly dependent on the defect density of epitaxial material.

In order to develop a platform of monolithic heteroepitaxy for III-V material for photonics (and electronics) applications, imec developed and optimized the growth of GaAs nano-ridges with embedded InGaAs QWs. By utilizing ART and NRE, the defect density of the as-grown nano-ridges can be suppressed to an extremely low level. The nano-ridges with the best quality exhibit a TD density of less than 3×10^6 cm^{-2}. (224) XRD-RSM reveals a fully relaxed GaAs barrier, a lattice-matched InGaP cap and fully-strained-to-GaAs QWs. Through the imaging inspections, we found strong correlations of the defect density with the aspect ratio of the trenches. As expected, the nano-ridges with broader trenches contain more defects.

These results already show that the advantages offered by ART and NRE in defect suppresion and shape optimisation. Further experimental characterization on the nano-ridge quality will be presented in the following chapters.

References

[1] Philip G Neudeck and J Anthony Powell. *Performance limiting micropipe defects in silicon carbide wafers*. IEEE Electron Device Letters, 15(2):63–65, 1994.

[2] Qing Cao, Oki Gunawan, Matthew Copel, Kathleen B Reuter, S Jay Chey, Vaughn R Deline, and David B Mitzi. *Defects in Cu (In, Ga) Se2 chalcopyrite semiconductors: A comparative study of material properties, defect states, and photovoltaic performance*. Advanced Energy Materials, 1(5):845–853, 2011.

[3] Ce Z Zhao, Jian F Zhang, Mo Huai Chang, AR Peaker, Stephen Hall, Guido Groeseneken, Luigi Pantisano, Stefan De Gendt, and Marc Heyns. *Stress-induced positive charge in Hf-based gate dielectrics: Impact on device performance and a framework for the defect*. IEEE Transactions on Electron Devices, 55(7):1647–1656, 2008.

[4] *Wavelength Engineering*. https://www.tf.uni-kiel.de/matwis/amat/semi_en/kap_5/backbone/r5_1_4.html. Accessed: 27-09-2019.

[5] R People and JC Bean. *Calculation of critical layer thickness versus lattice mismatch for Ge x Si1- x/Si strained-layer heterostructures*. Applied Physics Letters, 47(3):322–324, 1985.

[6] JW Morris. *The structure and properties of materials*. Instructor, 1999.

[7] P Kozodoy, JP Ibbetson, H Marchand, PT Fini, S Keller, JS Speck, SP DenBaars, and UK Mishra. *Electrical characterization of GaN pn junctions with and without threading dislocations*. Applied physics letters, 73(7):975–977, 1998.

[8] PJ Taylor, WA Jesser, JD Benson, M Martinka, JH Dinan, J Bradshaw, M Lara-Taysing, RP Leavitt, G Simonis, W Chang, et al. *Optoelectronic device performance on reduced threading dislocation density GaAs/Si*. Journal of Applied Physics, 89(8):4365–4375, 2001.

[9] Krishna C Saraswat, Chi On Chui, Tejas Krishnamohan, Ammar Nayfeh, and Paul McIntyre. *Ge based high performance nanoscale MOSFETs*. Microelectronic Engineering, 80:15–21, 2005.

[10] M. Baryshniskova N. Waldron A. Schulze B. Kunert, Y. Mols and R. Langer. *How to control defect formation in monolithic III/V hetero-epitaxy on (100) Si? A critical review on current approaches*. Semicond. Sci. Technol, 33(93002), 2018.

[11] W Chen and MA Capano. *Growth and characterization of 4 H-Si C epilayers on substrates with different off-cut angles*. Journal of applied physics, 98(11):114907, 2005.

[12] Gang Wang, MR Leys, Ngoc Duy Nguyen, Roger Loo, Guy Brammertz, Olivier Richard, Hugo Bender, Johan Dekoster, Marc Meuris, MM Heyns, et al. *Selective area growth of InP in shallow-trench-isolated structures on off-axis Si (001) substrates*. Journal of The Electrochemical Society, 157(11):H1023–H1028, 2010.

[13] G Wang, R Loo, E Simoen, L Souriau, M Caymax, MM Heyns, and Bart Blanpain. *A model of threading dislocation density in strain-relaxed Ge and GaAs epitaxial films on Si (100)*. Applied Physics Letters, 94(10):102115, 2009.

[14] Guy Brammertz, Yves Mols, Stefan Degroote, Maarten Leys, Jan Van Steenbergen, Gustaaf Borghs, and Matty Caymax. *Selective epitaxial growth of GaAs on Ge by MOCVD*. Journal of crystal growth, 297(1):204–210, 2006.

[15] Masafumi Yamaguchi, Masami Tachikawa, Mitsuru Sugo, Susumu Kondo, and Yoshio Itoh. *Analysis for dislocation density reduction in selective area grown GaAs films on Si substrates*. Applied Physics Letters, 56(1):27–29, 1990.

[16] JZ Li, J Bai, J-S Park, B Adekore, K Fox, M Carroll, A Lochtefeld, and Z Shellenbarger. *Defect reduction of GaAs epitaxy on Si (001) using selective aspect ratio trapping*. Applied physics letters, 91(2):021114, 2007.

[17] Yan-Ting Sun, Himanshu Kataria, Wondwosen Metaferia, and Sebastian Lourdudoss. *Realization of an atomically abrupt InP/Si heterojunction via corrugated epitaxial lateral overgrowth*. CrystEngComm, 16(34):7889–7893, 2014.

[18] Shigeya Naritsuka. *Microchannel epitaxy*. Progress in Crystal Growth and Characterization of Materials, 62(2):302–316, 2016.

[19] E Gil-Lafon, J Napierala, D Castelluci, A Pimpinelli, R Cadoret, and B Gérard. *Selective growth of GaAs by HVPE: keys for accurate control of the growth morphologies*. Journal of crystal growth, 222(3):482–496, 2001.

[20] YT Sun, E Rodrıguez Messmer, D Söderström, D Jahan, and Sebastian Lourdudoss. *Temporally resolved selective area growth of InP in the openings off-oriented from [1 1 0] direction*. Journal of crystal growth, 225(1):9–15, 2001.

[21] B Kunert, R Langer, M Pantouvaki, J Van Campenhout, and Dries Van Thourhout. *Gaining an edge with nano-ridges*. Compound Semiconductor, 24(5):36–41, 2018.

[22] Zhechao Wang, Bin Tian, Marianna Pantouvaki, Weiming Guo, Philippe Absil, Joris Van Campenhout, Clement Merckling, and Dries Van Thourhout. *Room-temperature InP distributed feedback laser array directly grown on silicon*. Nature Photonics, 9(12):837–842, 2015.

[23] W Guo, Y Mols, J Belz, A Beyer, K Volz, A Schulze, R Langer, and B Kunert. *Anisotropic relaxation behavior of InGaAs/GaAs selectively grown in narrow trenches on (001) Si substrates*. Journal of Applied Physics, 122(2):025303, 2017.

3
Optical characterization of InGaAs/GaAs nano-ridges

In Chapter 2, we explained the challenges associated with heteroepitaxy of lattice-mismatched III-V materials on a Si substrate. Driven by the lattice strain field, all kinds of defects start to nucleate from the interface between III-V and Si and thus greatly reduce devices' performance and lifetime if the growth conditions are not optimized. To overcome this ART and NRE were adopted to grow GaAs nano-ridges on Si. The first SEM, TEM and XRD-RSM inspections discussed in the previous chapter already indicated the good quality of the nano-ridges.

To further investigate whether the material is useful for laser applications, extensive optical characterization of the material was carried out and is discussed in this chapter. First, the energy band diagram was calculated in order to have a basic understanding of the emission spectra of the nano-ridges. Next, photoluminescence (PL) spectra were recorded to verify the emission wavelengths. Time-resolved PL measurements, which record the decay of the PL signal and reveals information on the overall material quality, will also be presented. This part of the work was submitted for publication in [1]. Additionally, the optical gain, an essential parameter to evaluate a laser material, is obtained for the nano-ridges by the variable stripe length (VSL) method. Discussions on how growth conditions influence the quality of the nano-ridges, supported by these experimental results, are also provided. We will show that the results presented in this chapter prove the good crystal quality of the nano-ridges and it also provides crucial clues for the design of laser devices in the upcoming chapters.

3.1 Electron-photon interaction

3.1.1 Energy band diagram for the InGaAs/GaAs nano-ridge

Optical transitions in semiconductor solids are closely associated with the energy levels that electrons in this materials occupy. The atomic structures of semiconductors decide these energy levels, which develop into two bands of many levels in a three-dimensional semiconductor crystal. The so-called valence band is entirely filled with electrons under no external excitation at $T = 0K$ while the conduction band is totally empty. When thermal or optical energy is added to the system, electrons in the valence band might be excited into the conduction band and create holes in the valence band. An electron from the conduction band can also recombine with a hole in the valence band and release the corresponding amount of energy. If the electron transition involves the absorption or emission of a photon, the material can be characterized by optical loss and gain. Given the energy conservation rule, the photons (with energy hv) interacting with electrons have to fulfil $hv \geq E_c - E_v$, where E_c and E_v are the lowest and highest energy in the conduction and valence band respectively. The bandgap energy E_g, defined by the difference $E_g = E_c - E_v$, then decides the cutoff of a material's absorption and emission spectra.

The situation becomes more complicated when moving from 3D bulk structures -as discussed above - to dimension-reduced structures, e.g., QWs or QDs. The energy band diagram is decided simultaneously by the atomic structure and the potential wells in these cases. The latter factor defines quantized energy levels inside the conduction and valence bands. The electron transitions are now supposed to occur at energy levels where hv has to equal a certain transition energy besides meeting $hv \geq E_g$. The dimension-reduced material with a more intensive density of states, which results in higher emission efficiency, is usually adopted for a semiconductor laser.

Four essential carrier recombination/generation (corresponding to photon emission/absorption) mechanisms are discerned:

1. Spontaneous recombination (photon emission)
2. Stimulated generation (photon absorption)
3. Stimulated recombination (coherent photon emission)
4. Nonradiative recombination

The transition rate of the above four processes is expressed by R_{sp}, R_{12}, R_{21}, R_{nr} respectively, with "2" presenting an energy level in the conduction band and "1" an energy level in the valence band. In the spontaneous recombination case, an electron in the conduction band recombines with a hole in the valence band and

simultaneously generates a photon in a random state (so-called incoherent photon). The second case is an electron-hole pair generation process stimulated by absorbing an incident photon. The third transition is a reverse process of "case 2", whereby a carrier pair recombines and simultaneously releases a new photon, which is coherent with the incident photon. The net combination $(R_{21} - R_{12})$ of stimulated emission R_{21} and absorption of photons R_{12} represents the net gain (positive value) or loss (negative value). Nonradiative recombination, as the name reveals, consumes electron-hole pairs but does not contribute to photon emission. Instead, the energy is dissipated, e.g., in the form of heat in the semiconductor crystal. Possible carrier-loss channels include nonradiative combinations via internal defect (and impurity) states, surface (and interface) recombination and Auger recombination.

To understand its basic optical properties, the energy band diagram of the as-grown GaAs nano-ridges was calculated by self-written code using Matlab [2]. As discussed in the previous chapter, the reference sample consists of a GaAs barrier, lattice-matched $In_{0.2}Ga_{0.8}As$ QWs and an $In_{0.5}Ga_{0.5}P$ passivation layer. The bandgap of a ternary $A_xB_{1-x}C$ is calculated by Equation 2.3. The offset of conduction band E_c and valence band E_v can be obtained through the same method. The bandgap E_g, offset E_c and E_v, electron effective mass m_e, effective mass of heavy hole m_{HH} and light hole m_{LH} of binaries GaAs, InAs, InP, GaP are obtained from [3, 4].

The calculated energy band diagram of the nano-ridges at room temperature (300 K) and low-temperature 80 K are shown in Figure 3.1. Only one QW is plotted in the image for simplification. The solid lines present the band edge of the conduction and valence band, while the dashed lines are the quantized energy levelss calculated for the 10 nm thick InGaAs finite-potential QWs with an offset of 0.171 eV in the conduction band and an offset of 0.048 eV in the valence band. As we will discuss later in section 3.1.2 that the electron-heavy-hole (HH) transitions dominate for the compressively-strained InGaAs QW, only the heavy hole energy levels are plotted. Compressive strain slightly blueshifts the bandgap, which, however, is not included in the calculation. As the bandgap energy is also temperature-dependent, the temperature is taken into account in the calculation with the parameter dependence derived from [5, 6]. Even though there are two quantized energy levels in the conduction band, it should be noted that electron transitions only take place between levels with the same quantum number (eg. E_{1-1HH}: the transition from the electron ground state in the conduction band to the heavy hole ground state in the valence band). This is because the wavefunctions for different quantized energies are orthogonal, which means the chance for an electron to meet a hole at a different level is null (at least in the ideal case). By cooling down the sample from 300 K to 80 K, the material bandgap energy blueshifts, resulting in a shift in bandgap wavelength for GaAs from 872 nm to 823 nm, for the QWs ($\sim$ 20%

In) from 998 nm to 938 nm and for the InGaP cap layer from 703 nm to 679 nm.

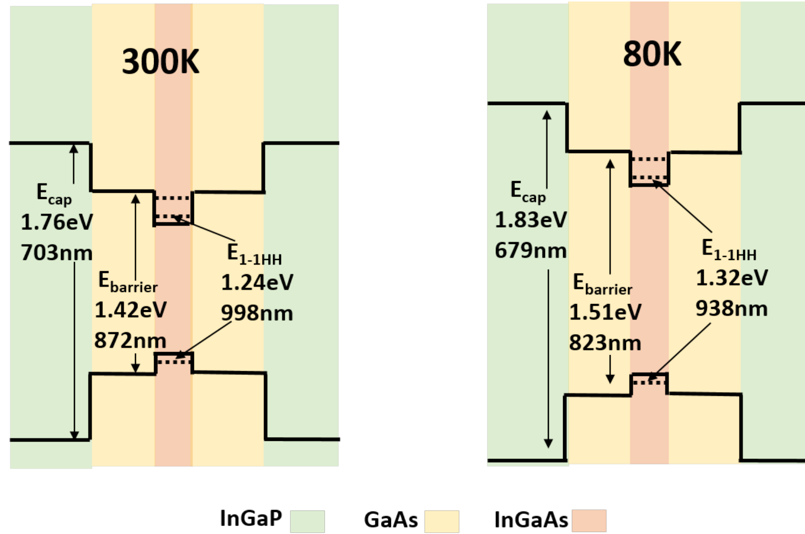

Figure 3.1: Calculated energy band diagram of the nano-ridge at temperature 300 *K(left) and* 80 *K(right) respectively. Only one QW is plotted in the image instead of 3QWs in the real samples.*

3.1.2 Effect of strain on optical gain

In Subsection 2.1.1, we discussed tensile and compressive strain originating from lattice mismatch. Besides crystal defect formation driven by the local elastic strain on the lattice, the lattice deformation also causes changes in the band diagram of semiconductors. It is found that tensile and compressive strain alter the energy band structure in different ways. This is especially the case for the HH and light-hole (LH) levels in the valence band. Furthermore, the HH and LH levels are found to interact differently with optical transverse electric (TE) modes and transverse magnetic (TM) modes [7–9]. This phenomenon provides the chance to control the lasing polarization and lessen the threshold because the optical gain can be enhanced for a select polarization. QWs with a thickness of several nanometers, typically thinner than its critical thickness h_{crt}, are ideal for applying this technique.

It is known that biaxial strain separates the HH and LH bands, which are degenerate in the unstrained state (split-off bands is not in the scope of discussion). Under tensile strain, both conduction band and valence band are pushed closer, resulting in a decrease in the bandgap. In the valence band, the LH band with lighter hole effective mass always undergoes a stronger impact from the tensile strain and

hence shifts more than the HH levels. As a result, the conduction band to LH band transition (C-LH) becomes the lowest-energy transition. Contrarily, compressive strain moves conduction band and valence band further away, increasing the bandgap. Again, the LH band shift is more significant, making the transition from the conduction band to the HH band (C-HH) the lowest-energy transition. The way that the lattice strain impacts the bands is illustrated in Figure 3.2. In one word, C-LH is the primary transition under tensile strain while under compressive strain the C-HH dominates.

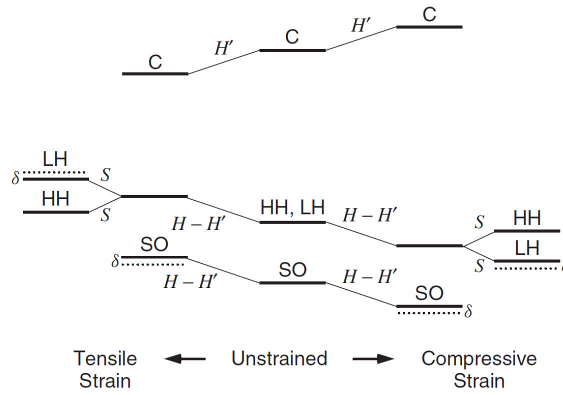

Figure 3.2: Qualitative shifts of the conduction band and heavy-hole (HH) and light-hole (LH) levels in the valence band for unstrained, biaxial compressive and tensile strain. Reproduced from [10].

In addition to the shifts in the bandgap energy, the optical gain of TE and TM polarization in the strained materials also alters due to band-to-band transitions. For instance, in a QW, the interaction strength of the C-HH transition is much stronger for electric fields in the QW plane than for those perpendicular to the QW plane. In the case of QWs parallel with the substrate, the optical TE mode with a mostly in-plane electrical field experiences stronger interaction with the C-HH transition than a TM mode. Considering C-HH recombination is enhanced by applying compressive strain on the QWs, TE polarised modes possess a higher optical gain than TM modes. Figure 3.3 shows a theoretical calculation of optical gain spectra for TE and TM modes under 0.25% compressive strain and 0.25% tensile strain respectively [11]. It is also experimentally proved that modifying the lattice strain increases the optical gain and hence enhances laser performance [9, 12, 13]. More discussions on the polarization selectivity of the nano-ridge gain and laser operation will follow in the next chapter.

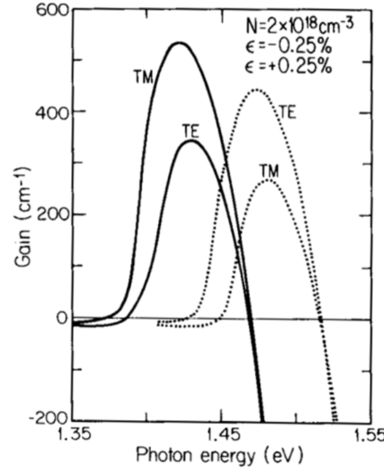

Figure 3.3: Polarization-dependent gain spectra for 0.25% *compressive strain (dotted) and tensile strain (solid) under* $2 \times 10^{18} cm^{-3}$ *carrier density injection. Reproduced from [11].*

3.2 Photoluminescence characterization

Photoluminescence (PL) is the spontaneous emission of light from the material under optical excitation. Measuring PL is a nondestructive and relatively fast analysis approach to gain a first insight into some basic properties of the material. The control parameters of the PL experiment include but are not limited to the excitation photon energy, excitation intensity, and measurement temperature. It can be carried out under continuous-wave (CW) or pulsed excitation. The most important features of the results include the spectral width, the peak wavelength and the PL signal intensity. Through combining the different measurement control parameters and/or monitoring different result features, material characteristics like energy band diagram structure, alloy composition, impurity levels, surface passivation effects and temperature dependent behavior can be obtained [14].

In this section, we focus on the PL investigation of the nano-ridges under CW excitation at room temperature to obtain a preliminary understanding of their optical characteristics. In the next section, the experiments are extended to pulsed-excitation, at room and low-temperature to investigate get inside in the life time of the PL signal.

3.2.1 Setup

The micro-PL setup used is shown in Figure 3.4 and consists of a CW 532-nm diode-pumped solid-state (DPSS) laser (model NO. MGL-FN-532-1.5WY) as the

pump source; a $\times 50$, 0.65-numerical-aperture objective; a 0.25-m monochromator; a thermo-electric-cooled InGaAs detector, a lock-in amplifier and some other optics.

The collimated beam (diameter $\sim 2\,$mm) from the CW laser is reflected by mirror $M1$ and then expanded by a $\times 5$ beam expander to a circular beam with a diameter of $\sim 1\,$cm. After that, the beam is focused by lens $L1$ and reflected into the left direction by a dielectric mirror (DM), which has a high reflectivity at wavelength $532\,$nm and high transmission at 1μm. The beam is focused by the $\times 50$ objective onto the sample and finally pumps a circular area with a diameter of $\sim 300\mu$m. The PL signal is then collected through the same objective. After lens $L2$, the image of the sample can be monitored by a CMOS camera to locate the excitation region on the sample. To conduct PL measurements, the camera is removed and the PL signal enters the input slit of the monochromator. A lock-in amplifier is used to enhance the signal-to-noise ratio (SNR) with a chopper inserted into the excitation optical path as a frequency reference.

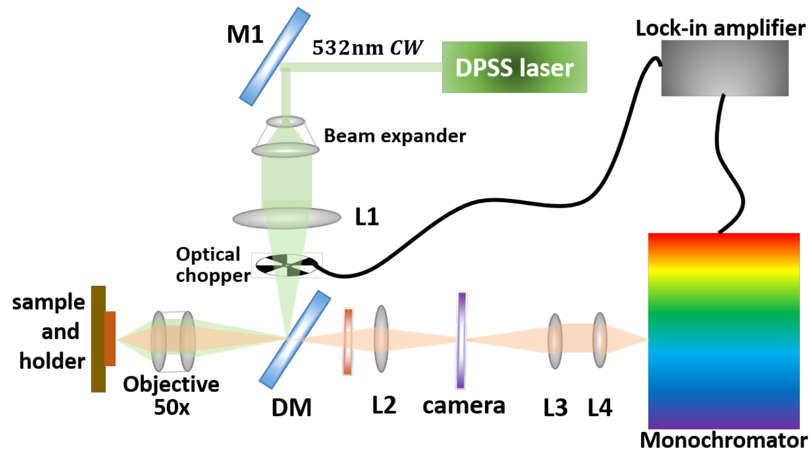

Figure 3.4: Schematic diagram of the experimental PL setup.

The current setup has a resolution down to $0.5\,$nm and a measurable wavelength range from $960\,nm - \sim 2\,\mu$m, limited by the reflection/transmission spectra of the available DMs and the responsivity of the available photodiodes. The shape of the pumped area on the sample can be modified by an iris inserted between $L1$ and the beam expander, with a maximum size of $300\,\mu$m. Because the monochromator takes the spectrum by sweeping the grating mechanically, the measuring period for one spectrum is relatively long.

3.2.2 Results

Although a large series of nano-ridge samples with varying ridge size, QW number and passivation layer, etc. have been investigated, we here discuss one typical sample as an example, to explain some general features of the nano-ridges under study. Figure 3.5 shows the PL spectra for GaAs nano-ridges with 3 InGaAs QWs for different trench widths [15] on linear and logarithmic scale.

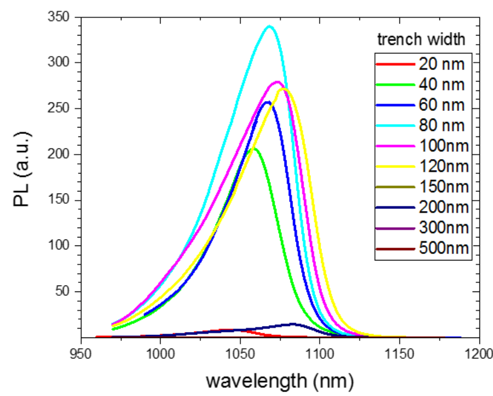

(a)

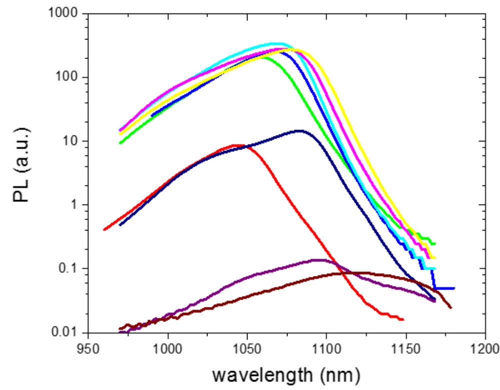

(b)

Figure 3.5: The photoluminescence spectra of sample S_{Ref}. Nano-ridges with trench width from 20 nm to 500 nm under CW 532 nm excitation.(a) on linear scale (b) on logarithmic scale.

With the 532 nm ($hv_{ex} = 2.33$ eV) CW pump, carriers are excited in all ma-

terials involved. Pronounced emission peaks between 1000 nm and 1050 nm are observed from all structures except for the nano-ridges with 500 nm-width trench. The emission is expected to originate from the active $In_{0.2}Ga_{0.8}As$ QWs, as calculated in Figure 3.1. The $\sim$ 1140 nm emission is from the doped Si substrate with an intensity of several orders of magnitude lower than the emission of the QWs. The emission around 875 nm from the GaAs barrier is weak as well, at the same order of magnitude as the Si emission. With reducing the trench width down to 80 nm, the PL intensity of the nano-ridges increases but then drops down for trenches below 20 nm width. However, even for the narrowest trench, the PL intensity from the QWs is still very noticeable. The red-shift in the PL peak with the increase of trench width can be explained by the change in Indium concentration or/and in QW thickness, which induces an energetic shift in the quantized states. Both effects are likely to take place because the epitaxy is sensitive to local growth conditions, which change due to the fixed fill-factor in the oxide-trench pattern.

The PL linewidth is usually regarded as an indicator of the material quality, yet it should be carefully treated because factors other than the crystal quality, e.g., the variation in QWs width, influence the linewidth as well. The comparison of the PL intensity for different trenches and different samples should be made carefully as well because the absorption of the excitation light can be different for nano-ridges with different dimensions. Although it is difficult to make accurate judgments, the dramatic decrease in PL intensity towards wide trenches likely correlates with the increase in defect density. As we know from section 2.2.3, the narrower trenches are more effective at defects trapping. Therefore, the high defect density for the low aspect ratio of broader trenches could lead to substantial carrier loss and explain the decline in PL intensity. More insight can be obtained by time-resolved PL measurements, which will be discussed in the following section.

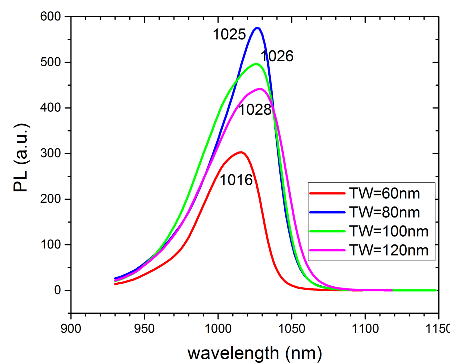

Figure 3.6: The PL spectra of an optimized nano-ridges sample S'_{Ref}. This selected sample is taken for laser device process in the following chapter.

Figure 3.6 shows the PL spectra of sample S'_{Ref}. The pronounced PL peaks around 1020 nm are observed for $60 - 120$ nm wide trenches, indicating the excellent crystal quality of the nano-ridges. As we explained above, there is a redshift in the spectra for wider trenches.

3.3 Time-resolved photoluminescence characterization

Time-resolved PL (TRPL) characterization allows to get insight in the carrier lifetime. If the material is pumped by a short pulse, a large number of carriers are generated instantaneously and start to recombine non-radiatively and radiatively. The transient PL intensity created by the radiative recombination reveals an important characteristic, the PL lifetime, which is used to identify and characterize various recombination mechanisms of the tested material. In this section, to further study how crystal quality is correlated with the nano-ridges' size and defect density, we extracted the PL lifetime from TRPL experiments at both room and low temperature. We also investigated how different types of passivation layers and blocking layers impact the PL lifetime. This experiment was conducted in collaboration with the Ruhr University at Bochum, Germany (N. Gerhardt group).

3.3.1 Setup

The nano-ridges were characterized by the time-resolved photoluminescence setup shown in Figure 3.7. A Mira-HP high-power wavelength-tunable ($680 - 1000$ nm) Titanium:Sapphire (Ti:Sa) laser emitting ~ 200 fs pulses at a repetition rate of 76 MHz is used as the pump source. After traveling through a 1 m long optical fiber, the pulses are broadened to ~ 1 ps, still substantially shorter than the lowest lifetimes measured in the nano-ridges. At the detection side, a spectrometer with a 2 nm resolution and a streak camera (up to 2.3 ps time resolution) are used. Mirror M1 and lens L1 generate an approximately circular pump spot with $\sim 200\,\mu$m diameter on the sample surface. Lenses L2, L3 are inserted between the sample and the spectrometer to couple the photoluminescence signal into the spectrometer while the filter blocks out the pump light. For low-temperature measurements, the samples are positioned in a cryo chamber at 80 K.

Figure 3.8(a) shows the TRPL spectrum for the reference sample S_{Ref} (trench width 100 nm, no InGaP blocking layer, pump power $500\,\mu$W). By integrating the signal over a certain time range, one can get the PL spectrum for that time interval. Vice-versa, by integrating over a certain wavelength range, one gets the time dependent PL signal. As an example, Figure 3.8(b) shows the time dependent PL signal, integrated over the wavelength range from 872 nm to 1200 nm. As 872 nm (1.42 eV) is the bandgap of bulk GaAs at room-temperature, this signal

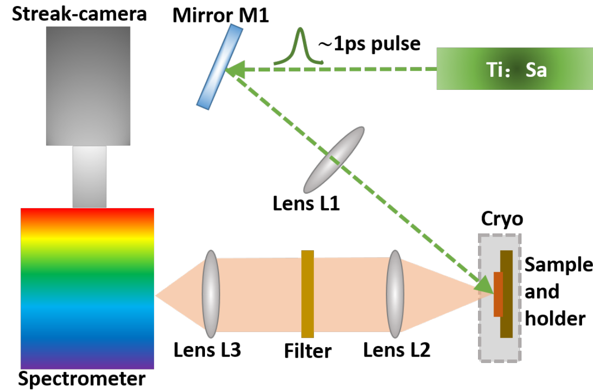

Figure 3.7: Schematic diagram of the experimental TRPL setup. The cryo chamber is only used for the low T measurements.

can be considered originating mainly from the InGaAs QW layers. To extract the PL lifetime from these curves, the background is subtracted from the detected signal and a one-term exponential model

$$I_{QW} = A \cdot e^{\frac{-(t-t_0)}{\tau_{QW}}} \tag{3.1}$$

is fitted to the experimental data, with I_{QW} the PL intensity integrated over the wavelength range 872 nm to 1200 nm, A a fitting parameter and τ_{QW} the decay time for the QW emission. The range over which the curve is fitted varies from sample to sample but is chosen to start from the time where the intensity peaks and to end when the signal reaches $1/10$ of its peak value to exclude the noisy signal in the low intensity tail. Similarly one can extract the life time τ_{GaAs} for the PL originating from the GaAs nano-ridge by integrating the TRPL signal over the wavelength range from 825 nm to 872 nm.

3.3.2 Results

To further investigate how growth quality is related to trench width, we carried out detailed TRPL experiments to extract the PL lifetime of the nano-ridges at both room and low temperature on the reference sample S_{Ref}. In addition, we investigated how passivation layers, blocking layers and doping impact the PL lifetime in comparison with the reference sample. Although the details of the measured samples can be found in Table 2.2, we specify their main characteristics again with the relevant experiment.

Impact of trench size

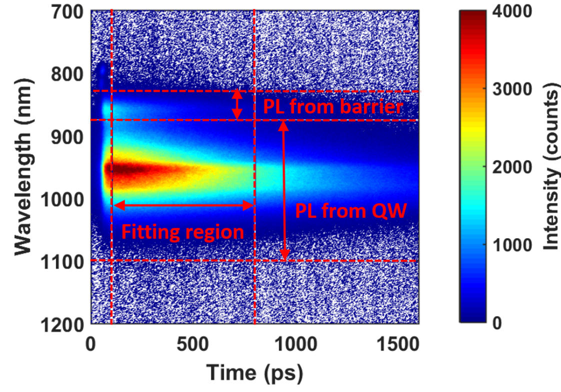

(a)

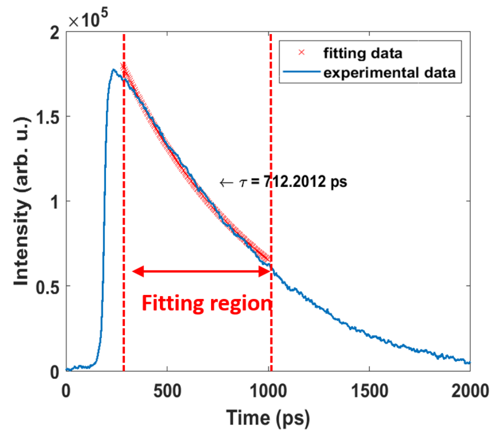

(b)

Figure 3.8: (a)TRPL result of sample S_{Ref}, as function of wavelength and time. Dashed lines in wavelength span indicate integration interval over wavelength range for nano-ridge QWs and GaAs respectively. Dashed lines in time span show the time range for PL lifetime fitting range. (b) Nano-ridges QW PL integrated over wavelength 872 nm to 1100 nm as a function of time. The region in between the dashed lines again indicates the fitting range.

In a first experiment we determined the PL lifetimes τ_{QW} and τ_{GaAs} of the reference sample:

- S_{Ref} (with $3\times\mathrm{In_{0.2}Ga_{0.8}As}$ QWs and $\sim$ 50 nm thick InGaP passivation layer, without lower InGaP blocking layer as its TEM image shown in Figure 2.11.)

The results for 10 μm long nano-ridges are summarised in Figure 3.9. Figure 3.9(a) shows the lifetimes τ_{QW} and τ_{GaAs} for a fixed excitation power of 500 μW versus the trench width changing from 20 nm to 500 nm comparing results based on the excitation wavelength of 800 and 900 nm.

For the excitation wavelength of 800 nm (1.55 eV), carriers are excited both in the GaAs nano-ridge material (bandgap 1.42 eV at RT) and in the QWs, while for the 900 nm (1.38 eV) pump wavelength electron-hole pairs are only generated in the QW material. Considering first the excitation wavelength of 800 nm, which allows to define the PL lifetime of the QWs as well as for the GaAs material, τ_{QW} is always larger than τ_{GaAs}. This is caused by the fact that carriers from the GaAs barrier also escape into the QWs, hence, this loss mechanism reduces the PL lifetime of GaAs additionally to all other loss paths e.g. caused by crystal defects. τ_{QW} as well as τ_{GaAs} peak for a trench width of 150 nm, and τ_{QW} reaches a value of about 1 ns. For wider trenches with lower aspect ratio both PL lifetimes decrease below 400 ps for 500 nm wide trenches due to the pronounced increase in TD density inside the nano-ridge material. But also for the smaller trench widths the PL lifetimes of the QWs and GaAs material quickly decrease.

This effect cannot be correlated to the presence of dislocation defects inside the bulk of the nano-ridges as the aspect ratio is rising for smaller trench width. Therefore we believe that the decrease is linked to a growing impact of surface defects inducing non-radiative recombination as smaller nano-ridges exhibit a large S/V ratio. Another carrier loss path is the leakage inside the defective trench region caused by MDs and TDs close to the III-V/Si interface, whose relative capture efficiency increases for smaller trench width. Furthermore we notice that the PL lifetime τ_{QW} for an excitation wavelength of 800 nm is slightly longer than that for an excitation wavelength of 900 nm. We believe this can be associated with carriers excited in the GaAs diffusing towards the QW in the case of pumping at 800 nm, thereby extending τ_{QW}. This "QW feeding" with additional carriers from the GaAs barrier is not possible with the 900 nm excitation wavelength, which is below the bandgap of GaAs. The effect of "QW feeding" is also visible in Figure 3.9(b), which depicts the measured PL lifetime of τ_{QW} and τ_{GaAs} versus the pump power for an excitation wavelength of 800 nm. The lifetime for the PL originating from the QWs first increases and then saturates for pump powers beyond 700 μW. We believe that increasing the pump power generates more electron-hole pairs in the GaAs nano-ridge material, which amplifies the impact of carriers diffusing to the QWs and thereby prolongs the PL lifetime. τ_{GaAs} decreases slowly with rising pump power. In all further experiments, to ensure a sufficient signal intensity and at the same time the integrity of the sample, the pump power is set to 500 μW.

Finally we investigated the impact of the trench length. By characterizing τ_{GaAs} for nano-ridges with trench length varying from 100 nm to 10 μm, we found

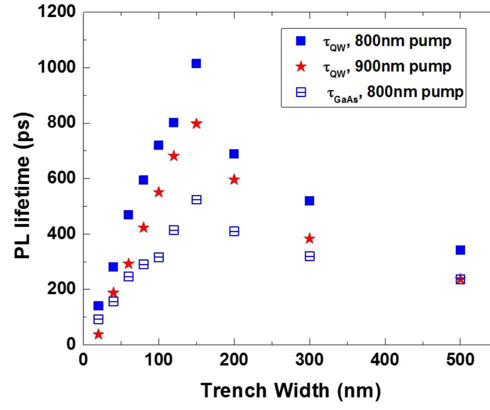

(a)

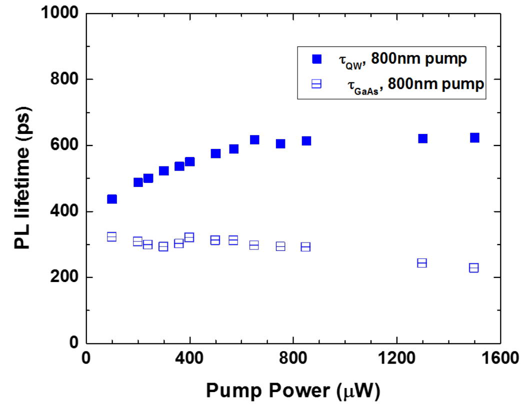

(b)

Figure 3.9: (a) Extracted PL lifetime for sample S_{Ref} with trench width from 20 *nm to* 500 *nm at room temperature under* 800 *nm and* 900 *nm excitation wavelength respectively. (b) PL lifetime as a function of excitation power. The excitation power is chosen to be* 500 μ*W for the other room-temperature measurement.*

a clear decrease in PL lifetime for a trench length below 3 μm. The TMAH etch step, which is applied to form a V-shape Si bottom, reveals also two $\{111\}$ facets at the ends of the trenches and perpendicular to the trench orientation. These facets induce anti-phase disorder inside the GaAs material that can cause additional carrier losses at the anti-phase boundaries. Furthermore, the box-shaped nano-ridges reveal different facets a the two nano-ridge ends as more crystal facets contribute to

the nano-ridge formation. The layer thicknesses as well as the interface quality of the different heterolayers are unknown and not controlled, hence, additional crystal and/or surface defects might be nucleated. Both anomalies might explain the strong lifetime reduction for short trenches. In all further experiments we focused on 10 μm long nano-ridges.

Impact of passivation layer

As we mentioned that carrier recombination on untreated semiconductor surface could be a serious problem, this issue is extraordinarily critical for the nano-ridges presented in this work because of the large surface-area-to-volume ratio (SA/V). As shown in Figure 2.11, the reference sample S_{ref} has a 50 nm thick InGaP (bandgap 1.76 eV at 300 K) passivation layer grown around the nano-ridge, lattice-matched to GaAs. To understand whether the surface recombination plays an important role in the PL lifetime of the nano-ridges and further investigate the performance of the 50 nm thick InGaP passivation layer, the reference sample is compared with a sample without passivation layer and a sample with a thicker passivation layer:

- S_{Ref} ($\sim$ 50 nm-thick cap layer)
- $S_{2\times Cap}$ ($\sim 100nm$ thick cap layer)
- $S_{0\times Cap}$ (without cap layer)

under $500\mu W$, $800nm$ excitation.

The results for τ_{QW} and τ_{GaAs} are shown in Figure 3.10. For the sample without passivation layer, the PL lifetime drops by a factor 8 compared to the reference sample. This shows the effectiveness of the InGaP passivation layer in reducing non-radiative recombination at the GaAs-air interfaces. Increasing the thickness of the passivation layer to 100 nm does not further improve the lifetime, indicating that the 50 nm passivation layer is sufficient to avoid carriers tunneling to the InGaP-air interface. Also thermal excitation of the carriers over the GaAs-InGaP barriers seems unlikely, given the large band-offsets between both materials. This leaves the GaAs-InGaP interface as a possible source for carrier losses. However, very low recombination rates of 1.3×10^{-3} cm/s to 2 cm/s have been reported in literature for this interface [16, 17], which points to the imperfectly passivated $\{111\}$ facets at the bottom of the nano-ridge and leakage losses to the defective trench as the most likely remaining carrier loss channels in the passivated samples.

Impact of carrier blocking layer

To investigate the implication of carrier losses into the defective trench region, in this experiment we make comparison among these samples:

- S_{Ref} ($3 \times QWs$ without InGaP blocking layer)

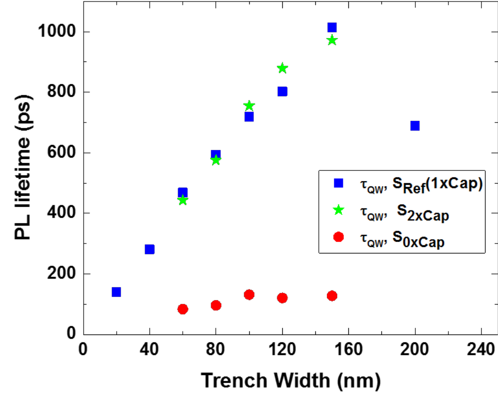

(a)

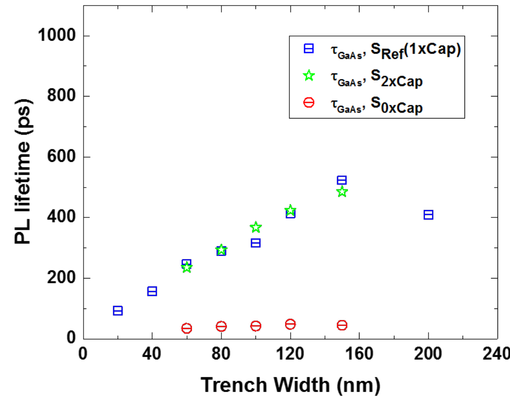

(b)

Figure 3.10: Room-temperature PL lifetime from the reference sample (S_{ref}) with 50 nm InGaP passivation layer, the sample without passivation layer $S_{0\times Cap}$ and the sample with 100 nm $S_{2\times Cap}$ passivation layer. (a) Lifetime τ_{QW} for QWs PL emission and (b) τ_{GaAs} for GaAs.

- $S_{2\times QWs}$ ($2 \times QWs$ without InGaP blocking layer)
- S_{blk1} ($2 \times QWs$ with $InGa_{0.5}P_{0.5}$ blocking layer)
- S_{blk2} ($2 \times QWs$ with $GaAs_{0.76}P_{0.24}$ blocking layer)

For sample S_{blk1} and S_{blk2}, we include an $InGa_{0.5}P_{0.5}$ carrier blocking layer

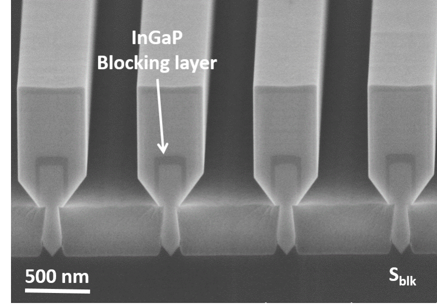

(a)

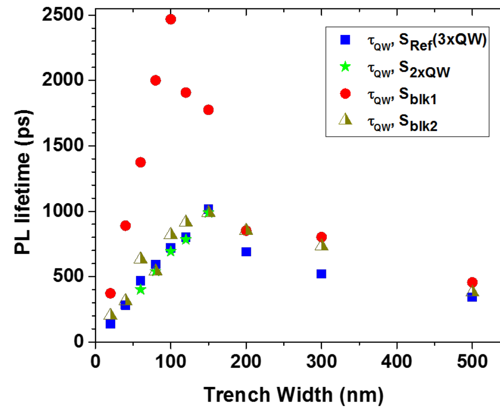

(b)

Figure 3.11: (a) XSEM image of nano-ridge with 2 QWs and an extra InGaP blocking layer. (b) PL lifetime of sample S_{Ref}, $S_{2\times QW}$, S_{blk1} and S_{blk2}.

(lattice-matched to GaAs) and a $GaAs_{0.76}P_{0.24}$ carrier blocking layer respectively in the nano-ridge before the QW growth. The SEM image of the cleaved sample S_{blk1} is shown in Figure 3.11 (a), where the InGaP barrier layer is clearly visible. Given the large bandgap (1.76 eV for $InGa_{0.5}P_{0.5}$ and 1.71 eV for unstrained $GaAs_{0.76}P_{0.24}$), this layer serves as a barrier preventing carriers from diffusing into the trench. To keep the nano-ridge size constant, sample S_{blk1} and S_{blk2} include only 2 QWs. Therefore another control sample $S_{2\times QW}$, identical to the reference sample S_{Ref} but only including 2 QWs was prepared. Figure 3.11(b) compares the trench width dependent PL lifetimes for the reference sample with 3 QWs (S_{ref}), the control sample with 2 QWs ($S_{2\times QW}$), the sample with InGaP blocking layer (S_{blk1}) and the sample with GaAsP blocking layer (S_{blk2}). The measured lifetimes for S_{ref} and $S_{2\times QW}$ are identical, showing that reducing the number of QWs has

no impact on the PL lifetime. Introducing the InGaP barrier layer underneath the QWs clearly increases the PL lifetime. It shifts the optimal trench width defined by the maximal PL lifetime of 150 nm to 100 nm and leads to more than a doubling of the maximum lifetime values. This shows that carrier losses towards the defective trench region has a considerable impact on the carrier lifetime but also that very long PL lifetimes, above 2 ns can be reached in the nano-ridge, proving the high quality of the material. Compared with the InGaP barrier layer, the enhancement of the PL lifetime by inserting a GaAsP barrier layer seems to be trivial. Given that tensile stain decreases the bandgap (Figure 3.2), the tensile-strained $GaAs_{0.76}P_{0.24}$ is supposed to have a bandgap smaller than 1.71 eV. Compared to S_{blk1}, the reduced bandgap of the blocking layer of S_{blk2} is less effective on carrier blocking, which might explain the big difference of PL lifetime. Therefore we could assume that the blocking layer—$GaAs_{0.89}P_{0.11}$ (bandgap 1.56 eV) for sample S'_{Ref} hardly affects carrier diffusion.

Impact of doping

To study the impact of doping, we compare these samples:

- S_{Ref} (undoped)
- S_{dope} (intrinsic QW region and low doping in the rest area.)

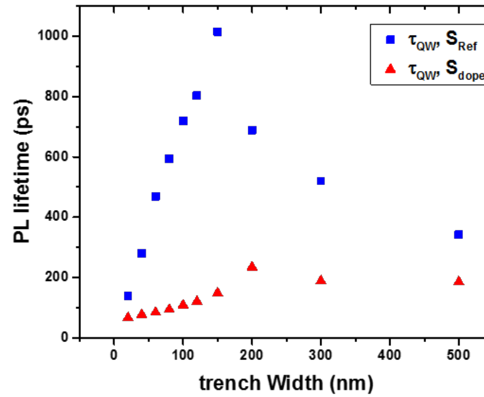

Figure 3.12: Extracted PL lifetime for sample S_{Ref} and S_{dope} as a function of trench width from 20 nm to 500 nm at room temperature.

To allow efficient current injection of the nano-ridges, p-i-n junctions have to be integrated in the structure. As the first trial for implementing doping, sample S_{dope} has an identical layer stack as S_{Ref}, and in addition is lowly doped.

Si is used for n-doping the GaAs trenches, and C is used for p-doping the periphery of the nano-ridges. The QW region is left undoped and the Si substrate is +n-doped by ion implantation. Figure 3.12 compares the trench-width dependent PL lifetimes of QWs for the reference sample S_{ref} and the doped sample S_{dope}. The maximal PL lifetime of the QWs of the doped sample is $\sim$ 230 ps, $\sim$ 4 times lower than that of the reference sample. The dopants, known as point defects, introduce defect states in the energy band diagram and might increase the nonradiative recombination rate. Additionally, the build-in electrical field in p-i-n junctions accelerates carriers, raises the possibility of extracting the carriers from the active region and have them recombine (radiatively or non-radiatively) in the GaAs region. A shift of the PL lifetime peak from the 150 nm trench for S_{ref} to the 200 nm trench for S_{dope} is also observed. Considering that the p-doping is around the surface area of the nano-ridges, the shift is attributed to the enhanced SA/V effect of the nano-ridges with narrow trenches. Further investigation on the carrier recombination of doped samples is needed to understand the impact of doping. Also, the doping process and profile might require further optimization.

Low-temperature characterization

To confirm that the strongly decreasing lifetime for smaller trench widths is indeed related to surface effects and not to an increasing number of defects in the MQW stack itself, we carried out TRPL measurements of the samples

- S_{Ref} ($\sim$ 50 nm-thick cap layer)
- $S_{0\times Cap}$ (without cap layer)

at low-temperature (80 K). At this temperature, we expect the carriers to have insufficient thermal energy to escape from the InGaAs QWs and hence the measured lifetime should be dominated only by the material quality of the QWs and not by surface defects or the highly defective trench region close to the III-V/Si interface. For this experiment the sample was placed in a cryo chamber, which reduced both the excitation and the collection efficiency. To get some insight in how this influences the measurements, Figure 3.13(a) shows the PL spectra measured before and after mounting the reference sample inside the cryostat, in the latter case both at 300 K and at 80 K. As the excitation efficiency declines, the RT spectrum of the sample inside the cryo chamber narrows down and is slightly red-shifted as less electron-hole pairs are generated leading to less band filling. The reduced collection efficiency results in a more noisy spectrum at RT.

By cooling the sample down to 80 K, the bandgap energy of all materials increases as illustrated by a simplified band diagrams in Figure 3.1. To compensate for this, we shifted the excitation wavelength to 750 nm. Comparing the PL spectra at 80 K with the one at RT in Figure 3.13(a) reveals that the PL peak is indeed blue-shifted by 62.9 nm as expected. Given the relatively low pump efficiency in

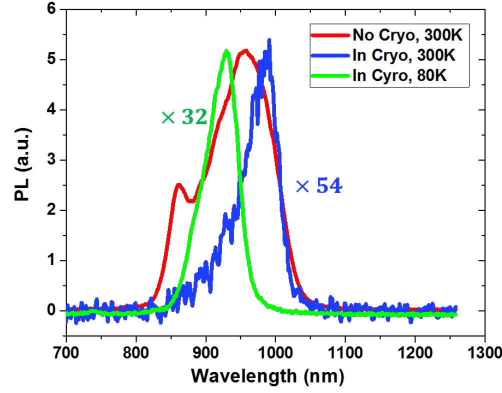

(a)

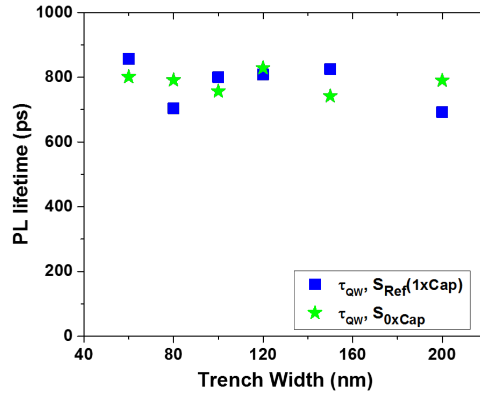

(b)

Figure 3.13: (a) Normalized spectra of sample S_{Ref} with $100\,nm$ trench under $0.5\,mW$ without cryo at $300\,K$, under $20\,mW$ with cryo at $300\,K$ and under $20\,mW$ with cryo at $80\,K$ respectively.(b) PL lifetime of sample S_{Ref} and $S_{0\times Cap}$ as a function of trench width at low temperature $80\,K$. The excitation is $750\,nm$ in wavelength and $20\,mW$ in power.

the cryo chamber, the GaAs peak which was visible in the RT spectrum taken in the free space setup is no longer present in the 80 K spectrum. Further, the intensity of the spectrum at 80 K increases compared to the RT spectrum taken in the cryostat, which we attribute to an increased radiative recombination efficiency. To cope with the increased background noise in the TRPL measurements, it was explicitly included in the fitting function, $I_{QW} = I_{bg} + A \cdot e^{\frac{-(t-t_0)}{\tau_{QW}}}$. This additional fitting parameter and the higher noise increased the uncertainty on the fitted

lifetimes to $\Delta\tau_{QW} \approx \pm 50\,ps$. Figure 3.13(b) shows the measured PL lifetimes as a function of the trench width for the reference sample S_{Ref} and the sample without passivation layer $S_{0\times Cap}$. At 80 K the lifetimes measured for both samples are identical within the measurement error. Furthermore the lifetime seems to be independent of the trench width, at least up to 200 nm. This is in strong contrast with the RT results shown in Figure 3.9(a) which exhibit a very pronounced trench width dependence and a strongly reduced lifetime for the sample without InGaP passivation layer. This confirms our hypothesis that the reduction in lifetime with decreasing trench width is related to non-radiative recombination at the imperfectly passivated bottom $\{111\}$ facets and/or to carrier losses in the highly defective trench region and not to a decrease in material quality of the nano-ridge material. Currently is it not possible to judge, if carrier recombination at the non-passivated bottom facet or the leakage into the trench is dominating the PL lifetime decrease. No reduction in PL lifetime is observed for the trench width of 200 nm, for which the aspect ratio is not sufficient enough to fully restrict all dislocation defects inside the trench. This can be explained by the fact that for this width dislocation defects start penetrating the GaAs nano-ridge but not yet the InGaAs MQW stack where the carriers are confined at low-temperature.

3.4 Characterisation of optical gain

The optical gain is one of the basic parameters that determine the performance of a laser, together with its optical loss and the feedback provided by the cavity (facet reflection for FP-lasers, grating coupling strength for a DFB laser). It has long been recognized as a significant parameter in evaluating the crystalline quality of the material and the possible utility of a laser device. In most cases, optical gain is determined from the threshold condition of a fabricated semiconductor laser device, whereby the gain is only obtained at the threshold pump (optical or current) intensity after the device is successfully made.

Although the modal gain is a key parameter, few state-of-the-art III-V materials epitaxially grown on Si were characterized in terms of their optical gain thus far. To get a more comprehensive understanding of the reported InGaAs/GaAs nano-ridges, the optical gain is characterized using the variable stripe length (VSL) method [18, 19]. As the name indicates, the measurement is conducted by exciting the test material in the form of an infinitely long stripe, with a length-variable beam as the optical pump source. The in-plane luminescence of the material consists of spontaneous emission and amplified spontaneous emission when the pump intensity exceeds the transparency condition. An important parameter is the length of the pumped region. At a short pump length, the luminescence output of the nano-ridge is dominated by spontaneous emission. This will be taken over by amplified spontaneous emission (ASE) when the pumped length increases such that the out-

put is found to have a linear dependence with pump length on a logarithm scale. As expected, saturation of the luminescence is observed at long lengths since the pump intensity limits the maximum output. The slope of the straight-line portion of the pump-length-dependent luminescence is then the optical gain. This method not only allows extracting optical gain of the GaAs nano-ridges over a wide range of pumping conditions but also provides information on the spontaneous emission, loss and saturation characteristics.

3.4.1 Setup

The VSL measurement setup (shown in Figure 3.7) consists of a Nd:YAG nanosecond pulsed laser (7 ns pulse width, 938 Hz repetition rate, 532 nm wavelength) to pump the nano-ridges from their top surface, a variable rectangular slit inserted in the optical path to control the length of the pumped region from 10 to 200 μm. The optical intensity of the linear-polarized pump is manipulated by the combination of a polarizer and a rotating half-wave plate (HWP). The PL signal is collected through a lensed fiber coupled at a cleaved facet of the nano-ridge and measured by an optical powermeter. Collection by a cleaved single-mode fiber was tested first but gave a $\sim$ 15 dB weaker signal than that by a lensed fiber, which possesses a larger numerical aperture. The images of the in-plane fiber-nano-ridge coupling are shown in Figure 3.15, (a) under a $\times$6-magnification lens and (b) under a $\times$50-magnification objective. Due to the fiber diameter of 125 μm, low magnification

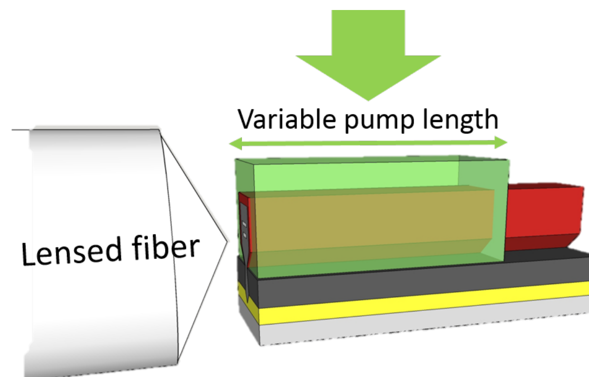

Figure 3.14: Schematic diagram of the VSL setup for characterizing optical gain.

imaging is first used to align the fiber to the sample facet coarsely. Higher magnification is needed to resolve the nano-ridges for fine alignment, considering the small dimensions of the nano-ridges ($\sim$ 500 nm in width for 100 nm trench)and spacings ($\sim$ 500 nm) between each other. Because only one camera is available to monitor the in-plane image of the sample, a visible red laser connected to the

lensed fiber is utilized as an auxiliary means to align the fiber in the direction perpendicular to the sample surface. Once the reflection of the red light from the cleaved facet is viewed in the camera, as is the case shown in Figure 3.15 (b), the lensed fiber is coarsely aligned with the sample in the perpendicular direction. Fine alignment is accomplished by connecting the fiber to a power meter and searching the maximal power P while finely adjusting the fiber in all three directions. Given that the lensed fiber has a focal length of $\sim 2\,\mu$m, the best alignment is obtained by positioning the cleaved facet at the lensed fiber's focus plane, $\sim 2\,\mu$m away from the fiber.

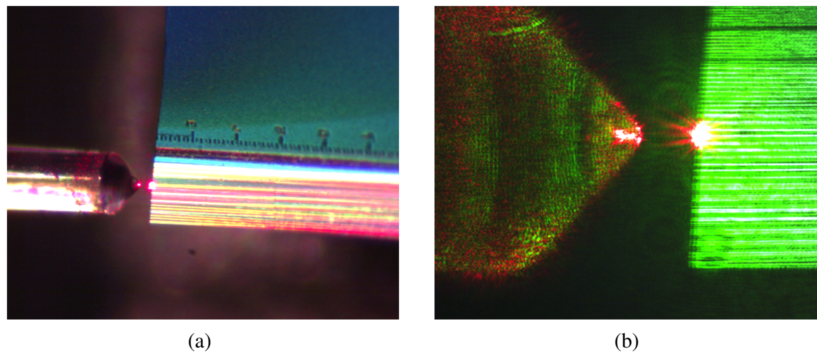

(a) (b)

Figure 3.15: CMOS camera images of edge coupling between nano-ridges(left) and lensed fiber(right) (a) under a magnification of $6\times$. *(b) under a magnification of* $50\times$.

To extract the gain at a certain excitation intensity, the collected power must be recorded as a function of pump length at a fixed excitation. To obtain the relation of optical gain versus excitation intensity, a full measurement is accomplished by controlling the variable slit length from $20\,\mu$m to $180\,\mu$m and changing the excitation intensity from $12\,$kW/cm^2 to $300\,$kW/cm^2. One significant assumption of the VSL measurement is that the fiber-to-sample coupling efficiency remains the same for every signal readout. Therefore, the fiber alignment should be kept undisturbed, such that the coupling efficiency can be treated as a constant. Nevertheless, the nanometer size of the ridges makes the alignment extremely sensitive to background mechanical vibrations. An uncertainty of $\Delta P \approx 0.3\,$dB in the collected PL power is observed during the measurement even after stabilizing the setup. Considering that the output power spans over $20\,$dB, $\Delta P \approx 0.3\,$dB is nearly negligible. To further optimize the reliability of the experiment, repeating the measurement and getting the average, which help eliminate the influence of the random background disturbance, are suggested.

3.4.2 Results

The raw experimental data is the power emitted by the nano-ridges as a function of the pump length at different pump intensities, as shown in Figure 3.16 with solid dots. For a given pump intensity, the measured signal is first dominated by spontaneous emission (SE) at short pump length and taken over by a linearly growing ASE signal with increased pump length. We barely saw the sublinear part of SE in Figure 3.16 before the linear ASE because the pump length for SE is always relatively small and decreases with increasing pump intensity. Note that the measurements were carried at high excitation intensities starting from $12.3\,\text{kW/cm}^2$ to reach a detectable signal level. The saturation of the output power becomes apparent at pump lengths longer than $150\,\mu$m and excitation beyond $109\,\text{kW/cm}^2$. The

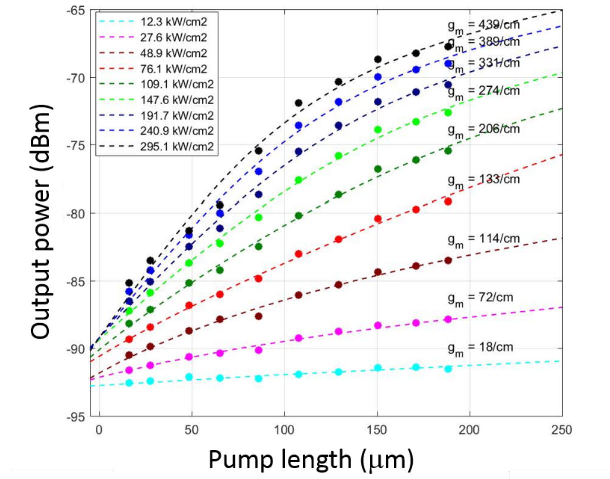

Figure 3.16: The output power versus pump length, for sample S'_{Ref} at different pump intensities. Dots are experimental results and dashed lines are the fitting. The modal gain can be derived from the slope of the linear region.

pump length dependence can be described by the equation [18]:

$$g_m \cdot L = \alpha(I - I_0) + ln[\beta(I - I_0) + 1] \tag{3.2}$$

with g_m the net modal gain, L the pump length, I_0 the background noise, α describing the gain saturation process and β a parameter related to the spontaneous emission. The key parameter g_m and α, β, I_0 can be obtained by fitting the experimental data using the above equation Eq. 3.2 for a given pump intensity. Through repeating this procedure for all pump intensities, the pump-intensity-dependent modal gain can be obtained. The fitting is shown in Figure 3.16 with dashed lines.

Taking into account that the TE ground mode $E_{TE}(x, y)$ has the smallest leakage loss and the highest confinement $\Gamma_{QWs}(x, y)$ in QWs as shown in the following Section 4.1, it is believed to be the dominant optical mode of ASE. The extracted net modal gain g_m not only includes gain but also all intrinsic nano-ridge loss α_i such as leakage into the Si substrate and scattering, and is expressed as

$$g_m = \Gamma_{QW}(x, y) \cdot g - \alpha_i \tag{3.3}$$

where g is the material gain of the active InGaAs QWs.

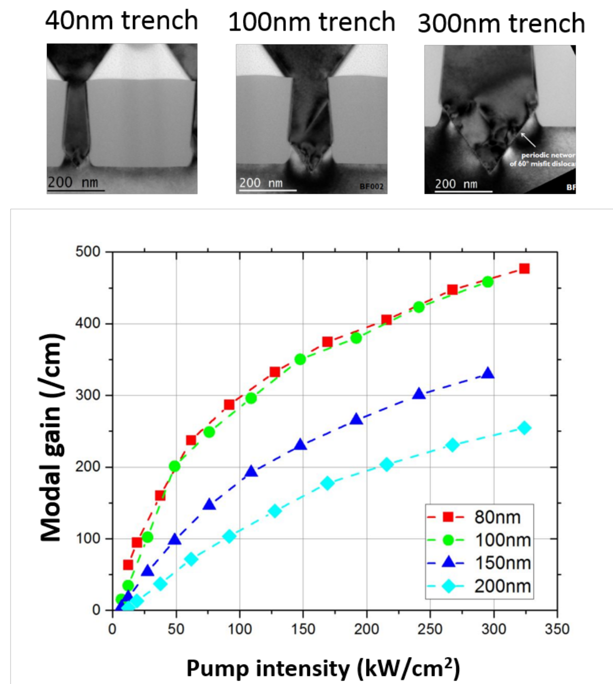

Figure 3.17: The extracted model gain vs. pump power for nano-ridges with 80 nm, 100 nm, 150 nm and 200 nm trench respectively of sample S'_{Ref}. The HR-STEM images of three samples with 40 nm-, 100 nm- and 300 nm- trench are shown at the top.

The TEM images and the extracted PL lifetime of the nano-ridges discussed in sections 2.2.3 and 3.3 already revealed the correlation of the crystal quality and trench size, resulting from the ART effect. Also the HR-STEM images of 40 nm, 100 nm and 300 nm trenches in Figure 3.17 visualise this increasing defect density. The dependence is confirmed again by investigating the optical modal gain, which is shown in Figure 3.17 and 3.18 for samples S'_{Ref} and S_{Ref}, respectively. The extracted g_m are then plotted for 80 nm- to 200 nm-trench nano-ridges.Nano-ridges with 80 nm- and 100 nm-trenches possess the highest modal

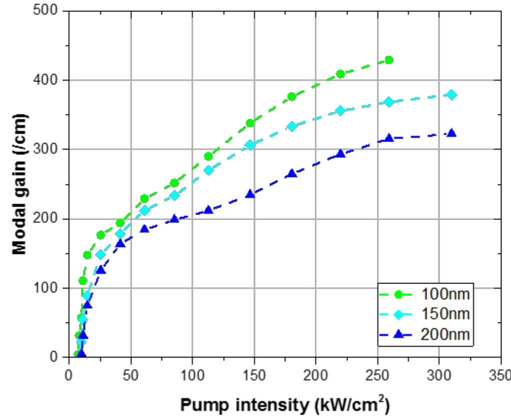

Figure 3.18: The extracted model gain vs. pump power for nano-ridges with 100 *nm,* 150 *nm and* 200 *nm trench respectively of sample* S_{Ref}.

gain of $g_m \approx 460\,\text{cm}^{-1}$ at $300\,\text{kW/cm}^2$ excitation. Given the Γ_{QW} in Table 4.2, the material gain is estimated to be above $5000\,\text{cm}^{-1}$, which is comparable with conventional GaAs material [20]. In addition, all modal gain curves present a sublinear behavior, which is typical for QWs which have a high differential gain at low pump intensity, which then saturates under increasing pump power. The modal gain for S_{Ref} is shown in Figure 3.18. Similar as for S'_{Ref}, 100 nm-trench nano-ridge exhibits the highest gain while the modal gain for the 200 nm-trench nano-ridge is the lowest. It seems that the gain dramatically rises at low pump intensity and slightly saturates around 50 kW/cm$^($2). Given the uncertainty in measurement and the fitting, it is difficult to conclude that the small difference compared with sample S'_{Ref} is due to the nano-ridge itself.

The modal gain is also dependent on the number of QWs N_{QW}. The confinement factor Γ_{QWs} of multiple QWs is approximated by $\Gamma_{QWs} = N_{QW} \cdot \Gamma_{QW}$ if the single QW confinement Γ_{QW} of each QW layer can be considered constant. The extracted modal gain of identical nano-ridges with $2\times$QWs and $3\times$QWs respectively are plotted in Figure 3.19. As expected, the modal gain of a nano-ridge with $3\times$QWs is higher than that with $2\times$QWs. The fact that the modal gain ratio of $2\times$QWs to $3\times$QWs at a particular pump intensity is not exactly $2:3$ is suspected to be due to the higher pump intensity per QW for the $2\times$QWs than that for the $3\times$QWs.

Unlike Figure 3.17, the modal gain curves in Figure 3.19 have a plateau region from pump intensity $\sim 50\,\text{kW/cm}^2$ to $\sim 150\,\text{kW/cm}^2$ between the two increasing gain parts. The cause of this behavior is not yet understood. Some possibilities are:

the first electron transition $E_{1\text{-}1HH}$ is saturated at the plateau region and other transitions such as $E_{1\text{-}1LH}$ or $E_{1\text{-}1SO}$ start to become important. Or the TE-like ground mode starts to get saturated from $\sim 50\,kW/cm^2$ and other TM-like or higher-order modes are excited under high pump power. This question could not be further investigated in this work but can be done through spectra and polarization analysis in the future to examine whether it is the switch between different electron transitions or between different transversal optical modes.

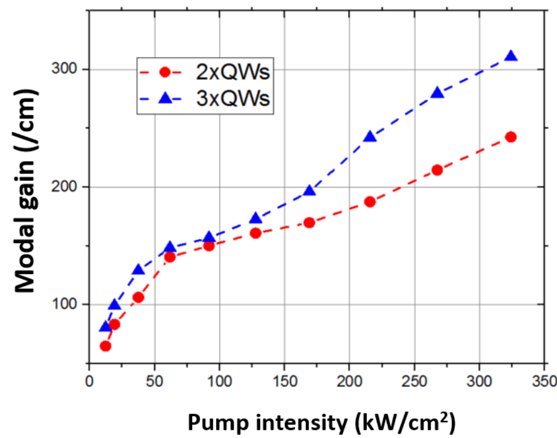

Figure 3.19: The extracted modal gain vs pump power for nano-ridges with 2×QWs and 3×QWs respectively. The two samples are not listed in Table 2.2, but they are suppposed to have the same configuration as the reference sample except for the number of QWs.

Excited by a pulsed laser, the emission power of the nano-ridge is below around $-65\,dBm$, which is still detectable by a powermeter that integrates the signal. However, the broad-band emission spectrum with such low power is below the measurement limit of most optical spectrum analyzers (OSA). Instead of using the pulsed pump, a $532\,nm$ CW laser with high average power is utilized to acquire a signal sufficiently high to be measurable by an optical spectrum analyser (OSA). The in-plane emission of the nano-ridge with $100\,nm$ trench at different pump lengths at an intensity of $990\,W/cm^2$ is shown in Figure 3.20. Compared with the PL spectra of the same sample shown in Figure 3.6, which is mostly SE scattered from the nano-ridge surface, a redshift of $\sim 30\,nm$ is observed for the spectra of the in-plane emission. This emission contains a higher fraction of ASE, which is more likely to be produced by electron transitions close to the band edge. When comparing the different pump lengths in Figure 3.20, we observe a redshift in the spectra. Different from peak blue-shift caused by increasing excitation density, the emission shifts to longer wavelengths when increasing the pump length. It is said

that the optical gain at short wavelength gets saturated quickly and causes a peak redshift [18].

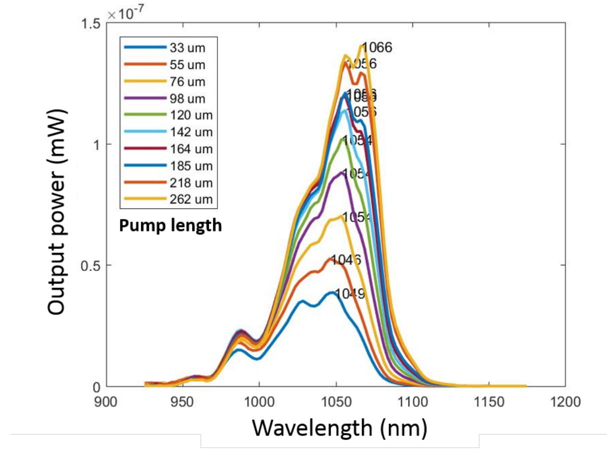

Figure 3.20: The emission spectra of nano-ridges under different pump lengths of sample $S_{Ref'}$, at CW pump intensity $990W/cm^2$. PL peak red-shifts with increasing pump length.

3.5 Conclusion

We experimentally characterized the optical properties of the GaAs nano-ridges through PL, TRPL and VSL based gain measurements. Before investigating these properties in detail, the energy band diagram of the reference nano-ridge structure was calculated both at room temperature and at low temperature. The results reveal a dominant QW emission at a wavelength of $1\,\mu$m, from the E_{1-1HH} transition. The PL measurement under CW pumping verified the calculation by showing a distinct emission peak at $\sim 1\,\mu$m. The decrease of the intensity of the PL signal towards wide trenches correlates with the increasing defect density observed in TEM images. Afterwards, the PL lifetime of the nano-ridge was characterized on a TRPL set-up at both room-temperature ($300\,$K) and low-temperature ($80\,$K). The influence of the trench width, nano-ridge size as well as the hetero-structure were studied. Surface recombination and recombination in the defective trenches were found to be two dominating carrier loss mechanisms. Passivating the nano-ridge with an InGaP cap and inserting a carrier-blocking layer of InGaP strongly suppresses the loss and prolongs the PL lifetime up to $2\,$ns. Also the characterization of the optical modal gain by a VSL approach shows a clear correlation with the ART effect. From these measurements the material gain was estimated to be above $5000\,$cm^{-1}, which is comparable with conventional GaAs material.

The optical characterization discussed in this chapter confirms that the combination of ART and NRE enables the integration of high-quality III-V nano-ridge material on Si substrates, and opens the road towards demonstration of laser operation in the next chapter.

References

[1] Yuting Shi, Lisa Kreuzer, C., Nils Gerhardt, Marianna Pantouvaki, Joris Van Campenhout, Marina Baryshnikova, Robert Langer, Dries Van Thourhout, and Bernardette Kunert. *Time-Resolved Photoluminescence Characterization of InGaAs/GaAs Nano-Ridges monolithically Grown on 300mm Si Substrates*. submitted.

[2] *Matlab = `https://www.mathworks.com/products/matlab.html`, note = Accessed: 2019-12-30.*

[3] I. Vurgaftman, J. áR Meyer, and L. áR Ram-Mohan. *Band parameters for III–V compound semiconductors and their alloys*. Journal of applied physics, 89(11):5815–5875, 2001.

[4] *Effective Carrier Mass*. `http://www.iue.tuwien.ac.at/phd/palankovski/node40.html`, 2008. Online; accessed 19-July-2018.

[5] *Temperature dependence of the energy bandgap*. `https://ecee.colorado.edu/~bart/book/eband5.htm`, 2008. Online; accessed 19-July-2018.

[6] *InP band structure*. `http://www.ioffe.ru/SVA/NSM/Semicond/InP/bandstr.html#Temperature`, 2008. Online; accessed 19-July-2018.

[7] Shun Lien Chuang. *Optical gain of strained wurtzite GaN quantum-well lasers*. IEEE Journal of quantum Electronics, 32(10):1791–1800, 1996.

[8] Doyeol Ahn and Chuang Shun-Lien. *Optical gain in a strained-layer quantum-well laser*. IEEE journal of quantum electronics, 24(12):2400–2406, 1988.

[9] Guobin Liu, Shun-Lien Chuang, and Seoung-Hwan Park. *Optical gain of strained GaAsSb/GaAs quantum-well lasers: A self-consistent approach*. Journal of Applied Physics, 88(10):5554–5561, 2000.

[10] Larry A Coldren, Scott W Corzine, and Milan L Mashanovitch. *Diode lasers and photonic integrated circuits*, volume 218. John Wiley & Sons, 2012.

[11] Tow C Chong and Clifton G Fonstad. *Theoretical gain of strained-layer semiconductor lasers in the large strain regime*. IEEE Journal of Quantum Electronics, 25(2):171–178, 1989.

[12] W Rideout, B Yu, J LaCourse, PK York, KJ Beernink, and JJ Coleman. *Measurement of the carrier dependence of differential gain, refractive index, and*

linewidth enhancement factor in strained-layer quantum well lasers. Applied physics letters, 56(8):706–708, 1990.

[13] Peter JA Thijs, Luuk F Tiemeijer, PI Kuindersma, JJM Binsma, and Teus Van Dongen. *High-performance 1.5 mu m wavelength InGaAs-InGaAsP strained quantum well lasers and amplifiers*. IEEE journal of quantum electronics, 27(6):1426–1439, 1991.

[14] Timothy H Gfroerer. *Photoluminescence in analysis of surfaces and interfaces*. Encyclopedia of analytical chemistry: applications, theory and instrumentation, 2006.

[15] B. Kunert, W. Guo, Y. Mols, B. Tian, Z. Wang, Y. Shi, D. Van Thourhout, M. Pantouvaki, J. Van Campenhout, R. Langer, and iii/v K. Barla. *nano ridge structures for optical applications on patterned 300 mm silicon substrate, Appl. Phys*. Lett., 109:9, 2016.

[16] RK Ahrenkiel, JM Olson, DJ Dunlavy, BM Keyes, and AE Kibbler. *Recombination velocity of the Ga0. 5In0. 5P/GaAs interface*. Journal of Vacuum Science & Technology A: Vacuum, Surfaces, and Films, 8(3):3002–3005, 1990.

[17] Richard R King, James H Ermer, David E Joslin, Moran Haddad, Jack W Eldredge, NH Karam, Brian Keyes, and Richard K Ahrenkiel. *Double heterostructures for characterization of bulk lifetime and interface recombination velocity in III-V multijunction solar cells*. In 2nd World Conference on Photovoltaic Solar Energy Conversion, pages 86–90, 1998.

[18] K. L. Shaklee and R. F. Leheny. *Direct determination of optical gain in semiconductor crystals*. Applied Physics Letters, 18(11):475–477, 1971.

[19] K. L. Shaklee, R. E. Nahory, and R. F. Leheny. *Optical gain in semiconductors*. Journal of Luminescence, 7(C):284–309, 1973.

[20] FRAKK Stern. *Gain-current relation for GaAs lasers with n-type and undoped active layers*. IEEE Journal of Quantum Electronics, 9(2):290–294, 1973.

4

1 µm-wavelength nano-ridge lasers

In the previous Chapter, we have characterized the optical properties of the nano-ridges by several means. From the PL spectra, we found the nano-ridges emit around 1020 nm. Through TRPL, we further confirmed that nano-ridges with trench width from 60 nm to 150 nm have the best crystal quality due to a good trade-off between ART effect and surface recombination. From modal gain measurements, we experimentally verified that the gain of the nano-ridges is comparable to that of traditional III-V materials [1, 2] to reach 5000 /cm.

In this Chapter, we commence developing nano-ridge lasers based on these fundamental but indispensable understandings of the material. As a start, the transversal optical mode is calculated in Section 4.1. The essential optical properties of the nano-ridges, e.g., the mode polarization, the effective refractive index n_{eff} and QWs confinement factor Γ_{QW}, are accordingly obtained. Afterwards, we will present several types of lasers. The starting point is the Fabry-Perot laser, given its straightforward design and fabrication, as discussed in Section 4.2. After that, single-mode index-coupled distributed feedback (DFB) lasers with a more complex cavity design are presented in Section 4.3. The distributed gratings enable a much narrower reflection linewidth and a more controllable reflectivity for the DFB laser. This work is published in [3]. Then, although thus far all the laser devices are currently optically pumped, single-mode partly-loss-coupled DFB lasers are demonstrated as a first step towards electrical injection. By depositing a metallic grating instead of a continuous metallic layer, the metal layer that could serve as future electrical contact pads introduces tolerable loss and at the same time forms a partly-loss-coupled DFB cavity. These loss-coupled devices discussed in

Section 4.4 also show single-mode lasing. The results are prepared for publication [4].

It should be noticed that in this chapter, we only consider sample S'_{Ref}, which was fabricated before the year 2018 and showed the best optical properties, as discussed in chapter 2 and 3. Although S_{blk1} does exhibit longer PL lifetime, it was only received after we developed the lasers. The configuration of sample S'_{Ref} (taking 100 nm trench as an example) can be found in Figure 2.15, its corresponding PL results in Figure 3.6 and the optical gain curve in Figure 3.17. Among all the nano-ridge sizes on this specific sample, nano-ridges with 60-150 nm wide trenches show the best performance as chapter 2 and 3 revealed and will be the focus to make laser devices. More details of the dimension of the nano-ridges are listed in Table 4.2 in this chapter.

4.1 Transversal optical mode

Due to the elongated rectangular configuration of the GaAs/InGaAs nano-ridges, the nano-ridges themselves can naturally serve as optical waveguides (WGs), confining the light transversally in the high-index GaAs volume. Nevertheless, the bottom of the nano-ridges, different from the other three sides, which exhibit a high index contrast of $\Delta n \approx 2.46$ between GaAs and air, has little index contrast $\Delta n \approx -0.1$ with Si. Hence, the leakage loss towards the high-index Si substrate is a critical question. In this section, we calculate the optical modes of the nano-ridge, from which the mode profile, the polarization, the effective refractive index, the QW confinement and the leakage loss can be obtained.

The guided transversal optical (electromagnetic) field can be derived by solving Maxwell's equations [5]. The obtained solutions with different eigenvalues are called eigenmodes. Each eigenmode propagates invariantly if the transversal shape of the waveguide is invariant. According to the optical modes' electrical and magnetic field direction (polarization) relative to their propagation direction, the two typical kinds of modes discussed in integrated WGs are:

- Transverse electric (TE) modes: the electrical field is dominantly perpendicular to the direction of propagation.

- Transverse magnetic (TM) modes: the magnetic field dominantly perpendicular to the direction of propagation.

The polarization , the effective refractive index (n_{neff}), the confinement in the three InGaAs QWs Γ_{QW} and the leakage loss α_{leak} are calculated by a Finite Difference Eigenmode (FDE) solver at the wavelength 1020 nm using commercial software Lumerical Mode Solution [6]. The results for the first four modes of the 100 nm-trench nano-ridge are listed in Table 4.1. The simulation is configured

using the real geometry of the nano-ridges, as shown in Table 4.2. One key parameter is the QW confinement factor (Γ_{QW}), which defines the fraction of optical intensity confined in the active QWs region. The Γ_{QW}, which together with the material gain directly determines the optical modal gain , is calculated by:

$$\Gamma_{QW} = \frac{\iint_{s_{QWs}} |E|^2 ds}{\iint_{s_{all}} |E|^2 ds} \tag{4.1}$$

Where E is the optical field, s_{QWs} and s_{all} the cross-section area of the QWs and the whole calculation region respectively. Calculating the leakage loss is a bit tricky. It is not directly given by the eigenmode calculation. However, we could artificially introduce an extremely high absorption loss of the Si substrate such that all the leakage towards Si is absorbed. In this way, the leakage loss could be regarded as the absorption loss of the optical mode, which is derived from the imaginary part of its effective refractive index $Im(n_{eff})$.

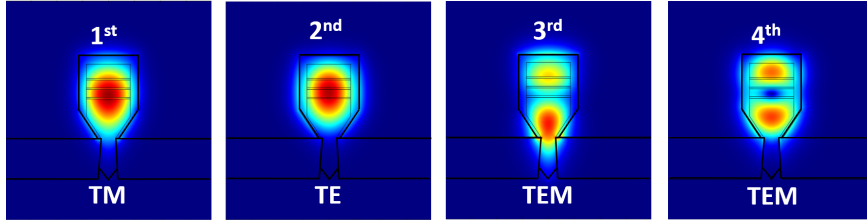

Figure 4.1: The first four optical modes of the nano-ridge with trench width 100 nm. The polarization of the modes is labelled at the bottom of the images.

Figure 4.1 shows the first four optical modes of the nano-ridge with a trench width of 100 nm. Additional higher-order modes found in the simulation are excluded in our discussion since they are not confined in the nano-ridge. The first mode is a TM-like mode, which is rather extended in the vertical direction and exhibits a relatively high leakage loss towards the Si substrate. The second mode is the TE-like ground mode with an effective refractive index of $n_{eff} = 3.167$. The 3rd and 4th modes are high-order TEM modes, which are less confined in the QWs with a Γ_{QW} of only around 2%. Among the four modes, the TE-like ground mode exhibits the highest confinement in the QWs with $\Gamma_{QW} = 9.33\%$. Besides, the TE-like ground mode possesses the lowest leakage loss towards Si substrate with a value of $\alpha_{leak} < 5$ dB/cm, ~ 10 times better than that of the TM-like ground mode.

Mode NO.	$TE\ fraction(\%)$	n_{eff}	$\Gamma_{QW}(\%)$	$\alpha_{leak}(dB/cm)$
1st	0	3.211	8.67	43
2nd	100	3.167	9.33	<5
3rd	4	2.861	2.61	-
4th	68	2.858	1.56	-

Table 4.1: The transverse electrical polarization fraction $TE\ fraction$, effective refractive index n_{eff}, QWs confinement factor Γ_{QW} and leakage loss α_{leak} of the first 4 modes of the nano-ridge with 100 nm wide trench.

Having the highest Γ_{QW} and the lowest α_{leak} makes the TE-like ground mode the most promising candidate for lasing. Therefore we focus on this particular optical mode and calculate the mode profile (Figure 4.2), effective refractive index n_{eff} and confinement in QWs Γ_{QW} (results shown in Table 4.2) for nano-ridges with trench widths of 60 nm, 80 nm, 100 nm and 120 nm respectively. The dimensional parameters: d, trench width; a, ridge width; b, ridge height; c, position of the lowest QW are labelled in Figure 2.11. As we know from chapter 2, the volume of the nano-ridges increases with their trench width. Thus, it is logic to find in Table 4.2 that the effective refractive index n_{eff} increases with trench width too. As for the Γ_{QW}, we derived increasing confinement in the QWs for wider-trench nano-ridges.

The $Absorption$ listed in Table 4.2 refers to the absorption of a 532 nm optical pump vertically illuminating the sample surface. This parameter is not relevant if the nano-ridge devices are electrically driven. However, for the optically pumped situation, which is the case of this thesis, the absorption is calculated to estimate the pump conditions for later laser characterization. Once the absorption is determined, the optical excitation can be calculated by the multiplication of the absorption coefficient and the pump intensity arriving on the sample surface. The absorption is calculated using a finite-difference time-domain (FDTD) solver through monitoring the fraction of a 532 nm plane wave absorbed by one nano-ridge, under a periodic boundary condition to simulate the real case of the on-chip nano-ridge array. Depending on the volume and period of the nano-ridges, the absorption decreases with trench width as the duty cycle of the nano-ridge drops (shown in Figure 2.13 (a)).

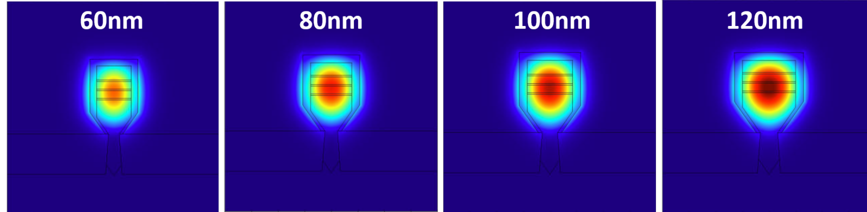

Figure 4.2: The TE-like ground modes of the nano-ridges with trench width 60 nm, 80 nm, 100 nm and 120 nm (left to right). As the III-V volume increases with trench width, the optical field is better confined inside the larger nano-ridges.

d(nm)	**a**(nm)	**b**(nm)	**c**(nm)	n_{eff}	$\Gamma_{QW}(\%)$	$Absorption^{\star}$
60	364	556	248	3.022	8.84	0.807
80	432	582	274	3.122	9.45	0.747
100	458	602	285	3.167	9.33	0.653
120	530	610	290	3.210	9.6	0.547

Table 4.2: The effective refractive index n_{eff}, QWs confinement factor Γ_{QW} and absorption of the TE-like ground modes of nano-ridge with trench widths 60 nm, 80 nm, 100 nm and 120 nm respectively.
* *The absorption coefficient of 532nm optical pump vertically illuminating sample surface.*

In this Section, we have shown the optical modes confined transversally in the nano-ridges. A laser device confines light in all three directions, and requires feedback in the propagation direction, which is provided by the so-called laser cavity. In the following, three types of cavities — Fabry-Perot (FP), index-coupled DFB and loss-coupled DFB — will be explored focusing on the TE-like ground mode as outlined above.

4.2 Fabry-Perot laser

4.2.1 Cavity design

An FP cavity consists of two (parallel) reflecting surfaces, between which the optical field can become resonant in the form of standing waves [7]. The wavelength of light and the optical length of the cavity has to meet the below equation:

$$2 \cdot n_{eff} \cdot L = m \cdot \lambda_m \tag{4.2}$$

with n_{eff} the effective refractive index of the propagating mode, L the geometrical length of the FP cavity and m a positive integer. The free spectral range λ_{FSR}, which indicates the spacing between two resonant wavelengths and decides the

number of longitudinal lasing modes within a certain gain spectrum, is expressed by

$$\lambda_{FSR} = \frac{\lambda_m^2}{n_g L} \tag{4.3}$$

where n_g is the group index. The feedback of the cavity is provided by the reflection of the two end facets, which can either be the interface of different materials or interfaces with high-reflection(HR) or anti-reflection(AR) coatings. Even though the reflectivity at the interface of two particular materials is fixed, decided by their indices, the reflectivity can be modified over a wide range, e.g., from 0.1% (AR coating) to 99.9% (HR coating) [8, 9] for a specific wavelength span by adding extra coatings. Usually, the reflection wavelength window is quite broad, wider than the λ_{FSR} of a FP cavity such that the FP cavity is not wavelength-selective. Therefore FP lasers are typically multi-mode once the cavity modes have enough gain. In many complex optical systems, the optical source is required to be single-mode, low-threshold and narrow-linewidth, which can not be realized with the simple FP laser. Even worse is that the spectrum of a FP laser is not stable as a function of bias point or temperature. The power distribution over the different longitudinal modes varies slowly with time such that the strongest peak in the spectrum could change from one longitudinal mode to another instantly. This mode-hopping behavior [10] is intolerable in many applications. To stabilize a FP laser, some methods such as adding feedback from an external cavity [11] or locking the wavelength by external light injection [12] are proved to be effective but makes the simple structure more complicated.

Nevertheless, given the simplicity of the FP cavity in terms of its configuration and fabrication, we used them as a first trial. To realize the two reflecting facets for forming a FP cavity, normally cleaving or dry etching is adopted. Cleaving the sample along with the crystal planes of the substrate always gives mirror-like and smooth surfaces. Nevertheless, cleaving does not allow for a lot of flexibility. E.g. it does not allow for varying the cavity length within one sample. We have tried cleaving FP cavities for several test samples and found it difficult to control the length shorter than $250\,\mu$m and meanwhile obtain good quality. Therefore, we applied dry etching, whereby the cavity lengths are defined by lithography. To further simplify the process, no coatings are applied to the cavity, and the reflection is only given by etched facets with index contrast between the nano-ridge (mostly GaAs) and air.

Even with optimized dry etching, it is challenging to obtain perfectly vertical facets. The facets can either have an acute angle or an obtuse angle. Figure 4.3 (a) shows the side view of a nano-ridge facet with an angle deviation of $-30°$(left) and $30°$(right). The simplified Fresnel reflectance equation [13], which is only applicable to the case of the plane wave, is not applicable here given the strongly confined mode. Figure 4.3 (b) gives the simulation result of the reflection versus

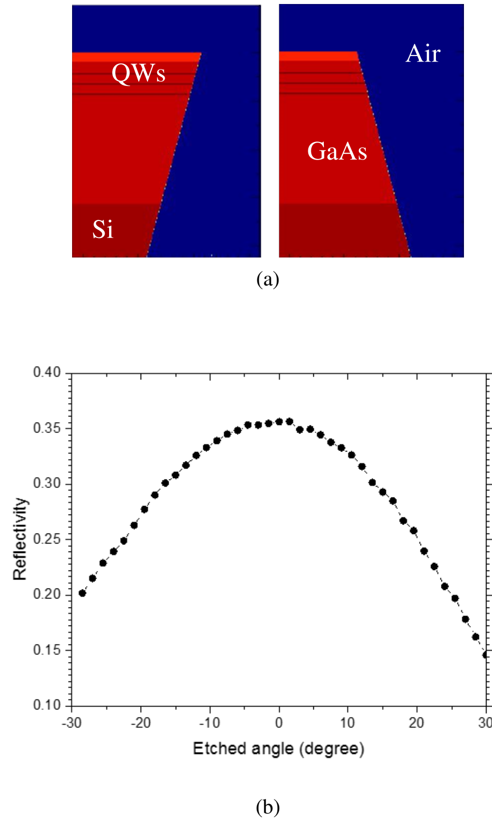

Figure 4.3: (a) Simulation setup of etched nano-ridge facet with an angle -30° (left) or 30° (right). (b) The reflectivity of etched Fabry-Perot cavity as a function of etched sidewall angle.

the etched angle varied from -30° to 30°, calculated by an FDTD solver. The maximal reflection of 0.35 happens when the facet is perfectly vertical.

4.2.2 Results

The etching quality is highly dependent on the process recipe and operation, whereby optimization is typically demanded. A layer of SiN is applied as a hard mask for high-selective dry etching because the nano-ridge outside the cavity has to be etched through to enable a full interface with air. The process started with depositing a 200 nm-thick SiN layer by plasma-enhanced chemical vapor deposition (PECVD). The FP cavities with varying lengths of $80\,\mu$m to $200\,\mu$m are first patterned by lithography and afterward transferred to the SiN layer by reactive-ion etching (RIE). The GaAs/InGaAs nano-ridges are finally etched by inductively

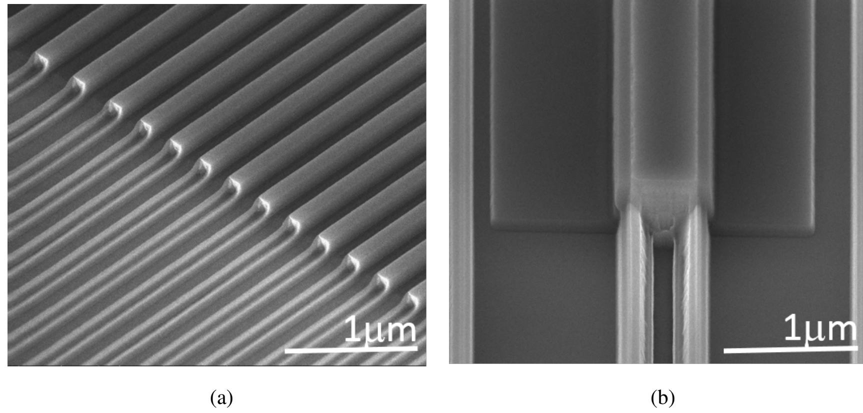

(a) (b)

Figure 4.4: The SEM images of fabricated FP device. (a)A tilted view of the FP array. (b) A tilted view of one FP cavity facet.

coupled plasma (ICP) etching using a recipe with $Cl_2 : CH_4 : Ar = 8 : 4 : 10$. The details of the recipe and the optimization of the nano-ridge dry etching can be found in Appendix A. Figure 4.4 shows the SEMs of the fabricated FP devices with (a) the tilted side view of the FP array where full nano-ridges outside the cavities are removed, (b) the tilted front view of one FP facet where the facet roughness, the residual side InGaP cap and the exposed trenches are observed.

The FP devices are characterized on the μ−PL setup shown in Figure 3.4 except that the pump source is a Nd:YAG nanosecond pulsed laser (7 ns pulse width, 938 Hz repetition rate, 532 nm wavelength) instead of the CW DPSS laser. Figure 4.5 shows an image of a $80\,\mu m$ long FP laser array under optical excitation seen by a Si CMOS camera. The FP cavities are horizontally oriented, with the two bright lines being the facets, from where the camera captures the strong scattering of the lasing light. From top to bottom, the picture shows nano-ridges with trench width $20 - 150$ nm respectively (10 devices per group). The wider trenches are not visible as they become defective and are less luminescent under the same excitation.

From Table 4.2 we know that n_{eff} is different for nano-ridges with different trench widths. Therefore lasing spectra of the different nano-ridges are expected to vary according to Equation 4.2, although the cavity length is uniform. To exclude the variations in the lasing spectra of nano-ridges with different configurations, we used a rectangular slit to limit the pumping spot to a group of FP devices, which only contains the ten alike nano-ridges. Figure 4.6 (a) shows the spectrum of the nano-ridges with 100 nm trench width at a pump intensity of ~ 300 kW/cm^2. Multiple equally-distributed lasing peaks in the spectrum are expected as the FP

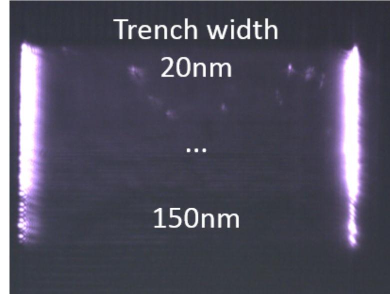

Figure 4.5: The 80 μm long FP laser array under optical excitation seen by a Si CMOS camera. The luminescent array includes ten nano-ridges of each trench width from $20 - 150$ nm. Wider trenches are not visible as they are less luminescent under the same excitation.

cavity is not wavelength-selective. The theoretical spacing between two peaks (FSR) can be calculated by Equation 4.3: $\lambda_{FSR} = \frac{\lambda_m^2}{n_g L} = 3.54$ nm with $n_g = 3.674$ at $\lambda = 1020$ nm. However, we found the calculation does not match the experimental results in Figure 4.6 (a), where the multiple peaks are not distribute equally nor is the spacing between the peaks 3.54 nm. The discrepancy is attributed to two reasons: one is that the spectrum is a summation of the individual spectra of multiple nano-ridges with the same trench width, whose n_{eff} can still slightly vary. The other is that the resolution of the measurement is ~ 2 nm, which should be sufficient to resolve peaks with $\lambda_{FSR} = 3.54$ nm but not to detect minor shifts. Figure 4.6 (b) shows the light-in light-out curve of the nano-ridges with 100 nm trench width for the emission within the wavelength range $1000 - 1011$ nm. The S-shaped curve shows a transition around 70 kW/cm^2 (threshold) from spontaneous emission to stimulated emission, which proves the FP devices are lasing. However, the multi-mode FP laser is not a popular option in many applications. Therefore we will focus on the more widely applied DFB-laser in the following section.

4.3 Index-coupled DFB laser

4.3.1 Introduction

After the demonstration of multi-mode FP lasers, we continue the exploration of the nano-ridge for light sources with more advanced DFB lasers that possess low threshold, stable single-mode behavior and high quantum efficiency. To enable single-mode lasing, the laser cavity should only allow one optical mode that has a significantly higher net gain and reflection than other modes. For the transversal mode of the nano-ridges, we have explained that the TE-like ground mode should have the highest net gain. As for the selection of longitudinal modes, cavity feed-

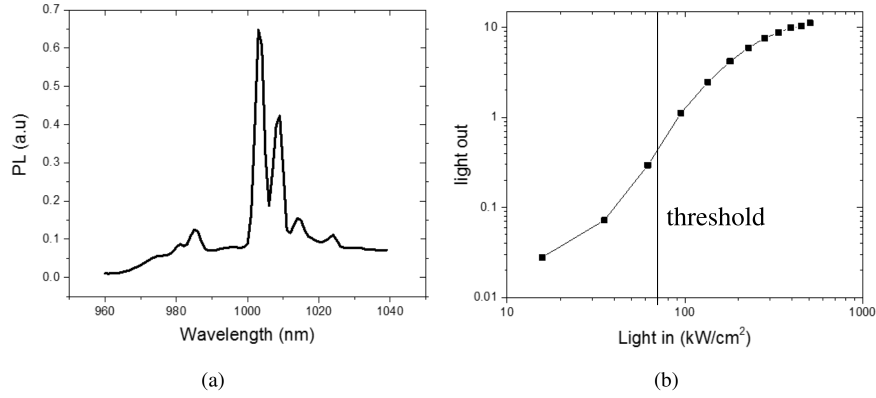

Figure 4.6: (a) The spectrum of pumped nano-ridges with $100\,nm$ *trench width. (b) The output light in wavelength range* $1000 - 1020\,nm$ *as a function of pump intensity.*

back can be wavelength-selective by utilizing wavelength-selective reflectors (e.g., distributed Bragg reflector) [14] and so on. For example, DFB lasers with high selectivity in wavelength are a key component in the fiber-optic communication system [15].

Instead of the discrete mirrors in FP lasers, the reflection in DFB lasers is provided by a periodic variation in the effective refractive index of the transversal mode. The variation can be a pure index modulation, for an index-coupled DFB-laser, or a pure gain(loss) modulation, for a gain-coupled DFB-laser. Both can also be combined, in which case the device is a so-called partly-gain-coupled DFB laser. In this section, we will focus on index-coupled devices. An example of (partly-)gain-coupled lasers realized by depositing metallic gratings will be shown in the following section.

To gain a basic understanding of DFB-devices, we can treat the feedback of the cavity provided by the grating as a summation of many small reflections. Only at one wavelength and its multiple, each reflection is added up in phase and results in a considerable net reflection. This particular wavelength is called the Bragg wavelength [14]. Under the small perturbation assumption, the Bragg wavelength is determined together by the grating period Λ and the effective refractive index n_{neff} of the resonant mode:

$$\lambda_B = 2\Lambda n_{eff} \tag{4.4}$$

In a more comprehensive treatment, the feedback provided by gratings can be considered as the coupling between forward and backward propagating wave [16]. By introducing a periodic perturbation along the propagation direction of the optical mode, coupling between the forward propagating mode ($E_f(z)$) and the back-

ward propagating mode ($E_b(z)$) can be facilitated [17, 18]. The small perturbation on the modes can be introduced as a linear term added to the equations:

$$\frac{dE_f(z)}{dz} = -j\beta_f E_f(z) - j\kappa_{fb}E_b(z) \tag{4.5}$$

$$\frac{dE_b(z)}{dz} = -j\beta_b E_b(z) - j\kappa_{bf}E_f(z) \tag{4.6}$$

where κ_{bf} is the coupling coefficient from $E_b(z)$ to $E_f(z)$, κ_{fb} is the coupling coefficient from $E_f(z)$ to $E_b(z)$, β_f and β_b are the propagation constants of $E_f(z)$ and $E_b(z)$ respectively. Exploiting reciprocity and symmetry, we find

$$\kappa = \kappa_{bf} = \kappa_{fb} = \frac{k_0^2}{2\beta}\frac{\iint \Delta\varepsilon(x,y)|U|^2 ds}{\iint |U|^2 ds} \tag{4.7}$$

where

$$\Delta\varepsilon(x,y,z) = \Delta\varepsilon(x,y)e^{-j\frac{2\pi z}{\Lambda}} \tag{4.8}$$

is the periodic perturbation of the electrical permittivity of the cavity and U is the normalized transversal field. From Equations. 4.5-4.8 we can derive the Bragg condition again: $\lambda_B = 2\Lambda n_{eff}$.

For a grating with finite length L, the reflectivity is calculated as $R = \frac{E_b(z)}{E_f(z)}$ at $z = 0$. $\frac{E_b(0)}{E_f(0)}$ can be obtained by solving Equations. 4.5 and 4.6 with the boundary condition $E_b(z = L) = 0$ (no reflection at the end of the grating). Figure 4.7 shows the field reflection spectra of the grating calculated by self-written code in Matlab for three different values of coupling strength κL versus the detuning parameter $\delta = \beta - \beta_B$. β_B is the propagation constant at the Bragg wavelength λ_B. Note that at $\delta = 0$, the reflectivity reaches the maximum. R also increases with increasing coupling strength, which can be achieved either by increasing the length of grating L or increasing the coupling strength κ. The other interesting parameter is the linewidth of the reflection peak, which is equivalent to the bandgap of the one-dimensional photonic crystal formed by the grating [19]. It widens with increasing κ as well.

The lasing wavelength of a DFB laser is expected to lie inside the bandgap due to the strong reflection. The exact location of the wavelength, however, is decided by some other cavity settings, e.g., phase shift section in the cavity or coatings applied at the facet. For a standard DFB laser with a continuous grating, there are two symmetric resonant peaks at each edge of the Bragg stopband, equally spaced from the Bragg wavelength (Figure 4.8 (a)). Introducing a phase shift section into the grating enables a single lasing peak (Figure 4.8 (b)) inside the stopband. For example, including a quarter-wave ($\lambda/4$) shift (preferably in the cavity center) [20] results in a single peak in the center of the stopband, at the Bragg wavelength. Because of the single-mode operation, high controllability of the wavelength and relatively easy fabrication, $\lambda/4$-shifted DFB lasers have

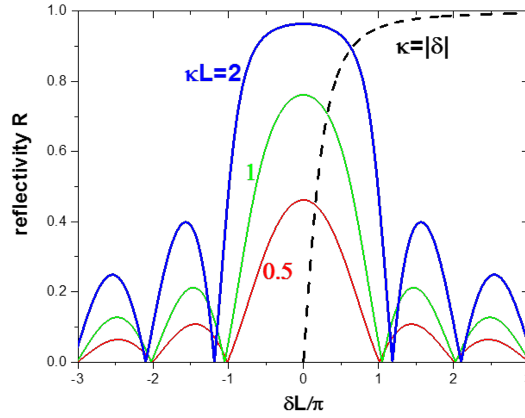

Figure 4.7: The calculated optical field reflection spectrum of the Bragg grating for four different values of coupling strength κL, versus the detuning parameter $\delta = \beta - \beta_0$.

become very popular in real-world applications. Breaking the symmetry of the standard DFB laser by applying different coatings at the facet is another way to make it single-mode. Figure 4.8 (c) shows the spectrum of a DFB with AR coating at one cleaved end and HR coating with $R = 0.9$ at the other end where the reflection phase is orthogonal ($\phi = 90°$). If the additive reflection is either exactly in-phase ($\phi = 360°$) or out-of-phase ($\phi = 180°$) [19], the high side mode suppression ratio (SMSR) shown in Figure 4.8 (c) will disappear and the device will perform as a standard DFB laser. Therefore, to enable the single-mode operation of a coated DFB laser, requires not only an extra process of coating but is also critically dependent on the exact cleaving position.

4.3.2 $\lambda/4$ shifted DFB simulation

In this Subsection, we implement $\lambda/4$ shifted index-coupled DFB lasers starting from the nano-ridges described in the previous sections. The most straightforward method to introduce a periodic index variation is etching the grating in the top surface of the nano-ridge together with a $\lambda/4$-shift section to ensure single-mode lasing.

The DFB laser is again optimized for working with the TE-like basic mode shown in Figure 4.2 and Table 4.1. The grating is designed using a finite difference time domain (FDTD) solver, taking into account the full three-dimensional configuration. Figure 4.9 shows the simulated configuration. The grating depth was limited to 110 nm to avoid etching the top QW layer. The duty cycle and sidewall angle are set to 25% and 65 ° respectively, matching the fabricated structures.

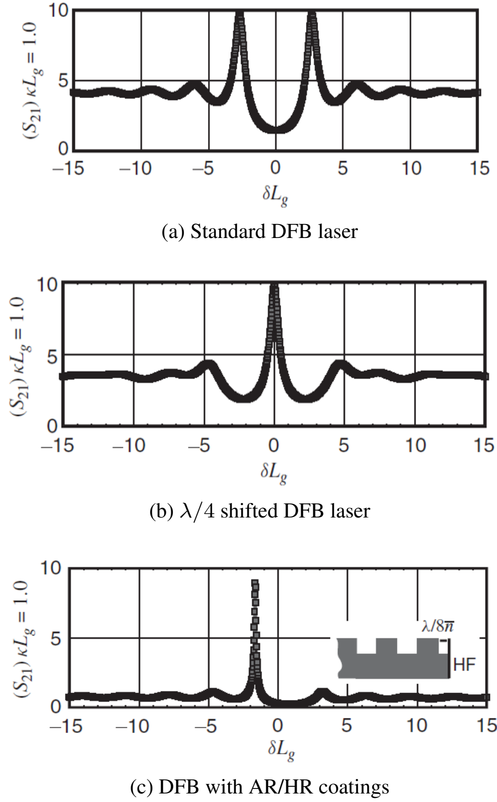

(a) Standard DFB laser

(b) $\lambda/4$ shifted DFB laser

(c) DFB with AR/HR coatings

Figure 4.8: The transfer function S_{21} spectra of three different kinds of index coupled DFB lasers (a)standard DFB laser (b) $\frac{\lambda}{4}$ shifted DFB laser (c) DFB with AR/HR coatings at the end facets. Source of figures [19].

Figure 4.10 (a) shows the calculated stop band of Bragg gratings as a function of grating period, defined in the nano-ridge with trench width 100 nm. The red and blue lines are the band edges extracted from the corresponding two Bloch mode of the DFB cavity [21]. The center of the stopband is the Bragg wavelength, which should be the lasing wavelength of the corresponding $\lambda/4$ shifted DFB laser. To have the grating reflection band overlap with the measured PL peak of nano-ridge centered at 1020 nm, the period of the grating is found to be 170 nm. Figure 4.10 (b) shows the reflection spectra for a grating with period 170 nm for the same nano-ridge. The reflectivity increases with increasing number of periods from $N = 50$ to $N = 300$, For a 300 period grating more than 90% reflectivity and ~ 4 nm wide stopband can be obtained, equivalent with a coupling strength $\kappa L = 3.3$. In the actually fabricated devices the grating period was swept from 164 nm to 180 nm for each of 4 ridge configurations (trench width 80 nm, 100 nm, 120 nm and 150 nm)

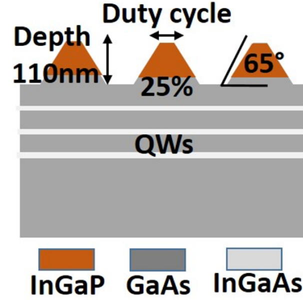

Figure 4.9: The side-view of the DFB laser with etched gratings at the top of the nano-ridge. The etch depth is set to be 110 *nm which gives good index modulation and meanwhile leaves the QWs untouched. Duty cycle and the sidewall angle are set as* 25% *and* 65°*, as obtained from the fabrication results.*

to accommodate for inaccuracies in the fabrication process and to investigate the relation between lasing wavelength and grating period. In addition, 20 μm away from the first order grating forming the laser cavity, a 50 period 2nd order grating was defined to vertically couple out the laser light and allow characterization of the devices in a standard μ -PL setup.

4.3.3 Fabrication and Characterization

After the growth, the GaAs nano-ridge array exhibits considerable surface topography. Therefore the sample was first planarized by spin coating a layer of 1.7 μm BCB (Benzocyclobutene), which then was etched back to the waveguide top surface. Next, the DFB laser was defined by etching a 600 period grating (300 periods each side) in the top surface of the GaAs ridge waveguide with a $\lambda/4$ phase shift section in the middle. The gratings were patterned using electron-beam lithography (EBL). The EBL pattern is shown in Figure 4.11, which also zooms-in the phase shift region and the 2nd order gratings. The DFB cavity is patterned on one out of 10 nano-ridges of same configuration from trench width (right to left) 500 nm, 300 nm, 200 nm, 150 nm, 120 nm, 100 nm, 80 nm and 60 nm respectively. Given the high density of the ridges, only one grating is defined per group of 10. This leaves enough space between two individual DFB devices to facilitate single device characterization and avoid crosstalk, taking into account the lateral extension of the optical pump area of around 5μ m. The 200 nm thick resist layer (AR-P 6200) was directly used as the mask for the inductive-coupled plasma (ICP) etching with a $Cl_2/CH_4/Ar$ gas recipe.

Figure 4.12 shows some details of the fabricated DFB device. Figure 4.12 is a tilted SEM image taken from the sample surface, showing a group of GaAs ridges, with trench width 120 nm, 100 nm, 80 nm and 60 nm respectively. Figure 4.12

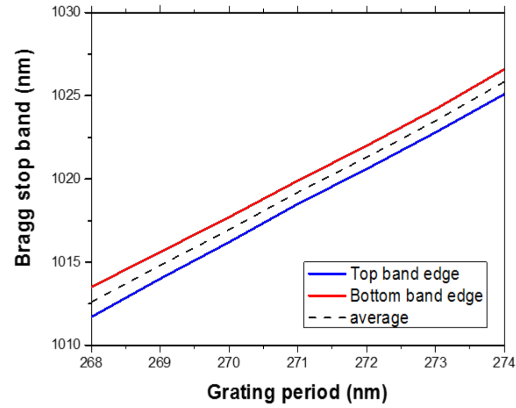

(a)

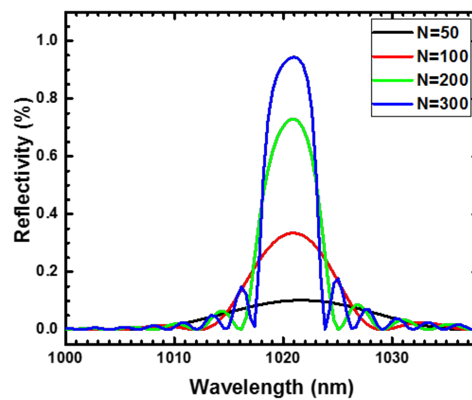

(b)

Figure 4.10: Bragg grating simulation result of 100 nm *wide nano-ridge. (a) The stopband of the gratings versus grating period. (b) The field reflection spectra of the Bragg gratings with increasing number of grating periods N=50, 100, 200, 300.*

(b) is a zoomed-in image of the central region of the grating with period 170 nm showing the $\lambda/4$ phase shift section. Figure 4.12 (c) shows the 2nd order grating coupler with period 340 nm. Note that the Figure 4.12 (c) scale bar is twice as long as the one in Figure 4.12 (b).

The devices were characterized on the same $\mu - PL$ setup used for the PL measurement, but using a Nd:YAG nanosecond pulsed laser (7 ns pulse width,

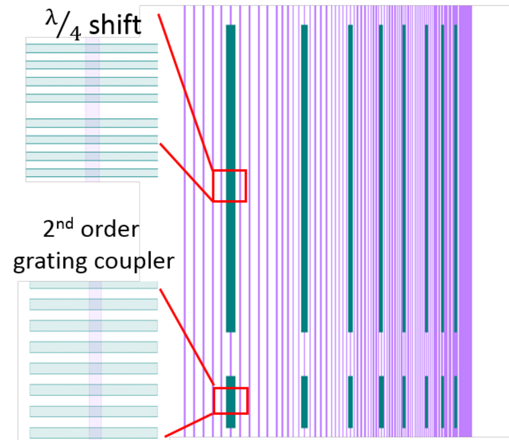

Figure 4.11: The ebeam lithographic mask of the DFB gratings at the top of nano-ridges from 60 nm (right) to 500 nm (left). The trenches of nano-ridges are in purple lines and the gratings are depicted in green, which can be more clearly seen from the magnifications.

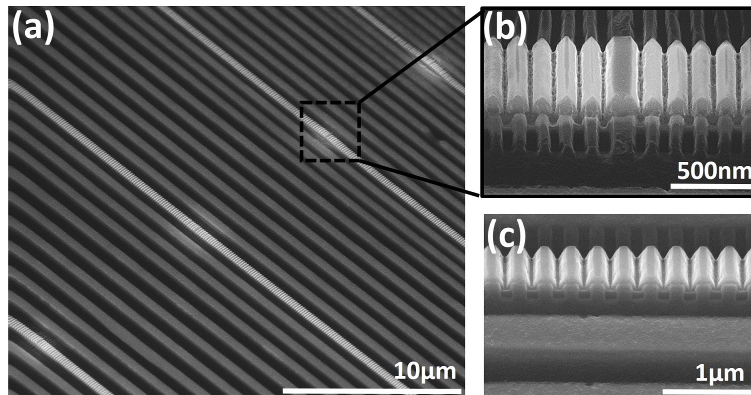

Figure 4.12: Tilted SEMs of (a) a DFB laser array, (b) the zoomed-in $\lambda/4$ phase shift section, and (c) the second-order grating coupler section.

938 Hz repetition rate, 532 nm wavelength) as the pump source. An image of the optically pumped sample caught by a Si CMOS camera is shown in Figure 4.13, which presents the same region as the mask Figure 4.11. The strongest emission comes from the $2^{nd}-$order gratings, which diffract the lasing light strongly into the detector. A rectangular aperture is inserted in the setup during measurement to limit the pump spot to a size of $5\,\mu m \times 200\,\mu m$, covering a single DFB device.

The pump intensity is controlled by the combination of a polarizer and a rotating half-wave plate (HWP) added in the setup. A chopper and a lock-in amplifier are used to improve the signal-to-noise ratio.

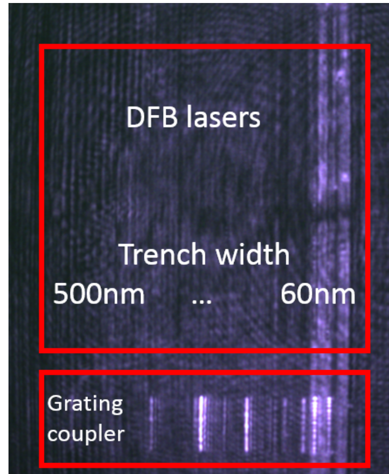

Figure 4.13: The same device region as shown in Figure 4.11 on a optically pumped sample seen by a Si CMOS camera.

The effective pump power is calculated by measuring the pump intensity and simulating how much of the incident pump light is effectively absorbed in the III-V nano-ridge. For the structures with trench width 100 nm, the absorption of the 532 nm pump light is calculated to be 65% (Table 4.2). Note that given the fact that the pump photon energy of 2.3 eV is higher than the bandgap of the InGaP passivation layer (1.90 eV), a considerable part of the pump light is absorbed in this layer, possibly leading to some pump loss due to surface recombination. Also, carriers generated inside the trench are likely to be susceptible to non-radiative recombination given the large defect density close to the GaAs/Si interface, leading to some extra pump loss. Therefore the effective pump absorption is expected to be less than 65%. Nevertheless, since these effects are hard to quantify, we take a conservative estimate and all pump powers for the 100 nm-trench nano-ridges are normalized with the estimated pump efficiency of 65%.

Figure 4.14 (a) shows the measured spectra of a DFB laser with trench width 100 nm and grating period 170 nm pumped at different powers. When the optical pump power is 17 mW (15.4 kW/cm^2, below threshold), a broad spectrum is observed, centered at 1026 nm with a full width at half maximum (FWHM) of 60 nm. As the pump power increases to 100 mW (90.8 kW/cm^2, $\sim 3 \times I_{th}$), a peak centered at 1028 nm appears in the spectrum. Finally, at a pump power of 215 mW (195.2 kW/cm^2) the lasing peak reaches more than 28 dB above the background,

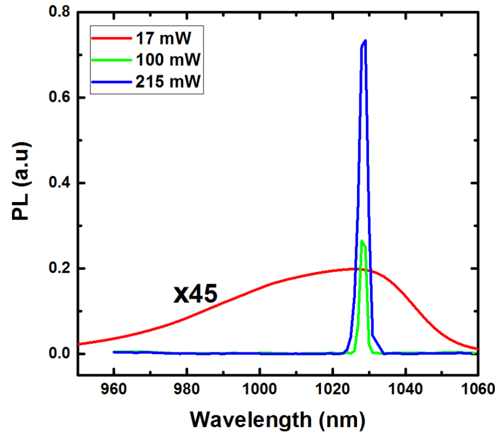

(a)

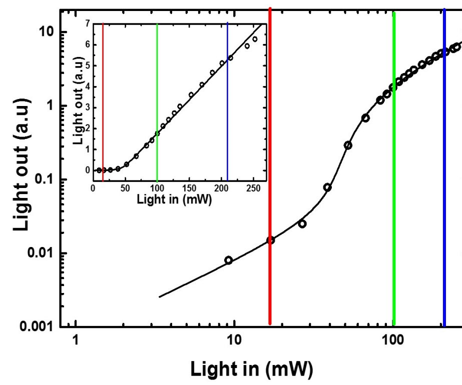

(b)

Figure 4.14: (a) Room-temperature spectra of a DFB laser under different pump powers (100 nm trench width, 170 nm grating period, and 340 nm second-order grating coupler period). (b) L-L curve on logarithmic and linear (inset) scale of the measured DFB nano-ridge laser. Black circles and solid line represent the experimental data and the rate equations fit, respectively.

demonstrating excellent single-mode laser performance. Note that the background PL remains clamped above the threshold. Figure 4.14 (b) plots the measured laser light-in light-out curve (L-L curve), both on a logarithm scale and on a linear scale (Figure 4.14 (b) insert). The distinct single lasing peak and the evident change in the slope of the L-L curve are reliable indicators of laser operation. The pump power at threshold is extracted to be $\sim 37mW(\sim 33.6\,\text{kW/cm}^2)$. The steady-

state thermal situation of the nano-ridge was estimated under this pump power in Appendix B.

For modeling the L-L curve, we used the rate equation model described in [22, 23]. As the duration of the pump pulse (7 ns) is significantly longer than the photoluminescence lifetime ($\sim$ 1 ns) of the nano-ridge as presented in Section 3.3, the pulsed pump can be treated static. The rate equations for the electron number n, and the lasing mode photon number s, can be written as [22, 23]:

$$\frac{dn}{dt} = p - \xi A_c sn - \frac{\xi n}{\tau_s} - \Gamma n - (1-\xi)An \tag{4.9}$$

$$\frac{ds}{dt} = \xi A_c sn - \gamma s + \beta \frac{\xi n}{\tau_s} \tag{4.10}$$

A_c is the cavity-dependent spontaneous emission rate, which is enhanced by a factor of F from free-space spontaneous emission rate A with $A_c = FA$. Normalize variables by

$$S = \xi F s, \;\; P = \xi \frac{F}{\gamma} p, \;\; N = \xi \frac{A_c n}{\gamma} \tag{4.11}$$

After elementary algebra work, the lasing photon intensity S as a function of the pump rate P is expressed by

$$S = \frac{1}{2}\left[U + \left(V^2 + \frac{4\xi(\beta-1)P}{A\tau_s} + \frac{4\xi(\xi-1)P}{A\tau_s}\right)^{1/2}\right] \tag{4.12}$$

where

$$U = P - 1 - \left(\frac{1}{A\tau_s} - 1\right)\xi \tag{4.13}$$

$$V = U + \frac{2\xi}{A\tau_s} \tag{4.14}$$

Thanks to the TRPL characterization conducted in Section 3.3, it is relatively easy to define a reasonable fitting range of $700\,ps < \tau_s < 2000\,ps$ for the PL lifetime. A denotes the free-space (without cavity) radiative emission rate such that $(1 - A\tau_s)$ expresses the non-radiative recombination ratio. Given the evidence in Section 3.3 proves that surface recombination and recombination in defective trenches do exist, we determine a fitting range of $0.5 < A\tau_s < 0.9$ for the radiative emission ratio. The fraction of the spontaneous emission lost from the open cavity $(1-\xi)$ can range between zero and unity $0 < (1-\xi) < 1$. β, the spontaneous emission factor is the fraction of the spontaneous emission coupled into the single lasing mode. It is defined as the reciprocal of the density of optical modes per unit volume per unit frequency [19]. For conventional macro-cavity lasers, β is the order of 10^{-5}, 10^{-4}. However, for micro-lasers, β can approach unity such that we take the range $10^{-4} < \beta < 1$.

By fitting the model (Equations 4.12 to 4.14) to the experimental data (black circles in Figure 4.14 (b)) under the above parameters' upper and lower boundaries, the photoluminescence lifetime $\tau_s = 819\,\text{ps}$, the free-space radiative emission ratio $A\tau_s = 0.65$, the fraction of the spontaneous emission lost from the open cavity $(1 - \xi) = 0.23$, the spontaneous emission factor $\beta = 0.008$. The fitted results shown in Figure 4.14 (b) with the solid black line are well-matched with the experimental results.

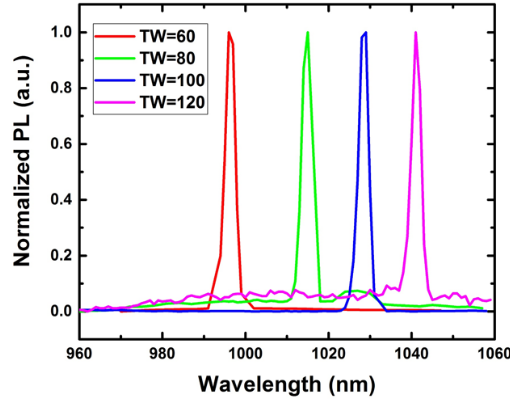

(a)

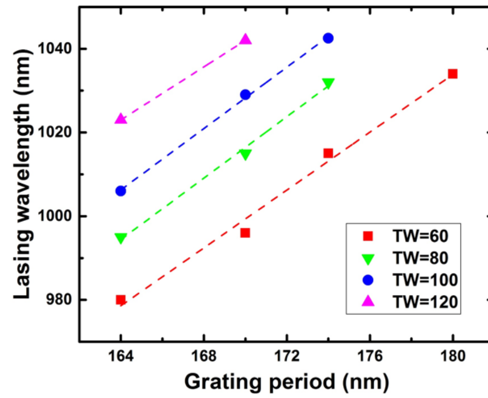

(b)

Figure 4.15: (a) Measured lasing spectra of DFB laser array with grating period $170\,\text{nm}$. *(b) Lasing wavelength versus grating period for trench size varying from* $60\,\text{nm}$ *to* $120\,\text{nm}$.

Wavelength division multiplexing (WDM), whereby different optical signals with slightly different wavelengths are combined in a single optical waveguide or fiber, is a commonly used approach to increase the capacity of communication links. An essential building block for such systems is an array of single-mode lasers with precisely controlled emission wavelength. To demonstrate the potential of further application of the presented laser, we defined DFB lasers with grating period varying from 164 nm to 180 nm for each of the four nano-ridge configurations considered. The grating duty cycle and etch depth was fixed at 25% and 110 nm respectively. The normalized spectra of four lasers with trench width 60 nm, 80 nm, 100 nm and 120 nm and fixed grating period of 170 nm are plotted in Figure 4.15 (a). Each of these devices operates as a single-mode DFB laser. In addition, a clear redshift of the lasing wavelength with increasing trench size is found. As explained above, the increasing trench width results in an increase in ridge volume and associated with that a higher effective refractive index of the TE-like ground mode (see Table 4.2). This illustrates the possibility to tune the DFB-laser emission wavelength already during the epitaxy process. Obviously, the lasing wavelength can also be controlled through the grating period. Figure 4.15 (b) summarizes the measured lasing wavelength for all different DFB laser configurations, measured at a pump power of 100 mW. One finds that the peak wavelength uniformly shifts with the grating period. The slope of this shift $\frac{\triangle\lambda}{\triangle\Lambda}$ is varying from 3.46 to 3.67 for the different trench sizes, very close to the calculated value $\frac{\triangle\lambda}{\triangle\Lambda} = 3.72$ for the 100 nm trench. The small discrepancy can be attributed to the uncertainty of the refractive index of the III-V ternary alloys in the nano-ridge. Some data for the larger ridges (trench width 80 nm, 100 nm and 120 nm) at longer grating period ($\geq$ 174 nm) is missing , as we did not find a lasing peak (expected beyond 1040 nm) for these structures (at pump power 100 mW). This can be explained by the decrease in optical gain for wavelengths above 1040 nm (see also Figure 3.5).

We also fabricated DFB cavities on nano-ridges with trench width from $150-500$ nm. Unfortunately, lasing was not observed under the same excitation intensity we applied to the lasing nano-ridges. The reasons are expected to be the reduced crystal quality related to sub-optimal ART for the wider trenches and/or high leakage loss towards the substrate.

4.4 Loss-coupled DFB laser

We presented optically pumped index-coupled DFB lasers in the previous section. The demonstration of single-mode lasing at room temperature proves the high quality of the proposed III-V on Si. Moreover, we demonstrate that the DFB laser emission wavelength can be precisely controlled not only by the grating design but also by the STI trench width and fine tuning the epitaxial process, providing more design and fabrication freedom towards optimizing devices for a given

application. However, it remains a question how to realize electrical excitation of the lasers. To further exploit the nano-ridges' potential of lasing and possibilities for electrical injection, we present partly-loss(gain)-coupled (PLC) DFB lasers in this section. The PLC DFB cavity is formed by metallic grating, which not only provides periodic modulation of the optical loss along the nano-ridge but also has the potential to serve as a pathway for electrical pumping in the future. We will show that by carefully selecting the duty cycle of the metallic grating, the optical loss that would be introduced by a continuous metal contact (> 74 /cm) could be decreased down to an acceptable value of 7 /cm. This design allows for a good trade-off between the coupling strength provided by the periodically modulated metallic layer and the cavity loss of the lasing mode.

The configuration of the nano-ridge DFB device with metallic gratings is illustrated in Figure 4.16. At the top of the nano-ridge, Au grating is deposited. The presence of Au with a complex refractive index of $n_{Au} = 0.242 - i6.704$ introduces changes both in the real and imaginary part of the effective refractive index of the TE-like ground mode $E_{TE}(x, y)$. Therefore, the cavity is partly index-coupled and partly loss-coupled, hence we call it a "PLC-DFB".

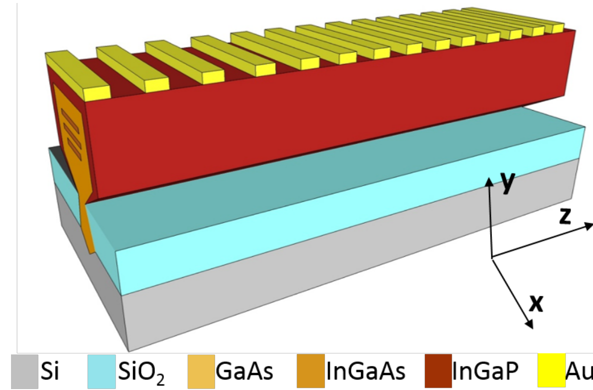

Figure 4.16: Schematic diagram of the nano-ridge DFB device with metallic gratings on top.

4.4.1 Cavity simulation

We have shown in Figure 4.8 (a) that for a standard DFB cavity, there are two symmetric resonant peaks, namely, the two first-order Bloch modes. The two Bloch modes resonate in the cavity in a stand-wave pattern with the same period but a half-period shift from each other [24], as shown in Figure 4.17 (a). In a pure index-coupled DFB cavity, high SMSR can be achieved by creating an extra phase shift inside the cavity (Figure 4.8 (b)) or applying reflection coatings at the

facet (Figure 4.8 (c)). A partly loss-coupled (PLC) cavity on the other hand has an inherent mode selection mechanism. The electrical field of the Bloch mode centered in the metal part "feels" more loss compared to the one centered in the dielectric part. The Bloch mode with less cavity loss will lase first. Simulation results (Figure 4.17(a), duty cycle 0.5) show that the confinement in Au of the low-loss Bloch mode $E_{BL}(x, y, z)$ is much lower than for the high-loss Bloch mode $E_{BH}(x, y, z)$, whose mode center is perfectly aligned with the Au part. Calculation show that the CF in Au of $E_{BL}(x, y, z)$ is indeed about ten times lower than that for $E_{BH}(x, y, z)$, which implies also the mode loss is 10 times smaller. The calculated results for different duty cycles are listed in Table 4.3. Consequently, $E_{BL}(x, y, z)$ having the lowest loss will win the competition and make the PLC-DFB single-mode without any need of $\lambda/4$ shift or facet coating.

The optical loss of mode $E_{BL}(x, y, z)$ can be further cut down by reducing the duty cycle $\frac{\Lambda_{Au}}{\Lambda}$ (Λ_{Au} the area of Au) of the metallic gratings, yet doing this the grating index and loss modulation is also weakened such that the coupling strength between forward and backward lasing modes in the DFB cavity is reduced. Therefore the duty cycle of the metallic gratings ought to be carefully designed to reach a good trade-off between the cavity loss of the lasing mode and the coupling strength provided by the periodically patterned metallic layer [25]. Hence calculation of the cavity loss and coupling strength (κL) versus the grating duty cycle is needed.

First, the period of the grating is simulated to be $\Lambda = 164$ nm with duty cycle 0.5 by the FDTD solver from Lumerical [21] to allow the grating bandgap to overlap with the nano-ridges gain spectrum around 1020 nm. With the grating period $\Lambda = 164$ nm, the metallic loss of the cavity mode $E_{BL}(x, y, z)$ can be calculated at the wavelength λ_{LB} of this mode by

$$\alpha_{BL} = \Gamma_{Au}(x, y, z) \cdot \alpha_{Au} \tag{4.15}$$

where $\Gamma_{Au}(x, y, z)$ is the 3D-confinement factor of the cavity mode in Au, α_{Au} the loss of Au at the wavelength 1020 nm $\alpha_{Au} = 8.18 \times 10^5$ cm^{-1}. Γ_{Au} is found from:

$$\Gamma_{Au}(x, y, z) = \frac{\int_0^{\Lambda_{Au}} \int_h^{h+\Delta h_{Au}} \int_{-w_{Au}/2}^{w_{Au}/2} |E_{BL}(x, y, z)|^2 dxdydz}{\iiint |E_{BL}(x, y, z)|^2 dxdydz} \tag{4.16}$$

where $E_{BL}(x, y, z)$ is the electrical field of the low-loss Bloch cavity mode within one period simulated using an FDTD solver with Bragg boundary conditions [21], W_{Au} is the width of the Au grating, i.e. the width of the nano-ridge. The calculated cavity mode loss α_{BL} as a function of duty cycle $\frac{\Lambda_{Au}}{\Lambda}$ is plotted in Figure 4.17 (b). As expected, α_{BL} increases with duty cycle and dramatically raises up when $\frac{\Lambda_{Au}}{\Lambda} > 0.5$, where metal starts to occupy the majority of the nano-ridge surface.

For a DFB cavity, the coupling strength κL is the product of the coupling coefficient κ and the length of the cavity L. In our case, L is always $300\,\mu$m,

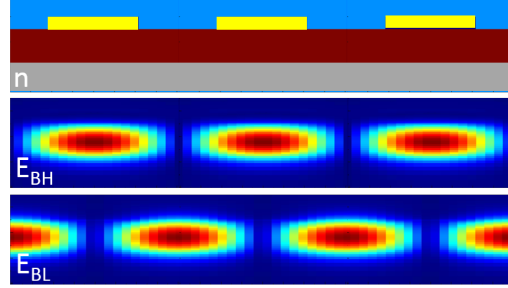

(a)

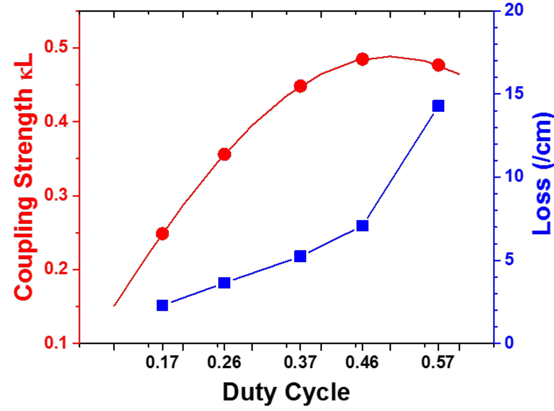

(b)

Figure 4.17: (a) The refractive index profile along the PLC-DFB and the field distribution of the two first-order Bloch modes along the PLC-DFB. One is high-loss E_{BH} while the other is low-loss E_{BL}. (b) The calculated coupling strength and loss of a metallic grating with length of 300 μm *as a function of grating duty cycle.*

restricted by the maximal optical pumping size. The loss coupling coefficient κ is a function of duty cycle $\frac{\Lambda_{Au}}{\Lambda}$ and the modulation depth $\Delta\varepsilon$,

$$\kappa = \frac{k_0^2}{2\beta}\frac{sin(\pi\frac{\Lambda_{Au}}{\Lambda})}{\pi}\Delta\varepsilon\Gamma_{Au}(x,y) \tag{4.17}$$

assuming a rectangular grating pattern [25, 26]. It should be noticed that $\Gamma_{Au}(x,y)$, different from the 3D-confinement factor of the cavity mode $\Gamma_{Au}(x,y,z)$, is the 2D-confinement of the transversal mode $E_{TE}(x,y)$ in the 40 nm thick Au layer. $k_0 = \frac{2\pi}{\lambda_0}$ is the free-space wave vector, $\beta = n_{eff}k_0$ the propagation constant of mode $E_{TE}(x,y)$, $\Delta\varepsilon = \varepsilon_{Au} - \varepsilon_{air} = (n_{Au} + ik_{Au})^2 - (n_{air} + ik_{air})^2 = 45.88 - i3.244$. Because the real part of ε is much greater than its imaginary part,

we ignore the imaginary part and let $\Delta\varepsilon \approx 45.88$ in calculation of κ and the laser threshold I_{th}. The calculated coupling strength κL as a function of duty cycle $\frac{\Lambda_{Au}}{\Lambda}$ is plotted in Figure 4.17(b). κL is a sinusoidal function of duty cycle, which first increases and then reaches a maximum when $\frac{\Lambda_{Au}}{\Lambda} = 0.5$ as expected. After $\frac{\Lambda_{Au}}{\Lambda} = 0.5$ the modulation is less efficient and κL starts to decrease again.

It is straightforward to speculate that the lowest laser threshold is held by a grating duty cycle no more than 0.5, as both the cavity loss and the coupling strength deteriorate for a duty cycle larger than 0.5. To calculate the optical threshold gain g_{th}, the calculated cavity loss α_{BL} and coupling coefficient κ and cavity length L can be plugged in the expression [27]:

$$\frac{|\kappa|^2}{(q+\Delta\beta)^2}e^{i2qL} = 1 \tag{4.18}$$

where

$$\Delta\beta = \kappa - i\frac{g_{th} - \alpha_{BL}}{2} \tag{4.19}$$

$$q = \sqrt{\Delta\beta^2 - |\kappa|^2} \tag{4.20}$$

These are applicable for a DFB laser without end facet reflection and with κ a real value. As already mentioned, the imaginary part of κ is ignored for simplicity. As for facet reflection, although the gratings continue beyond the pump region, it is considered negligible because outside the PLC cavity the light attenuation length is calculated to be $\sim 7\,\mu$m while the cavity length is $300\,\mu$m.

To move one step further after knowing the required modal gain at threshold g_{th} versus grating duty cycle, we can deduce the threshold pump intensity I_{th} of the PLC DFB lasers if $g_m(I)$ - the relations between modal gain g_m and pump intensity I is known. In Section 3.4, we have characterised the optical gain of the nano-ridge by the VSL method. To have an analytical expression of the net modal gain (g_m) vs. pump intensity (I), $g_m(I)$ can be well approximated by [28]

$$g_m = g_0 \cdot ln(I/I_0) \tag{4.21}$$

where the fitted parameters are $g_0 = 123.0\,\text{cm}^{-1}$, $I_0 = 8.7\,\text{kW/cm}^2$. The fitting is plotted in Figure 4.18 as a dashed red line with the black dots the experimental data originally shown in Figure 3.17.

So having calculated the cavity optical loss α_{BL} and the coupling strength κL, and having $g_m(I)$ experimentally obtained, the expected threshold I_{th} as a function of the grating duty cycle can be derived by substituting these parameters into Equation 4.18 to Equation 4.21. The result is depicted in Figure 4.22 (b), marked with triangular symbols. It is observed there is an optimal duty cycle at around 0.4 where the metal grating provides sufficiently strong coupling while only introducing a relative weak loss to the cavity mode, resulting in the lowest threshold intensity.

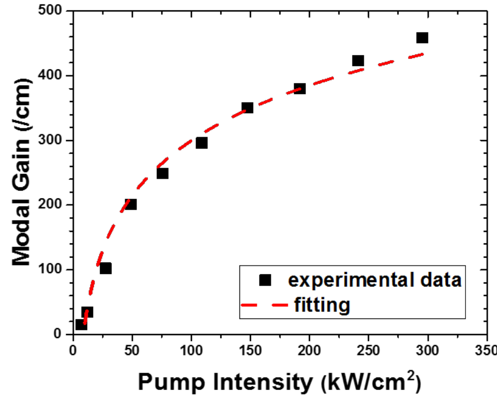

Figure 4.18: Modal gain of the InGaAs/GaAs nano-ridges at different pump intensity levels. The black squared dots are the experimental result already shown in Chapter 3, Figure 3.17 TW= $100\,nm$*, the red dashed line is a fit to this experimental data.*

4.4.2 Fabrication and Characterization

To verify the theoretical calculations experimentally, we have fabricated a series of PLC-DFB devices with the metallic grating duty cycle varied from 0.2 to 0.6 with an interval of 0.1 to cover the estimated optimal $\frac{\Lambda_{Au}}{\Lambda}$ value. The physical length of the gratings is 600 μm, however, the cavity length depends on the optical excitation window, which is $L = 300\,\mu$m In addition, 20 μm away from the DFB laser cavity, a 50-period second-order grating is defined to vertically couple light out for straightforward characterization of the devices on a standard $\mu - PL$ setup, similar as for the previously discussed index-coupled DFB laser. Following the epitaxy of the GaAs/InGaAs nano-ridges, only a single electron-beam lithography and lift-off step is required to deposit the 5 nm/40 nm Ti/Au metallic grating layer on top of the nano-ridges. The used electron-beam photoresist (AR-P 6200) is positive, which results in negative sidewalls (the opposite of optical lithography photoresists). It helps with the lift-off of the Au layer when the very thin electron-beam photoresist ($\sim$ 200 nm) makes the process challenging. Normally soaking the sample in acetone overnight could lift all $\sim$ 50 nm thick metal parts deposited on top of the resist.

Figure 4.19 (a)-(d) illustrates the top-view SEMs of the fabricated devices with the duty cycle $\frac{\Lambda_{Au}}{\Lambda}$ measured to be 0.17, 0.26, 0.37, 0.47 corresponding to 0.2-0.5 respectively as designed (0.6-duty-cycle device is not shown). The 0.02-0.03 reduction of duty cycle is attributed to overexposure .

The fabricated devices are characterized on a $\mu - PL$ setup with the Nd:YAG nanosecond pulsed laser to pump the devices from their top side. The setup is

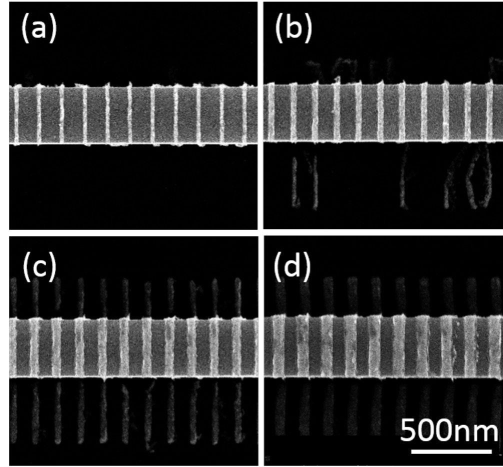

Figure 4.19: (a)-(d) The top-view SEM images of PLC DFB lasers with grating duty cycle 0.17, 0.26, 0.37, 0.46 respectively.

the same as the one used in gain and index-coupled DFB laser characterization in Section 3.4 and Section 4.3. A rectangular aperture is used to limit the pump spot to a size of $3\,\mu$m $\times 300\,\mu$m, to cover a single DFB device and exclude adjacent nano-ridges which have no gratings on top. The pump intensity is controlled by the combination of a polarizer and a rotating half-wave plate (HWP) added in the setup. The measured signal is the diffraction from the second-order-grating coupler, collected by a monochromator with a resolution of 2 nm. A chopper and a lock-in amplifier are used to improve the signal-to-noise ratio.

Figure 4.20 (a) shows the measured spectra of a PLC DFB device with metallic grating duty cycle of 0.37 pumped at different intensities. When the optical pump power is $9\,$kW/cm^2(just below threshold), a broad spectrum is observed, centered around $1030\,$nm with a full width at half maximum (FWHM) of $60\,$nm. As the pump power increases to $12\,$kW/cm^2, a peak at $1024\,$nm starts to appear in the spectrum. Continuous increase of the pump to $76\,$kW/cm^2($\sim 6 \times I_{th}$) makes the peak clearer. Finally, at a pump intensity of $417\,$kW/cm^2 the single peak becomes very distinct reaching around $15\,$dB above the background. It is believed that the measurement itself suppresses the peak to background ratio of the laser. On the one hand, the peak amplitude is weakened because the second-order grating coupler introduces massive absorption on the lasing wavelength. On the other hand, the background is elevated as the measured signal might also include the PL-signal of two to three as-grown nano-ridges given the fact that they are only $\sim 500\,$nm apart from the DFB device and the pump slit is $3\,\mu$m wide at least. Figure 4.20(b) plots the measured laser light-in light-out curve (L-L curve) over a wavelength range

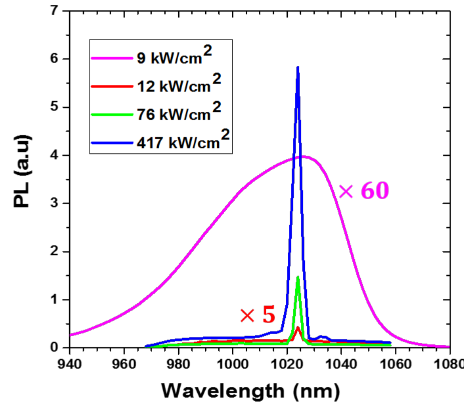

(a)

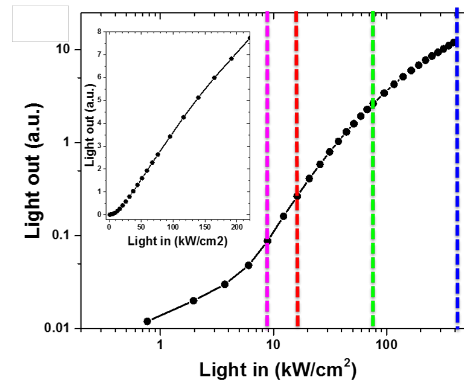

(b)

Figure 4.20: (a) Spectra of a PLC DFB laser with grating duty cycle 0.37 *under different pump intensities. (b) The Light-in Light-out curve of the same laser at its lasing peak* 1024 *nm in logarithm scale. Insert is the same data plotted in linear scale.*

of $\sim$ 5 nm centered at 1024 nm peak, both on a logarithm scale and on a linear scale (Figure 4.20 (b) insert). The distinct single lasing peak and the clear change in the slope of the L-L curve are strong indicators of single-mode laser operation. The threshold is derived to be $\sim 10\,\text{kW/cm}^2$, which is even slightly lower than the values obtained for nano-ridge lasers with etched, surface-damaging gratings from the same material [3].

In addition, all PLC DFB devices with duty cycle from 0.2-0.6 showed laser operation. Figure 4.21 displays the lasing spectra of the five devices under a pump

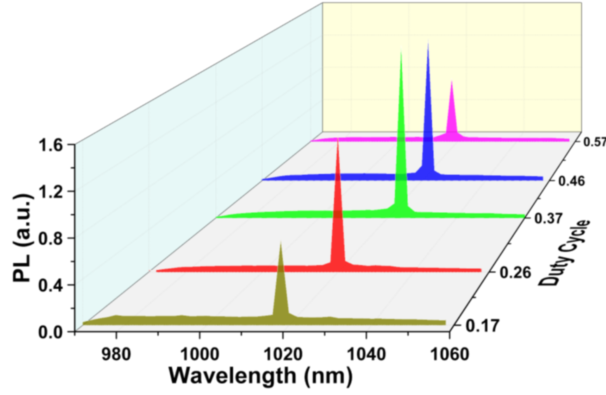

Figure 4.21: The spectra of PLC DFB lasers with grating duty cycle of 0.17, 0.26, 0.37, 0.46, 0.57 respectively, all under 417 kW/cm^2 excitation.

intensity of 417 kW/cm^2. The lasing wavelength vary slightly, being respectively 1018 nm, 1020 nm, 1024 nm, 1022 nm, 1018 nm for duty cycle 0.17, 0.26,0.37, 0.46, 0.57. Theoretically, the wavelength would remain almost constant for PLC DFB laser under the same grating period regardless of the different duty cycle as the real part of the cavity mode effective refractive index n_{eff_b} is hardly influenced. In reality, the discrepancy is reasonable given the small uncertainty Δn_{eff_b} brought by slight variations in the nano-ridge dimensions during the epitaxy process and the wavelength resolution of the measurement is 2 nm.

The light-in-light-out characterization of the five devices is shown in Figure 4.22 (a) where the dots are the experimental data. The dashed lines are the respective fittings using:

$$I_{out} = \eta_d \frac{hv_{out}}{hv_{in}}(I_{in} - I_{th}) \tag{4.22}$$

for the second linear part, where η_d is the differential quantum efficiency, v_{in} and v_{out} the frequency of the "input" pump and "output" lasing peak, I_{th} the threshold pump intensity, I_{in} and I_{out} the pump intensity and measured output signal intensity of the lasing peak. Due to the absorption of the pump in the metal, the pump efficiency η_{pump} decreases with duty cycle and is simulated to be 0.87, 0.84, 0.79, 0.73, 0.67 for duty cycle 0.17, 0.26, 0.37, 0.46, 0.57 respectively. The fitted experimental I_{th} of the lasers is then calibrated (denoted as I_{cal-th} with $I_{cal-th} = I_{th} \times \eta_{pump}$) with the pump efficiency to exclude the top-down optical pump loss. This is also more relevant for the case of electrical injection where metal absorption of the pump would no longer be relevant. The calibrated ex-

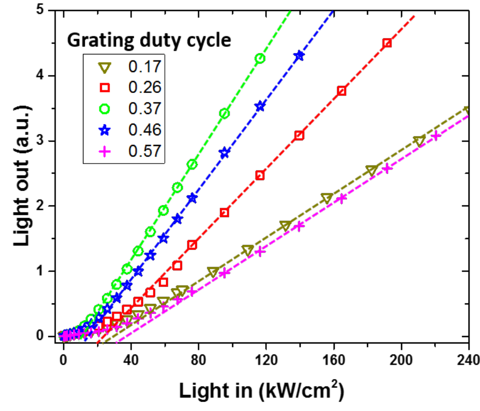

(a)

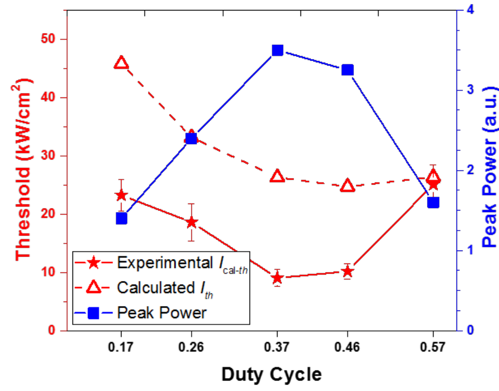

(b)

Figure 4.22: (a) The light-in light-out curves for PLC DFB lasers with grating duty cycle of 0.17, 0.26, 0.37, 0.46, 0.57 respectively. The dots are experimental data while the dashed lines are the fitting for their linear part with the intersections on horizontal axis the thresholds of lasers. (b) Experimental threshold with error bar, calculated threshold and the measured peak power of the lasers as a function of grating duty cycle.

perimental threshold I_{cal-th} with varying duty cycle is shown in Figure 4.22(b) together with the calculated I_{th} and the measured peak power.

It is noticed that, just as expected from the calculation, there is an optimal duty cycle 0.37 (0.4 as design) with the lowest threshold and the highest lasing peak power. Besides, the threshold and peak power show opposite tendency, which

means the high-loss and/or low-cavity-coupling-strength lasers tend to lose more photons from the cavity and require stronger excitation to lase. The calibrated experimental I_{cal-th} exhibits a minimal value between duty cycle 0.37 to 0.46 as expected from the calculated I_{th}, which holds the minimum at duty cycle 0.46. However, the value of I_{cal-th} is lower than the calculated I_{th}. The discrepancy can be attributed to several reasons: In the calculation of the threshold, the partly loss-coupled cavity is simplified to an index-coupled DFB without facet reflection. The exclusion of loss coupling part and facet reflection simplified the calculation but lifts up the calculated threshold value. Further, the experimental modal gain is extracted by assuming the pump intensity distribution is uniform. However, the profile of the pump beam is actually Guanssian-like in the VSL measurement, such that the optical gain could be underestimated.

The designed and fabricated duty cycle for each PLC DFB laser is listed in Table 4.3 together with the simulated loss from the Au grating $Loss_{Au}$, the calculated coupling strength κL and the threshold gain g_{th} derived from Equations 4.18-4.20.

Group	No.1	No.2	No.3	No.4	No.5
$\mathbf{\Lambda_{Au}/\Lambda(design)}$	0.2	0.3	0.4	0.5	0.6
$\mathbf{\Lambda_{Au}/\Lambda(fab)}$	0.17	0.26	0.37	0.46	0.57
$\mathbf{Loss_{Au}(cm^{-1})}$	2.4	3.8	5.2	6.8	14.5
$\kappa\mathbf{L}$	0.251	0.367	0.453	0.481	0.471
$\mathbf{g_{th}}$	176.0	99.7	41.9	41.4	76.8

Table 4.3: The properties of 5 PLC DFB lasers. $\Lambda_{Au}/\Lambda(design)$ is the designed duty cycle while $\Lambda_{Au}/\Lambda(fab)$ is the measurement from SEMs of fabricated devices. $Loss_{Au}$ is the calculated metallic loss for mode E_{BL}. κL, g_{th}, I_{th} are calculated coupling strength, optical modal gain at threshold and laser threshold respectively.

4.4.3 Alternative metallic grating

In the CMOS industry, the process of fabricating cylindrical metal "plugs" as vias between the metal layers is well-developed. After demonstrating the PLC nano-ridge laser, we have briefly tested one sample patterned with metallic disks to form a 1-D photonic crystal cavity. The disks were deposited at the top of the nano-ridges with the same period and cavity length as the metallic grating. Figure 4.23 shows the top-view SEM image of the fabricated device starting from a nano-ridge with a trench width of 100 nm. The diameter of the disk is measured to be $\sim$ 72 nm. Due to the misalignment of $\sim$ 40 nm during Ebeam lithography, the disks show a downwards shift from their designed center position. The characterization of the device is shown in Figure 4.24 with (a) the emission spectra at different pump intensity and (b) the light-in light-out (L-L) curve of the 1019 nm

peak. Although the output signal is low due to the weak coupling strength of the disks, considering the single peak in the spectrum and the slope change of the L-L curve, it seems the device is lasing. With this device, we demonstrate it is possible to utilize the cylindrical metallic vias—a mature process in CMOS fabs—for electrical injection to a DFB cavity and at the same time form a cavity.

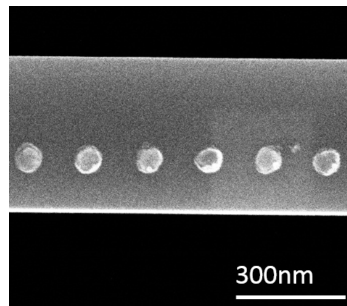

Figure 4.23: The top-view SEM image of the fabricated device starting from a nano-ridge with a trench width of 100 *nm.*

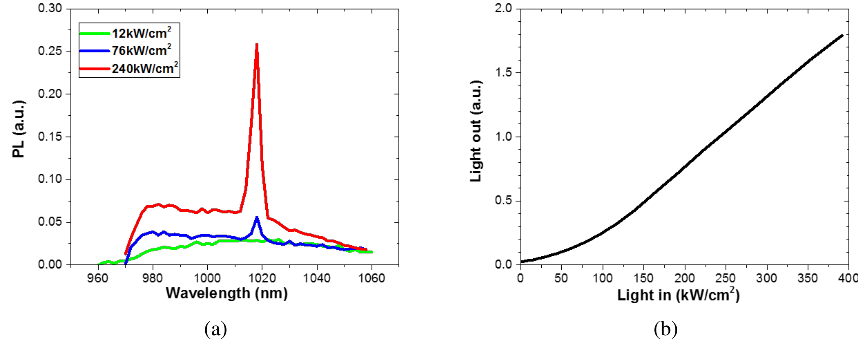

(a) (b)

Figure 4.24: Characterization of the device. (a) Emission spectra at different pump intensities and (b) the light-in light-out (L-L) curve of the 1019 *nm peak*

4.5 Conclusion

Starting from the novel GaAs nano-ridges, we designed and fabricated FP lasers, $\lambda/4$ shifted index-coupled DFB lasers and partly loss-coupled DFB lasers. FP lasers with the two simply etched facets show multiple-peak emission spectra. To develop a more advanced laser with single-mode lasing, index-coupled DFB cav-

ity with a $\lambda/4$ shift section was realized. Room-temperature measurement of the laser shows a SMSR better than $28\,$dB, a linewidth of $1.5\,$nm and a threshold of $33\,$kW/cm^2 for a $102\,\mu$m long DFB device. Moreover, we demonstrated that the DFB laser emission wavelength could be precisely controlled not only by the grating design but also by the STI trench width and finetuning the epitaxial process. To explore the electrical injection scheme for the nano-ridge laser, we presented PLC DFB cavity formed by metallic grating deposited at the top of nano-ridge. The design of the duty cycle well balances the cavity mode loss and the coupling strength both brought by the metallic grating. The PLC DFB nano-ridge lasers are proved to be single-mode lasing and exhibit a threshold of $\sim 10\,$kW/cm^2 at the optimized grating duty cycle 0.4.

The successful demonstration of different types of lasers proves the quality of the proposed III-V-on-Si epitaxial process and provides a first feasibility test for the future electrical injection. We also showed notable separation between the lasing mode and the defective Si/GaAs interface, which is thought a competitive feature against other planar nanowire approaches. E.g. the nanowire lasers presented by [29] and [30] exhibit a high overlap between the lasing mode and the defective regions, from where fatal dark line defects (DLD) are likely to appear and expand under high carrier density. More importantly, it opens up the road towards high-volume manufacturing of Si photonic ICs and holds the promise of co-integration of active and passive photonic devices based on a mature CMOS platform.

References

[1] WW Chow, AF Wright, and JS Nelson. *Theoretical study of room temperature optical gain in GaN strained quantum wells*. Applied physics letters, 68(3):296–298, 1996.

[2] Masakatsu Suzuki and Takeshi Uenoyama. *Optical gain and crystal symmetry in III–V nitride lasers*. Applied physics letters, 69(22):3378–3380, 1996.

[3] Yuting Shi, Zhechao Wang, Joris Van Campenhout, Marianna Pantouvaki, Weiming Guo, Bernardette Kunert, and Dries Van Thourhout. *Optical pumped InGaAs/GaAs nano-ridge laser epitaxially grown on a standard 300-mm Si wafer*. Optica, 4(12):1468–1473, 2017.

[4] Yuting Shi, Marina Baryshnikova, Marianna Pantouvaki, Joris Van Campenhout, Bernardette Kunert, and Dries Van Thourhout. *Partly Loss-Coupled DFB Nano-ridge Laser Monolithically Grown on a Standard 300-mm Si Wafer*. under preparation.

[5] James Clerk Maxwell. *The Scientific Papers of James Clerk Maxwell...*, volume 2. University Press, 1890.

[6] *Lumerical official website*. `https://www.lumerical.com`, 2008. Online; accessed 31-Dec-2018.

[7] A Perot and Charles Fabry. *On the application of interference phenomena to the solution of various problems of spectroscopy and metrology*. The Astrophysical Journal, 9:87, 1899.

[8] Hemant Kumar Raut, V Anand Ganesh, A Sreekumaran Nair, and Seeram Ramakrishna. *Anti-reflective coatings: A critical, in-depth review*. Energy & Environmental Science, 4(10):3779–3804, 2011.

[9] Konstantin V Popov, JA Dobrowolski, Alexander V Tikhonravov, and Brian T Sullivan. *Broadband high-reflection multilayer coatings at oblique angles of incidence*. Applied optics, 36(10):2139–2151, 1997.

[10] Minoru Yamada, Wataru Ishimori, Hironobu Sakaguchi, and Moustafa Ahmed. *Time-dependent measurement of the mode-competition phenomena among longitudinal modes in long-wavelength lasers*. IEEE journal of quantum electronics, 39(12):1548–1554, 2003.

[11] Yong Deok Jeong, Yong Hyub Won, Sang Ook Choi, and Jong Hyun Yoon. *Tunable single-mode Fabry-Perot laser diode using a built-in external cavity and its modulation characteristics*. Optics letters, 31(17):2586–2588, 2006.

[12] Hyun Deok Kim, Seung-Goo Kang, and Chang-Hee Le. *A low-cost WDM source with an ASE injected Fabry-Perot semiconductor laser*. IEEE Photonics Technology Letters, 12(8):1067–1069, 2000.

[13] Parry Moon. *A Table of Fresnel Reflections*. Journal of Mathematics and Physics, 19(1-4):1–33, 1940.

[14] Shyh Wang. *Principles of distributed feedback and distributed Bragg-reflector lasers*. IEEE Journal of Quantum Electronics, 10(4):413–427, 1974.

[15] Govind P Agrawal. *Fiber-optic communication systems*, volume 222. John Wiley & Sons, 2012.

[16] Amnon Yariv. *Coupled-mode theory for guided-wave optics*. IEEE Journal of Quantum Electronics, 9(9):919–933, 1973.

[17] H Kogelnik and CV Shank. *Stimulated emission in a periodic structure*. Applied Physics Letters, 18(4):152–154, 1971.

[18] H Kogelnik and CV Shank. *Coupled-wave theory of distributed feedback lasers*. Journal of applied physics, 43(5):2327–2335, 1972.

[19] Larry A Coldren, Scott W Corzine, and Milan L Mashanovitch. *Diode lasers and photonic integrated circuits*, volume 218. John Wiley & Sons, 2012.

[20] James EA Whiteaway, GHB Thompson, Andrew J Collar, and Christopher J Armistead. *The design assessment of lambda/4 phase-shifted DFB laser structures*. IEEE journal of quantum electronics, 25(6):1261–1279, 1989.

[21] *Bragg grating initial design with FDTD*. https://apps.lumerical.com/pic_passive_bragg_initial_design_with_fdtd.html. Accessed: 2010-09-30.

[22] H Yokoyama and SD Brorson. *Rate equation analysis of microcavity lasers*. Journal of Applied Physics, 66(10):4801–4805, 1989.

[23] KA Shore and M Ogura. *Threshold characteristics of microcavity semiconductor lasers*. Optical and quantum electronics, 24(2):S209–S213, 1992.

[24] Klaus David, Jens Buus, and Roel G Baets. *Basic analysis of AR-coated, partly gain-coupled DFB lasers: The standing wave effect*. IEEE journal of quantum electronics, 28(2):427–434, 1992.

[25] Klaus David, J Buus, G Morthier, and Roel Baets. *Coupling coefficients in gain-coupled DFB lasers: Inherent compromise between coupling strength and loss*. IEEE Photonics Technology Letters, 3(5):439–441, 1991.

[26] Geert Morthier and Patrick Vankwikelberge. *Handbook of distributed feedback laser diodes*. Artech House, 2013.

[27] Shun Lien Chuang. *Physics of photonic devices*, volume 80. John Wiley & Sons, 2012.

[28] Stephen R Chinn, Peter S Zory, and Axel R Reisinger. *A model for GRIN-SCH-SQW diode lasers*. IEEE journal of quantum electronics, 24(11):2191–2214, 1988.

[29] Yu Han, Wai Kit Ng, Ying Xue, Qiang Li, Kam Sing Wong, and Kei May Lau. *Telecom InP/InGaAs nanolaser array directly grown on (001) silicon-on-insulator*. Optics letters, 44(4):767–770, 2019.

[30] Bin Tian, Zhechao Wang, Marianna Pantouvaki, Philippe Absil, Joris Van Campenhout, Clement Merckling, and Dries Van Thourhout. *Room temperature O-band DFB laser array directly grown on (001) silicon*. Nano letters, 17(1):559–564, 2016.

5

1.3 μm-wavelength InGaAs nano-ridge light emitter

In Chapter 4 we have demonstrated FP lasers, single-mode index-coupled DFB lasers and single-mode partly loss-coupled DFB lasers post-fabricated from the InGaAs/GaAs nano-ridges introduced in Chapter 2 and Chapter 3. The successful demonstration of these lasers, on the one hand, proves the high crystal quality of the material. On the other hand, it opens the road towards future photonics applications.

To play an essential role in nowadays optical communication systems the extension of the current operating wavelength around $\sim 1\,\mu$m, which is determined by the composition, thickness and strain of the QWs, to $1.3\,\mu$m (O-band) or even to $1.5\,\mu$m (C-band) is inevitable. Because the $1.3\,\mu$m wavelength is preferred in data communication and extending the current emission wavelength to the closer O-band seems a more practical goal, we will explore the extension of the nano-ridges emission from $\sim 1\,\mu$m to $\sim 1.3\,\mu$m in this Chapter.

First, the possible approaches to extend the emission wavelength of the nano-ridges are discussed in Section 5.1. Among these options, we started with increasing the Indium content in the QWs to red-shift the bandgap. We first adopted a GaAs nano-ridge but quickly found a significant amount of defects in the QWs because of the increased lattice mismatch. This problem is then addressed by adding Indium to the nano-ridges themselves also. The as-grown InGaAs nano-ridges are inspected with SEM and TEM in Section 5.2 for a first quality check. The study of the optical properties of the new material, including the PL spectra, the

PL lifetime and optical gain, is described in Section 5.3. Finally, as a first attempt towards realising an O-band laser, the results obtained from index-coupled DFB cavities fabricated on the $\sim 1.3\,\mu$m-wavelength nano-ridges will be presented in Section 5.4.

5.1 Extension of wavelength to $1.3\,\mu\mathrm{m}$

Since the first fiber-optic communication system (OCS) was studied in the early 1970s [1, 2], the product (BL) of bit rate (B) and transmission length (L) has been continuously increased [3]. For every new generation of OCS, new techniques were introduced and boosted fast development. The first generation benefited from the discovery of GaAs semiconductor lasers [4], which operated at wavelengths of $0.8\,\mu$m. After that, it was realized the bit rate could increase by moving the wavelength to $1.3\,\mu$m, where the fiber loss is below 1 dB/km and more importantly, the minimal dispersion happens to exist [5, 6]. These advantages drove the introduction of InGaAsP semiconductor lasers [7] and detectors operating near $1.3\,\mu$m. Together with the adoption of single-mode fiber, low dispersion at $1.3\,\mu$m allowed to upgrade the bit rate up to 2 Gb/s [8] in the second generation OCS. Then the bottleneck shifted to the limited transmission length whereby the fiber losses play a significant role. The minimal Loss window of the silica fiber is located near $1.55\,\mu$m with a loss of ~ 0.2 dB/km , ~ 0.3 dB/km lower than ~ 0.5 dB/km at $1.3\,\mu$m. However, the O-band, centered at $1.31\,\mu$m, still remains a popular operating wavelength in short-distance dispersion sensitive applications. Therefore, the extension of the emission wavelength to $1.31\,\mu$m or even $1.55\,\mu$m is requested to broaden the application arena of the monolithic-grown nano-ridge.

In order to extend the emission wavelength, the bandgap energy of the nano-ridge active layers must be modified accordingly. For bulk III-V compound semiconductors, the bandgap can be engineered by controlling the composition of the material (see Figure 2.1). For example, through adjusting the fraction $x,\ y$ in $In_xGa_{1-x}As_yP_{1-y}$, the bandgap energy can be shifted over a wide range, including $E_g = 0.954$ eV ($\lambda = 1.31\,\mu$m) or $E_g = 0.800$ eV ($\lambda = 1.55\,\mu$m) while the lattice remains matched with that of InP. Besides through controlling the composition of the materials, it is possible to exploit quantum confinement in quantum structures as QWs and quantum dots (QDs) to modify the emmission wavelength. In these structures, additional boundary conditions (in one dimension for QWs and in three dimensions for QDs) have to be satisfied by the carrier wavefunctions, resulting in discretization of the electronic states. For an infinite square potential, the energy level of the nth state E_n^{∞} depends on the quantum size d (the thickness for QWs, the diameter for QDs) such that:

$$E_n^{\infty} = E_{gbulk} + \frac{\pi^2\hbar^2 n^2}{2m^{\star}d^2} \tag{5.1}$$

for QWs and

$$E^{\infty}_{n_x n_y n_z} = E_{gbulk} + \frac{\pi^2\hbar^2(n_x^2 + n_y^2 + n_z^2)}{2m^{\star}d^2} \quad (5.2)$$

for QDs. Thereby E_{gbulk} is the bandgap energy of the bulk material without quantum confinement, $\frac{1}{m^{\star}} = \frac{1}{m_h} + \frac{1}{m_e}$ and $n, n_x, n_y, n_z = 1, 2, 3...$ are the state levels along the confinement direction of the potential. From these expressions, we learn that changes in the dimension d of the quantum material have a direct impact on the band gap energy. The impact is larger for QDs than for QWs because the quantum confinement is present in all three dimensions. In addition, engineering the distribution of the size of the individual QDs in a larger ensemble enables modification of the gain spectrum, which can be adapted from narrow to broad (even with line-widths extending beyond 100 nm). Considering a real situation where the potential well is never infinite, the finite offset of the potential well impacts the energy levels and the equations above have to be adapted. This is taken into account in the calculation of the energy band diagram in Section 5.3.1.

5.2 InGaAs nano-ridge epitaxial growth

In a first attempt to increase the operating wavelength to $1.3\,\mu$m, the composition of the QWs was changed and the GaAs barriers forming the nano-ridge were kept. Because the effect on the shift of the emission wavelength by modifying the thickness of QWs is limited (several tens of nanometers), changing the composition of the QWs becomes the first choice. To red-shift the emission of bulk InGaAs to $1.3\,\mu$m (E_g is 0.954 eV at room temperature), the fraction of Indium x in $In_xGa_{1-x}As$ is derived to be $x \approx 0.35$ by using Vergard's law shown in Equation 2.3. The lattice constant of $In_{0.35}Ga_{0.65}As$ is then obtained accordingly: $a_{In_{0.35}Ga_{0.65}As} = 5.795$ Å. Considering the compressive strain on the QWs applied by the GaAs barrier with $a_{GaAs} = 5.653$ Å, a blue-shift in the band gap energy of the active region is expected, as already explained in Figure 3.2 [9]. In order to compensate for the blue-shift introduced by this strain, even more Indium should be added into the QWs. Therefore, the fraction of Indium is increased to $x = 0.45$ in the QWs with $a_{In_{0.45}Ga_{0.55}As} = 5.836$ Å (shown in Figure 5.1 marked by the grey dot), which rises the lattice mismatch from the original 1.4% (GaAs nano-ridge with $In_{0.2}Ga_{0.8}As$ QWs) to 3.2%.

Figure 5.2 shows a BF-STEM image of the 100 nm-trench GaAs nano-ridge with $2{\times}In_{0.45}Ga_{0.55}As$ QWs cut laterally along the nano-ridge. As aforementioned in the previous chapters, the defects originating from the Si/GaAs interface at the bottom are entirely trapped inside the trench once the aspect ratio is sufficient (as is the case here). However, new threading dislocations and planar defects start to appear from the QWs and penetrate the nano-ridge to its top surface. These new defects are introduced by the increased compressive strain originating from the

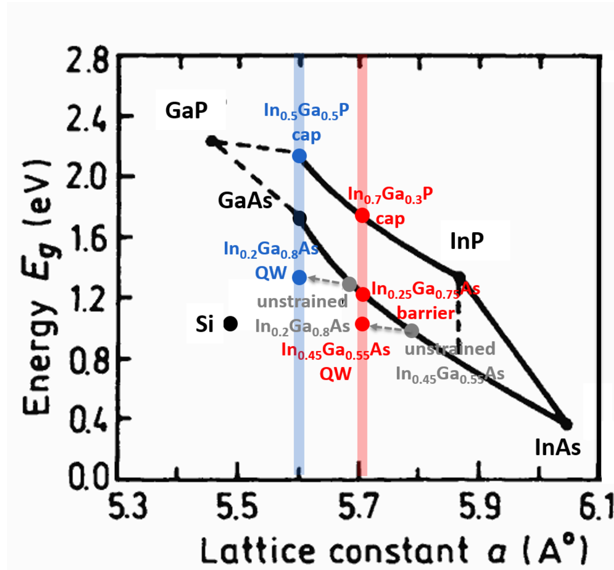

Figure 5.1: Bandgap vs. lattice constant of semiconductor compounds relevant for the nano-ridges. The materials of the 1 *µm GaAs nano-ridges and the* 1.3 *µm InGaAs nano-ridges are highlight in blue and red, respectively.*

lattice mismatch between the GaAs barrier and the $In_{0.45}Ga_{0.55}As$ QWs. Given the large lattice mismatch of 3.22%, the formation of defects is inevitable when the thickness of the QWs exceeds a particular thickness ($\sim$ 10 nm).

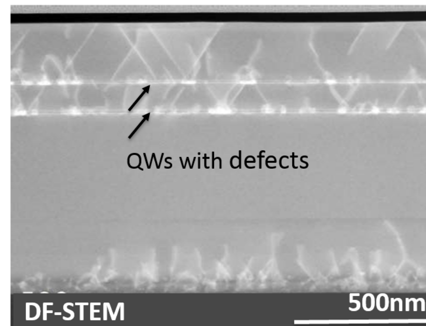

Figure 5.2: The bright-field (BF) STEM image of 100 *nm-trench GaAs nano-ridge with $In_{0.45}Ga_{0.55}As$ QWs. The sample is cut along nano-ridge where both the trench (bottom) and the QWs can be observed. Besides than the defects formed from the GaAs/Si interface, new defects formation in QWs appears.*

One alternative to extend the wavelength while maintaining a decent crystal

quality is reducing the lattice mismatch by adding Indium into the nano-ridge barrier. If we take $In_{0.25}Ga_{0.75}As$ as the barrier, the mismatch is reduced to 1.37%. Although the mismatch between the InGaAs barrier and Si substrate unavoidably rises, the ART technique introduced in Chapter 2 is still expected to be fully functional to suppress defects. To match the lattice constant of $In_{0.25}Ga_{0.75}As$, the composition of the passivation layer is then adjusted accordingly to $In_{0.72}Ga_{0.28}P$ from $In_{0.5}Ga_{0.5}P$ in the GaAs nano-ridge case. The barrier, QWs and cap layer of the $In_{0.25}Ga_{0.75}As$ nano-ridge embedded with $3\times In_{0.45}Ga_{0.55}As$ QWs (refer to InGaAs nano-ridge in the following text) are plotted in red in Figure 5.1. In comparison with the original GaAs nano-ridges (blue dots in Figure 5.1), the InGaAs nano-ridges have a smaller bandgap and larger lattice constant.

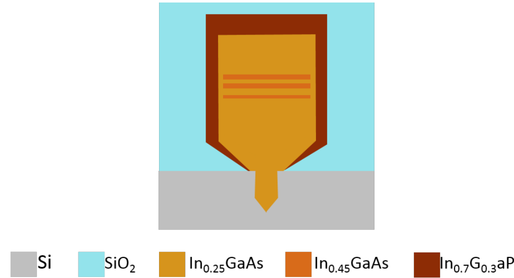

Figure 5.3: The schematic of the cross-section of the $In_{0.25}GaAs$ nano-ridge array with $In_{0.45}GaAs$ QWs on Si substrate. The nano-ridges are planarized with $\sim 1\,\mu m$ SiO_2 after the epitaxial growth.

The as-grown InGaAs nano-ridge is sketched in Figure 5.3. The epitaxy process, similar to the GaAs nano-ridge process described earlier and illustrated in Figure 2.9, starts from a 300 nm-thick oxide mask on Si. High-aspect-ratio V-shaped Si grooves with exposed $\{111\}_{Si}$ facets are achieved by a wet-etch step. The growth is carried out using MOVPE with the same precursors as for the GaAs nano-ridges but with more Indium pumped into the chamber. Figure 5.4 shows the SEM image of a cleaved 100 nm-trench $In_{0.25}Ga_{0.75}As$ nano-ridge array, planarized with $\sim 1\,\mu m$ thick SiO_2 after the growth. The Si substrate, nano-ridges and SiO_2 planarization can be observed but QWs and passivation layer are invisible. The dimensions measured from the SEMs for nano-ridges with different trenches are listed in Table 5.1. Thus far statistically relevant data from TEM or ECCI on the defect density for this material is currently not yet available. Nevertheless, in the next sections, the optical properties of these InGaAs nano-ridges are characterized to get an idea off their quality and potential performance.

d (nm)	**60**	**80**	**100**	**300**	**500**
a (nm)	365	497	541	710	1126
b (nm)	699	700	720	944	946

Table 5.1: InGaAs nano-ridges parameters noted in Figure 5.4. d: trench width; a: ridge width; b: ridge height.

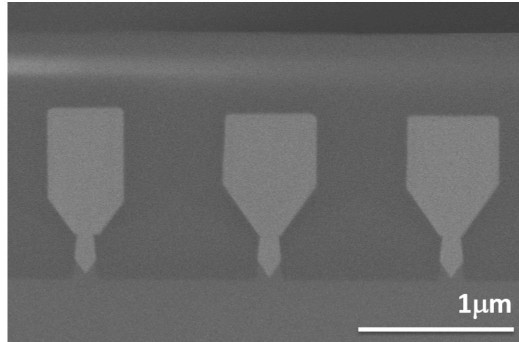

Figure 5.4: The SEM image of cleaved 100 nm-trench $In_{0.25}GaAs$ nano-ridge array with $In_{0.45}GaAs$ QWs. The nano-ridges are planarized with $\sim 1\ \mu m$ SiO_2.

5.3 Optical characterization

5.3.1 Energy band diagram

Before presenting the optical characterization of the $In_{0.25}Ga_{0.75}As$ nano-ridge, we first calculate its band diagram to have an understanding of the emission spectrum. The calculated result of the nano-ridge at room temperature (300K) is shown in Figure 5.5. Only one QW is plotted in the image instead of 3 QWs in the real situation for simplification . The solid lines present the band edge of both conduction band and valence band, while the dashed lines are the energy levels calculated for the 10 nm thick $In_{0.45}Ga_{0.55}As$ QWs in a finite-potential well. As we already know from Section 3.1.2 that the electron-heavy-hole (HH) transitions will dominate for the compressively-strained QW, only the energy levels for the heavy holes are plotted. Even though the second-quantized-level transition E_{2-2HH} exists theoretically, it is also neglected as the first-quantized-level transition dominates at low pumping power. Compared with the energy band diagram of the GaAs nano-ridge shown in Figure 3.1, we observe a clear reduction in bandgap energy due to the high Indium content. The calculated well-barrier offset is 0.168 eV for the conduction band and 0.046 eV for the valence band.

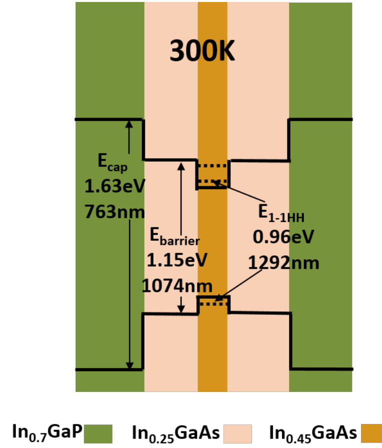

Figure 5.5: The calculated energy band diagram of the $In_{0.25}$GaAs nano-ridge at temperature 300 K. Only one QW is plotted in the image instead of three QWs in the real situation.

5.3.2 Photoluminescence characterization

Next, the emission spectrum of the $In_{0.25}Ga_{0.75}As$ nano-ridge is characterised through a PL measurement. The setup used is the same one as used for GaAs nano-ridge (shown in Figure 3.4). With a 532 nm ($hv_{ex} = 2.33$ eV) CW excitation, carriers in QWs, barrier and even the passivation layer are excited. The PL spectra at a pump intensity of 411W/cm^2 are shown in Figure 5.6. They show that the majority of the excited carriers diffuse to the low-energy-gap QWs and combine there. The PL peaks for nano-ridges with trench width from 60 nm to 120 nm are centered from 1324 nm to 1376 nm, approaching the transition energy calculated in the previous section. The red-shift of the peak position with the increase of trench width is attributed to a change in Indium concentration or QW thickness. Both effects are likely to take place because the epitaxy is sensitive to the local growth conditions.

Figure 5.7 shows the PL of the nano-ridges with 100 nm-wide trench at pump intensity varied from 6 kW/cm^2 to 127 kW/cm^2. The 532 nm CW pump with a maximum intensity of ~ 1 kW/cm^2 is replaced by a 532 nm 7 ns pulsed laser in this measurement to raise the maximum achievable pump intensity. The step-like profile of the spectra at low pump intensity is because the weak PL signal under nanosecond-pulse excitation is approaching the intensity resolution of the setup. At a pump intensity lower than 19 kW/cm^2, the most pronounced PL peak is at 1.35 μm, and attributed to emission from the QWs. However, under more intensive excitation, the $In_{0.25}Ga_{0.75}As$ barrier emission around 1.1 μm starts to take over. This behavior, not observed for the PL from the GaAs nano-ridge shown in Section 3.2, might be an indication of a lower crystal quality of the InGaAs

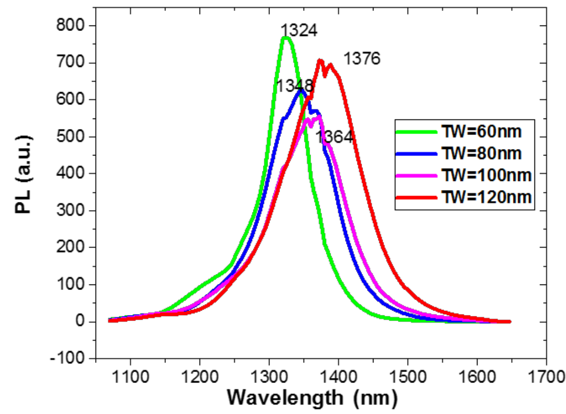

Figure 5.6: PL spectra of $In_{0.25}Ga_{0.75}As$ nano-ridges with trench width 60 nm, 80 nm, 100 nm and 120 nm, respectively under 411 W/cm^2 532 nm optical pumping. The peaks of the PL red-shift to $\sim 1.3\,\mu m$.

nano-ridges.

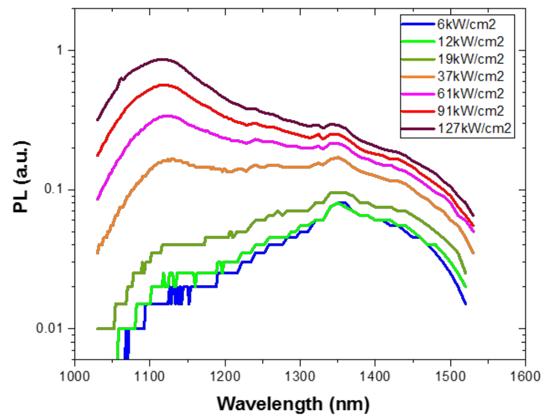

Figure 5.7: The PL spectra of InGaAs nano-ridges with trench width 100 nm, excited by a 532 nm pulsed laser at different pump intensity from 6 kW/cm^2 to 127 kW/cm^2.

5.3.3 Time-resolved PL

In this section, we carried out TRPL experiments to extract the PL lifetime of the nano-ridges in order to investigate the optical properties of the InGaAs nano-ridge

further. The experimental setup is the same as that for GaAs nano-ridges described in Section 3.3, Figure 3.7. The source has a wavelength of $800\,\text{nm}$ ($1.55\,\text{eV}$), whose photon energy is higher than the bandgap energy of the $In_{0.25}Ga_{0.75}As$ barrier ($1.15\,\text{eV}$) and QWs E_{1-1HH} ($0.96\,\text{eV}$) but lower than that of $In_{0.72}Ga_{0.28}P$ passivation layer. Therefore, carriers in both InGaAs barrier and QWs are excited by the $\sim 1\,\text{ps}$ pump pulse and the respective PL lifetimes could be extracted from the decay of the transient PL signals, as described in Section 3.3. The $500\,\mu\text{W}$ excitation is estimated to deliver $\sim 42\,\text{kW/cm}^2$ intensity on the sample.

Figure 5.8 (a) shows the time-resolved photo-luminescence spectrum (vertical axis) as a function of time (horizontal axis) for a 100nm-trench InGaAs nano-ridge. The PL peak is around $1100\,\text{nm}$, and attributed to the emission from the $In_{0.25}Ga_{0.75}As$ barrier according to the calculation of its bandgap in Figure 5.5. Unfortunately, no apparent emission from the QWs is observed in the TRPL characterization under the high intensity picosecond pump power. Through fitting the TRPL signal integrated over the wavelength range $1000-1200\,\text{nm}$ with a one-term exponential model for the decay of the barrier:

$$I_{barr.} = A \cdot e^{\frac{-(t-t_0)}{\tau_{barr.}}} \tag{5.3}$$

the PL lifetime $\tau_{barr.}$ can be extracted. The integrated spectrum is shown in Figure 5.8 (b) with the blue line the experimental data and the red crosses the fitted results. A much shorter lifetime of $\tau_{barr.} = 191\,\text{ps}$ for the barrier of the InGaAs nano-ridge is found compared to the GaAs nano-ridge with a typical $\tau_{barr.} \approx 400\,\text{ps}$ for the $100\,\text{nm}$-trench configuration. Moreover, the PL lifetime for the QWs in the InGaAs nano-ridge is believed to be nearly zero as the corresponding signal intensity is at the noise level.

We could draw a primary conclusion so far that the PL lifetime of the InGaAs nano-ridge is probably inferior to that of the previous GaAs nano-ridges. The faster non-radiative recombination rate could indicate the deficient crystal quality. The reasons are still unclear however. One conjecture is that besides the TDs, which are trapped efficiently by ART, other types of defects such as planar defects nucleated from the III-V/Si interface due to the increased lattice mismatch. These defects are not entirely trapped by ART and can penetrate through the nano-ridges. Additional characterisation is required to confirm this.

5.3.4 Optical gain characterization

After obtaining the PL of the InGaAs nano-ridge in the previous sections, we are going to get a more comprehensive understanding of the material by characterizing its modal gain g_m. The optical gain is characterized using the VSL method on the same setup shown before in Figure 3.7. The sample is pumped with the $532\,\text{nm}$ pulsed laser from the top surface. A variable rectangular slit is inserted in the setup

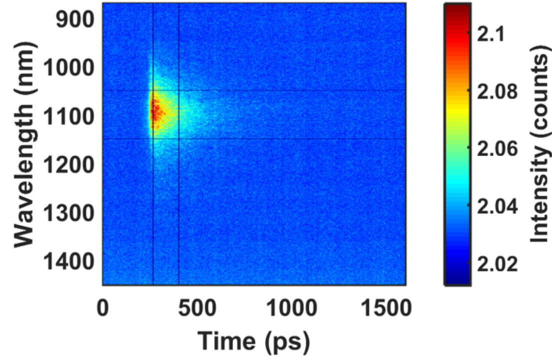

(a)

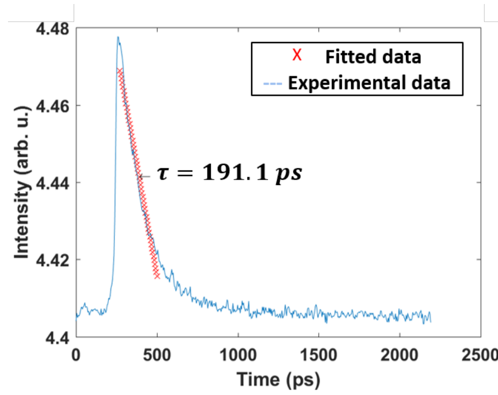

(b)

Figure 5.8: (a) The experimental TRPL result of 100 *nm-trench* $In_{0.25}$*GaAs nano-ridges as a function of wavelength and time. (b) Nano-ridges QW PL integrated over wavelength* 1050 *nm to* 1150 *nm as a function of time. The red crosses indicate the fitted data.*

to control the length of the pumped region from 10 to 200 μm. The output signal at the cleaved sample facet is first coupled to fiber and then collected by a power meter at different pump lengths and different pump intensities.

The approach to extract the modal gain has already been described in Section 3.4. The results for the InGaAs nano-ridges with 80 nm, 100 nm and 120 nm trenches are shown in Figure 5.9. Again we see that nano-ridges with narrower trenches possess a higher optical gain. We attribute this to the more efficient ART for the narrower trenches and it is consistent with what we observed for the GaAs nano-ridges shown in Figure 3.17. However, one difference of Figure 5.9 from Figure 3.17 is that the modal gain saturates at a relatively low pump intensity of $\sim$ 50 kW/cm^2. There it reaches a plateau until a second increase in gain around

$\sim$ 350 kW/cm^2. A possible explanation is that the increase in modal gain below 50 kW/cm^2 pump is the QW emission and the following plateau is likely due to the saturation of the QW gain. The second raise above 300 kW/cm^2 pump might be the emission from the barrier or from higher quantized QW transitions. Inspection of the ASE spectra under different pump intensity could clarify this further. This will be further discussed in the following section. By comparing with the optical gain of the GaAs nano-ridge shown in Figure 3.17, we found that both the highest achievable modal gain and the modal gain at low pump intensities (50 kW/cm^2) of the InGaAs nano-ridge are weaker.

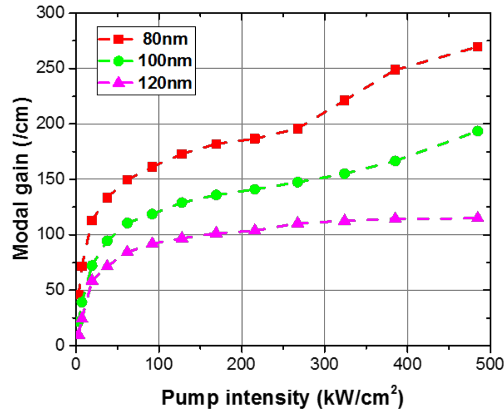

Figure 5.9: The extracted optical modal gain versus pump intensity. The data are from $In_{0.25}GaAs$ nano-ridges with 80 nm, 100 nm and 120 nm trench width.

Although the crystal quality of the InGaAs nano-ridge seems to be, at this moment, not as excellent as for the GaAs nano-ridge, we believe further optimization of the growth conditions could improve it. More inspections via SEM and TEM can also be helpful to figure out the problems and solutions to monolithically grow 1.3 μm-wavelength nano-ridges with higher quality.

5.4 ASE in DFB cavity

In the previous section, we have conducted PL, TRPL and optical gain measurements to get an initial impression of the quality of the newly developed InGaAs nano-ridges for 1.3 μm-wavelength emission. From the first PL characterization, we confirm that the emission spectrum of the nano-ridges can be extended to 1.3 μm. Although the results of TRPL and optical gain seem to indicate a reduced crystal quality, we still want to investigate if the InGaAs nano-ridge can lase in the

O-band. Therefore, given the successful experiments with the 1 μm-wavelength GaAs DFB laser in Section 4.3, we designed and fabricated also an index-coupled DFB cavity based on the InGaAs nano-ridges. The results are described in this section.

5.4.1 Bragg grating simulation

Before working on the design of the DFB cavity, the eigenmodes of the nano-ridge waveguides are calculated at 1.31 μm wavelength. Figure 5.10 shows the first three optical modes of the nano-ridge with 100 nm-wide trench. Other higher-order modes are not taken into consideration as they are not confined in the nano-ridge. The first mode is the TM-like ground mode with $n_{neff} = 3.1917$, $\Gamma_{QW} = 8.23\%$ and the second is the TE-like ground mode with $n_{neff} = 3.147$, $\Gamma_{QW} = 9.45\%$. The third mode is a high-order TEM-like mode. The TM-like mode is located closer to Si substrate compared with the TE-like mode and hence has a high leakage loss towards the Si layer, similar as for the GaAs nano-ridge mentioned in Section 4.1. Having the highest Γ_{QW} and the lowest α_{leak} make the TE ground mode the promising candidate mode for lasing.

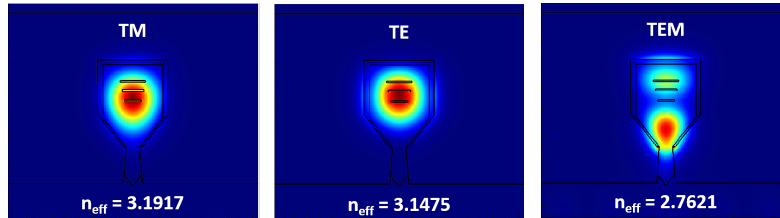

Figure 5.10: The first three optical modes of the InGaAs nano-ridge with trench width 100 nm. The polarization and effective refractive index of the modes are labelled in the images.

The $\lambda/4$ shifted DFB cavity is implemented by etching gratings in the top of the InGaAs nano-ridge. The calculation of the grating stopband for the TE ground modes versus the grating period by an FDTD solver is shown in Figure 5.11. To have the grating stopband overlap with the PL spectra (centered around 1350 nm), the period of the grating should be 218 nm, according to Figure 5.11.

The configuration of the $\lambda/4$ shifted index-coupled DFB device is similar with the 1 μm-wavelength DFB GaAs nano-ridge laser described in Section 4.3. Gratings with 300 periods are etched at each side of the $\lambda/4$ shift at the top of the nano-ridges with trench width 80 nm, 100 nm, 120 nm and 150 nm respectively. Besides, 20 μm away from the first order grating forming the laser cavity, a 50 period 2nd order grating was defined to vertically couple out the laser light and allow characterization of the devices in a standard μ -PL setup. The period is varied from

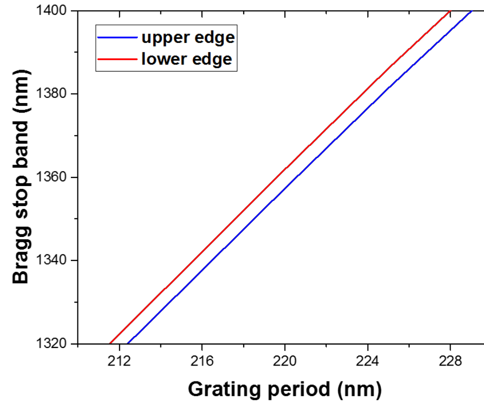

Figure 5.11: The simulated Bragg stopband of etched gratings at the top of 100 *nm-trench InGaAs nano-ridge with depth* 100 *nm as a function of grating period.*

212 nm to 232 nm with an interval of 4 nm to cover a broad wavelength range.

5.4.2 Fabrication and Characterization

Although the InGaAs nano-ridge array exhibits considerable surface topography, similar as was the case for the GaAs nano-ridge array, we realized that the electron-beam lithography (EBL) process can be carried out without much fabrication issues, even without planarization. Therefore different from Section 4.3, where BCB is applied to planarize the sample, we directly patterned the gratings using EBL after the growth of the nano-ridges. The EBL resist AR-P 6200 is then directly used as the mask for the grating etching with a $Cl_2/CH_4/Ar$ gas recipe in an inductive-coupled plasma (ICP) chamber. The fabricated devices with a period of 228 nm and an etch depth of 120 nm are shown in Figure 5.12. On the left is the tilted SEM image of a nano-ridge array (from bottom to top: trench width 80 nm, 100 nm) and on the right is the zoom-in image on the phase shift region of the 100 nm nano-ridge.

The devices were characterized on the same $\mu - PL$ setup used for the PL measurement, using the Nd:YAG nanosecond pulsed laser (7 ns pulse width, 938 Hz repetition rate, 532 nm wavelength) as the pump source. Similar to the measurement of the DFB GaAs nano-ridge lasers, a rectangular aperture is inserted in the setup during measurement to limit the pump spot to a size of $5\,\mu m \times 200\,\mu m$, covering a single DFB device.

Figure 5.13 (a) shows the measured spectra of a DFB device with trench width 100 nm and grating period 228 nm pumped at different pump intensities. When the

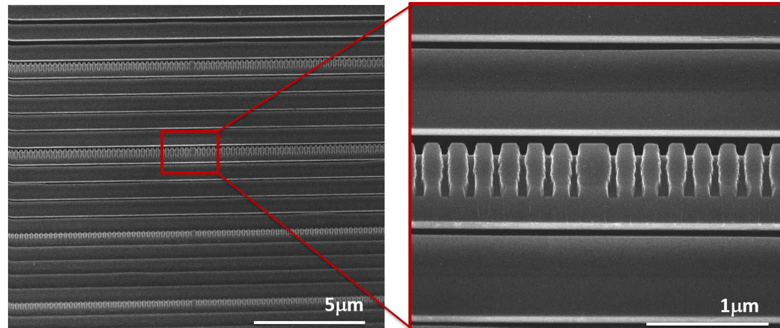

Figure 5.12: Tilted SEMs of a DFB laser array with $\lambda/4$ phase shift. Zoomed-in: the $\lambda/4$ phase shift section of a DFB device with trench width 100 nm.

optical pump power is 37 kW/cm^2, a quite broad spectrum is observed, centered at $\sim$ 1400 nm with a full width at half maximum (FWHM) of $\sim$ 300 nm. As the pump power increases to 91 kW/cm^2, a peak centered at 1330 nm starts to raise in the spectrum. Nevertheless, from a pump intensity of 168 kW/cm^2 and afterward, another peak at 1220 nm is growing with increased pump intensity. Additionally, we notice a substantial raise of the ground level of the signal, with the intensity growing faster at $\sim$ 1160 nm than at 1400 nm. Figure 5.13 (b) plots the measured laser light-in light-out curve (L-L curve) at wavelength 1330 nm, on a linear scale. A turning point of the slope is observed around 50 kW/cm^2, however the output saturates quickly at $\sim$ 270 kW/cm^2.

The emission peak at 1330 nm is expected to be the cavity mode as it is inside the Bragg grating stopband for the TE-like ground mode. We attribute the dramatic raise around 1160 nm to the emission of the InGaAs barrier of the nano-ridge. This matches what we observed in Section 5.3.2 and 5.3.3, namely that the QW emission dominates at a low pump intensity (see Figure 5.6) and then the barrier emission takes over at a high pump intensity (see Figure 5.8). The saturation of the peak at 1330 nm in Figure 5.13 (b) can be explained by the saturation of the QWs' emission. The reason for the appearance of the peak at 1220 nm is unclear. It is likely to be another resonant mode excited at high pump intensity. However, whether it is a higher-order transversal mode or a cavity mode due to a new cavity, e.g., an FP cavity formed by random defects, is unknown yet.

Due to the quite strong ASE background of the spectra, the unexpected peak at 1220 nm, the fast saturation of the DFB cavity peak, we do not consider the DFB InGaAs nano-ridge device a laser. We tried adjusting the period to shift the grating stopband to 1400 nm where the QW emits under $\sim$ 37 kW/cm^2 pump light. But the characterization of such a device also did not exhibit clear lasing.

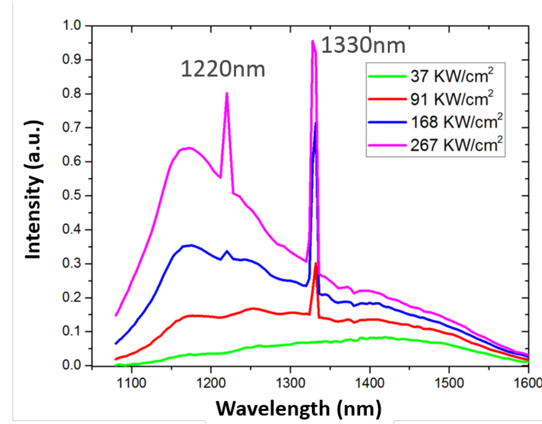

(a)

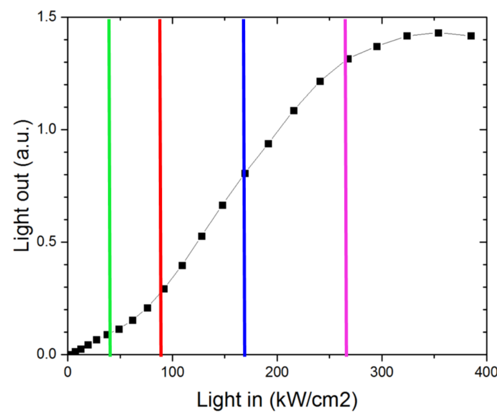

(b)

Figure 5.13: The characterization of the DFB device. (a) The ASE spectra of the DFB device with period 232 *nm at different optical pump intensities. (b) The light-in light-out curve of the device measured at the peak* 1330 *nm.*

5.5 Conclusion

In this Chapter, we presented the first trial to extend the emission wavelength of the nano-ridges from $1\,\mu$m to $1.3\,\mu$m, a wavelength relevant for data communication. The heterostructure consists of a $In_{0.25}Ga_{0.75}As$ nano-ridge barrier, $In_{0.45}Ga_{0.55}As$ QWs and $In_{0.72}Ga_{0.28}P$ passivation layer. The PL characterization of the InGaAs nano-ridges exhibits broad spectra from the QWs' emission centered around 1350 nm at low pump intensity. Nevertheless, only emission from the

InGaAs barrier was observed at a high pump intensity in the TRPL measurement. The extracted PL lifetime of the QWs is nearly zero. As for the InGaAs barrier, it is 191 ps, also shorter than that for the GaAs nano-ridge. The modal gain was measured to be 200 /cm at 300 kW/cm^2, lower than that for GaAs nano-ridge as well. Despite the inferior optical properties, $\lambda/4$-shifted index-coupled DFB cavities were designed and fabricated. The characterization of such devices shows a single peak at 1330 nm at a low pump intensity, but an undesired peak at 1220 nm starts to appear when the pump power increases.

Although the TRPL measurement, lower optical gain and the appearance of the unexpected lasing peak in the laser experiment point towards lower crystal quality of the InGaAs nano-ridge, the extension of the PL emission to 1.3 μm at limited optical pump region is achieved for the first time. The characterization of the nano-ridges proves the increase of the Indium content indeed redshifts the emission wavelength, but also leaves open questions with respect to the crystal quality. Further investigations and improvements on the InGaAs nano-ridge are therefore necessary. For instance, through TEM/ECCI, the locations and types of defects could be studied visually and quantitatively. The optical properties extracted experimentally through TRPL and gain measurement also provide direct feedback guidance to the epitaxial growth. Besides the QW-configuration, growing QDs as the active region are an alternative to develop O-band nano-ridge devices, but where not the subject of this thesis.

References

[1] SD Personick. *Baseband linearity and equalization in fiber optic digital communication systems*. The Bell System Technical Journal, 52(7):1175–1194, 1973.

[2] Stewart D Personick. *Receiver design for digital fiber optic communication systems, I*. Bell system technical journal, 52(6):843–874, 1973.

[3] Govind P Agrawal. *Fiber-optic communication systems*, volume 222. John Wiley & Sons, 2012.

[4] I Hayashi, MB Panish, PW Foy, and S Sumski. *Junction lasers which operate continuously at room temperature*. Applied Physics Letters, 17(3):109–111, 1970.

[5] D Marcuse. *Pulse distortion in single-mode fibers*. Applied Optics, 19(10):1653–1660, 1980.

[6] D Gloge, A Albanese, CA Burrus, EL Chinnock, JA Copeland, AG Dentai, TP Lee, Tingye Li, and K Ogawa. *High-Speed Digital Lightwave Communication Using LEDs and PIN Photodiodes at 1.3 μm*. Bell System Technical Journal, 59(8):1365–1382, 1980.

[7] Junichi Yamada, Yasuji Murakami, Junichi Sakai, and Tatsuya Kimura. *Characteristics of a hemispherical microlens for coupling between a semiconductor laser and single-mode fiber*. IEEE Journal of Quantum Electronics, 16(10):1067–1072, 1980.

[8] JI Yamada, S Machida, and T Kimura. *2 Gbit/s optical transmission experiments at 1.3 μm with 44 km single-mode fibre*. Electronics Letters, 17(13):479–480, 1981.

[9] Larry A Coldren, Scott W Corzine, and Milan L Mashanovitch. *Diode lasers and photonic integrated circuits*, volume 218. John Wiley & Sons, 2012.

6

Proposals for coupling between nano-ridge and waveguide

Following our roadmap towards realizing a practical device starting from the GaAs/InGaAs nano-ridge, we have successfully demonstrated single-mode lasing in Chapter 4 and also provided a first step towards electrical injection with the metal grating devices. However, an efficient scheme for interfacing these lasers with standard silicon photonics devices has not been presented yet.

In this Chapter, we present a novel design of an adiabatic coupler for interfacing the III-V nano-ridge grown on SOI with other silicon photonics components. In Section 6.1 we explain that the application of the coupler is not limited to our particular case but is also applicable to many other monolithic III-V growth cases. The integration process and design methodology is discussed afterwards. The starting point of the design is a directional coupler, which consists of a nano-ridge and a straight phased-matched Si waveguide. Following this, we design a linearly-tapered adiabatic coupler to improve the robustness and manufacturability of the coupler. In Section 6.5 we the design a more advanced adiabatic coupler whose geometry is varied along its propagation length. It has a relatively compact footprint and exhibits high coupling and decoupling efficiency. The presented coupler is expected to pave the way to integrating III-V lasers epitaxially grown on SOI wafers with other photonics components, one step closer towards a fully functional Silicon Photonics platform.

6.1 Introduction: interface with Si devices

Several groups, as aforementioned in the state of art in Section 1.1.3, have developed novel epitaxial processes providing high quality III-V materials directly grown on silicon substrates and demonstrated optically or electrically pumped lasing [1–6]. Nevertheless, none of them has presented an efficient scheme for interfacing these devices with standard silicon photonics devices.

The preferred coupling scenario obviously depends on the approach chosen for the hetero-epitaxy process. Some groups use a thick buffer layer to reduce the III-V defect density in the active layers [3, 7, 8]. In that case the lasing mode is typically separated from the Si layer by several micrometers, complicating the coupling process. Alternatively, several groups have demonstrated that it is possible to suppress defect formation by growing the III-V materials within a narrow opening defined in a SiO_2 mask deposited on the silicon substrate. In this case the extent of the III-V structure can be considerably smaller and coupling to a waveguide directly defined in the substrate becomes feasible. E.g. L. Megalini et al. from UCSB demonstrated the growth of an InGaAsP MQW structure on a V-groove-patterned SOI substrate with its QWs $\sim 500\,\text{nm}$ away from the Si layer [6]. Y. Han et al. recently demonstrated a nanolaser array emitting at telecom wavelengths grown on SOI, with InGaAs QWs $\sim 300\,\text{nm}$ separated from the Si layer [5], while M. Wang et al have shown the growth of InGaAs/InP nanowires on an SOI substrate with the QWs $\sim 500\,\text{nm}$ away from the Si layer [9]. Z. Wang et al. demonstrated single-mode lasing of $\sim 500\,\text{nm}$ high InP nanowires grown on a Si substrate [1]. Turning back to our nano-ridge, it fits this scheme with the active layer $\sim 600\,\text{nm}$ above the Si substrates. Therefore, in this chapter we develop a method to design couplers that allow to integrate this type of sub-micrometer scale lasers with silicon waveguides defined in the same substrate.

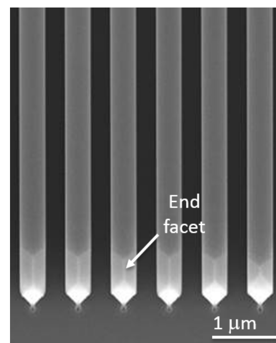

Figure 6.1: Tilted scanning electron microscopy (SEM) images of the nano-ridge array show the irregular shape of the end facets both at a front view and a end view.

A simple butt-coupling approach whereby the waveguide is placed in line with the laser cavity is thereby not desired as the selective area growth process often results in irregularly shaped facets [10, 11] as shown in Figure 6.1. This issue can be circumvented by coupling the light to the waveguide before it reaches the end of the III-V nano-ridge as we will discuss here. Finally it is important to note that although there are several reports on couplers for bonded heterogeneous III-V on Si integration [12–14], the requirements for monolithically integrated devices are quite different. In the case of heterogeneous integration the III-V and Si waveguide are separately defined and the design should allow for sufficient tolerance in the alignment between both layers to cope with that. In the case of monolithic integration the mask opening for growing the III-V nano-laser and the waveguide can be defined in the same patterning step, alleviating all issues in terms of alignment. However, since the dimensions of the III-V nano-ridge are directly determined through the epitaxial process and not through etching, the uncertainty on the precise dimensions of the III-V device might be larger than in classical structures defined through top-down processing. This influences the phase matching condition for the coupler, which has to be taken into account in the tolerance analysis. Further, due to the high index contrast, most demonstrated devices discussed above support multiple transversal modes. This makes that preventing coupling from the dominant lasing mode to undesired higher order modes is also a key requirement for the coupler.

6.2 Integration Process and Design Methodology

6.2.1 Integration Process

The proposed design approach considers the case of GaAs nano-ridges grown on Si using the ART technique described in [11]. A TEM image of a cross-section of such a nano-ridge grown on a standard Si substrate can be found in Chapter 2 Figure 2.11. In principle this nano-ridge can also be grown on an SOI wafer, which would allow for the straightforward implementation of Si waveguides on the same wafer. Figure 6.2 illustrates this and shows a schematic cross-section of the proposed coupler.

Figure 6.3 shows a possible process flow to fabricate such a coupler. Before III-V growth, the Si waveguide and the Si ridge, which will later define the trench for III-V epitaxy, as well as the SiO_2 isolation region (Figure 6.3(b)), can be defined in the silicon layer on a SOI wafer by a standard shallow trench isolation (STI) process. Next the high-aspect-ratio trench for growing the GaAs nanoridge can be defined using a tetramethylammonium hydroxide (TMAH) wet-etch step, resulting in exposed $\{111\}$ facets at the bottom as shown in Figure 6.3(c). After this the epitaxial growth process can be carried out using metal-organic vapor phase epi-

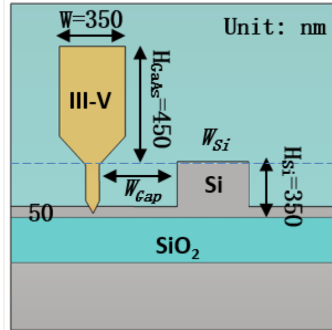

Figure 6.2: Schematic cross-section of the proposed coupler, consisting of the active GaAs nano-ridge and the passive Si waveguide on Si layer.

taxy (MOVPE) (Figure 6.3(d)). It starts with a thin nucleation layer, followed by the growth of the main GaAs structure, first inside and then outside of the trench. During the growth, three InGaAs QWs are embedded and a passivation layer of InGaP is deposited covering the full ridge. After nano-ridge growth,the whole structure can be planarized with SiO_2. Hitherto the proposed coupler structure illustrated in Figure 6.2 is accomplished. In line with our previous experiments, in the remainder of this Chapter the thickness of the silicon layer H_{Si} is chosen to be 350 nm, and it is etched 300 nm resulting in a 50 nm remaining Si layer next to the waveguides.

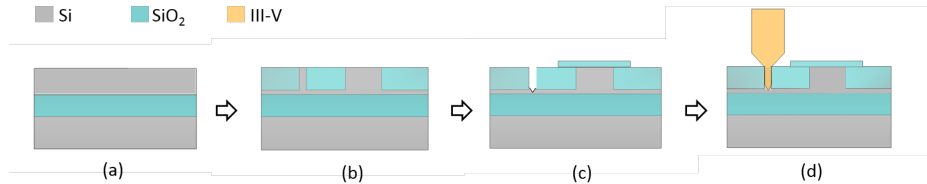

Figure 6.3: Proposed process flow of the III-V/Si coupler. (a) The process starts from a SOI wafer. (b) STI process to define high aspect ratio trench and Si WG by lithographic patterning, Si dry etch and SiO_2 deposition and CMP (chemical-mechanical polishing). (c) Prepare SiO_2 trench for III-V epitaxy by Si wet etch. (d) III-V nano-ridge epitaxy. Small structures(QWs and passivation layer) are not sketched. After this the sample is planarized with SiO_2, see Figure 6.2.

6.2.2 Design Methodology and Simulation Tools

As discussed in [15] the nano-ridge laser operates in the TE-like fundamental mode of the device. Therefore the coupler design should maximize the coupling effi-

ciency η_C from this mode to the fundamental TE-like mode of the Si WG. Given the aforementioned fabrication process, the height of the Si waveguide is fixed ($H_{Si} = 350$ nm) and only the geometrical parameters in plane can be manipulated. Hence the free variables include the width of the Si WG W_{Si}, the spacing W_{Gap} defined as the distance between the right edge of the GaAs trench and the left edge of the Si WG and the length of the coupler L. The GaAs nano-ridge itself is set to be 350 nm wide and 450 nm high. The effective refractive index for the TE-like ground mode of this nano-ridge is calculated to be $n^{TE}_{III-V} = 2.64$ at a wavelength of 1310 nm. In the case of the directional coupler considered in Section 6.3, W_{Si} and W_{Gap} are kept constant along the propagation direction (z). The optical field in the coupler can then be expressed as the superposition of the symmetric and anti-symmetric supermodes Ψ_+ and Ψ_- with propagation constants β_+ and β_- respectively. As well known from standard text books [16], the optical power will be exchanged periodically between both waveguides with a coupling length L_c, defined as $L_c = \frac{\pi}{\beta_+ - \beta_-}$. This power exchange reaches unity when the refractive indices of both individual WGs are equal, which is known as the phase matching condition. Directional couplers can be efficient and short but are not tolerant to process variations. To improve the robustness of the coupler, we introduce tapered couplers whereby the geometry is varied along the propagation direction. $W_{Si}(z)$ and $W_{Gap}(z)$ are now functions of the propagation length. In the simplest case, $W_{Si}(z)$ and $W_{Gap}(z)$ vary linearly with propagation length. This case is discussed in Section 6.4. In the more advanced case, discussed in Section 6.5, $W_{Si}(z)$ and $W_{Gap}(z)$ are more complex functions, optimized such that the coupling and decoupling between the desired optical modes happens more efficiently.

All the simulations were carried out using commercial software (Lumercial MODE Solution). The Finite Difference Eigenmode (FDE) solver is used to calculate the eigenmodes of the individual waveguides and within the coupler while the Bidirectional EigenMode Expansion (EME) solver is used to simulate the light propagation through the proposed couplers. We monitor the TE-like and TM-like ground modes for the standalone WGs and the lowest-order symmetric and anti-symmetric TE-like and TM-like supermodes at both input and output sides of the couplers but include 20 optical modes inside the simulation region for a good accuracy. Except where otherwise mentioned, all simulations were carried out for a wavelength of 1310 nm.

6.3 Directional coupler

As discussed above the free variables for optimising the directional coupler are the spacing W_{Gap} between both waveguides and the width W_{Si} of the Si waveguide (shown in Figure 6.2). To facilitate full coupling from the TE-like lasing mode Φ^{TE}_{III-V} of the III-V nano-ridge, shown in the inset of Figure 6.4, to the TE-like

mode Φ_{Si}^{TE} of the Si WG, the two modes have to be phase-matched. In practice this means the width of the Si WG has to be chosen such that the effective refractive index n_{Si}^{TE} of its TE-like ground mode is equal to that of the TE-like ground mode of the III-V nano-ridge, $n_{III-V}^{TE} = 2.64$. From Figure 6.4, which shows the effective indices of the first two eigenmodes of the Si WG as function of its width, we can derive this phase matching happens for $W_{Si} = W_{match} = 295$ nm (at wavelength 1310 nm).

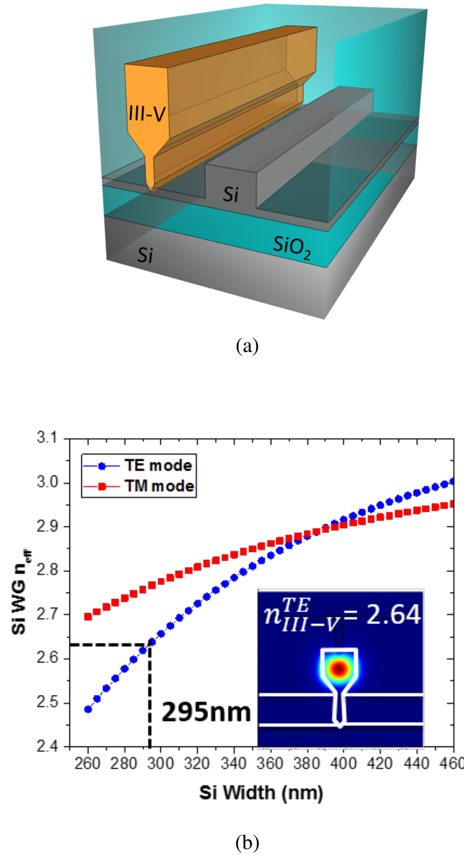

Figure 6.4: (a) The 3D schematic view of the directional coupler. (b) The calculated effective refractive indices of the TE-like and TM-like ground modes of the Si WG as a function of the width W_{Si} of the Si waveguide. The insert shows the lowest order TE-like mode of the III-V nano-ridge WG.

Figure 6.5, which shows a top view of the propagating field for $W_{Gap} = 240$ nm, proves the optical power is indeed fully exchanged between both WGs in a periodic fashion. The coupling length L_C for this configuration is $45\,\mu$m.

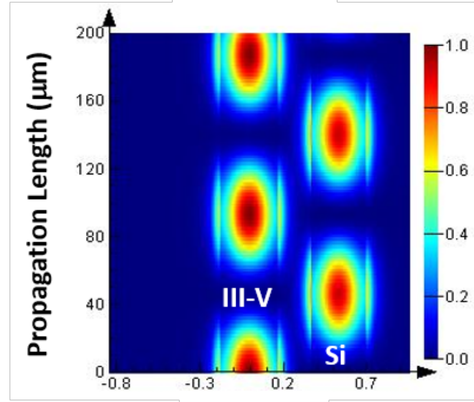

Figure 6.5: The 2-D top view of the optical field propagating in the coupler with $W_{Si} = W_{match} = 295$ nm at wavelength 1310 nm.

To obtain full field exchange in a directional coupler, the phase-matching condition has to be rigorously met and the coupler length has to be exactly equal to L_c, imposing stringent requirements to the fabrication process. Even if these requirements can be fulfilled, directional couplers are intrinsically not broadband because the phase matching condition is wavelength dependent. To illustrate this, Figure 6.6 shows that even though 100% coupling efficiency is achieved at 1310 nm, η_c rapidly drops away from this central wavelength, by 35% at 1260 nm. The coupling length L_c decreases from 57 μm to 35 μm in the wavelength range 1260 nm to 1360 nm. In addition, the coupling length is found to be extremely sensitive to variations of Si WG width ΔW_{Si} and of gap ΔW_{Gap}, with $\frac{\Delta L_C}{\Delta W_{Si}} = 6.2[\mu m/nm]$ and $\frac{\Delta L_C}{\Delta W_{Gap}} = 0.354[\mu m/nm]$. This proves the directional coupler can only operate within a narrow wavelength span and is highly sensitive to variations.

6.4 Linearly Tapered Adiabatic coupler

6.4.1 Proposed Configuration

Given that the directional coupler exhibits a low tolerance to fabrication and temperature variations, a more robust and variation-tolerant linearly tapered adiabatic coupler is proposed. Figure 6.7 (a) shows the proposed design. The left edge of the Si waveguide is kept parallel with the III-V nano-ridge such that W_{Gap} remains z-invariant. The right edge on the other hand is linearly varying along the coupler. The full coupler can be divided in three segments. In the first segment with length L_1 the Si waveguide starts with a sharp tip and ends with a width of W_1. It has a slope $\frac{W_1}{L_1}$. This segment is included in the coupler to reduce perturbations in-

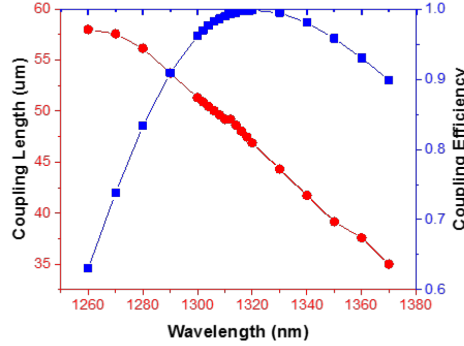

Figure 6.6: Coupling length and coupling efficiency as a function of wavelength.

troduced by the start of the Si coupler. In the second and main segment the width of the silicon waveguide varies from W_1 and expands to W_2 ($W_2 > W_1$) over a length L_2, with a slope $\frac{W_2 - W_1}{L_2}$. The variables W_1, W_2 and L_2 are the main parameters to be optimized for the coupler. The last segment consists of a straight WG with constant width W_2 to guide the coupled light away from the amplifier section, towards devices further away on the photonics IC.

The respective TE-like optical modes at different cross sections within the coupler are shown in Figure 6.7 (b): Φ^{TE}_{III-V} is the TE-like ground mode in the standalone III-V nano-ridge, Ψ^{TE}_{+1} is the symmetric TE-like supermode at the position of W_1, Ψ^{TE}_{+2} is the symmetric TE-like supermode at the position of W_2 and finally Φ^{TE}_{Si} is the TE-like ground mode in the standalone Si WG. For easier recognition of the different modes, the symbol Φ is used to represent the modes of the standalone waveguides while Ψ is used for denoting the supermodes in the coupling region. The TM-like optical modes are supposed to be highly suppressed in the amplifier section itself but given the asymmetric structure could be excited if the coupler is not well designed. They are denoted as Φ^{TM}_{III-V} and Φ^{TM}_{Si} (in the standalone WGs) and Ψ^{TM}_{+1} and Ψ^{TM}_{+2} for the TM-like supermodes at the position W_1 and W_2.

6.4.2 Optimisation of Coupler Width

The coupling from the III-V lasing mode Φ^{TE}_{III-V} to the Si WG mode Φ^{TE}_{Si} can be decomposed into three individual coupling processes. The initial optical mode Φ^{TE}_{III-V} in the active III-V nano-ridge is converted to Ψ^{TE}_{+1} at the start of the Si WG. The transition from Ψ^{TE}_{+1} to Ψ^{TE}_{+2} happens in the taper region. The last step is the conversion from Ψ^{TE}_{+2} to Φ^{TE}_{Si}, after which the optical field is guided further in the standalone Si WG towards following optical components. The total cou-

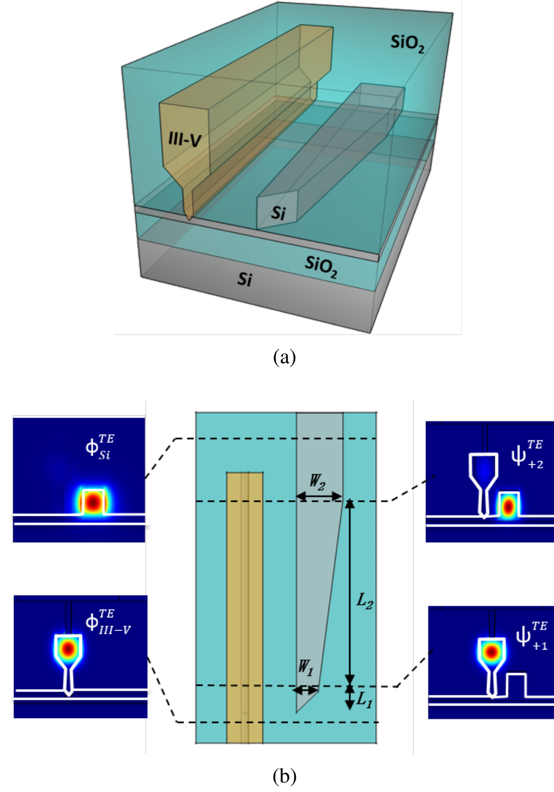

Figure 6.7: (a) 3-D schematic view of the linearly tapered coupler. (b) Top view of the tapered coupler and the field profile of the TE-like modes at different cross sections of the coupler.

pling efficiency is the product of the efficiency of each individual mode coupling process.

The widths W_1 and W_2 are optimized first. The coupling between two optical modes is approximated by taking the square of their overlap integral. Figure 6.8 shows the overlap of mode Ψ_{+}^{TE} with modes Φ_{III-V}^{TE} (solid line) and Φ_{Si}^{TE} (dashed line) as a function of W_{Si} for $W_{Gap} = 150\,\text{nm}$, 240 nm and 320 nm respectively. Each set of solid and dashed lines is found to intersect around the phase-matched width $W_{si} = W_{match} = 295\,\text{nm}$ where the effective indices of the individual waveguide modes are equal. Note that at this crossing point, the overlap between the supermode and each standalone waveguide mode is approximately 50%.

If we define the widths $W_{\Phi_{III\text{-}V}^{TE}}$ and $W_{\Phi_{Si}^{TE}}$ as those for which the coupling efficiency from respectively the lasing mode $\Phi_{III\text{-}V}^{TE}$ and the Si WG mode Φ_{Si}^{TE} to the supermode Ψ_{+1}^{TE} is 99%, W_1 and W_2 should satisfy $W_1 < W_{\Phi_{III\text{-}V}^{TE}}$ and

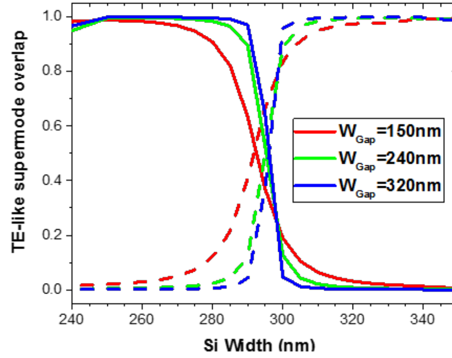

Figure 6.8: The overlap between TE-like supermode Ψ_{+}^{TE} and TE-like modes Φ_{III-V}^{TE} (solid lines) and Φ_{Si}^{TE}(dashed lines) of the standalone WGs as a function of W_{Si} for $W_{Gap} = 150$ nm, 240 nm and 320 nm respectively.

$W_2 > W_{\Phi_{Si}^{TE}}$. For example, when $W_{Gap} = 240$ nm, $W_{\Phi_{III\text{-}V}^{TE}} = 275$ nm and $W_{\Phi_{Si}^{TE}} = 315$ nm such that $W_1 < 275$ nm and $W_2 > 315$ nm. For the larger gap $W_{Gap} = 320$ nm these values can be relaxed to $W_1 < 285$ nm and $W_2 > 305$ nm while for the narrower gap $W_{Gap} = 150$ nm the range has to be increased to $W_1 < 235$ nm and $W_2 > 370$ nm.

In addition, coupling to the TM-like mode should be suppressed as much as possible. Figure 6.9 (a) and (b) plot the effective refractive indices n_{eff} of the TE- and TM-like ground modes of the stand-alone III-V and Si WGs (solid lines), and of the first four supermodes (dashed lines) of the coupler for $W_{Gap} = 150$ nm and 240 nm respectively. The overlap of a dashed line with a solid line reveals whether a supermode is rather TE-like or TM-like, and if it is centered mostly in the III-V or Si WG. Point A again indicates phase-matching for the modes $\Phi_{III\text{-}V}^{TE}$ and Φ_{Si}^{TE} with $W_A = W_{match} = 295$ nm, while B indicates phase-matching for the modes $\Phi_{III\text{-}V}^{TE}$ and Φ_{Si}^{TM} ($W_B = 235$ nm), C for the modes $\Phi_{III\text{-}V}^{TM}$ and Φ_{Si}^{TM} ($W_C = 325$ nm), and D for the modes $\Phi_{III\text{-}V}^{TM}$ and Φ_{Si}^{TE} ($W_D = 355$ nm).

To avoid the risk of coupling to TM-like modes, the tapered coupler should include point A but exclude B, C and D, namely $W_B < W_1 < W_A < W_2 < W_C < W_D$. Combining this set of conditions with the ones derived above we find 235 nm$< W_1 < 275$ nm and 315 nm$< W_2 < 325$ nm for $W_{Gap} = 240$ nm from Figure 6.9 (b). Obviously the last condition cannot be fulfilled, which means that for the narrower gaps no configuration can be defined which at the same time assures a high coupling efficiency and low coupling to unwanted modes.

This can also be seen from Table 6.1, which gives the allowable values for W_1 and W_2 for a wider range of values of W_{Gap} and shows that for this linearly tapered adiabatic coupler design the gap between the III-V nano-ridge and the sil-

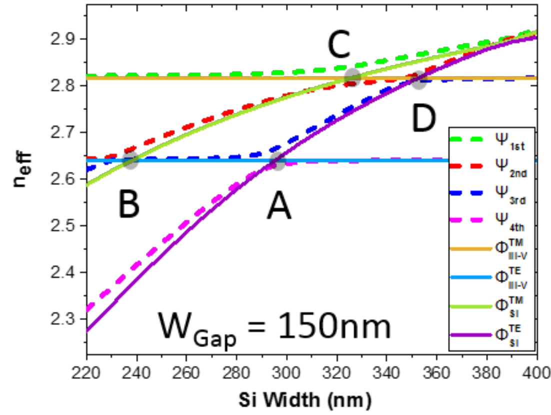

(a)

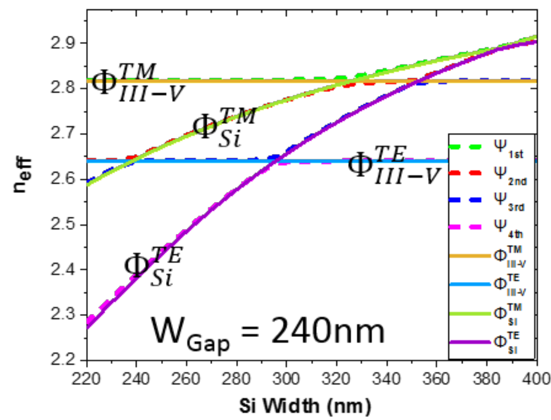

(b)

Figure 6.9: The effective refractive indices n_{eff} of the TE/TM-like ground modes of the separated III-V/Si WGs and of the first four supermodes as function of W_{Si}, for $W_{Gap} = 150\,nm$ (a) and $240\,nm$ (b).

icon waveguide W_{Gap} has to be chosen larger than 220 nm. As we will discuss in the next section this in turns limits how compact (short) we can make the coupler.

6.4.3 Optimisation of Coupler Length

If we follow the above derived design criteria for W_1 and W_2 a high coupling efficiency should in principle be possible, at least if the lengths L_1 and L_2 are

Gap	$W_B < W_1 < W_{\Phi^{TE}_{III\text{-}V}}$	$W_{\Phi^{TE}_{Si}} < W_2 < W_C$
150	$235 < W_1 < 235$	$370 < W_2 < 325$
200	$235 < W_1 < 260$	$330 < W_2 < 325$
240	$235 < W_1 < 270$	$315 < W_2 < 325$
280	$235 < W_1 < 280$	$310 < W_2 < 325$
320	$235 < W_1 < 285$	$305 < W_2 < 325$

Table 6.1: Conditions imposed on W_1, W_2 by our requirements for high coupling efficiency and avoiding coupling to TM-like modes (Unit: nm). The gray-colored cells indicate inconsistent conditions, excluding these values W_{Gap} for practical implementation.

chosen sufficiently long to allow for an adiabatic transition from Ψ^{TE}_{+1} to Ψ^{TE}_{+2}.

As discussed above, the first coupler segment with length L_1 is included in the coupler to avoid scattering at the point where the Si waveguide is introduced. Simulations showed that less than 0.3% loss is introduced as soon as $L_1 > 5\,\mu$m. In the remainder of this Section, we therefore take $L_1 = 10\,\mu$m. The second segment with length L_2, should convert supermode Ψ^{TE}_{+1} to Ψ^{TE}_{+2} adiabatically. Therefore, we swept L_2 to optimise the coupling efficiency while keeping a compact footprint. To illustrate that a too narrow separation W_{Gap} between both waveguides will indeed introduce coupling to unwanted TM-like modes, both the simulation results are shown for $W_{Gap} = 150\,$nm and $W_{Gap} = 240\,$nm. The parameters used in the simulations are $W_{Gap} = 150\,$nm, $W_1 = 235\,$nm, $W_2 = 370\,$nm for in Figure 6.10, Figure 6.11 and $W_{Gap} = 240\,$nm, $W_1 = 270\,$nm, $W_2 = 315\,$nm for in Figure 6.12, Figure 6.13. The green lines in Figure 6.10 (a) and Figure 6.12 (a) show how the coupling efficiency η_C to the desired mode Ψ^{TE}_{+2} varies as function of L_2. When $W_{Gap} = 150\,$nm the coupling shows an optimum $\eta_C \sim 80\%$ for $L_2 = 150\,\mu$m.

The remaining light is mostly coupled to the TM-like mode Ψ^{TM}_{-2} centered in the III-V nano-ridge. As L_2 further increases, more severe coupling between Ψ^{TE}_{+2} and Ψ^{TM}_{-2} can be seen. With W_2 close to the phase matching point D for the modes Φ^{TE}_{Si} and Φ^{TM}_{III-V} as shown in Figure 6.9 (b), the strong coupling to Ψ^{TM}_{-2} is indeed expected. Figure 6.10 (b) shows the evolution of the normalized field in the III-V and Si WGs respectively, when $L_2 = 150\,$nm. The ripples in the second half of the taper are attributed to the interference between the modes Ψ^{TE}_{+2} and Ψ^{TM}_{-2}. The related power exchange can be observed also clearly in Figure 6.11, which depicts the 2-D field distribution along the coupler.

If the gap is increased to $W_{Gap} = 240\,$nm, the maximum coupling happens at $L_2 = 310\,\mu$m with $\eta_C \sim 98\%$ (Figure 6.12 (a)). In this case, the remaining $\sim 2\%$ of the optical power is partly coupled to supermode Ψ^{TE}_{-2} centered in III-V nano-

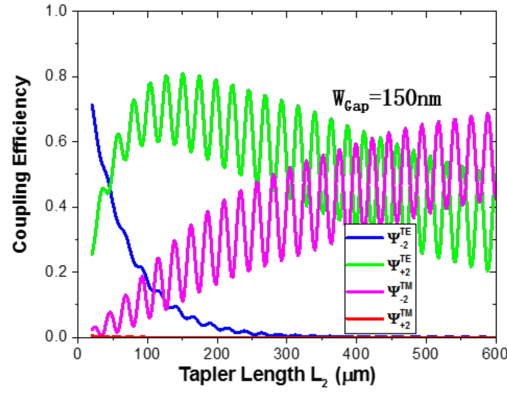

(a)

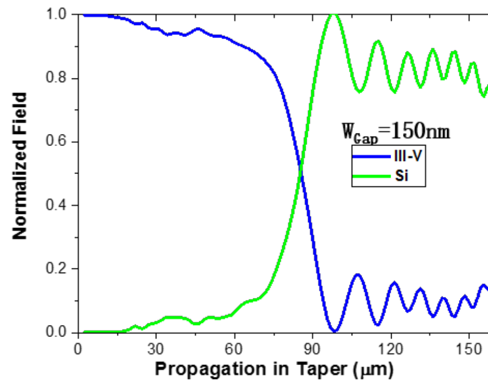

(b)

Figure 6.10: Simulation results for the configurations $W_{Gap} = 150\,nm$, $W_1 = 235\,nm$, $W_2 = 370\,nm$. (a) shows the coupling to several modes as function of taper length L_2. (b) depicts the field exchange between the III-V nano-ridge and Si waveguide along the propagation axis for the optimised taper lengths $L_2 = 150\,\mu m$.

ridge and partly coupled to the TM-like supermode Ψ^{TM}_{+2} centered in the Si WG. Figure 6.12 (b) and Figure 6.13 show how the field exchanges along the coupler when $L_2 = 310\,\mu$m. Some ripples are still present, due to interference between the supermodes Ψ^{TE}_{+2} and Ψ^{TE}_{-2}, but they gradually decrease in amplitude along the propagation axis as the two modes get decoupled. Hence, the chosen parameters $W_{Gap} = 240$ nm, $W_1 = 275$ nm, $W_2 = 315$ nm result in good coupling efficiency and an overall decent design, albeit at the cost of larger footprint, related to the reduced coupling strength between both waveguides for this wider gap. As we now

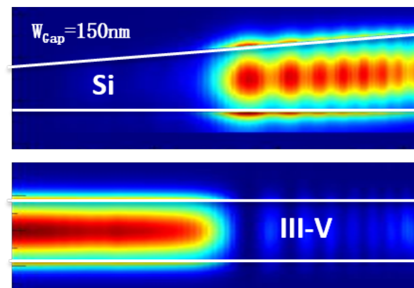

Figure 6.11: 2-D image of the field exchange between the III-V nano-ridge and the Si waveguide for the optimised couplers with parameters in Figure 6.10.

also clearly showed simply reducing the gap is not a good solution, in Section 6.5 we will propose a more advanced design which provides a better compromise between decoupling the optical modes at the entrance and exit of the coupler on the one hand and increasing the coupling strength in the center part.

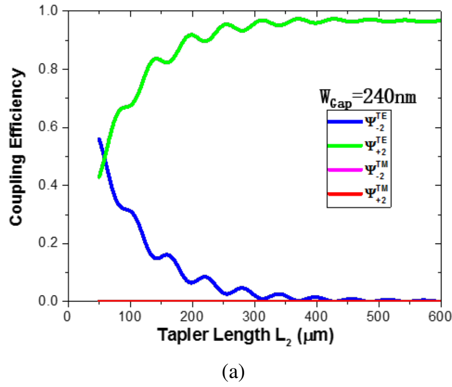

(a)

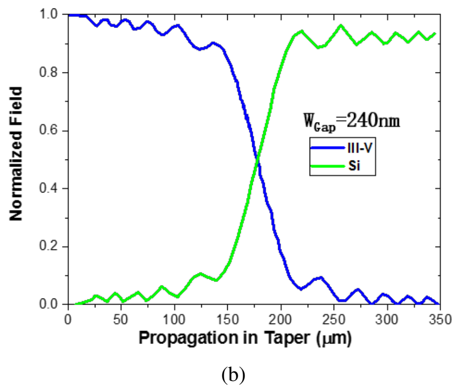

(b)

Figure 6.12: Simulation results for the configurations $W_{Gap} = 240\,nm$, $W_1 = 275\,nm$, $W_2 = 315\,nm$. (a) shows the coupling to several modes as function of taper length L_2. (b) depicts the field exchange between the III-V nano-ridge and Si waveguide along the propagation axis for the optimised taper lengths $L_2 = 310\,\mu m$.

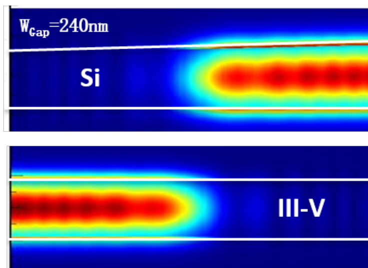

Figure 6.13: 2-D image of the field exchange between the III-V nano-ridge and the Si waveguide for the optimised couplers with parameters in Figure 6.12.

6.4.4 Tolerance to Fabrication Variations

In our process, the exact size of the III-V nano-ridge is determined by the epitaxy process. A change in growth temperature, growth time or mask loading might cause slight deviations in the nano-ridge dimensions.

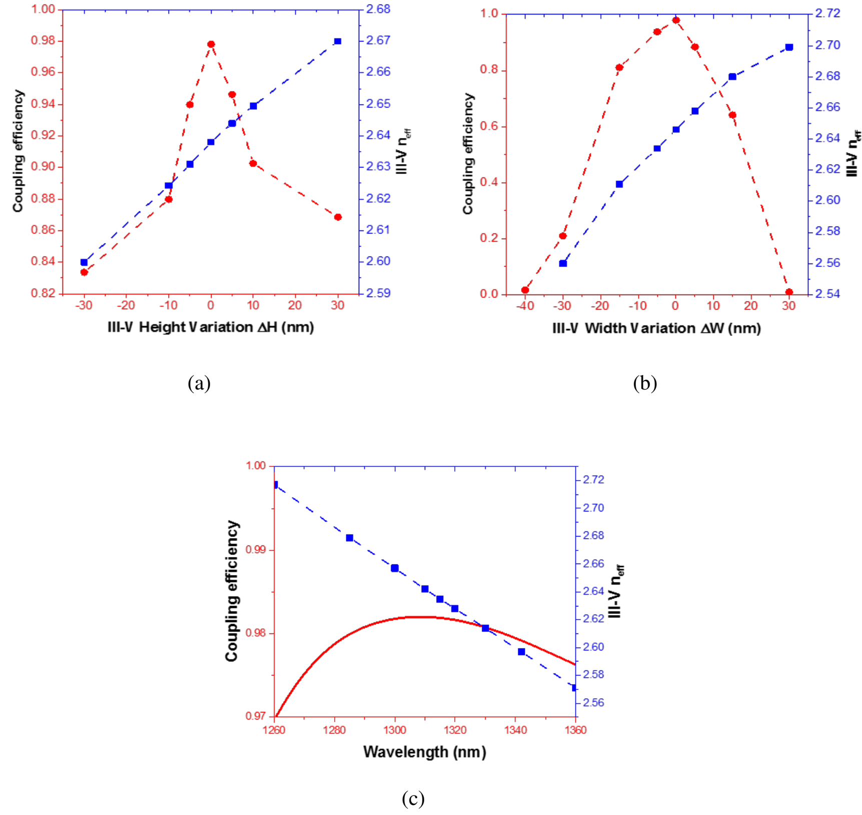

Figure 6.14: Coupling efficiency (left axis) and effective refractive index n^{TE}_{III-V} (right axis) as a function of (a) nano-ridge height variation, (b) width variation and (c) wavelength.

Figure 6.14 (a) and (b) plot the coupling efficiency η_C and the effective refractive index n^{TE}_{III-V} as function of a deviation in height ΔH or width ΔW of the nano-ridge dimensions, for a coupler with $W_{Gap} = 240\,\text{nm}$, $W_1 = 275\,\text{nm}$, $W_2 = 315\,\text{nm}$, $L_1 = 10\,\mu\text{m}$, $L_2 = 310\,\mu\text{m}$. Figure 6.14 (a) shows that 30 nm variation in III-V nano-ridge height has little impact on the coupling efficiency, which drops from 98% to 84%. The limited influence can be explained by the small (¡1.5%) changes in n^{TE}_{III-V}. Figure 6.14 (b) shows that 15 nm variation in width is

acceptable with η_C decreasing by 16% from 98% to 82%. But for width variations above 30 nm the coupling efficiency drastically drops. The different impact from the nano-ridge height and width variations on the coupling efficiency can be understood by the related changes in the effective index of the nano-ridge. The blue curves in Figure 6.14 (a) and (b) show that n_{III-V}^{TE} is more strongly influenced by width variations than by height variations. Figure 6.14 (c) shows how the coupling efficiency varies versus wavelength. Although n_{III-V}^{TE} varies relatively strongly with wavelength, the deviation from the phase matching condition remains small as also the effective index of the silicon waveguide decreases with wavelength. These simulations indicate that the linearly tapered coupler is strongly improved in terms of fabrication tolerances with respect to the directional coupler.

6.5 Optimized Adiabatic Coupler

Compared with the narrow-band and variation-intolerant directional coupler, the linearly tapered coupler already exhibits a broadband and more fabrication tolerant performance. Nevertheless, with a length of 310 μm its footprint is large compared to the length of a typical III-V integrated laser or amplifier ($100 - 600\,\mu$m) and in particular with respect to our earlier demonstrated nano-ridge laser, which was only $\sim 100\mu$m long [15]. In addition insufficient decoupling at the beginning and end of the linearly tapered coupler decreases the maximum coupling efficiency and introduces extra coupling to unwanted modes, which could impact the laser performance. Therefore, a more compact adiabatic coupler design with more efficient coupling and decoupling is desired.

6.5.1 Proposed Configuration

To improve the design, a semi-analytical approach as described in [17] is adopted. The schematic views of the coupler are shown in Figure 6.15. Now both the width $W_{Si}(z)$ of the Si WG and the spacing $W_{Gap}(z)$ between the III-V trench and the Si WG are allowed to vary along the propagation direction. Their values are derived from optimised functions $\kappa(z)$ and $\Delta\beta(z)$ for the coupling coefficient and the dephasing between the lasing mode Φ_{III-V}^{TE} and the Si WG mode Φ_{Si}^{TE}:

$$\kappa(z) = \kappa_{max} \cdot sin\theta(z) \tag{6.1}$$

$$\Delta\beta(z) = -\Delta\beta_{max} \cdot cos\theta(z) \tag{6.2}$$

with κ_{max} the maximum coupling coefficient, at the device center $z = \frac{L}{2}$, and $\Delta\beta_{max}$ the maximum dephasing, at the beginning $z = 0$ and the end $z = L$ of the device. $\theta(z)$ is a monotonically increasing function of z, with $\theta(0) = 0$ and $\theta(L) = \pi$.

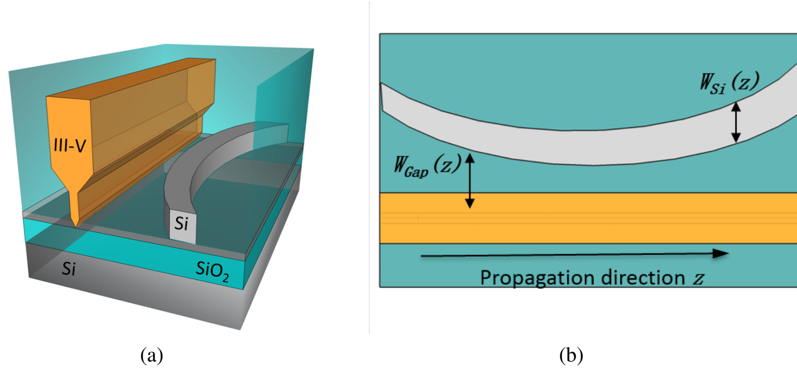

(a) (b)

Figure 6.15: (a)The 3D schematic view of the advanced adiabatic coupler. (b) Top view of the optimized adiabatic coupler. The gap W_{Gap} and Si WG width W_{Gap} are functions of the propagation direction z. Note that W_{Gap} is measured from the side of the III-V trench, at the bottom of the nano-ridge, see Figure 6.2

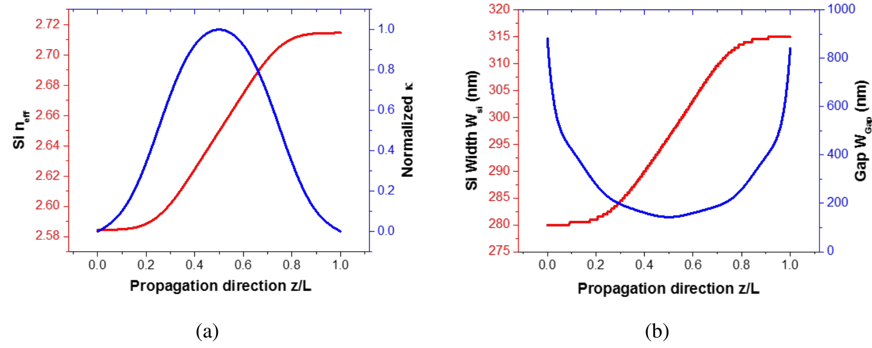

(a) (b)

Figure 6.16: (a) The calculated effective refractive index of the Si WG n_{eff} (left axis) and normalized coupling coefficient $\frac{\kappa(z)}{\kappa_{max}}$ as functions of propagation direction z. (b) Calculated Si WG width $W_{Si}(z)$ and gap $W_{Gap}(z)$ along taper.

The coupling coefficient κ is calculated as

$$\kappa = \sqrt{\kappa_{12}\kappa_{21}} \tag{6.3}$$

$$\kappa_{12} = \frac{k_0^2}{2\beta_1} \frac{\int_{WG1}(\varepsilon_1 - \varepsilon_2)U_1^* U_2 dA}{\int |U_1|^2 dA} \tag{6.4}$$

$$\kappa_{21} = \frac{k_0^2}{2\beta_2} \frac{\int_{WG2}(\varepsilon_2 - \varepsilon_1)U_2^* U_1 dA}{\int |U_2|^2 dA} \tag{6.5}$$

with the subscripts 1 and 2 referring to the III-V nano-ridge and the Si WG respectively. k_0 is the free-space wavevector, β_i is the propagation constant of the corresponding WG, ε_i is the permittivity function describing the waveguide profile and U_i is the TE-like optical field of the corresponding WG.

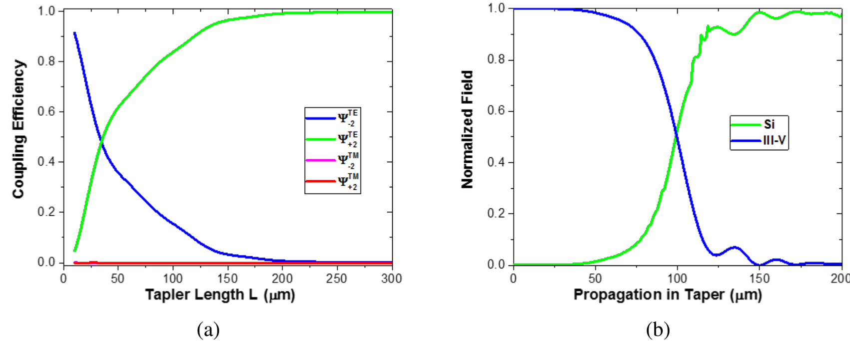

(a) (b)

Figure 6.17: Simulation results for the optimized adiabatic coupler configuration shown in Figure 6.16. (a) The coupling efficiency as a function of coupler length L. A coupling efficiency $\eta_C > 99\%$ can be reached for $L = 200\,\mu m$. (b) Field exchange between III-V nano-ridge and Si waveguide along propagation direction when $W_{Si}(\frac{L}{2}) = W_{match} = 295\,nm$, $W_{Si}(0) = 280\,nm$, $W_{Si}(L) = 310\,nm$, $W_{Gap}(\frac{L}{2}) = 150\,nm$, $W_{Gap}(0) = W_{Gap}(L) = 820\,nm$, $L = 200\,\mu m$.

The maximum coupling constant κ_{max} is calculated by choosing $W_{Si}(\frac{L}{2}) = W_{match} = 295\,\text{nm}$ (the phase matching condition) and $W_{Gap}(\frac{L}{2}) = 150\,\text{nm}$ to realize a high coupling strength. Although above we found that the choice $W_{Gap} = 150\,\text{nm}$ introduces high coupling to unwanted modes in the linearly tapered coupler, we will show this is not the case for the optimised adiabatic coupler discussed here. $\Delta\beta(z)$ is given by:

$$\Delta\beta(z) = \frac{2\pi}{\lambda_0}(n^{TE}_{III-V} - n^{TE}_{Si}(z)) \tag{6.6}$$

The maximum dephasing $\Delta\beta_{max}$ occurs at the positions $z = 0$ and $z = L$, where we choose $W_{Gap}(0) = W_{Gap}(L) = 850\,\text{nm}$, $W_{Si}(0) = 280\,\text{nm}$ and $W_{Si}(L) = 310\,\text{nm}$ to assure complete decoupling between both WGs.

It is found that the most efficient taper is obtained if $\theta(z)$ varies as a Blackman function [18]. We let

$$\theta(z) = \frac{\pi z}{L} - 0.25 sin\frac{2\pi z}{L} - 0.07 sin\frac{4\pi z}{L} \tag{6.7}$$

The values for the Si WG effective index $n^{TE}_{Si}(z)$ and the normalized coupling coefficient $\frac{\kappa(z)}{\kappa_{max}}$ optimized according to this procedure are plotted in Figure 6.16

(a). Figure 6.16 (b) shows the according geometrical parameters W_{Gap} and W_{Si}. They are obtained from the known κ_{max}, $\Delta\beta_{max}$ and $\theta(z)$ using an FDE mode solver. The staircase-like pattern in the curve for $W_{Si}(z)$ in Figure 6.16 (b) originates from the simulation resolution of 1 nm.

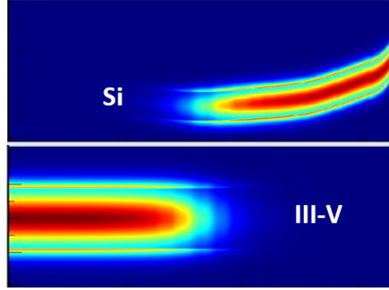

Figure 6.18: 2-D image of field exchange between III-V nano-ridge and Si waveguide for $L = 200\,\mu m$ for the optimized adiabatic coupler configuration shown in Figure 6.16.

Figure 6.17 (a), shows how the coupling efficiency towards the different supermodes varies as function of L. The green curve shows how the coupling efficiency η_C towards Ψ^{TE}_{+2} firstly rapidly increases with L, and then approaches unity for $L = 150\,\mu$m and beyond while the undesired coupling towards the TM-like modes Ψ^{TM}_{+1} and Ψ^{TM}_{+2} remains low. Figure 6.17 (b) and Figure 6.18 show how the optical power is exchanged between both waveguides for the optimized coupler with $L = 200\,\mu$m. These results confirm the optimized adiabatic coupler allows for a high coupling efficiency and improves the coupling and decoupling processes along the taper, without spurious coupling to undesired modes.

6.5.2 Tolerance to Fabrication Variations

Figure 6.19 (a) and (b) plot how the coupling efficiency η_C varies as function of deviations in the III-V nano-ridge height ΔH and width ΔW, for the coupler with parameters as shown in Figure 6.19 (b). A variation of 30nm in the III-V nano-ridge height reduces the coupling efficiency from 99% to 78%. As for the linearly tapered coupler, also here a variation in the III-V nano-ridge width has a larger impact on the coupling efficiency, with a 10 nm variation reducing η_C from 99% to 80%. Finally Figure 6.19 (c) shows the wavelength dependence of the coupling efficiency throughout the O-band, proving the broadband character of the coupler with a variation in coupling efficiency $\sim 2\%$ over a 100nm wide wavelength range.

The tolerance of the optimized adiabatic coupler is slightly worse than that of the longer linearly tapered adiabatic coupler, but can easily be improved by increasing the taper length. Figure 6.19 (a) and (b) plot the coupling efficiency η_C varies versus the deviations in the III-V nano-ridge height ΔH and width ΔW, for

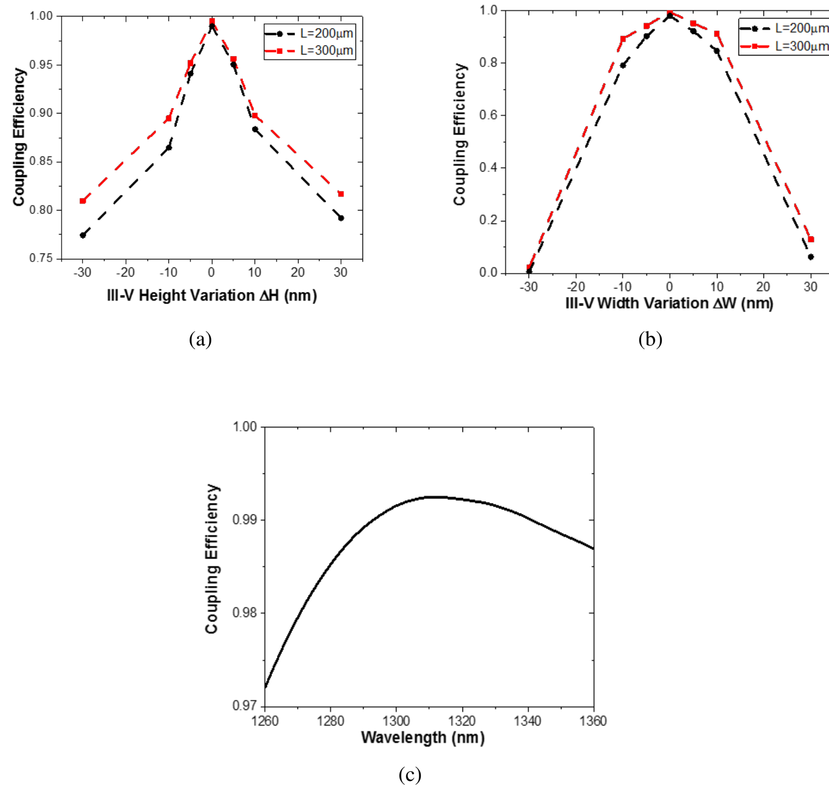

Figure 6.19: Coupling efficiency of the optimized adiabatic coupler with length 200 *μm as a function of (a) nano-ridge height variation, (b) width variation and (c) wavelength.*

the coupler with the samoe configuration shown in Figure 6.16 (b) but the length is prolonged to 300 μm. A variation of 30 nm in the III-V nano-ridge height reduces the coupling efficiency from 99% to 81%. As for variation in the III-V nano-ridge width, a 10 nm change reduces η_C from 99% to 89%. The 300 μm-long taper reveals better tolerance both to height and width variations in the nano-ridge compared with the 200 μm-long one.

6.6 Conclusion

In this chapter, we proposed a novel adiabatic coupler working in the O-band for coupling light from a GaAs nano-ridge laser to a Si waveguide. The coupler is compatible with our earlier presented process for the direct epitaxy of GaAs on

silicon using the aspect ratio trapping approach and requires no extra effort to fabricate (although it might require a recallibration of the epitaxy process for growth on an SOI substrate). We showed that a directional coupler design can reach a coupling efficiency of 100% but is very sensitive to process and wavelength variations. To improve this, a more robust linearly tapered adiabatic coupler is presented, which is more tolerant to process variations and can still achieve a 98% coupling efficiency. However, this comes at the cost of an increased footprint and some residual coupling to unwanted modes. To prevent this undesired coupling from influencing the laser operation, a more advanced adiabatic couple, which better decouples the modes at the beginning and end of the coupler was then proposed. The dimensions of the optimized adiabatic coupler are varied in a way such that a coupling efficiency $> 99\%$ is achieved for a coupler length of 200 μm, without coupling to undesired modes. The tolerance with respect to process variations of the optimized adiabatic coupler is not as good as that of the linearly tapered coupler, but can be improved by increasing the taper length. In this way the design provides, depending on the application, the freedom to optimise either towards compact size or towards high processing tolerance. Finally it is important to note that the design procedure proposed here can directly be transferred to other III-V nano-lasers epitaxially grown on silicon recently proposed in literature.

The presented adiabatic coupler is expected to connect III-V devices with the whole on-chip Si photonics circuit. Besides, it helps explore the potential of the epitaxial III-V to make more complex and functional devices with the help of external Si circuits to provide feedback or/and form a cavity.

References

[1] Zhechao Wang, Bin Tian, Marianna Pantouvaki, Weiming Guo, Philippe Absil, Joris Van Campenhout, Clement Merckling, and Dries Van Thourhout. *Room-temperature InP distributed feedback laser array directly grown on silicon*. Nature Photonics, 9(12):837–842, 2015.

[2] Siming Chen, Wei Li, Jiang Wu, Qi Jiang, Mingchu Tang, Samuel Shutts, Stella N Elliott, Angela Sobiesierski, Alwyn J Seeds, Ian Ross, et al. *Electrically pumped continuous-wave III–V quantum dot lasers on silicon*. Nature Photonics, 10(5):307, 2016.

[3] Yating Wan, Justin Norman, Qiang Li, MJ Kennedy, Di Liang, Chong Zhang, Duanni Huang, Zeyu Zhang, Alan Y Liu, Alfredo Torres, et al. *1.3 μm submilliamp threshold quantum dot micro-lasers on Si*. Optica, 4(8):940–944, 2017.

[4] Yu Han, Wai Kit Ng, Chao Ma, Qiang Li, Si Zhu, Christopher CS Chan, Kar Wei Ng, Stephen Lennon, Robert A Taylor, Kam Sing Wong, et al. *Room-temperature InP/InGaAs nano-ridge lasers grown on Si and emitting at telecom bands*. Optica, 5(8):918–923, 2018.

[5] Yu Han, Wai Kit Ng, Ying Xue, Qiang Li, Kam Sing Wong, and Kei May Lau. *Telecom InP/InGaAs nanolaser array directly grown on (001) silicon-on-insulator*. Optics letters, 44(4):767–770, 2019.

[6] Ludovico Megalini, Bastien Bonef, Brian C Cabinian, Hongwei Zhao, Aidan Taylor, James S Speck, John E Bowers, and Jonathan Klamkin. *1550-nm InGaAsP multi-quantum-well structures selectively grown on v-groove-patterned SOI substrates*. Applied Physics Letters, 111(3):032105, 2017.

[7] HK Choi, CA Wang, and NH Karam. *GaAs-based diode lasers on Si with increased lifetime obtained by using strained InGaAs active layer*. Applied physics letters, 59(21):2634–2635, 1991.

[8] Michael E Groenert, Christopher W Leitz, Arthur J Pitera, Vicky Yang, Harry Lee, Rajeev J Ram, and Eugene A Fitzgerald. *Monolithic integration of room-temperature cw GaAs/AlGaAs lasers on Si substrates via relaxed graded GeSi buffer layers*. Journal of Applied Physics, 93(1):362–367, 2003.

[9] Mengqi Wang, Zhibo Li, Xuliang Zhou, Yajie Li, Pengfei Wang, Hongyan Yu, Wei Wang, and Jiaoqing Pan. *InGaAs/InP Multi-quantum-well Nanowires Directly Grown on SOI Substrates and Optical Property Characterizations*. In CLEO: Applications and Technology, pages JTh2A–76. Optical Society of America, 2018.

[10] B. Kunert, W. Guo, Y. Mols, B. Tian, Z. Wang, Y. Shi, D. Van Thourhout, M. Pantouvaki, J. Van Campenhout, R. Langer, and iii/v K. Barla. *nano ridge structures for optical applications on patterned 300 mm silicon substrate, Appl. Phys*. Lett., 109:9, 2016.

[11] Bernardette Kunert, Weiming Guo, Yves Mols, Robert Langer, and Kathy Barla. *Integration of III/V hetero-structures by selective area growth on Si for nano-and optoelectronics*. Ecs Transactions, 75(8):409–419, 2016.

[12] Alexander W Fang, Erica Lively, Ying-Hao Kuo, Di Liang, and John E Bowers. *A distributed feedback silicon evanescent laser*. Optics express, 16(7):4413–4419, 2008.

[13] M Lamponi, Shahram Keyvaninia, C Jany, F Poingt, F Lelarge, G De Valicourt, Günther Roelkens, Dries Van Thourhout, S Messaoudene, J-M Fedeli, et al. *Low-threshold heterogeneously integrated InP/SOI lasers with a double adiabatic taper coupler*. IEEE photonics technology letters, 24(1):76–78, 2011.

[14] Sören Dhoore, Sarah Uvin, Dries Van Thourhout, Geert Morthier, and Gunther Roelkens. *Novel adiabatic tapered couplers for active III–V/SOI devices fabricated through transfer printing*. Optics express, 24(12):12976–12990, 2016.

[15] Yuting Shi, Zhechao Wang, Joris Van Campenhout, Marianna Pantouvaki, Weiming Guo, Bernardette Kunert, and Dries Van Thourhout. *Optical pumped InGaAs/GaAs nano-ridge laser epitaxially grown on a standard 300-mm Si wafer*. Optica, 4(12):1468–1473, 2017.

[16] Charles Vassallo. *Optical waveguide concepts*. Optical Wave Sciences and Technology, 1:Sec–5, 1991.

[17] Hiroshi Ishikawa. *Fully adiabatic design of waveguide branches*. Journal of lightwave technology, 25(7):1832–1840, 2007.

[18] Hsien-kai Hsiao, Kim A Winick, and John D Monnier. *Midinfrared broadband achromatic astronomical beam combiner for nulling interferometry*. Applied optics, 49(35):6675–6688, 2010.

7
Conclusions and perspectives

7.1 Conclusion of the presented work

In this thesis, we presented the development of a leading-edge material - the novel InGaAs/GaAs nano-ridge monolithically grown on 300 mm Si substrates - for laser applications. We have elevated the technology readiness level (TRL) of the nano-ridge by proving the concept that practical laser devices could be formulated from the innovate material.

First, the structure and growth details of the novel GaAs nano-ridge was presented. We discussed the challenges (e.g. lattice mismatch and polarity difference) involved in growing such materials and the practical techniques (i.e., aspect-ratio trapping and nano-ridge engineering) utilized to suppress defect and form a waveguide-like profile.

Then the material's optical properties were characterised. The calculation of the energy band diagram of the nano-ridges showed that the E_{1-1HH} transition for the $\sim 10\,\text{nm}$ thick $In_{0.2}Ga_{0.8}As$ quantum wells (QWs) emits at $1\,\mu$m. The emission wavelength was verified experimentally by photoluminescence (PL) measurements using a micro-PL (μ-PL) setup. To investigate the influence of trench width on defect density, surface recombination as well as the non-radiative recombination in the defective trenches, we conducted time-resolved PL (TRPL) measurements to extract PL lifetime both at room temperature (RT) and low temperature (300 K). A strong dependence of the PL lifetime on the trench width was observed as the trench width defines the dislocation defect density in the nano-ridge material

as well as the nano-ridge size and, therefore, the surface-to-volume ratio. Nano-ridges with 150 nm-wide trench (always with fixed trench height of 300 nm) exhibited the most extended PL lifetime as a result of the trade-off between dislocation defect density and non-radiative recombination at surfaces and in the defective trenches. An InGaP passivation layer was shown to significantly reduce carrier loss by surface recombination, however thickening it beyond 50 nm does not improve the performance further. The insertion of an InGaP carrier-blocking layer underneath the QWs prevents non-radiative recombination in the defective trenches and increases the lifetime up to 2 ns at RT. The optical gain of the nano-ridges was characterized, using the variable stripe length (VSL) method. The measurement confirmed the correlation between crystal quality and the trench width again as 80 nm- and 100 nm-trench nano-ridges possess a material gain above 5000 cm^{-1} under 300 kW/cm^2, higher than that for 120 nm- and 150 nm-trench nano-ridges. We also experimentally certified that the modal gain is higher for nano-ridges with 3$\times$QW than that for nano-ridges with 2$\times$QW. The optical characterization is crucial to understand the correlation between the crystal quality and the nano-ridge configuration and growth conditions. The long PL lifetime and strong optical gain supports the efficiency of ART for defect suppression and confirms the excellent material quality. Furthermore, the knowledge on the optical properties provides a fundamental understanding of the following laser device design and fabrication.

We then proceeded to explore the potential of the nano-ridges by designing and fabricating lasers, starting from the novel material. Simulations showed that the TE-like fundamental optical mode has the highest CF and smallest leakage loss, and is most likely to lase. As a start, Fabry-Perot cavities of a length of 180 μm were fabricated by etching two facets on the nano-ridge. These devices were lasing but the precise operating regime was challenging to be resolved due to their small free spectrum range (FSR) and the limited resolution of the measurement. Afterward, we designed index-coupled DFB cavities with a $\lambda/4$ shift for single-mode lasing. The grating period was calculated to be 170 nm to have the TE-like fundamental mode lase at the center of the PL spectrum - 1020 nm. The fabrication of these lasers included planarization of the nonuniform sample surface, electron beam lithography (EBL) and dry etching of gratings at the top of the nano-ridges. Room temperature measurements showed single-mode lasing at 1020 nm with a side-mode suppression ratio (SMSR) better than 28 dB, a linewidth of 1.5 nm and a threshold of 33 kW/cm^2 for a 102 μm long DFB device with a grating period of 170 nm. Moreover, we demonstrated that the emission wavelength could be precisely controlled not only by the grating design but also by the trench width and finetuning of the epitaxial process. We also presented a partly loss-coupled DFB cavity formed by metallic gratings, which might provide a pathway towards electrical injection in the future. The gratings can effectively reduce the loss by ten times, from 72 cm^{-1} for continuous metal to 7 cm^{-1} for the metal grating. Op-

timising the duty cycle to balance the cavity mode loss and the coupling strength introduced by the metallic grating. The PLC DFB nano-ridge lasers further only require a single metallic grating deposition and are hence relatively straightforward to process. Devices with duty cycle ranging from 0.2 to 0.6 showed single-mode lasing. Among them, the one with duty cycle 0.4 exhibited the lowest threshold of $10\,\text{kW/cm}^2$, matching our simulations. The successful demonstration of different types of lasers proves again the high quality of the nano-rides, which opens up the road toward high volume manufacturing of silicon photonic ICs, including III-V lasers and amplifiers on a mature CMOS platform.

In line with the current fiber optic-communication system, we also endeavored to develop a new heterostructure operating in the O-band ($1.26-1.31\,\mu$m), or even the C-band ($1.53 - 1.65\,\mu$m). To redshift the emission spectra, we increased the Indium content in the QWs to 0.45% and to 0.25% for the barriers to keep the strain reasonable. The PL of the $In_{0.25}Ga_{0.75}As$ nano-ridges with $In_{0.45}Ga_{0.55}As$ shows emission spectra up to $1.4\,\mu$m. Nevertheless, only the emission centered at $1.1\,\mu$m from the InGaAs barrier was observed in TRPL measurement. The extracted PL lifetime for the InGaAs barrier was 191 ps. We also characterized the optical gain for the InGaAs nano-ridge. A fast saturation around $50\,\text{kW/cm}^2$ and an inferior gain of 150 /cm at $300\,\text{kW/cm}^2$ for the 100 nm-trench nano-ridge was found. However, we still designed $\lambda/4$-shifted index-coupled DFB cavities working with the ground TE-like mode for the O-band emission. This device showed a peak at 1330 nm at a low pump intensity, but multiple peaks started to appear when the pump increases. This first trial verifies that extension of the wavelength can be achieved. However, even though PL and amplified spontaneous emission (ASE) in the O-band have been obtained, further improvement on the material's quality is still demanded.

Finally, as a first step towards co-integration with Si PICs, we proposed novel adiabatic couplers to realize the interfacing between the III-V nano-ridges and Si waveguides (WGs) in the O-band. We first showed a directional coupler design of length $50\,\mu$m that can reach a coupling efficiency of 100% but is very sensitive to process and wavelength variations. A more robust linearly tapered adiabatic coupler with a length of $310\,\mu$m was then presented, which is more tolerant to process variations and can still achieve a 98% coupling efficiency. However, the large footprint motivated us to develop a more advanced adiabatic couple design, which better decouples the modes at the beginning and end of the coupler. The dimensions of the optimized adiabatic coupler are varied in a way such that a coupling efficiency $> 99\%$ is achieved for a coupler length of $200\,\mu$m. The decrease in the coupling efficiency is only 2% across the entire O-band, 13% for a variation of 10 nm in nano-ridge height and 18% for a variation of 10 nm in nano-ridge width. The tolerance to variations can be improved, at the cost of larger footprint The design strategy developed here is not only compatible with the nano-ridge presented

in this work, but also with several other state-of-art approaches of monolithic III-V growth on Si. As such, the presented coupler is expected to pave the way to integrating III-V lasers epitaxially grown on SOI wafers with other photonics components, bringing us one step closer towards a fully functional Silicon Photonics platform.

7.2 Perspectives for future work

As the work on this unique platform started in 2014, we were able to conduct the initial proof-of-principle demonstrations and first feasibility tests. To be able to deliver mature devices for the commercial market, still many efforts are needed to be invested. Requirements for being able to fully exploit the epitaxial nano-ridges include but are not limited to:

- improving the material quality and realizing a CW-pumped laser
- realizing electrical injection
- extending the operating wavelength to the O-band and the C-band
- developing the III-V nano-ridge on Si into a more versatile platform with diverse active devices and passive Si components.

Thus far we demonstrated lasing under pulsed optical pumping. The realization of CW pumping requires a further reduced threshold and more efficient heat dissipation. Engineering the laser design, e.g., increasing cavity coupling strength by extending the cavity length, reducing the optical loss by optimizing the gratings and/or nano-ridge sidewall roughness, can be helpful. The thermal issue is general for micro-scale active devices due to the huge amount of heat generated in a small volume. The heat dissipation for the current nano-ridge laser is limited by the narrow trenches towards the Si substrate, which is calculated to cause a high operating temperature of $65°$. More efficient heat dissipation can be realized by adding heat-conducting materials such as SiN/SiO_2 for planarization and Ti/Cu for metalization. Reliability - another significant laser issue - has not been tested yet for the nano-ridges. This experiment requests long-term (thousands of hours) monitoring of threshold current, lasing power, wavelength and linewidth [1] and can only be done once electrical injection is available.

Realizing electrical injection is a further crucial step. The implementation of an efficient injection scheme faces many challenges however. Given the small volume of the nano-ridges it can be extremely challenging to achieve a uniform p- and n-doping profile and an intact intrinsic QWs region to form a p-i-n junction. Besides, new defects might be introduced to the nano-ridges during doping process. An annealing [2] or regrowth [3] step after doping might be helpful. The selection

of dopants and their concentration needs to be investigated to reach good ohmic contacts between III-V and metal pads [4]. The way to position metal pads on the nanostructure without bringing huge loss to the optical mode has to be scrutinized as well. After the realization of electrical injection, high-speed characterization can be finally conducted to study the nano-ridges' feasibility for fiber-optic communication.

The studies on the extension of achievable wavelength to the O-band should be continued. The preliminary results in Chapter 5 already provide some feedback on how to optimize the structure. Knowing the ultrashort PL time and fast saturation of the $In_{0.45}Ga_{0.55}As$ QWs, we could start with the investigation of the crystal quality of the active region through TEM inspection, etc. The origin of defects - the intensive compressive strain on the QWs - can maybe be compensated by adding tensile-strained layers to the heterostructure [5]. Other approaches to improve the quality, including increasing the aspect ratio of the STI trenches, inserting additional strain-compensating layers, annealing, etc. can be tested. An alternative to extent the operating wavelength is growing self-assembled QDs [6]. QDs are proved to be more resistant to threading dislocations [7] but new challenges such as how to reach a relatively large gain volume, how to control the size distribution [8] might arise.

The ultimate goal of the monolithic III-V nano-ridge epitaxy is to develop a versatile platform, which not only co-integrates with passive Si photonics (e.g., WGs, tapers, gratings), but also incorporates other active III-V devices such as amplifiers, modulators and photodiodes (PDs) made from the nano-ridges. We have taken the first step to interface the nano-ridge with other silicon photonics components with a coupler design in Chapter 6. The next step is to realize the design and optimize the fabrication process. Afterward, the tolerance to fabrication variations and the yield of the nano-ridges lasers and couplers can be tested. Furthermore, the application scope of the III-V nano-ridges can be broadened beyond the on-chip light source. III-V semiconductor, as a material with efficient light-electron interaction, is popular for amplifiers [9], modulators [10] and photodetectors [11] as well. To better develop the diverse active components, we still need to investigate further the optical properties of the nano-ridges like absorption coefficient, optical loss, high-speed properties, and so on.

References

[1] Daehwan Jung, Zeyu Zhang, Justin Norman, Robert Herrick, MJ Kennedy, Pari Patel, Katherine Turnlund, Catherine Jan, Yating Wan, Arthur C Gossard, et al. *Highly reliable low-threshold InAs quantum dot lasers on on-axis (001) Si with 87% injection efficiency*. ACS photonics, 5(3):1094–1100, 2017.

[2] JE Ayers, LJ Schowalter, and SK Ghandhi. *Post-growth thermal annealing of GaAs on Si (001) grown by organometallic vapor phase epitaxy*. Journal of crystal growth, 125(1-2):329–335, 1992.

[3] MG Grimaldi, BM Paine, M-A Nicolet, and DK Sadana. *Ion implantation and low-temperature epitaxial regrowth of GaAs*. Journal of Applied Physics, 52(6):4038–4046, 1981.

[4] Emlyn Huw Rhoderick. *Metal-semiconductor contacts*. IEE Proceedings I-Solid-State and Electron Devices, 129(1):1, 1982.

[5] JL Regolini, S Bodnar, JC Oberlin, F Ferrieu, M Gauneau, B Lambert, and P Boucaud. *Strain compensated heterostructures in the Si1- x- y Ge x C y ternary system*. Journal of Vacuum Science & Technology A: Vacuum, Surfaces, and Films, 12(4):1015–1019, 1994.

[6] Lars Samuelson. *Self-forming nanoscale devices*. Materials today, 6(10):22–31, 2003.

[7] Alan Y Liu and John Bowers. *Photonic integration with epitaxial III–V on silicon*. IEEE Journal of Selected Topics in Quantum Electronics, 24(6):1–12, 2018.

[8] David J Norris, Al L Efros, M Rosen, and Moungi G Bawendi. *Size dependence of exciton fine structure in CdSe quantum dots*. Physical Review B, 53(24):16347, 1996.

[9] Hyundai Park, Alexander W Fang, Oded Cohen, Richard Jones, Mario J Paniccia, and John E Bowers. *A hybrid AlGaInAs–silicon evanescent amplifier*. IEEE Photonics Technology Letters, 19(4):230–232, 2007.

[10] Robert G Walker. *High-speed III-V semiconductor intensity modulators*. IEEE Journal of Quantum Electronics, 27(3):654–667, 1991.

[11] Joost Brouckaert, Gunther Roelkens, Dries Van Thourhout, and Roel Baets. *Thin-film III–V photodetectors integrated on silicon-on-insulator photonic ICs*. Journal of Lightwave Technology, 25(4):1053–1060, 2007.

Fabrication of GaAs nano-ridge lasers

In this appendix, we will describe the fabrication process of the nano-ridge lasers presented in Chapter 4. As aforementioned, the heteroepitaxy of the nano-ridges was accomplished by Imec and afterwards, the material was transferred to Ghent University for post-growth fabrication and device characterization. The target of the post-growth process is to fabricate laser cavities, including FP, index-coupled DFB and loss-coupled DFB cavities, starting from the as-grown nano-ridges. Given the considerable surface topography of the material and complicated InGaP-GaAs-InGaAs-GaAs stacks (topdown), achieving uniform patterning and high-quality dry etching is challenging. The attempt to address these two challenges will also be discussed in the following.

A.1 Optimization of GaAs nano-ridge dry etching

In order to fabricate laser cavities, high-quality dry etching is needed no matter the laser cavity is with mirror-like nano-ridge facets or Bragg gratings. To obtain full nano-ridge facets for FP lasers, etching depth should exceed the height of the nano-ridges, which is $\sim 500\,\text{nm}$. In the case of DFB lasers, Bragg gratings etched at the top of the nano-ridges should avoid touching the top QW layer, whereby the etchable room is limited to a depth of $\sim 150\,\text{nm}$. Although the GaAs nano-ridge consists of different layers of materials, GaAs, as the nano-ridge body, makes up the majority. Considering the above requirements of dry etching, we take a 2-inch GaAs wafer as an etching test sample for process optimization, targeting to achieve

500 nm-deep etching with smooth and vertical sidewalls at speed not exceeding 200 nm/s by using ICP.

The optimized parameters of ICP include the gas recipe, flow rate, chamber temperature T, ICP power, RF power and etch duration. Adjusting these parameters allows control on the etching rate, quality, selectivity and so on. More information can be found in [1]. After testing several recipes and sweeping ICP power and RF power, we found recipe $Cl_2 : Ch_4 : Ar = 8 : 4 : 10$, ICP $P = 75$ W, RF $P = 100$ W, $T = 20\,^{\circ}C$ resulted a smooth sidewall and a reasonable etching speed of ~ 125 nm/min. Figure A.1 shows a pure GaAs sample after three minutes of etching. The roughness of the 512 nm deep sidewall can be seen in the insert.

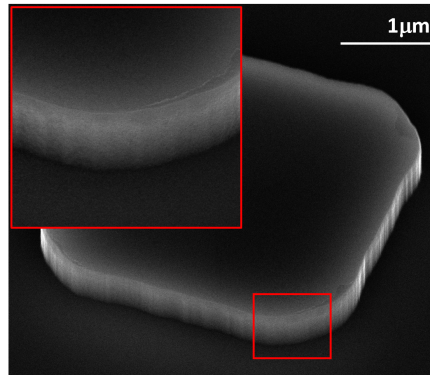

Figure A.1: The SEM image of a GaAs sample after three-minute etching. The insert is a zoom-in image of the sidewall.

Etching the GaAs nano-ridges is more difficult than etching a GaAs sample due to the multi-layer stacks of the material, the nonuniform surface topology and the nanoscale feature sizes of Bragg gratings. Figure A.2 (a) shows the etched facets of a FP device array using an unoptimized etching recipe with a layer of photoresist (AZ5214) as the mask. The nano-ridges were thoroughly etched in the mask opening area, where STI trenches were exposed. Nevertheless, the terrible facet quality is not expected to provide much reflection. It also seems that the etching presents some degree of selectivity on InGaP and GaAs because the layering of the different stacks is visible. Moreover, the photoresist is found to be nonuniform, probably caused by the deformation or burning under high etching temperature. An improved FP facet after optimizing the fabrication is shown in Figure A.2 (b), where EBL was utilized to pattern a single nano-ridge while a more robust SiN hard mask was used during dry etching.

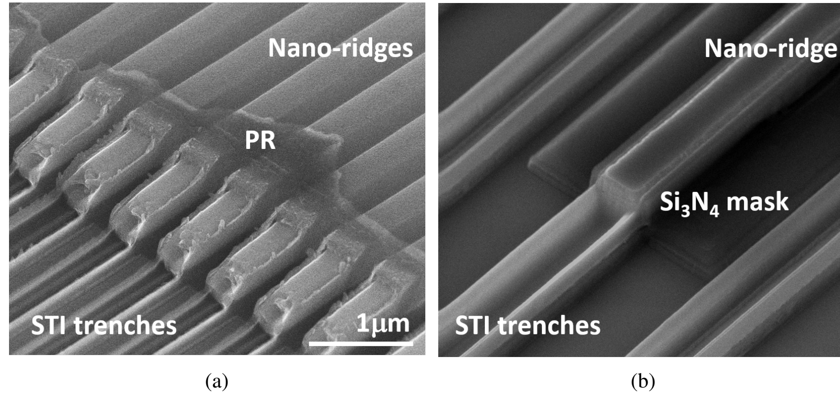

(a) (b)

Figure A.2: (a)The SEM image of etched facets of a FP device array using an unoptimized etching recipe with a layer of photoresist (AZ5214) as mask. (b) The SEM image of an improved FP facet with Si_3N_4 hard mask.

A.2 planarization with BCB

Depending on the trench size, the height of nano-ridges ranges from $400-700$ nm, which introduces a high degree of nonuniformity on the surface. Thus, it is difficult for the following process, especially defining fine structures by EBL. The electron-beam resist is so thin (~ 200 nm) that little resist is expected to be left on the nano-ridges after spin coating due to the nonuniformity. Therefore we developed a planarization process using a layer of BCB (CYCLOTENE 3022-35) with a thickness of $\sim 1.5\,\mu$m. The BCB was spin-coated at a speed of 2000 rpm for 50 s and then soft-baked at $150\,°C$ for 5 min, cured at $270\,°C$ for 5 hr. To etch gratings at the top of the nano-ridges, the top surfaces have to be exposed for access. The exposure was achieved by reactive ion etching (RIE) to etch BCB back by using the recipe $O_2 : SF_6 = 5 : 50$ with an etch rate of 350 nm/min. The planarized nano-ridge is shown in Figure A.3 (a), where the height contract can be well controlled within 100 nm. As a polymer dielectric with refractive index $n \approx 1.5$, BCB was selected for the planarization process due to its easy handling and decent planarizing effect, which could reduce the degree of nonuniformity to 10% of the initial difference. Nevertheless, BCB with a low boiling point ($\sim 180\,°$C) is a quite unstable material during fabrication. SiO_2, as a standard dielectric in CMOS process, appears to be a better option for planarizing the sample. Imec has obtained high uniformity by using a chemical-mechanical polishing (CMP) step after depositing a thick layer of SiO_2 on the nano-ridges.

The planarized nano-ridge is shown Figure A.3 (a), where exhibits a height contrast of 40 nm after etching back BCB. Figure A.3 (b) shows the same sample

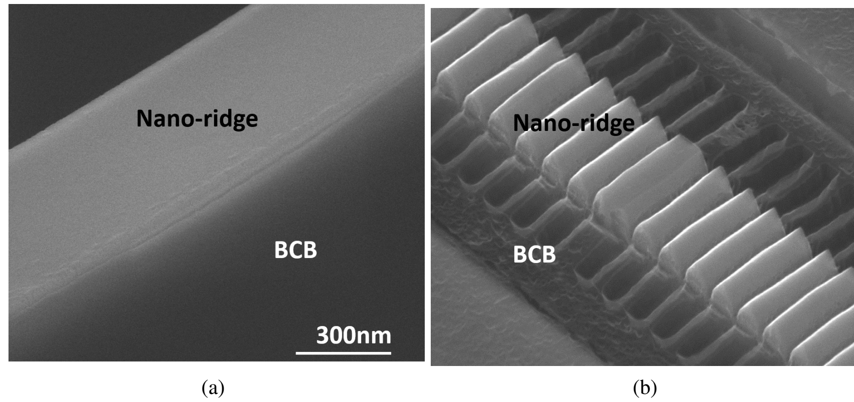

(a) (b)

Figure A.3: a)The SEM image of a planarized nano-ridge. (b)The SEM image of the same sample after dry etching grating at the top of the nano-ridge.

but with the Bragg grating dry-etched at the top of the nano-ridge. The etched grating on the BCB layer shows the poor stability of BCB during dry etching.

A.3 Metalization for loss-coupled DFB laser

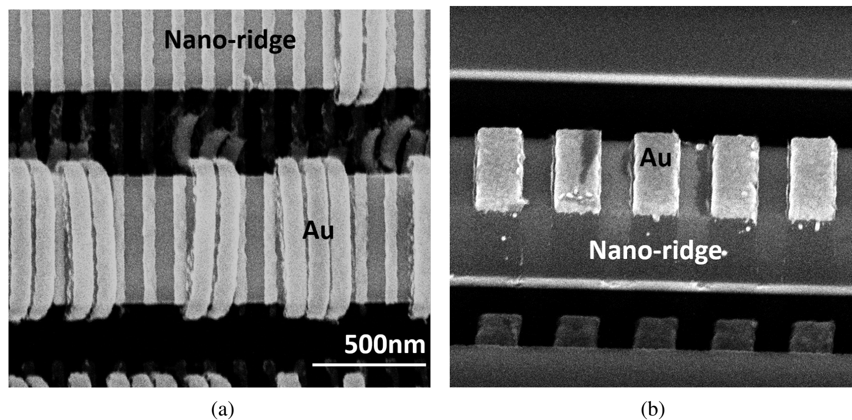

(a) (b)

Figure A.4: (a) The top view of an incompletely lifted-off sample with 80 nm *thick Au (b) The tilted view of a complete lifted-off sample.*

The main challenge in metallization for the loss-coupled DFB laser remains on the complete lift-off of the metal layer. The metallic residual is problematic as it can introduce high optical loss that inhibits lasing. The non-uniform topology and

the thin electron-beam resist ($\sim$ 200 nm on a flat substrate but thinner on protruding nano-ridges) already complicate lift-off process. Using positive-tone resist to reduce the exposure time further increases the lift-off area, which, in other words, requires longer lift-off time. Fortunately, negative sidewalls give by the positive-tone electron-beam resist (opposite to light-beam lithography where negative-tone resist gives negative sidewalls) helps lift-off. Reducing the thickness of the metal layer also eases the lift-off process. Figure A.4 (a) shows a top view of an incompletely lifted-off sample with 80 nm thick Au after soaking in acetone for 4 hrs. The sample shown in Figure A.4 (b) was fabricated with a reduced metal thickness (50 nm) and left in acetone overnight on a gentle shaker for complete lift-off.

References

[1] Russ A Morgan. *Plasma etching in semiconductor fabrication*. 1985.

B
Heating of nano-ridge laser device

The self-heating effect and local intensive power distribution are some of the key reasons for device instability and degradation. In terms of PICs, where high optical power is always demanded for high signal-to-noise ratio, active components such as lasers and modulators are typically intensively powered. Part of the power supply raises the temperature even up to $200\,^{\circ}\mathrm{C}$ and generates severe heat problems if no heat spreader is presented. As the optical gain is reduced with increased temperature [1] due to the increment of non-radiative recombination, lasers are proved to suffer from depressed output power, increased threshold and short lifetime under high temperature [2]. Moreover, wavelength-selective devices, such as micro-rings, are so susceptible to fluctuations in temperature [3] such that unstable behaviors can be triggered by the thermal coupling from adjacent heated-up devices. Therefore, efficient thermal management is not only an important design concern for ultra-dense electronics integrated circuits but also for PICs.

In this appendix, we set up a steady-state thermal simulation for the $\lambda/4$-shifted DFB nano-ridge laser described in Section 4.3 to get an insight into its working temperature and possible heat dissipation approaches. A finite-element solver COMSOL [4] is used to carry out the simulation. First, the trench width's impact on heating temperature was investigated under the optical pump intensity of the laser's threshold. Followed by this, the thermal situation of nano-ridges grown on a SOI substrate was calculated for three scenarios: as-grown nano-ridges, nano-ridge with $2\,\mu$m SiO_2 planarization, nano-ridge with planarization and metallization.

In line with the geometry of the $\lambda/4$-shifted DFB nano-ridge laser with $100\,\mathrm{nm}$

wide trench in Section 4.3, the simulated object is shown in Figure B.1 (b). The Si substrate is 770 μm thick with a 300 nm thick SiO_2 mask. The area above the nano-ridge and below the substrate is set to be air. The whole simulation region is a rectangle as large as 0.5×1 mm^2 such that the temperature of the boundaries can be kept constant as the ambient temperature (room temperature 20 °C). The initial temperature of the simulated region was set to 20 °C too. In the case of the $\lambda/4$-shifted DFB nano-ridge laser with 100 nm-wide trench, whose threshold was extracted to be $I_{th} = 37$ mW, the power of the heat source can be estimated by assuming the pumping efficiency is 10% while the other 90% (33.3 mW) of the pump converts to heat. The density of the heat source is directly calculated to be 1.83×10^{15} W/m^3 by dividing the heat power by the nano-ridge volume. The simulation result is calculated by the module *Heat Transfer in Solids* under the above boundary conditions and initial values. Figure B.1 (b) shows that the QWs remain 55 °C (the stationary temperature) under the laser threshold. The severe heating probably suppresses the device from CW lasing.

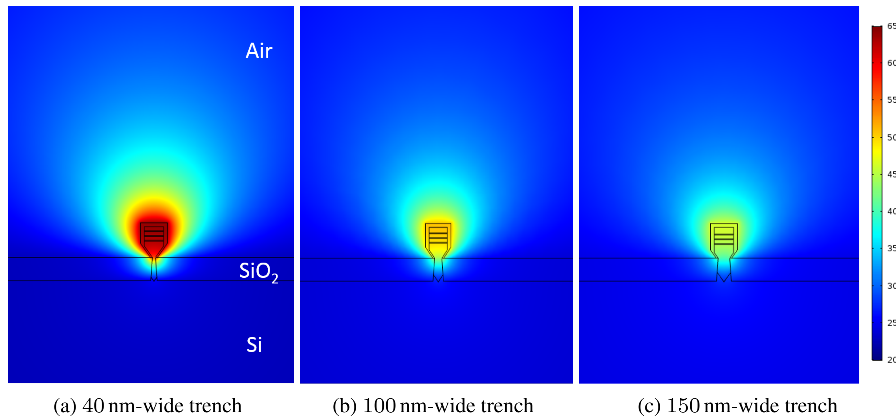

(a) 40 nm-wide trench (b) 100 nm-wide trench (c) 150 nm-wide trench

Figure B.1: The steady-state thermal simulation results under 37 mW optical excitation (threshold) for nano-ridge with (a) 40 nm-wide trench, (b) 100 nm-wide trench and (c) 150 nm-wide trench respectively.

The results show in Figure B.1 (a) and (c) are calculated at the same conditions with (b) except that the trench widths are 40 nm and 150 nm respectively. The highest stationary temperature 63 °C comes from the narrowest 40 nm-wide trench, while nano-ridge with 150 nm-wide trench is heated to a relative low temperature of 46 °. This is as expected because Si with a thermal conductivity of 130 $W/(m \cdot K)$ dissipates heat much faster than air and SiO_2 (thermal conductivity 1.4 $W/(m \cdot K)$) and the wider GaAs (thermal conductivity 33 $W/(m \cdot K)$) trench, enables a broader channel for thermal flow towards Si.

SOI substrate is widely used in PICs where the leakage loss of Si waveguides

is significantly decreased compared to that on Si substrate. Besides, growing nano-ridges on SOI is an essential enabling precondition to realize the coupling between III-V and Si waveguides, as we proposed in Chapter 6. Consequently, the thermal simulation shown in Figure B.2 considers the case of growth on SOI substrate for future development. The SOI substrate consist of a 350 nm thick Si layer on a 2 μm thick buried SiO_2 layer. After STI process, which introduces a 300 nm thick SiO_2 isolation in the top Si layer, the left Si layer is 50 nm thick (process flow see Figure 6.3). The geometry and thermal conditions of the nano-ridge are set the same as the 100 nm trench in Figure B.1 (b). Due to the lack of bulk Si as a heat sink, the heating of the nano-ridge becomes exceptionally severe, with the temperature boosting to $110\,^\circ$. Planarizing the nano-ridge with 2 μm thick SiO_2 declines the temperature to $89\,^\circ$. Metallization with Au (thermal conductivity of $317\, W/(m \cdot K)$) of the nano-ridge for electrical injection further decreases the temperature to $65\,^\circ$.

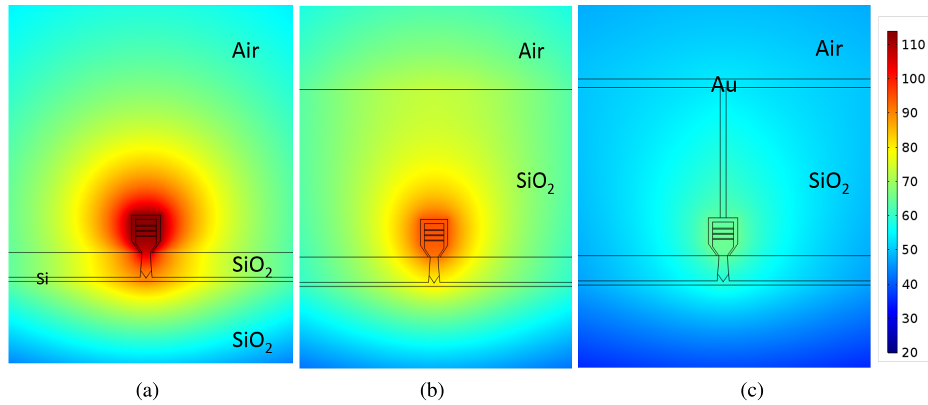

Figure B.2: Thermal simulation of 100 nm-wide-trench nano-ridge at an optical pump of 37 mW of (a) nano-ridge grown on SOI substrate, (b) nano-ridge grown on SOI substrate planarized with 2 μm SiO_2, (c) nano-ridge with SiO_2 planarization and Au metallization.

Given that the simulated stationary temperature is $55\,^\circ$ for the DFB laser, whereby CW excitation was not successfully demonstrated, $65\,^\circ$ is already a risky operation temperature for the laser. To apply better thermal management and guarantee the long-term stability of the laser on SOI substrate, inserting an extra heat sink could be one of the solutions.

References

[1] Hiroshi Ishikawa and Ikuo Suemune. *Analysis of temperature dependent optical gain of strained quantum well taking account of carriers in the SCH layer*. IEEE photonics technology letters, 6(3):344–347, 1994.

[2] Hajime Shoji, Yoshiaki Nakata, Kohki Mukai, Yoshihiro Sugiyama, Mitsuru Sugawara, Naoki Yokoyama, and Hiroshi Ishikawa. *Temperature dependent lasing characteristics of multi-stacked quantum dot lasers*. Applied physics letters, 71(2):193–195, 1997.

[3] Magdalena S Nawrocka, Tao Liu, Xuan Wang, and Roberto R Panepucci. *Tunable silicon microring resonator with wide free spectral range*. Applied physics letters, 89(7):071110, 2006.

[4] *COMSOL Multiphysics is a cross-platform finite element analysis, solver and multiphysics simulation software.* `https://https://www.comsol.com/`. Accessed: 23-09-2019.